



University  
of Glasgow

McHugh, Niall (2024) *Search for time-dependent CP violation in  $D^0 \rightarrow \pi^+ \pi^- \pi^0$  decays and precision luminosity measurements at LHCb*. PhD thesis

<http://theses.gla.ac.uk/84456/>

Copyright and moral rights for this work are retained by the author

A copy can be downloaded for personal non-commercial research or study, without prior permission or charge

This work cannot be reproduced or quoted extensively from without first obtaining permission in writing from the author

The content must not be changed in any way or sold commercially in any format or medium without the formal permission of the author

When referring to this work, full bibliographic details including the author, title, awarding institution and date of the thesis must be given



Enlighten: Theses

<https://theses.gla.ac.uk/>  
[research-enlighten@glasgow.ac.uk](mailto:research-enlighten@glasgow.ac.uk)

# Search for time-dependent $CP$ violation in $D^0 \rightarrow \pi^+ \pi^- \pi^0$ decays and precision luminosity measurements at LHCb

NIALL MCHUGH

Supervised by PROF. PAUL SOLER



University  
of Glasgow | School of Physics  
& Astronomy

University of Glasgow  
Department of Physics and Astronomy

*Submitted in fulfilment of the requirements  
for the degree of Doctor of Philosophy*

---

# Abstract

---

The results of an absolute luminosity measurement at the LHCb experiment and a search for time-dependent  $CP$  violation in  $D^0$  meson decays are presented in this thesis. An overview of the underlying theory relevant to time-dependent  $CP$  violation in the neutral meson systems is also provided, with a particular focus on neutral charmed-mesons. The LHCb detector that recorded the data used for these measurements is also described in detail, along with its recent upgrade for Runs 3 and 4 of the LHC.

An absolute determination of the luminosity at the LHCb experiment between 2016 and 2018 in  $pp$  collisions at  $\sqrt{s} = 13$  TeV is obtained by directly reconstructing the beam profiles from beam-gas interactions. A cross section of

$$\sigma_{\text{Vertex}} = 58.00 \pm 0.02 (\text{stat}) \pm 0.46 (\text{syst}) \text{ mb}$$

for the Vertex counter is obtained, with a preliminary relative precision of 0.83%. The largest systematic uncertainties arise from corrections to the beam-gas vertex resolution, measurement spread believed to be caused by an imperfect bunch profile description, and uncertainty on the bunch current measurements. The dominant systematic uncertainties are largely uncorrelated with the complementary van der Meer analysis. The combination of the two measurements therefore has the potential to be the most precise determination of the absolute luminosity at a hadron collider to date.

A measurement of time-dependent  $CP$  violation in  $D^0 \rightarrow \pi^+\pi^-\pi^0$  decays collected by the LHCb experiment in 2012 and from 2015 to 2018, corresponding to an integrated luminosity of  $7.7 \text{ fb}^{-1}$ , is also presented. The flavour of each  $D^0$  candidate is determined from the decay  $D^*(2010)^+ \rightarrow D^0\pi^+$ . Detection asymmetries are corrected with a data-driven weighting procedure. The gradient of the time-dependent

$CP$ -asymmetry,  $\Delta Y$ , is measured to be

$$\Delta Y = (-1.3 \pm 6.3 \text{ (stat)} \pm 2.4 \text{ (syst)}) \times 10^{-4},$$

which is compatible with  $CP$  conservation. The decay  $D^0 \rightarrow K^-\pi^+\pi^0$  is used as a control channel to validate the measurement procedure. After correcting for detection asymmetries, the control channel is also found to be compatible with no time-dependent  $CP$  asymmetry.

---

# Acknowledgements

---

The past three and a half years have been an incredible journey, which would not have been possible without the support and advice of far too many people to mention explicitly; I hope, however, to briefly highlight the most significant here.

Firstly, I owe a great debt of gratitude to my supervisor, Paul, and to Michael and Patrick with whom I have worked closely throughout my PhD. Their endless patience, particularly in the face of my great ignorance of the field three and a half years ago (and arguably still today), and generosity with their time has allowed me to greatly improve my knowledge of particle physics, develop a wide range of new skills, and produce the work contained in this thesis. I am particularly indebted to Paul for his constant guidance and support, both academic and otherwise, throughout my PhD and for his careful reading of and useful comments to improve this thesis. To Michael, I am extremely grateful for introducing me to LHCb and the world of flavour physics in the first place, for supervising me during my summer and masters projects, and for providing the ideas behind the  $CP$  violation measurement presented here. To Patrick, I also owe a great deal of thanks for sharing his knowledge (and at times incredibly detailed and useful notes) of all things LHCb, and otherwise, whenever I had a question.

I have always found everyone else in the Glasgow LHCb group to be similarly approachable and generous with their time, particularly Lucia, Mark and Manuel outside those I have already mentioned. I am specifically grateful to Manuel for welcoming me to Geneva and CERN, and for teaching me many useful things about physics, and statistics, during my stay. To Aleksandrina and Hasret I would like to wish good luck in the remainder of their PhDs. I look forwards to continuing to work with the rest of the Glasgow group, including Gary and Naomi, over the coming years.

During my 12 months in Geneva I was fortunate enough to meet many new

colleagues and friends from the wider LHCb and LHC community. In particular, I wish good luck to Aidan, Alex and Dan in finishing writing up their theses, and I hope our paths continue to cross in the future. I am particularly grateful to Elena for supporting the 2022 ghost charge measurements (and to Patrick for writing the trigger lines at extremely short notice). I am thankful to the wider luminosity group for their support with the beam-gas imaging measurements, in particular to Vladik, Fabio, Elisabeth and Valeriia for their feedback on how to improve the analysis. On the topic of reviewers, I am grateful to Dominik, Giulia, Jacco, Ao and Jolanta for their many useful suggestions on our  $CP$ -violation analysis.

I would also like to thank my examiners, Paul Harrison and Craig Buttar, for their thorough reading of this thesis, helpful comments to improve it, and for managing to make the defence a (relatively) enjoyable experience.

Outside of physics, I owe a great debt to all of my friends and family for all of their support and enthusiasm for my work. In particular, I am grateful to my parents for their constant support, both throughout my PhD and earlier education, and all other facets of life. Collectively, I would like to thank them together with my siblings, Ciaran, Niamh and Ronan, for listening to my ramblings about my work, and for always keeping me grounded.

Finally, I would like to specifically thank my wife, Jemma, for helping preserve my sanity and for her unending support and encouragement. In particular, I am extremely grateful for her accompanying me in Geneva for the latter 7 months of my LTA, and affording us the chance to experience many new cultures and see many new places together. I look forward to welcoming our little one later in the year, and I cannot wait to see what new experiences the future holds for us.

---

# Declaration

---

The research results presented in this thesis are the product of my own work. Appropriate references are provided when results of third parties are mentioned. The research presented here was not submitted for another degree in any other department or university.

*Niall McHugh*

---

# Preface

---

This thesis presents the results of a search for time-dependent  $CP$  violation in multi-body  $D^0$  decays, and a measurement of the absolute luminosity at the LHCb interaction point. Both analyses were carried out in their entirety by the author, with regular support from Michael Alexander, Paul Soler and Patrick Spradlin. The luminosity analysis was built on previous works by Colin Barschel and George Coombs who performed similar analyses using the Run 1 and 2016 LHCb luminosity calibration datasets, respectively, although the analysis software has been entirely redeveloped by the author for this measurement.

Chapter 1 presents an introduction to the mathematical formulation of the Standard Model of particle physics. A particular emphasis is placed on the weak interactions, which provide mechanisms for mixing and  $CP$  violation in the neutral meson systems, which are of particular relevance to this thesis. The formalism of mixing and  $CP$  violation in  $D^0$  decays is presented, and expressions for the time-dependent  $CP$  asymmetries in both  $CP$ -eigenstate and multi-body decays are derived. It is demonstrated that the decay channel of interest here,  $D^0 \rightarrow \pi^+\pi^-\pi^0$ , is an ideal candidate for a phase-space integrated, time-dependent  $CP$  violation measurement. A short study is presented to estimate the value of the corresponding time-dependent asymmetry in the channel  $D^0 \rightarrow K^-\pi^+\pi^0$  to motivate its usefulness as a control channel for this analysis.

Chapter 2 provides a detailed overview of the LHCb detector that was operational during Runs 1 and 2 of the LHC. Particular emphasis is placed on the VELO, the performance of which is crucial for both analyses presented in this thesis. Overviews of charged track and  $\pi^0$  reconstruction in the LHCb detector are presented. The SMOG system, which allows a significant increase in the number of events collected for the luminosity measurements presented here is discussed. Finally, an overview of the recently upgraded LHCb detector is presented.

Chapter 3 presents an introduction to methods for absolute luminosity measurements at the LHC. Components which are common to different analysis techniques, namely the determination of the relative luminosity and bunch populations, are presented. The analysis work in this chapter was carried out by the author, using measurements of the bunch populations from LHC instrumentation as an input.

Chapter 4 presents the results of the beam-gas imaging analysis to calibrate the absolute luminosity in  $pp$  collisions at  $\sqrt{s} = 13$  TeV at the LHCb experiments in Run 2 of the LHC. Particular focus is given to the determination of the overlap integral, which forms the main component of the analysis. The analysis work in this chapter was carried out entirely by the author.

Chapter 5 describes the selection requirements applied to the LHCb datasets to select  $D^0 \rightarrow h^- \pi^+ \pi^0$  candidates. A detailed description of the requirements applied at each online and offline stage is presented. Studies for potential sources of misidentified and mis-reconstructed backgrounds are presented. The offline selection presented in this chapter was developed by the author.

Chapter 6 presents the measurement of the time-dependent  $CP$  asymmetry gradient  $\Delta Y$ . The weighting procedure used to correct for detection asymmetries is described in detail. The blinding procedure used to avoid experimenters' bias is presented. Finally, the unblinded results of the analysis are presented. The results of the control channel used to validate the measurement are also shown. The analysis work in this chapter was carried out entirely by the author.

Chapter 7 describes studies performed to determine the systematic uncertainties associated with the measurement of  $\Delta Y$ . A detailed description of the treatment of each potential source of systematic uncertainty is provided, and the final uncertainties obtained for both the signal and control channels are presented. Several cross-checks which were performed to validate the measurement are also described. The analysis work in this chapter was carried out entirely by the author.

Chapter 8 presents a summary and conclusion of the entire thesis, and briefly motivates the potential directions of future studies in the two areas presented in this thesis.

---

# Contents

---

<b>Abstract</b>	<b>i</b>
<b>Acknowledgements</b>	<b>iii</b>
<b>Declaration</b>	<b>v</b>
<b>Preface</b>	<b>vi</b>
<b>List of Tables</b>	<b>xii</b>
<b>List of Figures</b>	<b>xv</b>
<b>1 The Standard Model and <math>CP</math> violation</b>	<b>1</b>
1.1 Particle content . . . . .	2
1.2 Mathematical formulation of the Standard Model . . . . .	3
1.2.1 Symmetries as a guiding principle . . . . .	4
1.2.1.1 Quantum electrodynamics . . . . .	4
1.2.1.2 An aside: discrete symmetries . . . . .	5
1.2.1.3 The electroweak force . . . . .	6
1.2.1.4 Spontaneous symmetry breaking and the CKM matrix	9
1.2.1.5 Quantum chromodynamics . . . . .	13
1.3 Mixing and $CP$ violation in the neutral meson systems . . . . .	14
1.3.1 Classification of $CP$ violation . . . . .	18
1.3.2 Mixing behaviour in the different neutral meson systems . . .	19
1.3.3 The time-dependent $CP$ -violating parameter $\Delta Y$ . . . . .	21
1.3.3.1 The parameter $A_\Gamma$ . . . . .	23
1.3.4 Accessing $\Delta Y$ with multi-body final states . . . . .	24
1.3.5 The analogous parameter $\Delta Y_{K\pi\pi}$ . . . . .	28

1.4	Summary . . . . .	30
<b>2</b>	<b>The LHCb Experiment at the LHC</b>	<b>31</b>
2.1	The LHC accelerator complex . . . . .	32
2.2	The LHCb detector . . . . .	34
2.2.1	Vertex LOcator . . . . .	35
2.2.2	Magnet . . . . .	41
2.2.3	Tracking stations . . . . .	42
2.2.3.1	Silicon tracker . . . . .	42
2.2.3.2	Outer tracker . . . . .	44
2.2.4	Track reconstruction . . . . .	46
2.2.5	Tracking performance . . . . .	50
2.2.6	Ring Imaging CHerenkov detectors . . . . .	53
2.2.7	Calorimeters . . . . .	56
2.2.7.1	Neutral pion reconstruction . . . . .	57
2.2.8	Muon stations . . . . .	58
2.2.9	Particle identification performance . . . . .	60
2.2.10	Trigger . . . . .	60
2.2.10.1	Level-0 trigger . . . . .	61
2.2.10.2	High-level trigger . . . . .	62
2.2.11	System for Measuring Overlap with Gas . . . . .	63
2.2.12	The LHCb upgrade . . . . .	64
2.3	Summary . . . . .	66
<b>3</b>	<b>Luminosity measurements at the LHC</b>	<b>68</b>
3.1	Luminosity calibration fills in Run 2 . . . . .	71
3.1.1	Data taking instabilities . . . . .	72
3.2	Bunch population measurements . . . . .	73
3.2.1	Overview of LHC instrumentation . . . . .	73
3.2.2	Ghost and satellite charge corrections . . . . .	74
3.2.3	Systematic uncertainties . . . . .	78
3.3	Ghost-charge measurements in 2022 . . . . .	82
3.4	Relative luminosity measurements . . . . .	84
3.4.1	Counter definitions . . . . .	84
3.4.2	Measurements of the interaction rate . . . . .	85

3.4.2.1	Background subtraction . . . . .	85
3.4.2.2	Efficiency correction . . . . .	87
3.4.3	Systematic uncertainties . . . . .	87
3.5	Summary . . . . .	90
<b>4</b>	<b>Absolute luminosity determination at LHCb</b>	<b>92</b>
4.1	Useful definitions . . . . .	92
4.2	Primary vertex selections . . . . .	93
4.3	Overlap integral measurements . . . . .	94
4.3.1	Overlap integral in the case of Gaussian beams . . . . .	94
4.3.2	Crossing angle measurements . . . . .	96
4.3.3	Vertex resolution measurements . . . . .	98
4.3.3.1	Determination with the split-vertex method . . . . .	98
4.3.3.2	Differences with respect to previous measurements . . . . .	100
4.3.3.3	Global correction factor on the vertex resolution . . . . .	101
4.3.4	Transverse bunch profile fits . . . . .	103
4.3.4.1	One-dimensional description of the bunch profiles . . . . .	104
4.3.4.2	Non-factorisable description of the bunch profiles . . . . .	105
4.3.5	Longitudinal bunch profile fits . . . . .	106
4.3.6	Systematic uncertainties on the overlap integral . . . . .	109
4.4	Final cross section determination . . . . .	114
4.5	Summary . . . . .	120
<b>5</b>	<b>Selection of <math>D^0 \rightarrow h^- \pi^+ \pi^0</math> candidates</b>	<b>121</b>
5.1	Definitions of kinematic variables . . . . .	121
5.2	Event selection and reconstruction . . . . .	123
5.2.1	Trigger selection . . . . .	123
5.2.2	Stripping selection . . . . .	125
5.2.3	Offline selection and reconstruction . . . . .	126
5.2.4	Mis-identified and mis-reconstructed backgrounds . . . . .	131
5.2.5	Final signal yields . . . . .	134
5.3	Summary . . . . .	136
<b>6</b>	<b>Measurement of <math>\Delta Y</math></b>	<b>138</b>
6.1	Origin and correction of detection asymmetries . . . . .	138
6.1.1	Origin of detection asymmetries . . . . .	138

6.1.2	Correction of detection asymmetries . . . . .	139
6.1.3	Dilution of measured $\Delta Y$ due to kinematic weighting . . . . .	143
6.2	Measurement of $\Delta Y$ . . . . .	145
6.2.1	Blinding strategy . . . . .	147
6.3	Final results . . . . .	147
<b>7</b>	<b>Systematic uncertainties and stability checks</b>	<b>154</b>
7.1	Choice of $\Delta m$ fit model . . . . .	154
7.1.1	Test of underestimation of $\sigma_{\text{stat}}$ . . . . .	154
7.1.2	Test of bias from $\Delta m$ fit model . . . . .	155
7.2	Contamination from secondary decays . . . . .	156
7.2.1	Measurement of the secondary fraction . . . . .	157
7.2.2	Measurement of the secondary asymmetry . . . . .	160
7.2.3	Final secondary contamination systematic . . . . .	161
7.2.4	Potential bias on the mean decay times . . . . .	163
7.3	Choice of decay-time binning scheme . . . . .	163
7.4	Choice of kinematic weighting binning scheme . . . . .	164
7.5	Effect of phase-space efficiency on the $CP$ -even fraction . . . . .	165
7.6	Uncertainty on the $CP$ -even fraction . . . . .	168
7.7	Uncertainty on the $D^0$ meson lifetime . . . . .	169
7.8	Decay-time resolution . . . . .	170
7.9	Phase-space dependent detection asymmetries . . . . .	171
7.9.1	Procedure for determining the detection asymmetry . . . . .	172
7.9.2	Results and toy studies for $D^0 \rightarrow \pi^+ \pi^- \pi^0$ . . . . .	173
7.9.3	Results and toy studies for $D^0 \rightarrow K^- \pi^+ \pi^0$ . . . . .	177
7.9.4	Final detection asymmetry systematic uncertainties . . . . .	178
7.10	Additional cross-checks . . . . .	180
7.10.1	Effect of L0 trigger selections . . . . .	180
7.10.2	Comparison of 2D and 3D kinematic weighting . . . . .	181
7.10.3	Counting method . . . . .	182
7.10.4	Alternative $\Delta m$ fit model . . . . .	183
7.11	Summary . . . . .	184
<b>8</b>	<b>Conclusions and outlook</b>	<b>185</b>

<b>Appendices</b>	<b>188</b>
A Additional selection MVA plots . . . . .	188
A.1 Run 1, merged . . . . .	188
A.2 Run 1, resolved . . . . .	191
A.3 Run 2, merged . . . . .	193
A.4 Run 2, resolved . . . . .	195
A.5 BDT cut optimisation plots . . . . .	197
B Potential bias on the measured time-dependent asymmetry from $D^0 \rightarrow K^- \pi^+ \pi^0$ contamination . . . . .	198
C Additional kinematic weighting plots . . . . .	200
C.1 Kinematic distributions at intermediate weighting steps . . . . .	200
C.2 Kinematic distributions in the signal channel . . . . .	204
D Systematic errors from fit model toy studies . . . . .	208
E Additional $h^+ h'^-$ asymmetry study plots . . . . .	209
E.1 Phase-space distributions of $D_{(s)}^+ \rightarrow 3h$ decays . . . . .	209
E.2 Alternative description of time-dependent $K\pi$ asymmetry maps	209
F Stability checks . . . . .	213
<b>Bibliography</b>	<b>216</b>

---

# List of Tables

---

1.1	Properties of the fundamental bosons in the SM. . . . .	2
1.2	Properties of the leptons in the SM. . . . .	2
1.3	Properties of the quarks in the SM. . . . .	3
1.4	Mixing parameters in each of the heavy neutral meson systems. . . .	19
3.1	Summary of fills studied in this analysis. . . . .	72
3.2	Bunch timing efficiency correction factors applied in the ghost-charge measurements. . . . .	78
3.3	Average ghost-charge measurements from beam-gas imaging for each beam in each calibration fill. . . . .	78
3.4	Average satellite fraction measured for each beam throughout each calibration fill. . . . .	79
3.5	DCCT uncertainties affecting the bunch current scale product of both beams in each calibration fill. . . . .	81
3.6	Definitions of selected counters used in this measurement. . . . .	85
4.1	L0 selections utilised for the BGI analysis in Run 2. . . . .	93
4.2	HLT1 selections utilised for the BGI analysis in Run 2. . . . .	93
4.3	Average crossing angles measured in each calibration fill. . . . .	98
4.4	Summary of the relative size of uncertainties affecting the absolute BGI calibration. The column labelled ‘Contribution’ indicates the reduction in the total uncertainty if the relevant component is removed	119
5.1	HLT1 lines used in this analysis. . . . .	123
5.2	HLT2 lines used in this analysis. . . . .	123
5.3	Selection requirements for the HLT1 lines used in this analysis. . . .	125

5.4	Selection requirements for the Dstr_Hlt2CharmHadD02HHXDst_hhX trigger line. . . . .	126
5.5	Selection requirements for the $D^0 \rightarrow h^+h^-\pi^0$ decays' exclusive HLT2 trigger lines in Run 2. . . . .	127
5.6	Stripping lines used in this analysis. . . . .	127
5.7	Stripping selection requirements. . . . .	128
5.8	Offline cut-based selection requirements. . . . .	129
5.9	Variables used by the offline BDTs for Run 1. . . . .	129
5.10	Variables used by the offline BDTs for Run 2. . . . .	130
5.11	Offline BDT selection requirements. . . . .	132
5.12	Fraction of multiple candidates in each subset of the data. . . . .	132
5.13	List of potential mis-identified or mis-reconstructed background sources.	134
5.14	Fraction of candidates passing each HLT1 line in each sub-sample of the data. . . . .	135
5.15	Fraction of candidates passing each HLT2 line in each sub-sample of the data. . . . .	136
7.1	Contributions to the final secondary contamination systematic. . . . .	163
7.2	Shifts in $F_+$ for each $\pi^0$ category and efficiency representation. . . . .	168
7.3	HLT2 lines used to select $D_{(s)}^+ \rightarrow 3h$ candidates. . . . .	173
7.4	Absolute value of systematic uncertainties affecting $\Delta Y_{\pi\pi\pi}^{\text{eff}}$ ( $\Delta Y_{K\pi\pi}$ ) in the signal (control) channel. . . . .	184
8.1	Results of combining the independent sub-samples from each stability test in both the signal and control channels. . . . .	215

---

# List of Figures

---

1.1	$D^0$ - $\bar{D}^0$ mixing diagrams for box-mixing and re-scattering. . . . .	15
1.2	Unnormalised probabilities of mixed and unmixed heavy neutral meson decays. . . . .	20
1.3	Current world average of the time-dependent $CP$ violation parameter $A_\Gamma$ . . . . .	24
1.4	Example Feynman diagrams for the signal and control channels. . . .	28
1.5	Results of toy study to estimate the value of $\Delta Y_{K\pi\pi}$ . . . . .	29
2.1	Layout of the LHC ring. . . . .	32
2.2	Instantaneous luminosity throughout a single fill at ATLAS, CMS, and LHCb. . . . .	33
2.3	Layout of the LHCb detector. . . . .	35
2.4	Two-dimensional angular distribution of $b\bar{b}$ pairs produced at the LHC. . . .	36
2.5	Layout of the LHCb VELO modules. . . . .	37
2.6	Strip layout on a single VELO $r$ - and $\phi$ -sensor. . . . .	38
2.7	VELO hit resolution as a function of strip pitch and track incidence angle. . . . .	39
2.8	Photograph of a single VELO module. . . . .	40
2.9	Layout of the VELO modules inside the RF box for one VELO half. . . .	40
2.10	Diagram and magnetic field distribution of the LHCb magnet. . . . .	42
2.11	Layout of one layer and one half-module of the TT. . . . .	43
2.12	Layout of the IT modules in a single layer of a tracking station. . . .	44
2.13	Layout of OT modules around the IT. . . . .	45
2.14	Layout of an OT module and a single straw tube. . . . .	46
2.15	Example hit efficiency curve from a single straw tube of the OT. . . .	46
2.16	Example iterative one-dimensional Kalman fit procedure. . . . .	48

2.17	Illustration of the different track types defined within the LHCb detector. . . . .	48
2.18	Relative momentum and mass resolution measured with the LHCb detector. . . . .	50
2.19	Long track reconstruction efficiency measured with the LHCb detector.	51
2.20	Primary vertex and impact resolution measured with the LHCb VELO.	52
2.21	Decay time resolution measured with the LHCb detector. . . . .	52
2.22	RICH1 layout and Cherenkov angle versus momentum for various particle species and radiator materials. . . . .	53
2.23	RICH2 layout and arrangement of HPDs. . . . .	54
2.24	Diagram and photograph of a RICH HPD. . . . .	55
2.25	Layout of tiles and modules in the LHCb calorimeter. . . . .	55
2.26	Arrangement of absorber and sampling layers in the HCAL. . . . .	57
2.27	Layout of the muon stations and absorbers. . . . .	58
2.28	Layout of regions and pads within the muon stations. . . . .	59
2.29	PID performance of the LHCb detector. . . . .	60
2.30	Flowchart for the LHCb trigger operation in Runs 1 and 2. . . . .	61
2.31	Layout of the SMOG system. . . . .	63
2.32	Layout of the upgraded LHCb detector. . . . .	64
2.33	Distribution of beam-gas vertices collected with SMOG2 gas-injection.	65
2.34	Layout of the PLUME luminometer . . . . .	66
3.1	Average split vertex position distribution in the $y$ -direction for beam 2-gas collisions with $z \in (250, 1000)$ mm in BCID 975 of Fill 6012, Run 195818 with a Gaussian fit overlaid. . . . .	73
3.2	DCCT measurements from systems A and B for both beams in each calibration fill. . . . .	75
3.3	Ratio of DCCT system A to system B measurements for both beams in each calibration fill. . . . .	76
3.4	Illustration of the definitions of ghost and satellite charges. . . . .	77
3.5	Ghost-charge measurements for each calibration fill in this analysis. .	79
3.6	Comparison between LHCb and BSRL ghost-charge measurements in fill 8379. . . . .	82
3.7	Comparison between LHCb and BSRL ghost-charge measurements in fill 8381. . . . .	83

3.8	Distribution of interaction rate measurements for the Track and Vertex counters before and after beam-gas background subtraction in each integration period for each BCID. . . . .	86
3.9	Ratio of interaction rate measurements for the Track and Vertex counters before and after beam-gas background subtraction in each integration period for each BCID. . . . .	88
3.10	Efficiency of interactions for the Track and Vertex counters as a function of luminous region center, assuming $\sigma_{zl} = 50$ mm. . . . .	89
3.11	Ratio of interaction rate measurements for the PV3D counter before and after beam-gas background subtraction in each integration period for each BCID. . . . .	89
3.12	Ratio of the Track to Vertex and PV3D to Vertex counters for all calibration measurements in this analysis. . . . .	90
4.1	Example crossing angle measurement from Fill 4937, Run 174627. . .	97
4.2	Half-crossing angle measurements for each run considered in this measurement. . . . .	97
4.3	Beam-gas vertex resolution parameterisations in the $x$ -axis for fill 4937, run 174630. . . . .	100
4.4	Example beam-gas vertex resolution fit. . . . .	100
4.5	Linear fit to the dependence of the Vertex cross section on the beam-gas vertex resolution in each fill, and a fit to the measured gradient across all fills. . . . .	102
4.6	Split-vertex resolution versus true vertex resolution on a simulated 2016 pHe beam 1 sample for the $x$ -axis and $y$ -axis. . . . .	103
4.7	Vertex cross section versus beam-gas resolution gradients after correction and dependence of the combined gradient on the global resolution correction factor. . . . .	104
4.8	Overlap integral measurements assuming single Gaussian bunch profiles across all calibration fills per-BCID and integration period. . . .	105
4.9	Overlap integral measurements assuming triple Gaussian bunch profiles across all calibration fills per-BCID and integration period. . . .	106
4.10	Ratio of overlap integral measurements assuming single Gaussian and triple Gaussian bunch profiles across all calibration fills per-BCID and integration period. . . . .	107

4.11	Illustration of the luminous region geometry for beams colliding with and without an offset in the $x$ -direction. . . . .	108
4.12	Relative vertex reconstruction efficiency as a function of longitudinal position from simulation. . . . .	109
4.13	Example fit to the luminous region vertex distribution and split-vertex residual distribution for fill 4937, run 174626, BCID 222. . . .	110
4.14	Dependence of the combined Vertex cross section versus beam-gas vertex resolution gradient across all fills on the resolution correction offset. . . . .	111
4.15	Example beam drift measurement for the $x$ -axis of beam 2 in fill 6868, run 211006, integrated across all BCIDs. . . . .	113
4.16	Cross section measurements split by interaction points at which each BCID collides. . . . .	113
4.17	Rate of positive trigger decisions for the Hlt1BeamGasBeam{1,2} trigger lines throughout fill 4937 per $10^{11}$ protons in each beam. . . .	115
4.18	Example rate of selected beam-gas vertices integrated over 5 minutes for each BCID colliding at LHCb over an example run. . . . .	115
4.19	Measured cross section per-fill with statistical uncertainties only. . . .	116
4.20	All cross section measurements using the triple Gaussian bunch profile model. . . . .	116
4.21	Time evolution of quantities entering the cross section calculation for each fill, averaged over all BCIDs. . . . .	118
4.22	All cross section measurements using the single Gaussian bunch profile model. . . . .	118
4.23	Measurement spread of the cross section averaged across individual runs and individual bunches. . . . .	119
5.1	Effect of the constrained reconstruction on $\Delta m$ and decay-time resolutions. . . . .	128
5.2	Output distributions for offline Run 1 BDTs. . . . .	130
5.3	Output distributions for offline Run 2 BDTs. . . . .	131
5.4	Optimisation metric against offline BDT cuts on example subsets of the signal channel data. . . . .	131
5.5	Example resolved category $\Delta m$ distribution before and after offline selection. . . . .	133

5.6	Example merged category $\Delta m$ distribution before and after offline selection. . . . .	133
5.7	Example distributions of $m(D^0)$ after offline selection. . . . .	134
5.8	Fits to the $\Delta m$ distributions of selected candidates in the signal channel.	135
5.9	Fits to the $\Delta m$ distributions of selected candidates in the control channel. . . . .	136
6.1	Example two-dimensional background-subtracted distributions and asymmetries in a subset of the control channel data. . . . .	140
6.2	Example tagging pion kinematic distributions before and after kinematic weighting. . . . .	142
6.3	Example $D^0$ and tagging pion kinematic distributions before and after kinematic weighting. . . . .	143
6.4	Asymmetry-gradient dilution in the signal channel due to the kinematic weighting. . . . .	144
6.5	Asymmetry-gradient dilution in the control channel due to the kinematic weighting. . . . .	144
6.6	Example flavour-tagged fit to the $\Delta m$ distribution used in the asymmetry measurement. . . . .	146
6.7	Example decay-time evolution of the $\Delta m$ signal shape in merged and resolved sub-samples of the control channel data. . . . .	147
6.8	Combination of $\Delta Y_{\pi\pi\pi}^{\text{eff}}$ values for the signal channel across all sub-samples. . . . .	148
6.9	Combination of $\Delta Y_{K\pi\pi}$ values for the control channel across all sub-samples. . . . .	149
6.10	Linear fits to measured $\mathcal{A}_f^{CP}(t)$ at each stage of the weighting procedure for the merged $D^0 \rightarrow \pi^+\pi^-\pi^0$ sub-samples. . . . .	150
6.11	Linear fits to measured $\mathcal{A}_f^{CP}(t)$ at each stage of the weighting procedure for the resolved $D^0 \rightarrow \pi^+\pi^-\pi^0$ sub-samples. . . . .	151
6.12	Linear fits to measured $\mathcal{A}_f^{CP}(t)$ at each stage of the weighting procedure for the merged $D^0 \rightarrow K^-\pi^+\pi^0$ sub-samples. . . . .	152
6.13	Linear fits to measured $\mathcal{A}_f^{CP}(t)$ at each stage of the weighting procedure for the resolved $D^0 \rightarrow K^-\pi^+\pi^0$ sub-samples. . . . .	153
7.1	$\Delta Y$ pull distributions from $\Delta m$ fit model toy studies. . . . .	155
7.2	$\Delta Y$ pull distributions from alternative $\Delta m$ fit model toy studies. . . . .	156

7.3	Comparison of measured and actual secondary fractions from simulated data. . . . .	157
7.4	Example secondary fraction fits to the 2017 <i>MagUp</i> merged control channel sample. . . . .	158
7.5	Example secondary fraction fits to the 2012 <i>MagUp</i> resolved control channel sample. . . . .	159
7.6	Secondary fractions used for the final systematic calculation. . . . .	160
7.7	Secondary asymmetry across all sub-samples of the control channel data. . . . .	161
7.8	$\Delta$ distributions from varying $\mathcal{A}_{\text{meas}}(t)$ , $f_{\text{sec}}(t)$ and $\mathcal{A}_{\text{sec}}$ . A Gaussian fit is overlaid in red. . . . .	162
7.9	Ratio of mean decay-times measured from data and simulation. . . . .	164
7.10	Results of decay-time binning study. . . . .	164
7.11	Results of kinematic weighting binning study. . . . .	165
7.12	Efficiency variation across the Dalitz plot from simulation for both $\pi^0$ categories. . . . .	166
7.13	Efficiency variation across the Dalitz plot from simulation for the merged $\pi^0$ category. . . . .	167
7.14	Efficiency variation across the Dalitz plot from simulation for the resolved $\pi^0$ category. . . . .	167
7.15	Dalitz distribution and CP-even fraction toy results using the BaBar-2016 model in EvtGen. . . . .	169
7.16	Example output of a toy study to investigate the effect of the phase-space efficiency on the <i>CP</i> -even fraction. . . . .	169
7.17	Example decay-time resolution and acceptance fits for the resolved $\pi^0$ category. . . . .	170
7.18	Example individual toy-study results and dilution gradient fit for the decay-time resolution studies. . . . .	171
7.19	$\pi^+\pi^-$ detection asymmetry maps split by parent particle and $\pi^0$ reconstruction category. . . . .	174
7.20	$\pi^+\pi^-$ detection asymmetry maps in the $(\theta_{\pi\pi}, t/\tau_{D^0})$ -plane. . . . .	174
7.21	Linear fit to the time-dependent asymmetry in each $\theta_{\pi\pi}$ bin for the resolved category. . . . .	175
7.22	$A_{\text{det}}^{\pi\pi}$ toy studies without time-dependence in the asymmetry maps. . . . .	176
7.23	$A_{\text{det}}^{\pi\pi}$ toy studies with time-dependence in the asymmetry maps. . . . .	176

7.24	$A_{\text{det}}^{\pi\pi}$ toy studies, with time-dependence, using a single toy dataset and fluctuating the asymmetry maps. . . . .	177
7.25	$K\pi$ detection asymmetry maps. . . . .	177
7.26	$K\pi$ detection asymmetry maps, allowing for a time-dependence. . . .	178
7.27	Linear fit to the time-dependent asymmetry in each $\theta_{K\pi}$ bin for the resolved category. . . . .	179
7.28	$A_{\text{det}}^{K\pi}$ toy studies without time-dependence in the asymmetry maps. . .	179
7.29	$A_{\text{det}}^{K\pi}$ toy studies with time-dependence in the asymmetry maps . . . .	180
7.30	$A_{\text{det}}^{K\pi}$ toy studies, with time-dependence, using a single toy dataset and fluctuating the asymmetry maps. . . . .	180
7.31	Results of L0 trigger selection cross-check. . . . .	181
7.32	Results of 3D kinematic weighting cross-check in the control channel. . .	182
7.33	Results of counting method cross-check in the control channel. . . . .	183
7.34	Comparison of measured time-dependent $CP$ asymmetries using the alternative $\Delta m$ model. . . . .	183
A.1	Input variable distributions for the Run 1 merged BDT. . . . .	189
A.2	Input variable correlations for the Run 1 merged BDT. . . . .	189
A.3	Background rejection against signal efficiency for the Run 1 merged BDT. . . . .	190
A.4	Input variable distributions for the Run 1 resolved BDT. . . . .	191
A.5	Input variable correlations for the Run 1 resolved BDT. . . . .	192
A.6	Background rejection against signal efficiency for the Run 1 resolved BDT. . . . .	192
A.7	Input variable distributions for the Run 2 merged BDT. . . . .	193
A.8	Input variable correlations for the Run 2 merged BDT. . . . .	194
A.9	Background rejection against signal efficiency for the Run 2 merged BDT. . . . .	194
A.10	Input variable distributions for the Run 2 resolved BDT. . . . .	195
A.11	Input variable correlations for the Run 2 resolved BDT. . . . .	196
A.12	Background rejection against signal efficiency for the Run 2 resolved BDT. . . . .	196
A.13	Optimisation metric as a function of BDT cut for the 2012 control channel data, Run 2 signal channel data and Run 2 control channel data. . . . .	197

C.1	2018 <i>MagUp</i> resolved control channel tagging pion kinematic distributions (left) before any kinematic weighting, (center) after the $\pi_{\text{tag}}^{\pm}$ kinematics' weighting and after the full kinematic weighting (right).	200
C.2	2018 <i>MagUp</i> resolved control channel $D^0$ and tagging pion kinematic distributions (left) before any kinematic weighting, (center) after the $\pi_{\text{tag}}^{\pm}$ kinematics' weighting and (right) after the full kinematic weighting.	201
C.3	2018 <i>MagUp</i> merged control channel tagging pion kinematic distributions (right) before any kinematic weighting, (center) after the $\pi_{\text{tag}}^{\pm}$ kinematics' weighting and (right) after the full kinematic weighting.	202
C.4	2018 <i>MagUp</i> merged control channel $D^0$ and tagging pion kinematic distributions (left) before any kinematic weighting, (center) after the $\pi_{\text{tag}}^{\pm}$ kinematics' weighting and (right) after the full kinematic weighting.	203
C.5	2016 <i>MagUp</i> resolved signal channel tagging pion kinematic distributions before (left) and after (right) kinematic weighting.	204
C.6	2016 <i>MagUp</i> resolved signal channel $D^0$ and tagging pion kinematic distributions before (left) and after (right) kinematic weighting.	205
C.7	2016 <i>MagUp</i> merged signal channel tagging pion kinematic distributions before (left) and after (right) kinematic weighting.	206
C.8	2016 <i>MagUp</i> merged signal channel $D^0$ and tagging pion kinematic distributions before (left) and after (right) kinematic weighting.	207
E.1	Phase-space distribution of reconstructed and selected $D^0 \rightarrow K^- \pi^+ \pi^0$ candidates.	209
E.2	Phase-space distribution of reconstructed and selected $D^+ \rightarrow K^- \pi^+ \pi^+$ candidates.	210
E.3	Phase-space distribution of reconstructed and selected $D^0 \rightarrow \pi^+ \pi^- \pi^0$ candidates.	210
E.4	Phase-space distribution of reconstructed and selected $D^+ \rightarrow \pi^+ \pi^+ \pi^-$ and $D_s^+ \rightarrow \pi^+ \pi^+ \pi^-$ candidates.	210
E.5	$K\pi$ detection asymmetry maps split by $\pi^0$ reconstruction category.	211
E.6	Linear fit to the time-dependent asymmetry in each $m^2(K^-, \pi^+)$ bin for the resolved category.	211
E.7	Linear fit to the time-dependent asymmetry in each $m^2(K^-, \pi^+)$ bin for the merged category.	212
E.8	$A_{\text{det}}^{K\pi}$ toy study results with time-dependence parameterised in terms of $m^2(K^-, \pi^+)$ .	212

F.1	Measured asymmetries in the control (left) and signal (right) channels when the data is divided by $\log(\chi_{\text{IP}}^2(D^0))$ . . . . .	213
F.2	Measured asymmetries in the control (left) and signal (right) channels when the data is divided by $D^0$ meson $p_{\text{T}}$ . . . . .	214
F.3	Measured asymmetries in the control (left) and signal (right) channels when the data is divided by tagging pion $p_{\text{T}}$ . . . . .	214
F.4	Measured asymmetries in the control (left) and signal (right) channels when the data is divided by HLT1 trigger line. . . . .	214

# The Standard Model and $CP$ violation

---

THE Standard Model of particle physics (SM) is the most accurate fundamental theory of nature that has ever been devised. Based on a local  $SU(3)_C \times SU(2)_L \times U(1)_Y$  symmetry, it provides a theoretical description of all the known fundamental particles and their interactions. Several important predictions have been made in the development of the SM before their experimental observation, such as parity violation [1], the charm quark [2], the third generation of quarks [3], and the Higgs boson [4, 5]. Despite its many triumphs, there are several obvious flaws with the SM. It does not provide any candidates for dark matter or dark energy, necessary to explain cosmological observations [6]. It does not include a description of the weakest fundamental force, gravity. Perhaps most strikingly, it fails to sufficiently explain why we live in a matter dominated universe and a complete matter-antimatter annihilation did not occur after the Big Bang [7].

This chapter aims to motivate the main concepts behind the SM, in particular the introduction of the gauge bosons which mediate interactions based on the preservation of local symmetries. A discussion of the Brout-Englert-Higgs mechanism — which generates the gauge boson and fermion masses, and allows charge-parity symmetry ( $CP$ ) violation in the SM Lagrangian through complex Yukawa couplings — is presented. The origins of the CKM matrix, which describes the probabilities for charged weak current transitions between the quark generations, are discussed. A more detailed discussion is then provided on the effective theory of mixing and  $CP$  violation in the neutral meson systems, with a particular focus on time-dependent  $CP$  violation in multi-body  $D^0$  decays.

## 1.1 Particle content

Particles in the SM can be grouped into two categories: bosons and fermions. The bosons have integer spin, and are listed in Table 1.1.<sup>1</sup> The spin 1 bosons mediate the interactions between the matter fields: the electromagnetic force is mediated by the photon; the weak force is mediated by the charged  $W^\pm$  bosons and the neutral  $Z^0$  boson; the strong force is mediated by the gluons. The Higgs boson has spin 0, and represents an excitation of the Higgs field which generates the masses of the fermions and weak bosons after spontaneous symmetry breaking (SSB).

Particle	Mass	Spin
$\gamma$	0	1
$W^\pm$	80.36 GeV	1
$Z^0$	91.19 GeV	1
$g$	0	1
$H$	125.11 GeV	0

Table 1.1: Properties of the fundamental bosons in the SM [8].

Particle	Mass	Spin	Electric charge ( $e$ )	Electromagnetic	Weak	Strong
$e$	0.511 MeV	1/2	-1	✓	✓	
$\mu$	106 MeV	1/2	-1	✓	✓	
$\tau$	1.78 GeV	1/2	-1	✓	✓	
$\nu_e$	< 1.0 eV	1/2	0		✓	
$\nu_\mu$	< 0.17 MeV	1/2	0		✓	
$\nu_\tau$	< 18.2 MeV	1/2	0		✓	

Table 1.2: Properties of the leptons in the SM. The last three columns indicate whether each lepton interacts with the gauge bosons of the relevant interaction [8].

Matter is represented by fermions in the SM, which can be further divided into two categories: leptons and quarks. The fermions in the SM have a generational structure, with three somewhat symmetrical generations for both the quarks and leptons. Each generation of leptons contains a charged<sup>2</sup> particle —  $e$ ,  $\mu$  and  $\tau$  — and a corresponding neutral particle —  $\nu_e$ ,  $\nu_\mu$  and  $\nu_\tau$ . All of the leptons interact weakly, and none interact strongly. Some basic properties of each of the leptons are listed in Table 1.2. The quarks also exist in three generations, with each generation

---

<sup>1</sup>Natural units with  $\hbar = c = 1$  will be assumed throughout this thesis, unless explicitly stated otherwise.

<sup>2</sup>In our everyday sense of the word, *i.e.* under electromagnetism.

containing an ‘up-type’ quark with electric charge  $(2/3)e$  and a ‘down-type’ quark with electric charge  $(-1/3)e$ . All of the quarks interact through the strong, weak and electromagnetic interactions. Some basic properties of each of the quarks are listed in Table 1.3.

Particle	Mass	Spin	Electric charge ( $e$ )	Electromagnetic	Weak	Strong
$d$	4.7 MeV	1/2	$-1/3$	✓	✓	✓
$u$	2.2 MeV	1/2	$2/3$	✓	✓	✓
$s$	96 MeV	1/2	$-1/3$	✓	✓	✓
$c$	1.28 GeV	1/2	$2/3$	✓	✓	✓
$b$	4.18 GeV	1/2	$-1/3$	✓	✓	✓
$t$	173.1 GeV	1/2	$2/3$	✓	✓	✓

Table 1.3: Properties of the quarks in the SM. The last three columns indicate whether each lepton interacts with the gauge bosons of the relevant interaction [8].

## 1.2 Mathematical formulation of the Standard Model

The SM is often concisely distilled into a single equation as [9]

$$\begin{aligned}
 \mathcal{L} = & -\frac{1}{4}F_{\mu\nu}F^{\mu\nu} \\
 & + i\bar{\psi}\not{D}\psi \\
 & + |D_{\mu}\Phi|^2 - V(\Phi) \\
 & + \bar{\psi}_i Y_{ij}\Phi\psi_j + h.c.,
 \end{aligned} \tag{1.1}$$

where  $h.c.$  stands for Hermitian conjugate. The first line represents kinetic terms for the gauge fields of the strong and electroweak interactions. The second line contains kinetic terms for the fermions, and interaction terms between the fermions and the gauge fields. The third line represents the kinetic term of the scalar Higgs field and the Higgs potential. The final line contains the Yukawa interactions of the fermions with the Higgs field. The following sections will aim to motivate briefly this structure, and highlight the relationship between the underlying dynamics and mixing and  $CP$  violation in the neutral meson systems.

### 1.2.1 Symmetries as a guiding principle

Symmetries have long held a key role in the mind of theoretical physicists. Perhaps most famously, Einstein's theory of special relativity is built upon the principle that the laws of physics are invariant under Lorentz transformations [10]. More profoundly, Noether showed that conservation laws can be derived from continuous symmetries [11]. More recently, symmetries have played a key role in theoretical particle physics. One of the leading questions in building the SM was the following: *can the dynamics of some Lagrangian be inferred simply from imposing a set of symmetries [12]?*

#### 1.2.1.1 Quantum electrodynamics

The Lagrangian of the Dirac equation for a free fermion field,  $\psi$ , can be written as

$$\mathcal{L} = \bar{\psi}(i\not{\partial} - m)\psi, \quad (1.2)$$

where  $\bar{\psi} = \psi^\dagger \gamma^0$ ,  $\not{\partial} = \gamma^\mu \partial_\mu$ ,  $\gamma^\mu$  are the Dirac matrices and  $m$  is the mass of the fermion. The Einstein summation convention will be assumed throughout this section (1.2) for repeated indices. Such a Lagrangian is already invariant under a global transformation given by

$$\psi \rightarrow e^{-i\alpha} \psi, \quad (1.3)$$

where  $\alpha$  is some real constant. However, if we consider a local transformation,  $\alpha = \alpha(x)$ , Equation 1.2 is no longer invariant. The invariance can be restored by introducing a gauge field,  $A_\mu$ , and covariant derivative,  $D_\mu$ , defined by

$$D_\mu \equiv \partial_\mu + ieA_\mu, \quad (1.4)$$

where  $e$  is some arbitrary coupling strength that can be identified as the electric charge. The gauge field is required to transform as

$$A_\mu \rightarrow A_\mu + \frac{1}{e} \partial_\mu \alpha(x) \quad (1.5)$$

under a local transformation  $\psi \rightarrow e^{-i\alpha(x)}\psi$ . An invariant form of Equation 1.2 can then be written as

$$\begin{aligned}\mathcal{L} &= \bar{\psi}(i\not{D} - m)\psi \\ &= \bar{\psi}(i\not{\partial} - m)\psi - e\bar{\psi}\psi\mathcal{A}.\end{aligned}\tag{1.6}$$

The last term of Equation 1.6 represents a coupling between the fermions and the gauge field. A kinetic term involving the derivative of the gauge field which is also invariant under such a local transformation can be written as

$$-\frac{1}{4}F_{\mu\nu}F^{\mu\nu},\tag{1.7}$$

where  $F_{\mu\nu} = \partial_\mu A_\nu - \partial_\nu A_\mu$  is the field strength tensor. Finally, one can note that a mass term for the gauge field,  $\propto A_\mu A^\mu$ , violates our local symmetry and therefore the gauge field must be massless; the field  $A_\mu$  can therefore be identified as the photon field. The full Lagrangian for QED containing a single fermion field,  $\psi$ , is thus given by

$$\mathcal{L}_{QED} = -\frac{1}{4}F_{\mu\nu}F^{\mu\nu} + \bar{\psi}(i\not{D} - m)\psi.\tag{1.8}$$

We have therefore arrived at a description of QED which includes interactions between a massless gauge field, the photon, and the fermion field,  $\psi$ , ‘simply’ by requiring that the local, continuous symmetry  $\psi \rightarrow e^{-i\alpha(x)}\psi$  is preserved. Such a transformation can also be identified with the group of complex, unitary,  $1 \times 1$  matrices,  $U(1)$  (*i.e.* the group of complex numbers with unit magnitude); our theory of QED is therefore said to be invariant under local gauge transformations of the  $U(1)$  group.

### 1.2.1.2 An aside: discrete symmetries

In addition to the continuous symmetries which provide a theoretical mechanism for introducing interactions to a theory, there exist several important discrete symmetries. Charge conjugation,  $C$ , replaces all particles with their corresponding anti-particles, and therefore reverses the sign of all internal quantum numbers. Parity,  $P$ , inverts spatial coordinates such that  $\vec{r} \rightarrow -\vec{r}$ . Time inversion,  $T$  performs an analogous operation to  $P$  on the time coordinate,  $t \rightarrow -t$ .

The combination of all three transformations,  $CPT$ , is a fundamental symmetry of the SM [13]. When the maximal violation of both  $C$  and  $P$  by the weak interaction was experimentally established in the 1950s [1, 14], the preservation of the  $CP$  trans-

formation was proposed as an alternative symmetry [15]. However,  $CP$  violation in the neutral kaon system was discovered shortly after parity violation. Subsequently, the violation of both the  $C$  and combined  $CP$  symmetry were shown to be necessary conditions for a dynamical generation of the matter-antimatter asymmetry observed in the visible universe to be explained by baryogenesis [16].  $CP$  violation, which allows for an unambiguous definition of what constitutes matter and antimatter has been a vibrant source of both experimental and theoretical effort in recent years.  $CP$  violating effects are now well-established in many hadron decays [15, 17–21], however it is also well-established that the possible size of the  $CP$  violating effects allowed within the SM are insufficient for baryogenesis to completely explain the observed asymmetry within our universe [22]. Measurements of  $CP$  violation are therefore potentially sensitive to beyond the standard model (BSM) effects which generate additional  $CP$  violation. Experimental efforts are also ongoing to search for  $CP$  violation in the neutrino sector [23], where leptogenesis provides an alternative scenario for generating a matter-antimatter asymmetry [24].

### 1.2.1.3 The electroweak force

The arguments presented in Section 1.2.1.1 can straightforwardly be extended to more complex symmetry groups. It was realised in the 1970s that the electromagnetic and weak interactions could be unified into a single interaction, known as the electroweak interaction, under the combined gauge group  $SU(2)_L \times U(1)_Y$  [25–27]. The subscripts ‘ $L$ ’ and ‘ $Y$ ’ stand for left-handed and hypercharge, respectively, to distinguish which objects transform under the symmetry groups. The group  $SU(2)$  contains all  $2 \times 2$  complex, unitary matrices with unit determinant. The weak force is known to maximally violate parity and only couples to ‘left-handed’ fermions (‘right-handed’ anti-fermions) [14]. The ‘handedness’, or chirality, of a massless fermion is defined by whether its spin is oriented parallel (right-handed) or anti-parallel (left-handed) to its direction of motion. The fermion fields can be separated into left- and right-handed parts by introducing the projection operators,  $P_{R,L}$ , which are given by

$$P_{R,L} = \frac{1 \pm \gamma^5}{2}, \quad (1.9)$$

where  $\gamma^5 = i\gamma^0\gamma^1\gamma^2\gamma^3$  is a product of the Dirac matrices. The projection operators have the following properties:  $P_R + P_L = 1$ ,  $P_R P_L = P_L P_R = 0$ , and  $P_{L,R}^2 = P_{L,R}$ .

The fermion fields can then be expressed as

$$\psi = (P_L + P_R)\psi = \psi_L + \psi_R, \quad (1.10)$$

where  $\psi_{L,R} = P_{L,R}\psi$ . Since the weak force only couples to left-handed fermions (right-handed anti-fermions), the structure of the theory should naturally introduce different interactions for the left- and right-handed parts of the fermion fields. This can be achieved by assuming the left-handed fermions form doublets under  $SU(2)_L$ , and the right-handed fermions form singlets (*i.e.* do not transform) under  $SU(2)_L$ . More explicitly, for a single generation of fermions, the electroweak Lagrangian is constructed from lepton terms of the form

$$L_L = \begin{pmatrix} \nu_L \\ e_L \end{pmatrix}, \quad \nu_R, \text{ and } e_R, \quad (1.11)$$

and quark terms of the form

$$Q_L = \begin{pmatrix} u_L \\ d_L \end{pmatrix}, \quad u_R, \text{ and } d_R. \quad (1.12)$$

The right handed neutrinos,  $\nu_R$ , can be ignored — assuming the neutrinos are massless<sup>3</sup> — since they are not charged under the strong or electromagnetic interactions, and the weak force maximally violates parity; thus, they are ‘invisible’ to our theory. The kinetic terms in the electroweak Lagrangian can then be written as

$$\mathcal{L}_{\text{kinetic}} = i\bar{L}_L \not{\partial} L_L + i\bar{e}_R \not{\partial} e_R + i\bar{Q}_L \not{\partial} Q_L + i\bar{u}_R \not{\partial} u_R + i\bar{d}_R \not{\partial} d_R. \quad (1.13)$$

Analogously to the  $U(1)$  case for QED described in Section 1.2.1.1, such a Lagrangian is not invariant under either of the local  $SU(2)_L$  or  $U(1)_Y$  transformations. Again, the solution will be to introduce gauge fields to create covariant derivatives, which will introduce interactions to the theory. The right-handed fermions carry only hypercharge, and so the covariant derivative is almost identical to the QED case,

---

<sup>3</sup>Of course, the existence of neutrino oscillations requires the neutrinos to have some mass. One possibility is that the right-handed neutrinos are so massive that they have eluded observation thus far.

and can be expressed for some right-handed fermion,  $f_R$ , as

$$D_\mu^{f_R} = \partial_\mu + i\frac{g_1}{2}y_{f_R}B_\mu, \quad (1.14)$$

where  $g_1$  is the coupling constant of the  $U(1)_Y$  interaction mediated by the gauge field  $B_\mu$ , and  $y_{f_R}$  is the hypercharge of  $f_R$ . The left-handed fermions also transform under  $SU(2)_L$ , and therefore we must include additional gauge fields to preserve the symmetry. In particular, a local  $SU(2)$  transformation can be expressed in the following way:

$$\psi \rightarrow e^{-i\tau_a\alpha^a(x)}\psi, \quad (1.15)$$

where each  $\tau_a$  represents a Pauli matrix — one choice of representation of the generators of  $SU(2)$  — and each  $\alpha^a(x)$  represents some local transformation parameter. This is entirely analogous to the  $U(1)$  case for QED, with a more complex set of generators for the group  $SU(2)$ . To preserve the symmetry, we introduce a gauge field for each generator, and the covariant derivative for some left-handed doublet,  $D_L$ , is given by

$$D_\mu^{D_L} = \partial_\mu + i\frac{g_1}{2}y_{D_L}B_\mu + i\frac{g_2}{2}\tau_a W_\mu^a, \quad (1.16)$$

where the  $W_\mu^a$  are the gauge fields of the  $SU(2)_L$  symmetry. Finally, kinetic terms for each of the gauge fields are again invariant under the combined symmetry and can be added to the Lagrangian. The electroweak Lagrangian for a single generation of fermions is therefore given by

$$\mathcal{L}_{EW} = \sum_\psi i\bar{\psi}\not{D}\psi - \sum_F \frac{1}{4}F_{\mu\nu}F^{\mu\nu}, \quad (1.17)$$

where the index  $\psi$  runs over the left-handed quark and lepton doublets and the right-handed fermion singlets,  $F_{\mu\nu}$  represents a field strength tensor, and the index  $F$  runs over the gauge fields  $B$  and  $W^a$ . Examining more closely the interaction terms introduced by the gauge fields, it becomes clear they do not align with the ‘physical’ boson mediators introduced in Section 1.1. The interaction terms between the left-handed leptons and the gauge fields can be written as

$$\mathcal{L}_{\text{int}} = - \begin{pmatrix} \bar{\nu}_L & \bar{e}_L \end{pmatrix} g_2 \gamma_\mu \begin{pmatrix} \frac{g_1}{g_2}B_\mu + W_\mu^3 & W_\mu^1 + iW_\mu^2 \\ W_\mu^1 - iW_\mu^2 & \frac{g_1}{g_2}B_\mu - W_\mu^3 \end{pmatrix} \begin{pmatrix} \nu_L \\ e_L \end{pmatrix}. \quad (1.18)$$

The relationships between the physical fields and the gauge fields can be derived by considering each of the terms produced after multiplying out Equation 1.18. The  $W^+$  ( $W^-$ ) boson should couple to the vertex  $\bar{e}_L \nu_L$  ( $e_L \bar{\nu}_L$ ), and therefore we can identify the physical fields as  $W^\pm = \frac{1}{\sqrt{2}}(W_\mu^1 \mp iW_\mu^2)$ . The photon should couple to vertices containing only a pair of charged leptons, whilst the  $Z^0$  boson should couple to both  $ee$  and  $\nu\nu$  vertices. This can be satisfied by introducing the Weinberg angle,  $\theta_W \equiv \arctan(g_1/g_2)$ , such that

$$\begin{pmatrix} A_\mu \\ Z_\mu \end{pmatrix} = \begin{pmatrix} \cos \theta_W & \sin \theta_W \\ -\sin \theta_W & \cos \theta_W \end{pmatrix} \begin{pmatrix} B_\mu \\ W_\mu^3 \end{pmatrix} = \cos \theta_W \begin{pmatrix} 1 & \frac{g_1}{g_2} \\ -\frac{g_1}{g_2} & 1 \end{pmatrix} \begin{pmatrix} B_\mu \\ W_\mu^3 \end{pmatrix}, \quad (1.19)$$

where  $A_\mu$  and  $Z_\mu$  are the fields representing the photon and  $Z^0$  boson, respectively.

Similarly to the QED case, we have now constructed a theory of weak interactions by requiring the invariance of the Lagrangian under the combined symmetry  $SU(2)_L \times U(1)_Y$ . However, there is one significant problem with our formulation of the combined electroweak interactions: all of the particles in the theory are massless. For the gauge bosons, this is no different to the QED case. Contrary to QED, the fact that parity is maximally violated by the weak interaction prevents fermion mass terms from being allowed in the Lagrangian. One can expand a mass-like term for an arbitrary fermion field,  $\psi$ , as

$$\bar{\psi}\psi = \bar{\psi}_L\psi_R + \bar{\psi}_R\psi_L, \quad (1.20)$$

using the properties of the projection operators,  $P_{L,R}$ . Since the left- and right-handed fermions transform differently under  $SU(2)_L$ , such a term is manifestly non-invariant. Therefore, to explain our experimental observation of massive fermions and weak bosons, an alternative approach to introducing masses to the theory must be employed: spontaneous symmetry breaking.

#### 1.2.1.4 Spontaneous symmetry breaking and the CKM matrix

The ideas behind SSB were first introduced by Goldstone for global symmetries [28], and later extended to local gauge symmetries by Higgs, Brout and Englert [4, 5]. The principle of SSB is that a symmetry may be respected by the Lagrangian of a given theory, but broken by the vacuum state of a field. In the single-fermion electroweak model we have introduced in Section 1.2.1.3, this can be achieved by

introducing a complex scalar doublet under  $SU(2)_L$  given by

$$\Phi = \begin{pmatrix} \phi^+ \\ \phi^0 \end{pmatrix}. \quad (1.21)$$

The field  $\Phi$  couples to the gauge bosons through a covariant derivative in the same fashion as Equation 1.16, to itself via a potential term  $V(\Phi^\dagger\Phi)$ , and to the fermions through a set of Yukawa interactions. The additional terms containing  $\Phi$  which are added to the single-generation electroweak Lagrangian can be written as

$$\begin{aligned} \mathcal{L}_\Phi = & -V(\Phi^\dagger\Phi) + |D_\mu^\Phi\Phi|^2 \\ & -\bar{Q}_L Y_u \Phi^c u_R + \bar{u}_R Y_u \Phi^{c\dagger} Q_L \\ & -\bar{Q}_L Y_d \Phi d_R + \bar{d}_R Y_d \Phi^\dagger Q_L \\ & -\bar{L}_L Y_l \Phi e_R + \bar{e}_R Y_l \Phi^\dagger L_L \end{aligned} \quad (1.22)$$

where  $V(\Phi^\dagger\Phi) = -\mu^2(\Phi^\dagger\Phi) + \lambda(\Phi^\dagger\Phi)^2$ ,  $\Phi^c = i\tau_2\Phi$ , and  $Y_{u,d,l}$  are the (real) Yukawa couplings for the up quarks', down quarks' and leptons' interactions with the scalar field, respectively. If both  $\lambda$  and  $\mu^2$  are positive, the potential  $V(\Phi^\dagger\Phi)$  has an infinite set of degenerate minima satisfying  $\Phi^\dagger\Phi = \mu^2/2\lambda$ . Defining the vacuum expectation value,  $v \equiv \sqrt{\mu^2/\lambda}$ , we can arbitrarily choose to expand the field  $\Phi$  about a single minimum — breaking the  $SU(2)_L$  symmetry — as

$$\Phi = \begin{pmatrix} 0 \\ \frac{v+H}{\sqrt{2}} \end{pmatrix}, \quad (1.23)$$

where  $H$  is the physical Higgs field. Considering, for example, the down quarks, the Lagrangian now contains a mass term given by

$$\frac{vY_d}{\sqrt{2}}(\bar{d}_L d_R + \bar{d}_R d_L), \quad (1.24)$$

and the down quarks have a mass of  $m_d = vY_d/\sqrt{2}$ . Extending to three quark generations and neglecting the leptons, the most general form of the Yukawa couplings between the fermions and the scalar field are given by

$$\begin{aligned} \mathcal{L}_{\text{Yukawa}} = & -\bar{\chi}_L \hat{Y}^u \Phi \chi_{u,R} - \bar{\chi}_{u,R} \hat{Y}^{u\dagger} \Phi^\dagger \chi_L \\ & -\bar{\chi}_L \hat{Y}^d \Phi \chi_{d,R} - \bar{\chi}_{d,R} \hat{Y}^{d\dagger} \Phi^\dagger \chi_L, \end{aligned} \quad (1.25)$$

where  $\hat{Y}^u$  and  $\hat{Y}^d$  are the Yukawa coupling matrices for the up- and down-type quarks, respectively, and the additional quark generations are introduced as

$$\chi_L^T = (Q_{1,L}, Q_{2,L}, Q_{3,L}), \quad Q_{1,L} = \begin{pmatrix} u_L \\ d_L \end{pmatrix}, \quad Q_{2,L} = \begin{pmatrix} c_L \\ s_L \end{pmatrix}, \quad Q_{3,L} = \begin{pmatrix} t_L \\ b_L \end{pmatrix} \quad (1.26)$$

and

$$\chi_{u,R}^T = (u_R, c_R, t_R), \quad \chi_{d,R}^T = (d_R, s_R, b_R). \quad (1.27)$$

In the single-generation model, the Yukawa couplings were trivially diagonal, since they were just numbers. However, in the three-generation model the Yukawa matrices can, in general, be non-diagonal. Multiplying out Equation 1.26 gives the following mass terms for the quarks after SSB:

$$\begin{aligned} \mathcal{L}_{\text{masses}} = & -\frac{v}{\sqrt{2}}(\bar{u}_{i,L}Y_{ij}^u u_{j,R} + \bar{u}_{j,R}Y_{ij}^{u*} u_{i,L}) \\ & -\frac{v}{\sqrt{2}}(\bar{d}_{i,L}Y_{ij}^d d_{j,R} + \bar{d}_{j,R}Y_{ij}^{d*} d_{i,L}), \end{aligned} \quad (1.28)$$

where  $Y_{ij}^{u/d}$  represents an indexed entry of the matrices  $\hat{Y}^{u/d}$ . The mass eigenstates, which diagonalise the Yukawa matrices, can be obtained from a transformation of the weak eigenstates, which we have already defined. A set of unitary matrices are defined such that

$$\hat{Y}_{\text{diag}}^u = U_L \hat{Y}^u U_R^\dagger, \quad \hat{Y}_{\text{diag}}^d = D_L \hat{Y}^d D_R^\dagger, \quad (1.29)$$

where  $U_{L(R)} U_{L(R)}^\dagger = D_{L(R)} D_{L(R)}^\dagger = \mathbb{I}$ . The quark mass eigenstates are given by

$$\begin{pmatrix} u'_{L/R} \\ c'_{L/R} \\ t'_{L/R} \end{pmatrix} = U_{L/R} \begin{pmatrix} u_{L/R} \\ c_{L/R} \\ t_{L/R} \end{pmatrix}, \quad \text{and} \quad \begin{pmatrix} d'_{L/R} \\ s'_{L/R} \\ b'_{L/R} \end{pmatrix} = D_{L/R} \begin{pmatrix} d_{L/R} \\ s_{L/R} \\ b_{L/R} \end{pmatrix}. \quad (1.30)$$

The electromagnetic and neutral weak current terms are left unaffected by such a transformation, due to the unitarity of the matrices  $U_{L/R}$  and  $D_{L/R}$ . This is equivalent to saying the mass and flavour eigenstates are equivalent for the neutral currents, and hence interactions which change the flavour of a quark upon emission of a photon or  $Z^0$  boson — known as flavour-changing neutral currents (FCNC) — do not appear at tree level in the SM. The charged weak interactions however now

contain the structure

$$\begin{pmatrix} \bar{u}'_L & \bar{c}'_L & \bar{t}'_L \end{pmatrix} V_{CKM} \begin{pmatrix} d'_L \\ s'_L \\ b'_L \end{pmatrix}, \quad (1.31)$$

where  $V_{CKM} \equiv U_L^\dagger D_L$  is known as the Cabibbo-Kobayashi-Maskawa (CKM) matrix [3, 29] and it follows that  $V_{CKM}^\dagger V_{CKM} = \mathbb{I}$ . Thus, the charged weak currents allow tree-level transitions between the different generations of fermions, if the matrix  $V_{CKM}$  is non-diagonal.

Additionally, the Yukawa couplings between the quarks and the scalar field — and therefore the CKM matrix after diagonalisation of the mass matrices — provide the only possible source of  $CP$  violation in the three-generation, quark only electroweak model. If the leptons are included, an additional source of  $CP$  violation is possible in the analogous PMNS matrix [30, 31]. It is most straightforward to understand this possibility by re-phrasing, for example, the up-type quark Yukawa couplings as

$$\mathcal{L}_{\text{masses}}^u = -\frac{v}{\sqrt{2}}(\bar{u}_i Y_{ij}^u P_R u_j + \bar{u}_j Y_{ij}^{u*} P_L u_i) \quad (1.32)$$

using the properties  $P_L^2 = P_L$  and  $P_R^2 = P_R$  of the projection operators. Under the  $CP$  transformation, the quarks transform as  $u_i \rightarrow \bar{u}_i$  and the projection operators as  $P_{L,R} \rightarrow P_{R,L}$ . Thus, we have

$$CP(\mathcal{L}_{\text{masses}}^u) = -\frac{v}{\sqrt{2}}(\bar{u}_j Y_{ij}^u P_L u_i + \bar{u}_i Y_{ij}^{u*} P_R u_j), \quad (1.33)$$

and the Lagrangian is invariant under the  $CP$  transformation only if the Yukawa couplings,  $Y_{ij}$ , are real. A general  $n \times n$  complex matrix has  $2n^2$  real parameters. Unitarity imposes  $n^2$  (real) constraints, and the unphysical relative phases of the quark fields can be rotated to remove a further  $2n - 1$  degrees of freedom. Thus, the CKM matrix has  $(n - 1)^2$  free real parameters. A real, orthogonal  $n \times n$  matrix can be described in terms of  $\frac{1}{2}n(n - 1)$  parameters. We therefore find that a  $3 \times 3$  CKM matrix with three generations of quarks can be described in terms of four parameters: three angles,  $\theta_{ij}$  that define the magnitude of the elements, and an additional angle,  $\delta$ , that generates complex elements. Consequently, within the SM a single parameter,  $\delta$ , determines all of the allowed  $CP$  violating effects in hadrons, although precisely predicting the size of such effects is highly non-trivial. One possible convention to

represent the CKM matrix, known as the standard parameterisation, is given by [32]

$$V_{CKM} = \begin{pmatrix} c_{12} & s_{12} & 0 \\ -s_{12} & c_{12} & 0 \\ 0 & 0 & 1 \end{pmatrix} \begin{pmatrix} c_{13} & 0 & s_{13}e^{-i\delta} \\ 0 & 1 & 0 \\ -s_{13}e^{i\delta} & 0 & c_{13} \end{pmatrix} \begin{pmatrix} 1 & 0 & 0 \\ 0 & c_{23} & s_{23} \\ 0 & -s_{23} & c_{23} \end{pmatrix}, \quad (1.34)$$

where  $c_{ij} \equiv \cos(\theta_{ij})$  and  $s_{ij} \equiv \sin(\theta_{ij})$ . An alternative parameterisation, known as the Wolfenstein parameterisation [32], allows the hierarchy of transitions between generations to be interpreted more clearly. The Wolfenstein parameterisation employs four real parameters —  $\lambda$ ,  $A$ ,  $\rho$ , and  $\eta$  — such that

$$V_{CKM} = \begin{pmatrix} 1 - \frac{1}{2}\lambda^2 & \lambda & A\lambda^3(\rho - i\eta) \\ -\lambda & 1 - \frac{1}{2}\lambda^2 & A\lambda^2 \\ A\lambda^3(1 - \rho - i\eta) & -A\lambda^2 & 1 \end{pmatrix} + \mathcal{O}(\lambda^4). \quad (1.35)$$

The most recent global fit of the four parameters by the CKMFitter group gives [33]

$$\begin{aligned} \lambda &= 0.22498^{+0.00023}_{-0.00021} \\ A &= 0.8215^{+0.0047}_{-0.0082} \\ \rho &\approx \bar{\rho} = 0.1562^{+0.0112}_{-0.0040} \\ \eta &\approx \bar{\eta} = 0.3551^{+0.0051}_{-0.0057}, \end{aligned} \quad (1.36)$$

where  $\bar{\rho} = \rho(1 - \lambda^2/2)$  and  $\bar{\eta} = \eta(1 - \lambda^2/2)$ . Comparing Equations 1.35 and 1.36, it is therefore clear to see that the CKM matrix is approximately diagonal, with transitions between quarks in the same generation heavily favoured over transitions between quarks of different generations. Such transitions between the generations, known as flavour-changing charged currents, are critical to allow the mixing of neutral mesons which will be discussed in the next section.

### 1.2.1.5 Quantum chromodynamics

Before proceeding to the effective theory which governs mixing and  $CP$  violation in charmed mesons, a short description of the strong force is given here to provide a complete<sup>4</sup> picture of the SM. The dynamics of the strong force are known as Quantum Chromodynamics (QCD). The strong force arises from an  $SU(3)_C$  symmetry,

---

<sup>4</sup>Albeit, brief.

where the subscript ‘ $C$ ’ stands for ‘colour’. Colour is an additional charge which is introduced to the SM particles. Of the fermions, only the quarks possess colour charge. There are three colour charges: red, green and blue (and their corresponding anti-charges). These can be represented, for example, as a set of vectors:

$$r = \begin{pmatrix} 1 \\ 0 \\ 0 \end{pmatrix}, \quad g = \begin{pmatrix} 0 \\ 1 \\ 0 \end{pmatrix}, \quad \text{and} \quad b = \begin{pmatrix} 0 \\ 0 \\ 1 \end{pmatrix}. \quad (1.37)$$

The  $SU(3)_C$  symmetry group — which can be represented by a set of  $3 \times 3$  matrices — acts on the colour charge of each of the quark fields. Again, a Lagrangian containing only kinetic terms for each of the quarks will not be invariant under a local transformation as in Equation 1.15 (with an appropriate choice of generators for  $SU(3)$ ). Thus, another gauge field must be introduced to preserve the symmetry. The corresponding covariant derivative is given by

$$D_\mu = \partial_\mu + ig_s \tau_\alpha G_\mu^\alpha, \quad (1.38)$$

where  $g_s$  is a coupling constant and  $G_\mu^\alpha$  are the new gauge fields, which represent the gluons. Since the group  $SU(3)$  has 8 generators, there are eight gluons. To conserve colour charge in interactions, the gluons must carry a combination of colour and anti-colour. Similarly to the electroweak gauge bosons, mass terms for the gluons violate the gauge symmetry. The gluons, however, do not interact with the scalar field  $\Phi$  and therefore remain massless after SSB. Thus, the strong force is distinct from the weak and EM forces after SSB in that it contains gauge bosons which are both massless and self-interacting. It is this unique property of QCD that gives rise to colour confinement, where coloured states (*e.g.* individual quarks) do not propagate freely.

### 1.3 Mixing and $CP$ violation in the neutral meson systems

The phenomenon of particle and anti-particle oscillations, also known as mixing, is experimentally well-established in both the meson and neutrino systems [34–40]. The discussion presented here is generic to all of the neutral meson systems which

exhibit mixing ( $K^0, D^0, B^0, B_s^0$ ) and is therefore phrased in terms of some arbitrary meson,  $P^0$ . Oscillations between  $P^0$  and  $\bar{P}^0$  mesons are possible so long as some interaction couples  $P^0$  and  $\bar{P}^0$ . In the neutral meson systems, such couplings are provided either by so-called ‘box-diagrams’, or by re-scattering of decays to final states common to  $P^0$  and  $\bar{P}^0$ , as illustrated in Figure 1.1.

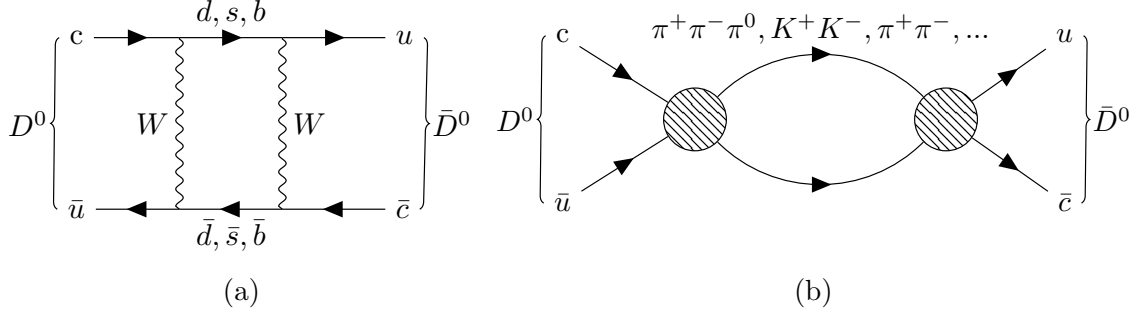


Figure 1.1:  $D^0$ - $\bar{D}^0$  mixing diagrams for (a) box-mixing and (b) re-scattering.

The state of this system can generically be written at some time,  $t$ , as

$$|\psi(t)\rangle = a(t)|P^0\rangle + b(t)|\bar{P}^0\rangle + \sum_{i=0}^n c_i(t)|f_i\rangle, \quad (1.39)$$

where  $a(t)$ ,  $b(t)$  and the set  $\{c_i(t)\}$  are some normalised set of coefficients,  $|P^0\rangle$  and  $|\bar{P}^0\rangle$  represent the states of definite flavour and  $\{|f_i\rangle\}$  represents the set of all final states available for  $P^0$  and  $\bar{P}^0$  to decay into. Considering only the coefficients  $a(t)$  and  $b(t)$ , assuming the initial state satisfies  $c_i(0) = 0 \forall i \in \{0, 1, \dots, n\}$ , and applying the Weisskopf-Wigner approximation [41, 42], the strong and electromagnetic interactions which conserve flavour can be ignored. The time-evolution can be expressed in terms of a simplified (weak) effective Hamiltonian as

$$i\hbar \frac{\partial}{\partial t} |\psi(t)\rangle = \mathcal{H}_{\text{eff}} |\psi(t)\rangle. \quad (1.40)$$

The effective Hamiltonian is given by

$$\mathcal{H}_{\text{eff}} = \mathbf{M} - \frac{i}{2}\mathbf{\Gamma} = \begin{pmatrix} M_{11} - \frac{i}{2}\Gamma_{11} & M_{12} - \frac{i}{2}\Gamma_{12} \\ M_{21} - \frac{i}{2}\Gamma_{21} & M_{22} - \frac{i}{2}\Gamma_{22} \end{pmatrix} = \begin{pmatrix} m - \frac{i}{2}\Gamma & M_{12} - \frac{i}{2}\Gamma_{12} \\ M_{12}^* - \frac{i}{2}\Gamma_{12}^* & m - \frac{i}{2}\Gamma \end{pmatrix}. \quad (1.41)$$

The first equality in Equation 1.41 separates  $\mathcal{H}_{\text{eff}}$  into a Hermitian mass-matrix,  $\mathbf{M}$ , and anti-Hermitian term defined in terms of the Hermitian decay matrix  $\mathbf{\Gamma}$ . Non-zero

off-diagonal terms of  $\mathcal{H}_{\text{eff}}$  allow mixing between the  $|P^0\rangle$  and  $|\bar{P}^0\rangle$ . In particular,  $M_{12}$  describes contributions from off-shell — or virtual — states, while  $\Gamma_{12}$  describes contributions from on-shell states. The last equality imposes the hermicity of  $\mathbf{M}$  and  $\mathbf{\Gamma}$ , and  $CPT$  conservation which implies  $m \equiv M_{11} = M_{22}$  and  $\Gamma \equiv \Gamma_{11} = \Gamma_{22}$ . Diagonalising  $\mathcal{H}_{\text{eff}}$  provides the most straightforward solution to Equation 1.40. Defining some arbitrary (complex) eigenvector,  $\vec{x}^T = (p, q)$ , and eigenvalue,  $\lambda_i = m_i - \frac{i}{2}\Gamma_i$ , it follows that

$$(\mathcal{H}_{\text{eff}} - \lambda_i) \begin{pmatrix} p \\ q \end{pmatrix} = 0. \quad (1.42)$$

This is equivalent to a state given by  $|\psi\rangle = p|P^0\rangle + q|\bar{P}^0\rangle$ , with  $p$  and  $q$  satisfying  $|p|^2 + |q|^2 = 1$ . Solving Equation 1.42 yields the following expression:

$$\left(\frac{q}{p}\right)^2 = \frac{\mathcal{H}_{21}}{\mathcal{H}_{12}} = \frac{M_{12}^* - \frac{i}{2}\Gamma_{12}^*}{M_{12} - \frac{i}{2}\Gamma_{12}}, \quad (1.43)$$

where  $\mathcal{H}_{ij}$  represents a single entry of  $\mathcal{H}_{\text{eff}}$ . From Equation 1.43, one can identify that  $\vec{x}^T = (p, -q)$  is also a linearly independent solution to Equation 1.42. Thus, the mass eigenstates which diagonalise the effective Hamiltonian are given by

$$\begin{aligned} |P_1\rangle &= p|P^0\rangle - q|\bar{P}^0\rangle \\ |P_2\rangle &= p|P^0\rangle + q|\bar{P}^0\rangle. \end{aligned} \quad (1.44)$$

The phase convention  $CP|P^0\rangle = -|\bar{P}^0\rangle$  with  $|P_1\rangle$  ( $|P_2\rangle$ ) defined as  $CP$ -even ( $CP$ -odd) in the limit of  $CP$  conservation ( $|p| = |q|$ ) is adopted [43]. The respective eigenvalues can be found from the diagonal form given by  $A^{-1}\mathcal{H}_{\text{eff}}A$ , where  $A$  is a matrix constructed from the column eigenvectors of  $\mathcal{H}_{\text{eff}}$ . Using the result presented in Equation 1.43, one can show that

$$\begin{aligned} A^{-1}\mathcal{H}_{\text{eff}}A &= \frac{1}{2pq} \begin{pmatrix} q & -p \\ q & p \end{pmatrix} \begin{pmatrix} \mathcal{H}_{11} & \mathcal{H}_{12} \\ \mathcal{H}_{21} & \mathcal{H}_{11} \end{pmatrix} \begin{pmatrix} p & p \\ -q & q \end{pmatrix} \\ &= \begin{pmatrix} \mathcal{H}_{11} - \frac{q}{p}\mathcal{H}_{12} & 0 \\ 0 & \mathcal{H}_{11} + \frac{q}{p}\mathcal{H}_{12} \end{pmatrix}. \end{aligned} \quad (1.45)$$

Thus, the mass and decay widths of the mass eigenstates of  $\mathcal{H}_{\text{eff}}$  are given by the

real and imaginary parts of the eigenvalues, respectively:

$$\begin{aligned} m_{1,2} &= \text{Re} \left( \mathcal{H}_{11} \mp \frac{q}{p} \mathcal{H}_{12} \right) = m \mp \text{Re} \left( \frac{q}{p} \left[ M_{12} - \frac{i}{2} \Gamma_{12} \right] \right) \\ -\frac{1}{2} \Gamma_{1,2} &= \text{Im} \left( \mathcal{H}_{11} \mp \frac{q}{p} \mathcal{H}_{12} \right) = -\frac{1}{2} \Gamma \mp \text{Im} \left( \frac{q}{p} \left[ M_{12} - \frac{i}{2} \Gamma_{12} \right] \right). \end{aligned} \quad (1.46)$$

The time-evolution of the mass eigenstates from solving Equation 1.40 is then

$$|P_{1(2)}(t)\rangle = e^{-im_{1(2)}t - \frac{1}{2}\Gamma_{1(2)}t} |P_{1(2)}(0)\rangle. \quad (1.47)$$

It is convenient to introduce the dimensionless mass and width differences given by

$$\begin{aligned} x &\equiv \frac{\Delta m}{\Gamma} = -\frac{2}{\Gamma} \text{Re} \left( \frac{q}{p} \left[ M_{12} - \frac{i}{2} \Gamma_{12} \right] \right) \\ y &\equiv \frac{\Delta \Gamma}{2\Gamma} = \frac{2}{\Gamma} \text{Im} \left( \frac{q}{p} \left[ M_{12} - \frac{i}{2} \Gamma_{12} \right] \right), \end{aligned} \quad (1.48)$$

where  $\Delta m \equiv m_1 - m_2$  and  $\Delta \Gamma \equiv \Gamma_1 - \Gamma_2$ . Then, using Equations 1.44 and 1.47, the time evolution of an initially pure  $P^0$  or  $\bar{P}^0$  state is given by

$$\begin{aligned} |P^0(t)\rangle &= g_+(t)|P^0\rangle + \frac{q}{p}g_-(t)|\bar{P}^0\rangle \\ |\bar{P}^0(t)\rangle &= g_+(t)|\bar{P}^0\rangle + \frac{p}{q}g_-(t)|P^0\rangle, \end{aligned} \quad (1.49)$$

where

$$g_{\pm}(t) = \frac{1}{2}e^{-imt - \frac{1}{2}\Gamma t} \left( e^{\frac{i}{2}x\Gamma t} e^{\frac{1}{2}y\Gamma t} \pm e^{-\frac{i}{2}x\Gamma t} e^{-\frac{1}{2}y\Gamma t} \right). \quad (1.50)$$

The (unnormalised) probabilities for an initially pure flavour eigenstate to decay in either the same or opposite flavour eigenstate at some later time,  $t$ , are thus given by

$$\begin{aligned} P_{P^0 \rightarrow P^0}(t) &= |\langle P^0 | P^0(t) \rangle|^2 = |g_+(t)|^2 = \frac{1}{2}e^{-\Gamma t} [\cosh(y\Gamma t) + \cos(x\Gamma t)] \\ P_{\bar{P}^0 \rightarrow \bar{P}^0}(t) &= |\langle \bar{P}^0 | \bar{P}^0(t) \rangle|^2 = |g_+(t)|^2 = \frac{1}{2}e^{-\Gamma t} [\cosh(y\Gamma t) + \cos(x\Gamma t)] \\ P_{P^0 \rightarrow \bar{P}^0}(t) &= |\langle \bar{P}^0 | P^0(t) \rangle|^2 = \left| \frac{q}{p}g_-(t) \right|^2 = \frac{1}{2} \left| \frac{q}{p} \right|^2 e^{-\Gamma t} [\cosh(y\Gamma t) - \cos(x\Gamma t)] \\ P_{\bar{P}^0 \rightarrow P^0}(t) &= |\langle P^0 | \bar{P}^0(t) \rangle|^2 = \left| \frac{p}{q}g_-(t) \right|^2 = \frac{1}{2} \left| \frac{p}{q} \right|^2 e^{-\Gamma t} [\cosh(y\Gamma t) - \cos(x\Gamma t)]. \end{aligned} \quad (1.51)$$

One can see from Equation 1.51 that oscillations between  $P^0$  and  $\bar{P}^0$  can occur so long as at least one of  $x$  or  $y$  is non-zero. The width difference,  $y$ , modifies the exponential decay behaviour, while the mass difference,  $x$ , drives a periodic behaviour in the mixing probabilities. If  $|q/p| \neq 1$  (and  $x \neq 0$  or  $y \neq 0$ ), then  $CP$  violation occurs in mixing through different rates for the processes  $P^0 \rightarrow \bar{P}^0$  and  $\bar{P}^0 \rightarrow P^0$ .

### 1.3.1 Classification of $CP$ violation

The  $CP$  symmetry is broken in mixing when  $|q/p| \neq 1$ , since this gives

$$P_{P^0 \rightarrow \bar{P}^0}(t) \neq P_{\bar{P}^0 \rightarrow P^0}(t). \quad (1.52)$$

Such  $CP$  violation is classified as *indirect*  $CP$  violation.  $CP$  violation can also occur directly in the decays of  $P^0$  and  $\bar{P}^0$  mesons to  $CP$  conjugate final states. Defining  $A_f = \langle f | \mathcal{H} | P^0 \rangle$  ( $\bar{A}_{\bar{f}} = \langle \bar{f} | \mathcal{H} | \bar{P}^0 \rangle$ ) — where  $\mathcal{H}$  is the Hamiltonian — to be the amplitude for the decay  $P^0 \rightarrow f$  ( $\bar{P}^0 \rightarrow \bar{f}$ ),  $CP$  symmetry is violated in the decay if

$$\left| \frac{\bar{A}_{\bar{f}}}{A_f} \right| \neq 1. \quad (1.53)$$

Such  $CP$  violation is defined as *direct*  $CP$  violation.

A third kind of  $CP$  violation is also possible, even in the case where the  $CP$  symmetry is preserved in both mixing and decays. Defining the parameter  $\lambda_f$  to be

$$\lambda_f \equiv \frac{q\bar{A}_{\bar{f}}}{pA_f}, \quad (1.54)$$

then  $CP$  violation occurs in the interference between mixing and decay if  $|\lambda_f| = 1$  and  $\text{Im}(\lambda_f) \neq 0$ . For a  $CP$  eigenstate,  $f = f_{CP}$ ,  $\lambda_f$  can be expressed as [44]

$$\lambda_f = -\eta_{f_{CP}} \left| \frac{q\bar{A}_{\bar{f}}}{pA_f} \right| e^{i\phi_f}, \quad (1.55)$$

where  $\eta_{f_{CP}}$  is the  $CP$ -eigenvalue of the final state  $f_{CP}$ . The weak phase,  $\phi_f$ , becomes final-state independent in the absence of direct  $CP$  violation; consequently, we can define the universal phase  $\phi \equiv \arg(q/p)$ .<sup>5</sup> For a  $CP$ -eigenstate,  $\lambda_f$  does not carry a

---

<sup>5</sup>In general, the absolute phase of  $q/p$  is unphysical, and so this expression relies on the adopted phase convention.

strong phase since it does not change sign under the  $CP$  transformation and cancels in the ratio  $\bar{A}_f/A_f$ ; if  $f$  is not a  $CP$ -eigenstate,  $\lambda_f$  can generally carry some strong phase.

### 1.3.2 Mixing behaviour in the different neutral meson systems

The  $D^0$  meson is unique amongst the neutral meson systems which exhibit mixing for two reasons. Firstly, it is the only system in which  $x$  is not of  $\mathcal{O}(1)$  or larger. Consequently, mixing effects in charm are small and require large statistical samples to distinguish from the no-mixing case. In addition, the  $K^0$  ( $d\bar{s}$ ) and  $B^0/B_s^0$  ( $\bar{d}b/\bar{s}b$ ) systems probe mixing and  $CP$  violation in states with down-type quarks, however the  $D^0$  ( $c\bar{u}$ ) system provides a unique opportunity to probe possible new physics which couples differently to up- and down-type quarks.

Meson	$x$	$y$
$K^0$	$0.946 \pm 0.002$	$0.997 \pm 0.001$
$D^0$	$(0.407 \pm 0.044)\%$	$(0.645^{+0.024}_{-0.023})\%$
$B^0$	$0.769 \pm 0.004$	$0.0005 \pm 0.0050$
$B_s^0$	$27.01 \pm 0.10$	$0.064 \pm 0.0035$

Table 1.4: Mixing parameters  $x$  and  $y$  for each of the neutral meson systems which contain a heavy quark [8, 43].

Table 1.4 shows the dimensionless mass- and width-differences<sup>6</sup> for each of the neutral meson systems. The probabilities of a particle produced in a pure meson state at time  $t = 0$  decaying before and after mixing at a later time — neglecting  $CP$  violation in mixing — are shown in Figure 1.2 for each of the  $K^0$ ,  $D^0$ ,  $B^0$  and  $B_s^0$  systems. The presence of mixing — although its exact effect differs considerably — is clearly evident in the  $K^0$ ,  $B^0$ , and  $B_s^0$  systems. In the  $D^0$  system, however, the curve representing unmixed  $D^0$  decays is indistinguishable from the pure exponential curve. Experimentally, mixing in the  $D^0$  system was only very recently unambiguously distinguished from the no-mixing case in 2021 by LHCb [45].

The smallness of  $D^0$ - $\bar{D}^0$  mixing can be motivated by a simple argument based on the structure of the CKM matrix. Considering the box-diagram shown in Figure 1.1

<sup>6</sup>Since the expressions in Equation 1.51 are insensitive to the sign of  $x$  and  $y$ , the conventions for the sign of the mass and widths differences in each of the systems are chosen here such that  $x, y > 0$ , to be compatible with mixing measurements in the  $D^0$ - $\bar{D}^0$  system [45, 46].

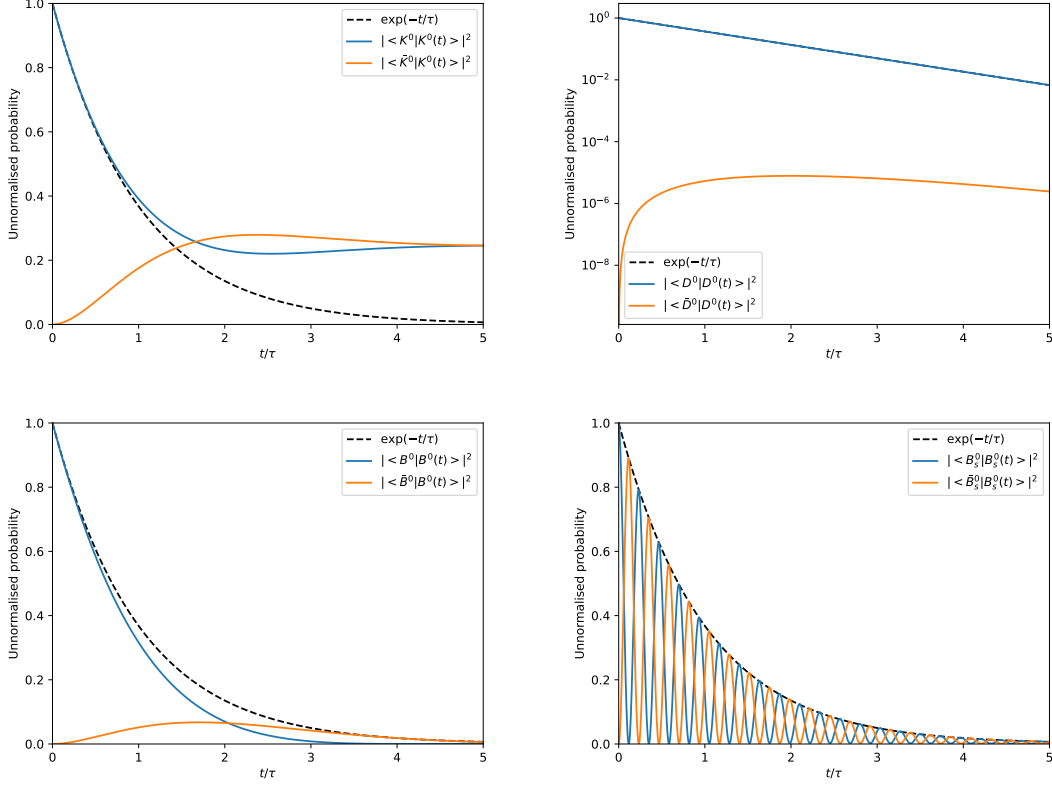


Figure 1.2: Unnormalised probabilities of initially pure neutral meson states decaying before and after mixing in each of the neutral meson systems containing a heavy quark, assuming  $|q/p| = 1$ . A pure exponential curve is also shown as the dotted black line. The  $K^0$ ,  $D^0$ ,  $B^0$ , and  $B_s^0$  systems are shown on the top left, top right, bottom left and bottom right, respectively. Note that the  $D^0$  plot is shown on a logarithmic scale.

(left), mixing is at least doubly Cabibbo-suppressed (DCS) no matter which choice of down-type quarks are made on the internal lines. Similarly, mixing is DCS for the re-scattering process shown in Figure 1.1 (right), since common final states are generally singly Cabibbo-suppressed (SCS) from both  $D^0$  and  $\bar{D}^0$ , or Cabibbo-favoured (CF) from one flavour and DCS from the other. The existence of CF final states however indicates that mixing is highly suppressed compared to the overall decay rate of  $D^0$  mesons. Now consider, for example, the case of  $B^0$ - $\bar{B}^0$  mixing: again, the lowest order mixing diagrams are DCS. However, final states available to  $B^0$  or  $\bar{B}^0$  mesons are necessarily at lowest order SCS, since the  $B^0$  mass is  $\sim 5 \text{ GeV}$ , and CF decays would require a transition  $\bar{b} \rightarrow \bar{t}$ , while  $m_t \sim 175 \text{ GeV}$ . Thus, although the mixing process is equally suppressed, its contribution relative to the overall decay rate is enhanced with respect to the neutral charmed meson

system [47].

### 1.3.3 The time-dependent $CP$ -violating parameter $\Delta Y$

From this point, we will rely on the assumption that mixing and  $CP$  violation effects in the  $D^0$  meson system are small in order to make finite order Taylor expansions of the decay rates, and therefore the discussion is now specific to  $D^0$  mesons alone. The most recent global fit results for the  $D^0$  mixing parameters and  $CP$  violating parameters are  $x = (0.407 \pm 0.044)\%$ ,  $y = (0.645^{+0.024}_{-0.023})\%$ ,  $|q/p| = 0.994^{+0.016}_{-0.015}$  and  $\phi = (-2.6^{+1.1}_{-1.2})^\circ$  [43]. The time-dependent decay rate of a state which represents a  $D^0$  meson at  $t = 0$  to some self-conjugate final state,  $f = \bar{f}$ , can be expressed as

$$\Gamma_{D^0 \rightarrow f}(t) = |\langle f | \mathcal{H} | D^0(t) \rangle|^2 = \left| g_+(t) A_f + \frac{q}{p} g_-(t) \bar{A}_f \right|^2. \quad (1.56)$$

Using the time evolution of such a state from Equations 1.49 and 1.50, this can be written as

$$\begin{aligned} \Gamma_{D^0 \rightarrow f}(t) = \frac{1}{2} |A_f|^2 e^{-\Gamma t} \{ & (1 + |\lambda_f|^2) \cosh(y\Gamma t) + (1 - |\lambda_f|^2) \cos(x\Gamma t) \\ & + 2 \operatorname{Re}(\lambda_f) \sinh(y\Gamma t) - 2 \operatorname{Im}(\lambda_f) \sin(x\Gamma t) \}. \end{aligned} \quad (1.57)$$

The time-dependent decay rate for a  $\bar{D}^0$  meson to the final state can be obtained by the substitutions  $A_f \rightarrow \bar{A}_f$  and  $\lambda_f \rightarrow \lambda_f^{-1}$ . If the final state  $f$  is a  $CP$  eigenstate, the decay rates for  $D^0$  and  $\bar{D}^0$  mesons can be expanded to  $\mathcal{O}(x\Gamma t, y\Gamma t)$  as

$$\begin{aligned} \Gamma_{D^0 \rightarrow f}(t) &\approx |A_f|^2 e^{-\Gamma t} \{ 1 - \eta_{fCP} |\lambda_f| [y \cos \phi_f - x \sin \phi_f] \Gamma t \} \\ \Gamma_{\bar{D}^0 \rightarrow f}(t) &\approx |\bar{A}_f|^2 e^{-\Gamma t} \{ 1 - \eta_{fCP} |\lambda_f|^{-1} [y \cos \phi_f + x \sin \phi_f] \Gamma t \}. \end{aligned} \quad (1.58)$$

In addition, the decay rates can be approximated as a single exponential,  $\Gamma(t) \propto \exp(-\hat{\Gamma}t)$ , to define the effective decay rates  $\hat{\Gamma}_{D^0 \rightarrow f}$  and  $\hat{\Gamma}_{\bar{D}^0 \rightarrow f}$  as

$$\begin{aligned} \hat{\Gamma}_{D^0 \rightarrow f} &\approx \Gamma \{ 1 + \eta_{fCP} |\lambda_f| [y \cos \phi_f - x \sin \phi_f] \} \\ \hat{\Gamma}_{\bar{D}^0 \rightarrow f} &\approx \Gamma \{ 1 + \eta_{fCP} |\lambda_f|^{-1} [y \cos \phi_f + x \sin \phi_f] \}. \end{aligned} \quad (1.59)$$

From the difference of the effective decay rates for  $D^0$  and  $\bar{D}^0$  mesons, the  $CP$ -violating parameter  $\Delta Y_f$  is defined to be

$$\begin{aligned}\Delta Y_f &\equiv \frac{\hat{\Gamma}_{\bar{D}^0 \rightarrow f} - \hat{\Gamma}_{D^0 \rightarrow f}}{2\Gamma} \\ &= \frac{\eta_{fCP}}{2} \left\{ (|\lambda_f| + |\lambda_f|^{-1}) x \sin \phi_f - (|\lambda_f| - |\lambda_f|^{-1}) y \cos \phi_f \right\},\end{aligned}\tag{1.60}$$

and will shortly be identified as the slope of the time-dependent  $CP$  asymmetry.

The  $CP$ -asymmetry as a function of the  $D^0$  decay time is defined in terms of the decay rates as

$$\mathcal{A}_f^{CP}(t) \equiv \frac{\Gamma_{D^0 \rightarrow f}(t) - \Gamma_{\bar{D}^0 \rightarrow f}(t)}{\Gamma_{D^0 \rightarrow f}(t) + \Gamma_{\bar{D}^0 \rightarrow f}(t)}.\tag{1.61}$$

Substituting in the expressions from Equation 1.58 and expanding again to first order in time gives the expressions

$$\mathcal{A}_f^{CP}(t) \approx a_{\text{dir}}^f + a_{\text{ind}}^f \frac{t}{\tau_{D^0}},\tag{1.62}$$

where  $\tau_{D^0}$  is the mean lifetime of a  $D^0$  meson, and we have defined

$$\begin{aligned}a_{\text{dir}}^f &= \frac{|A_f|^2 - |\bar{A}_f|^2}{|A_f|^2 + |\bar{A}_f|^2} \\ a_{\text{ind}}^f &= \eta_{fCP} \frac{2|A_f|^2 |\bar{A}_f|^2}{(|A_f|^2 + |\bar{A}_f|^2)^2} \left\{ [|\lambda_f| + |\lambda_f|^{-1}] x \sin \phi_f - [|\lambda_f| - |\lambda_f|^{-1}] y \cos \phi_f \right\}.\end{aligned}\tag{1.63}$$

Thus, a non-zero  $a_{\text{dir}}^f$  results from direct  $CP$  violation only, while  $a_{\text{ind}}^f$  receives contributions from both direct and indirect  $CP$  violation. The expression for  $a_{\text{ind}}^f$  can be written as

$$a_{\text{ind}}^f \approx (1 - (a_{\text{dir}}^f)^2) \Delta Y_f \approx \Delta Y_f,\tag{1.64}$$

since even for a direct  $CP$  asymmetry of  $\mathcal{O}(\%)$  — much larger than predicted in the SM [48] and strongly disfavoured by experiment [49, 50] — the term multiplying  $\Delta Y_f$  would differ from unity by only  $\mathcal{O}(10^{-4})$ . Thus, the time-dependent  $CP$  asymmetry of the decay  $D^0 \rightarrow f$  is given, up to a negligible correction, by

$$\mathcal{A}_f^{CP}(t) \approx a_{\text{dir}}^f + \Delta Y_f \frac{t}{\tau_{D^0}}.\tag{1.65}$$

The parameter  $\Delta Y_f$  can therefore be experimentally determined by measuring the gradient of the  $CP$ -asymmetry observed in  $D^0 \rightarrow f$  decays as a function of the decay

time of the  $D^0$  meson.

In the absence of direct  $CP$  violation,  $\Delta Y \equiv \eta_{fCP} \Delta Y_f$  carries no final state dependence, and can be expressed as

$$\Delta Y = \frac{1}{2} \left\{ \left( \left| \frac{q}{p} \right| + \left| \frac{p}{q} \right| \right) x \sin \phi - \left( \left| \frac{q}{p} \right| - \left| \frac{p}{q} \right| \right) y \cos \phi \right\}. \quad (1.66)$$

Deviations from the universal parameter  $\Delta Y$  in each final state are predicted to arise at  $\mathcal{O}(xa_{\text{dir}}^f, ya_{\text{dir}}^f)$  [51]. Direct  $CP$  asymmetries in charm decays are predicted to be small in the SM [48], and have only very recently been observed in the difference between the  $CP$  asymmetries in  $D^0 \rightarrow K^+ K^-$  and  $D^0 \rightarrow \pi^+ \pi^-$  decays, at the level of  $10^{-3}$  [50, 52]. The decay  $D^0 \rightarrow \pi^+ \pi^- \pi^0$  proceeds primarily through resonances of the form  $D^0 \rightarrow \pi \rho$  [53]. The  $CP$  asymmetries in such decays are predicted to be below the  $10^{-3}$  level [54], and are experimentally compatible with no  $CP$  asymmetry at the percent level [8]. Thus, together with the most recent global fit for the  $D^0$  mixing parameters [43], final state corrections to  $\Delta Y$  are expected to be  $\mathcal{O}(10^{-5})$ . The gradient of the time-dependent asymmetry is therefore expected to be universal at the current experimental precision of  $\mathcal{O}(10^{-4})$ . No evidence for a non-zero gradient has been measured to date [43].

### 1.3.3.1 The parameter $A_\Gamma$

Historically, the time-dependent  $CP$  asymmetry in  $D^0$  decays has more commonly been measured in terms of the parameter  $A_\Gamma$  [55–59] than  $\Delta Y$ . The observable  $A_\Gamma$  is defined in terms of the effective decay widths as

$$A_\Gamma \equiv \frac{\hat{\Gamma}_{D^0 \rightarrow f} - \hat{\Gamma}_{\bar{D}^0 \rightarrow f}}{\hat{\Gamma}_{D^0 \rightarrow f} + \hat{\Gamma}_{\bar{D}^0 \rightarrow f}}. \quad (1.67)$$

While the two observables have often been used interchangeably, there is a distinction depending on the analysis technique. In analyses where the effective lifetimes of  $D^0$  and  $\bar{D}^0$  to some common final state are measured (*e.g.* Ref. [56]), the parameter  $A_\Gamma$  can be directly constructed as in Equation 1.67. In analyses, such as that presented in this thesis, where the gradient of the time-dependent  $CP$  asymmetry is measured, the observable of interest is  $\Delta Y$ . Comparing with Equation 1.60, the

relationship between  $\Delta Y$  and  $A_\Gamma$  is given by

$$A_\Gamma = \frac{-2\Gamma}{\hat{\Gamma}_{D^0 \rightarrow f} + \hat{\Gamma}_{\bar{D}^0 \rightarrow f}} \Delta Y = \frac{-\Delta Y}{1 + y_{CP}}, \quad (1.68)$$

where  $y_{CP}$  is defined as

$$y_{CP} \equiv \frac{\hat{\Gamma}_{\bar{D}^0 \rightarrow f} + \hat{\Gamma}_{D^0 \rightarrow f}}{2\Gamma} - 1. \quad (1.69)$$

The most precise experimental measurements of  $y_{CP}$  to date indicate  $1 + y_{CP}$  differs from unity below the percent level [60]. Thus, the current level of experimental precision,  $\Delta Y$  and  $A_\Gamma$  are indistinguishable. The observable  $\Delta y$ , employed for example in Ref. [45], is also related to  $\Delta Y$  by the expression  $\Delta y = -\Delta Y$ . Figure 1.3 shows the current world average of  $A_\Gamma \approx -\Delta Y$  from HFLAV [43].

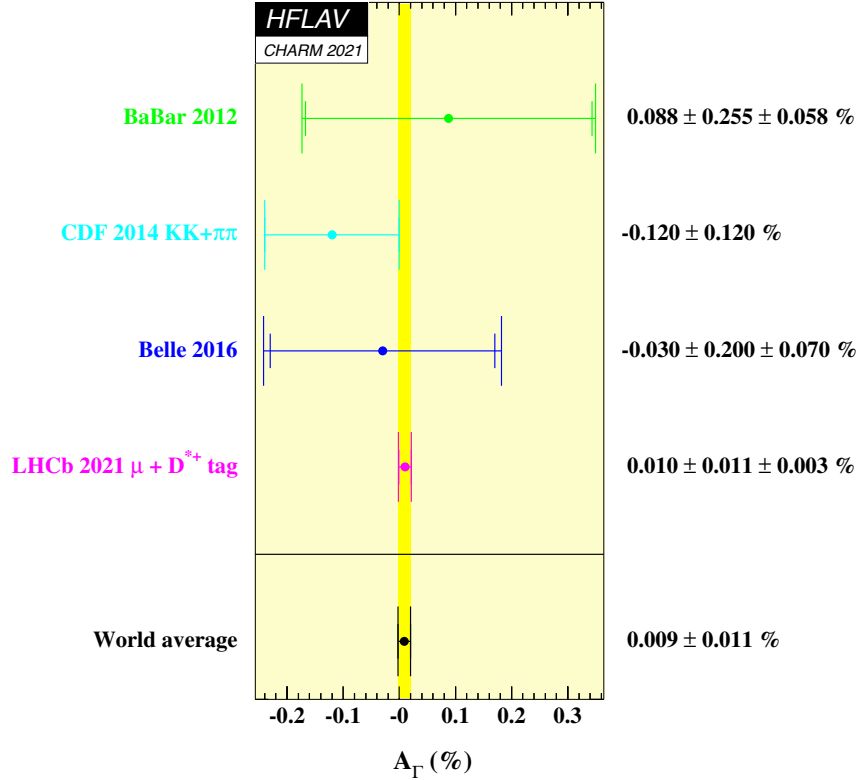


Figure 1.3: Current world average of the time-dependent  $CP$  violation parameter  $A_\Gamma$  [43].

### 1.3.4 Accessing $\Delta Y$ with multi-body final states

The discussion in Section 1.3.3 holds only for  $CP$  eigenstates such as  $f = K^+K^-, \pi^+\pi^-$ . The decay of interest in this thesis,  $D^0 \rightarrow \pi^+\pi^-\pi^0$ , is self-conjugate

but not a  $CP$  eigenstate; rather, it can proceed through many intermediate resonances and thus has contributions from both  $CP$ -even and  $CP$ -odd final states. Consequently, sensitivity to  $\Delta Y$  in a phase-space integrated measurement is potentially diluted by opposite-sign contributions to the  $CP$  asymmetry from opposite  $CP$ -eigenvalue intermediate states. Ref. [61] presents a quantitative description of this effect, which is reproduced here. Direct  $CP$  violation will be neglected here, but the more general expressions allowing for direct  $CP$  violation can be found in the original source.

The phase-space of a 3-body decay such as  $D^0 \rightarrow \pi^+\pi^-\pi^0$  has two degrees of freedom, and can therefore be parameterised in terms of the pair of masses  $s_{12} \equiv m^2(\pi^+\pi^0)$  and  $s_{13} \equiv m^2(\pi^-\pi^0)$ . The amplitude of the decay at a given phase-space co-ordinate can then be expressed as

$$A(s_{12}, s_{13}) \equiv a_{12,13} e^{i\delta_{12,13}}, \quad (1.70)$$

where  $\delta_{12,13}$  is a phase-space dependent strong phase and  $A(s_{12}, s_{13})$  is normalised such that  $\int |A(s_{12}, s_{13})|^2 ds_{12} ds_{13} = 1$ , where the integration limits run over the kinematically-allowed phase-space. Neglecting direct  $CP$  violation, the amplitudes for the  $D^0$  and  $\bar{D}^0$  decays at a given phase-space position are related<sup>7</sup> by

$$\bar{A}(s_{12}, s_{13}) \equiv \bar{a}_{12,13} e^{i\bar{\delta}_{12,13}} = -a_{13,12} e^{i\delta_{13,12}}. \quad (1.71)$$

If the phase-space is separated into two regions by the bisector  $s_{12} = s_{13}$ , the fraction of  $D^0$  decays — with the flavour known at the time of decay — lying in each of the two regions can be expressed as

$$K_i \equiv \int_i |a_{12,13}|^2 ds_{12} ds_{13}, \quad (1.72)$$

where the integration limits run over the relevant region. Defining the region  $s_{13} > s_{12}$  ( $s_{12} > s_{13}$ ) to be  $i = 1$  ( $i = -1$ ), one can immediately see the following relationships:

$$\bar{K}_i = K_{-i}, \text{ and } \sum_i K_i = \sum_i \bar{K}_i = 1, \quad (1.73)$$

where  $\bar{K}_i$  is defined analogously to  $K_i$  in terms of the amplitude for the  $\bar{D}^0$  decay. The average sine and cosine of the difference between the strong phases from  $D^0$

---

<sup>7</sup>In the phase convention adopted here.

and  $\bar{D}^0$  decays in each region can be expressed as

$$\begin{aligned} c_i &= \int_i a_{12,13} \bar{a}_{12,13} \cos(\delta_{12,13} - \bar{\delta}_{12,13}) ds_{12} ds_{13} \\ s_i &= \int_i a_{12,13} \bar{a}_{12,13} \sin(\delta_{12,13} - \bar{\delta}_{12,13}) ds_{12} ds_{13}. \end{aligned} \quad (1.74)$$

In the two-bin case,  $c_{-1}$  can be obtained from  $c_1$  with the substitution  $s_{12}, s_{13} \rightarrow s_{13}, s_{12}$ . Together with Equation 1.71, this is equivalent to a sign-flip on the strong-phase difference. Thus, we have the relationships  $c_i = c_{-i}$  and  $s_i = s_{-i}$ . The  $CP$ -even ( $CP$ -odd) fraction of decays in each bin,  $N_i^+$  ( $N_i^-$ ), can then be expressed as

$$N_i^\pm = n(K_i + \bar{K}_i \pm 2c_i), \quad (1.75)$$

where  $n$  is some common normalisation factor. The  $CP$ -even fraction is defined simply as the ratio of the  $CP$ -even yield to the total yield,  $F_+ = N^+/(N^+ + N^-)$ . Thus, using the total tagged yields,  $N^\pm = \sum_i N_i^\pm$ , the overall  $CP$ -even fraction of the decay can be expressed as

$$F_+ = \frac{1}{2}(1 + 2c_1). \quad (1.76)$$

The time-dependence of the decay amplitude for a  $D^0$  meson tagged at production can be inferred from Equation 1.49 and written as

$$\begin{aligned} A(s_{12}, s_{13}, t) &= A(s_{12}, s_{13})g_+(t) + \bar{A}(s_{12}, s_{13})\frac{q}{p}g_-(t) \\ &= a_{12,13}e^{i\delta_{12,13}}g_+(t) - a_{13,12}e^{i(\phi+\delta_{13,12})}\left|\frac{q}{p}\right|g_-(t). \end{aligned} \quad (1.77)$$

Expanding to first order in the decay-time, the decay rate is given at a single point of the phase-space by

$$\begin{aligned} \Gamma(s_{12}, s_{13}, t) &= |A(s_{12}, s_{13}, t)|^2 \\ &= e^{-\Gamma t} \left\{ a_{12,13}^2 - a_{12,13}a_{13,12} \left|\frac{q}{p}\right| [y \cos(\delta_{12,13} - \delta_{13,12} - \phi) \right. \\ &\quad \left. + x \sin(\delta_{12,13} - \delta_{13,12} - \phi)] \Gamma t \right\}. \end{aligned} \quad (1.78)$$

Integrating Equation 1.78 across the two regions of the Dalitz plot separately gives

the following expression for the total decay rate:

$$\Gamma_{D^0 \rightarrow f}(t) = e^{-\Gamma t} \left\{ 1 - (2F_+ - 1) \left| \frac{q}{p} \right| [y \cos(\phi) - x \sin(\phi)] \Gamma t \right\}. \quad (1.79)$$

The analogous expression for the decay  $\bar{D}^0 \rightarrow f$  can be obtained using the substitution  $q/p \rightarrow p/q$ . The effective decay rates for  $D^0$  and  $\bar{D}^0$  can then be written as

$$\begin{aligned} \hat{\Gamma}_{D^0 \rightarrow f} &\approx \Gamma \left\{ 1 + (2F_+ - 1) \left| \frac{q}{p} \right| [y \cos(\phi) - x \sin(\phi)] \right\} \\ \hat{\Gamma}_{\bar{D}^0 \rightarrow f} &\approx \Gamma \left\{ 1 + (2F_+ - 1) \left| \frac{p}{q} \right| [y \cos(\phi) + x \sin(\phi)] \right\}. \end{aligned} \quad (1.80)$$

Thus, the observable  $\Delta Y_f^{\text{eff}}$  can be defined exactly as in Equation 1.60 and is given by

$$\Delta Y_f^{\text{eff}} = \frac{2F_+ - 1}{2} \left\{ \left( \left| \frac{q}{p} \right| + \left| \frac{p}{q} \right| \right) x \sin(\phi) - \left( \left| \frac{q}{p} \right| - \left| \frac{p}{q} \right| \right) y \cos(\phi) \right\}. \quad (1.81)$$

By comparing Equations 1.66 and 1.81, one can see that the relationship between  $\Delta Y$  and  $\Delta Y_f^{\text{eff}}$  is

$$\Delta Y_f^{\text{eff}} = (2F_+ - 1) \Delta Y. \quad (1.82)$$

Thus, the gradient of the time-dependent asymmetry integrated across the phase-space of a multi-body decay such as  $D^0 \rightarrow \pi^+ \pi^- \pi^0$  is related to  $\Delta Y$  by the dilution factor  $2F_+ - 1$ .

A measurement of the  $CP$ -even fraction for the decay  $D^0 \rightarrow \pi^+ \pi^- \pi^0$  has been performed using data from the CLEO-c experiment, where quantum correlated  $D^0$ - $\bar{D}^0$  pairs are produced in  $e^+ e^-$  collisions at the  $\psi(3770)$  resonance. This correlation is exploited by reconstructing either the  $D^0$  or  $\bar{D}^0$  meson in a  $CP$  eigenstate, and the other in the final state for which  $F_+$  is unknown. Since the  $\psi(3770)$  resonance is  $CP$  even, this allows the decay of interest to be tagged as either even or odd, depending on the  $CP$  eigenstate with which it is detected concurrently. The most recent measurement for the  $D^0 \rightarrow \pi^+ \pi^- \pi^0$  decay is [62]

$$F_+^{\pi\pi\pi} = 0.973 \pm 0.017. \quad (1.83)$$

Substitution into Equation 1.82 yields a dilution factor of  $\sim 0.95$ , and thus the decay  $D^0 \rightarrow \pi^+ \pi^- \pi^0$  is an excellent candidate for such a phase-space integrated

measurement of indirect  $CP$  violation, since it provides almost undiluted sensitivity to the underlying  $CP$  asymmetry gradient.

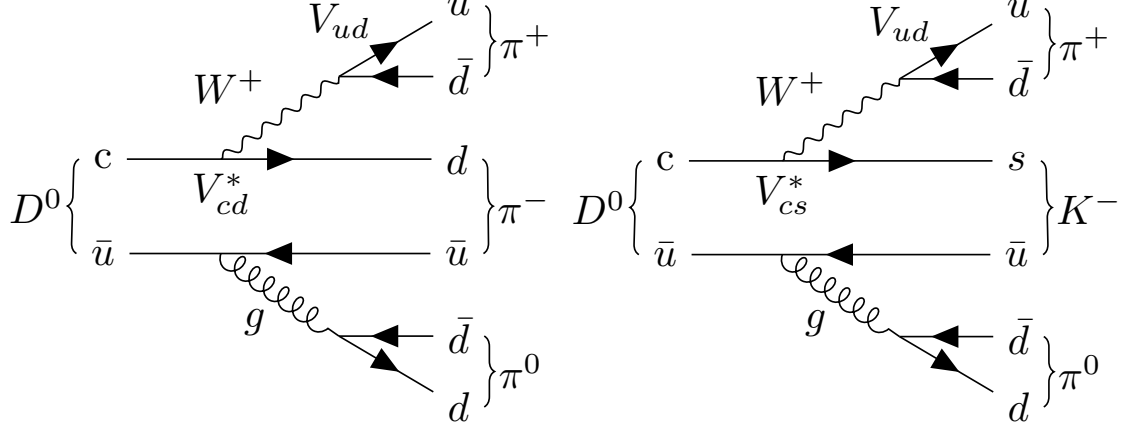
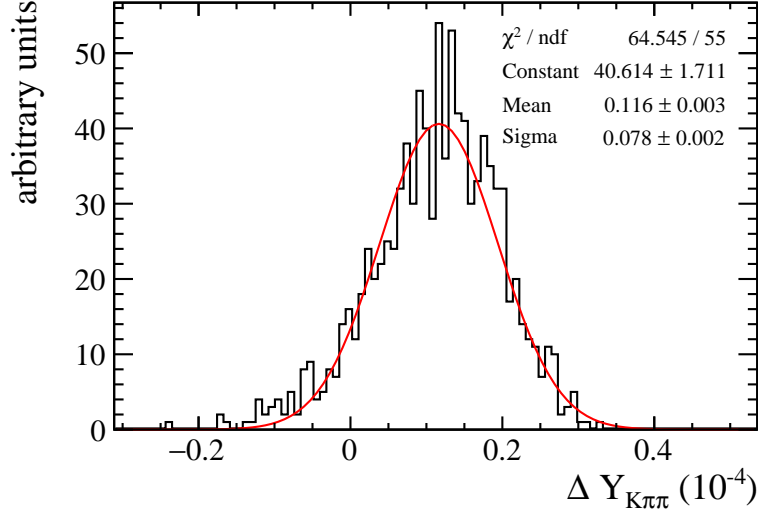


Figure 1.4: Example tree-level Feynman diagrams for the (left) signal and (right) control channels. The CKM elements which contribute to each decay are indicated at the relevant vertices.

### 1.3.5 The analogous parameter $\Delta Y_{K\pi\pi}$

The signal decay that we study here,  $D^0 \rightarrow \pi^+ \pi^- \pi^0$ , can proceed in two ways: directly through the SCS decay  $D^0 \rightarrow \pi^+ \pi^- \pi^0$ , or through mixing,  $D^0 \rightarrow \bar{D}^0$ , followed by the SCS decay  $\bar{D}^0 \rightarrow \pi^+ \pi^- \pi^0$ . The same is true for an initial  $\bar{D}^0$  state. The decay  $D^0 \rightarrow K^- \pi^+ \pi^0$  has similar kinematics to the signal mode, but proceeds through either a direct CF decay,  $D^0 \rightarrow K^- \pi^+ \pi^0$ , or mixing followed by a DCS decay,  $D^0 \rightarrow \bar{D}^0 \rightarrow K^- \pi^+ \pi^0$ . An initial  $\bar{D}^0$  meson decays to the final state  $K^+ \pi^- \pi^0$  in a similar manner. Figure 1.4 shows example tree-level diagrams for the signal and control decays, with the relevant CKM elements indicated. Since time-dependent  $CP$  violation arises from mixing and/or the interference of mixing and decay, the  $D^0 \rightarrow K^- \pi^+ \pi^0$  decay provides a suitable control channel for this measurement since the CF decay dominates and thus indirect  $CP$  violation effects are strongly suppressed compared to the signal channel. Thus, the analogous parameter to  $\Delta Y$  in this decay mode,  $\Delta Y_{K\pi\pi}$ , can be considered negligible at the current level of precision. Any time-dependent asymmetry observed in the data with the current level of statistics for this channel therefore must be some non-physical, detection-induced asymmetry.

To quantify the above argument, one can show that the expression for the time-


 Figure 1.5: Results of toy study to estimate the value of  $\Delta Y_{K\pi\pi}$ .

dependent  $CP$  asymmetry in the control mode ( $f = K^-\pi^+\pi^0$ ) is given by

$$\Delta Y_f \approx \sqrt{\frac{\Gamma_{\bar{f}}}{\Gamma_f}} \left( -[x \cos(\delta_f) + y \sin(\delta_f)] \phi + [y \cos(\delta_f) - x \sin(\delta_f)] \left[ \left\{ \left| \frac{q}{p} \right| - 1 \right\} - \frac{1}{2} \{a_f^d + a_{\bar{f}}^d\} \right] \right). \quad (1.84)$$

Here,  $\delta_f$  is the average strong phase across the phase space,  $a_f^d$  and  $a_{\bar{f}}^d$  are the decay-rate asymmetries of the Cabibbo-favoured and double Cabibbo-suppressed decays, respectively, and all other parameters have their usual meanings. To evaluate the value of  $\Delta Y_{K\pi\pi}$ , we perform a toy study taking as input the HFLAV global fit results — including all correlations and allowing for all types of  $CP$  violation — for the mixing parameters and strong phase [43], and the PDG averages for the decay-rate ratio and asymmetries [8]. The set of parameters is sampled 1000 times, and the resulting distribution of values of  $\Delta Y_{K\pi\pi}$  is shown in Figure 1.5. By fitting a Gaussian curve to the resulting distribution, we find the value of  $\Delta Y_{K\pi\pi}$  to be

$$\Delta Y_{K\pi\pi} = (1.16 \pm 0.78) \times 10^{-5}, \quad (1.85)$$

which corresponds to an upper limit of  $|\Delta Y_{K\pi\pi}| < 2.45 \times 10^{-5}$  at 90% confidence level. Thus, the measured value of  $\Delta Y_{K\pi\pi}$  should be compatible with zero at the precision measured in this analysis of  $\mathcal{O}(10^{-4})$ . The impact of a non-uniform phase-space acceptance is not considered in this study. This effect is nonetheless not

expected to inflate the effective asymmetry to a level which can be resolved by this analysis.

## 1.4 Summary

A general overview of the electroweak theory within the SM has been provided, in particular demonstrating how the Brout-Englert-Higgs mechanism leads to off-diagonal terms in the charged current weak interactions which allow for transformations between the quark generations and, in particular, the presence of mixing in the flavoured neutral meson systems. A detailed discussion of time-dependent  $CP$  violation in the  $D^0$  system has been presented, including an overview of determining the parameter  $\Delta Y$  from  $D^0 \rightarrow \pi^+\pi^+\pi^0$  decays. An estimate of the corresponding asymmetry in the channel  $D^0 \rightarrow K^-\pi^+\pi^0$ ,  $\Delta Y_{K\pi\pi}$ , has also been presented to demonstrate its suitability as a control channel with similar kinematic properties but a negligible time-dependent asymmetry within the SM.

# The LHCb Experiment at the LHC

---

THE LHCb experiment is one of four major experiments situated on the Large Hadron Collider (LHC) ring, which straddles the Swiss-French border outside Geneva. The LHC is the largest and most energetic particle collider ever built. With a circumference of roughly 27 km, the LHC ring has an approximately circular shape consisting of eight arc sections and eight straight sections. The layout of the LHC ring is shown in Figure 2.1. During operation, two counter-rotating beams are circulated around the ring, and brought to collide at four interaction points (IPs). While the primary physics programme of the LHC utilises proton beams, heavy-ion collisions exploiting lead beams have been extensively studied during Runs 1 and 2 [63]; Xenon beams have briefly been injected [64], and there are also plans to inject oxygen beams in Run 3 [65]. The discussion presented here will refer to the proton-proton programme throughout, without explicit mention. The two largest<sup>1</sup> experiments at the LHC, ATLAS and CMS, are situated at opposite sides of the LHC ring. Both ATLAS and CMS are so-called ‘general-purpose’ detectors, and have an approximately complete angular ( $4\pi$ ) acceptance to allow as close to a full reconstruction of each  $pp$  collision as possible. A  $4\pi$  acceptance provides useful kinematic constraints in events where some decay products (*i.e.* neutrinos) are ‘invisible’ to the detector. The physics programmes of ATLAS and CMS are primarily concerned with exploiting the energy frontier of the LHC to directly search for heavy new particles, studying the top quark, and — since its discovery [66, 67] — probe the properties of the Higgs boson. The ALICE experiment, located at interaction point 2 (IP2), also possesses a  $4\pi$  acceptance, but is optimised for the

---

<sup>1</sup>Largest in number of authors, not the physical size of the detector.

study of heavy-ion collisions, and in particular the properties of the quark-gluon plasma. The LHCb experiment is unique amongst the principal four experiments at the LHC in that its acceptance only covers the region  $2 < \eta < 5$ , where  $\eta \equiv -\ln(\tan(\theta/2))$  is the pseudorapidity, and  $\theta$  is the angle between a particle and the beam-axis. In this chapter, Section 2.1 will be dedicated to describing the LHC and how collisions are produced at each IP, and Section 2.2 will describe in detail the operation of the LHCb detector.

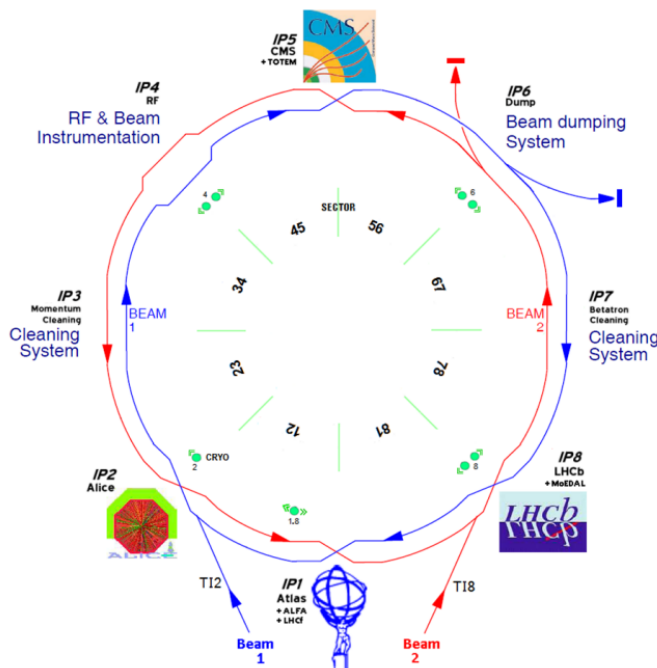


Figure 2.1: Layout of the LHC ring. Reproduced from Ref. [68].

## 2.1 The LHC accelerator complex

Protons which are collided at each of the experiments situated on the LHC ring begin as constituents of atoms in a bottle of Hydrogen gas. In Runs 1 and 2, an electric field was used to ionise the atoms, and the resulting nuclei, *i.e.* protons, were passed into the Linear Accelerator 2 (Linac2) and accelerated to an energy of 50 MeV. In preparation for Runs 3 and 4 of the LHC, Linac2 was upgraded to a new linear accelerator, Linac4, which accelerates  $H^-$  ions to 160 MeV before injection into the Proton Synchrotron Booster (PSB), where they are stripped to bare protons [69]. The PSB further accelerates the protons to an energy of 1.4 GeV. Following the PSB,

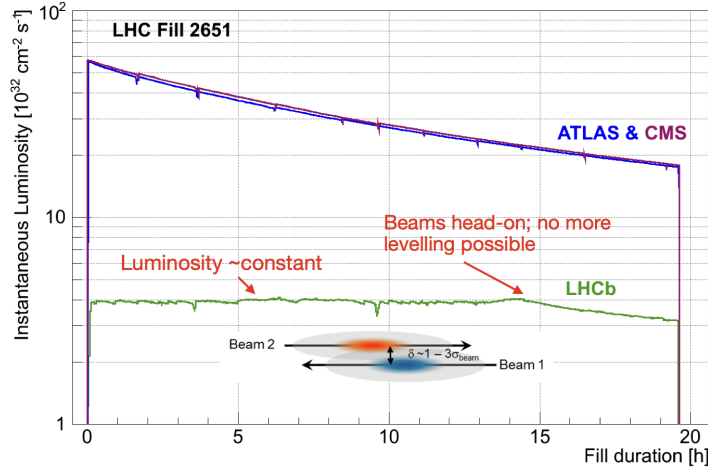


Figure 2.2: Evolution of instantaneous luminosity throughout fill 2651 for ATLAS, CMS and LHCb to illustrate the levelling procedure at LHCb. Adapted from [70].

the beams are passed to the Proton Synchrotron (PS) to be further accelerated to an energy of 26 GeV. Finally, the Super Proton Synchrotron (SPS) boosts the energy of the proton bunches to 450 GeV, at which point they are injected into the LHC. Once injected into the LHC, the bunches are accelerated up to the collision energy, before being ‘squeezed’ (essentially focused) to the nominal parameters for collisions, at which point ‘stable beams’ are declared and the experiments begin recording data. The radio-frequency (RF) cavities which accelerate the bunches in the LHC operate at a frequency of 401 MHz. Combined with the circumference of the ring, this gives 35,640 2.5 ns-long windows defined as ‘RF buckets’. The buckets are further grouped into 25 ns long periods defined as ‘bunch slots’. When beams are injected into the LHC, only the central<sup>2</sup> RF bucket of each bunch slot is nominally filled, giving a maximum possible number of bunches of 3,564. For practical reasons, due to the injection scheme from the SPS and the requirement of an empty region of the ring — known as the abort gap — to allow ramp up of the beam dump magnets, this number was limited to  $\sim 2,800$  during Runs 1 and 2 [68]. For the measurements described in this thesis, the LHC was operated at centre of mass energies of  $\sqrt{s} = 8$  and 13 TeV in 2012 and 2015-18, respectively. In Run 3, the LHC is being operated at a centre of mass energy of  $\sqrt{s} = 13.6$  TeV.

The ATLAS and CMS experiments typically operate at the maximum available instantaneous luminosity of the LHC,  $\sim 10^{34} \text{ cm}^{-2} \text{ s}^{-1}$ . For the physics programme

<sup>2</sup>Or, pedantically, one of the central pair of buckets.

at LHCb however, it is beneficial to reduce the luminosity and therefore reduce occupancy in the detector to improve reconstruction efficiencies and the quality of measured kinematic quantities. In addition, consistent running conditions allow the LHCb trigger to be optimised for a known, fixed set of conditions. A constant luminosity is achieved using a process known as luminosity levelling [71]. At the beginning of each fill, the beams are displaced from head-on in the transverse plane at the LHCb interaction point. Throughout the fill, the beams are gradually moved towards head-on collisions, keeping the luminosity constant as far as beam intensity decay allows. In Runs 1 and 2 the luminosity at the LHCb interaction point was optimised such that the average number of (visible) inelastic  $pp$  collisions per bunch crossing was  $\sim 1$ . This corresponds to an instantaneous luminosity of  $\sim 4 \times 10^{32} \text{ cm}^{-2}\text{s}^{-1}$ . The levelling procedure is illustrated in Figure 2.2.

## 2.2 The LHCb detector

The layout of the LHCb detector is shown in Figure 2.3. The relatively small angle around the beam-axis covered by the detector is motivated by the fact that  $b\bar{b}$  and  $c\bar{c}$  pairs at the LHC are primarily produced at a small, highly correlated, angle with respect to the beam-axis, as shown for the  $b\bar{b}$  case in Figure 2.4. Constructing a detector with a reduced acceptance reduces the material cost of the detector and allows the finite resources available to be focused on the physics performance. While the LHCb detector was constructed with a physics programme focused on  $b$ -hadron physics, a much wider range of analyses has since developed. Of particular relevance to this thesis, a significant charm physics programme has emerged, including a number of world-leading mixing and  $CP$  violation measurements [45, 50, 52, 59, 60].

The LHCb detector is optimised for precise tracking measurements and accurate particle identification (PID), particularly of charged hadrons and leptons. The tracking system is composed of a silicon detector close to the collision point and a set of tracking stations upstream and downstream of a room-temperature magnet. Particle identification for charged hadrons is provided by a pair of Ring Imaging Cherenkov (RICH) detectors before and after the magnet. A calorimeter system provides neutral hadron and photon reconstruction, and helps to identify electrons. Finally, a set of muon stations provide additional tracking measurements and PID for muons. Each of the sub-systems will be described in detail in the following sections. A description of the reconstruction and triggering procedure will also be

provided.

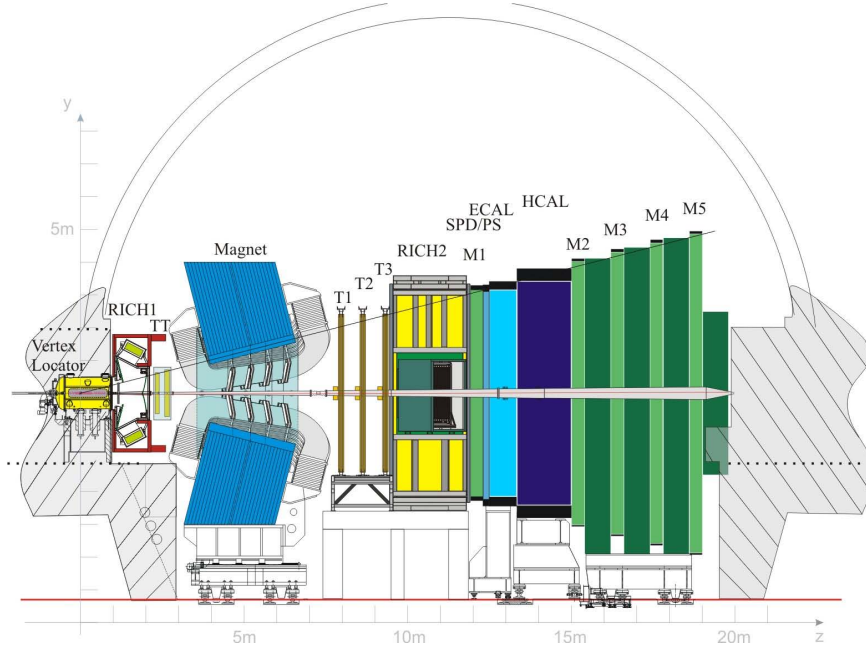


Figure 2.3: Layout of the LHCb detector [72].

The LHCb detector has recently been upgraded to an almost entirely new detector in preparation for Runs 3 and 4 of the LHC. The discussion presented here pertains to the original LHCb detector which was operational during Runs 1 and 2 and is most relevant to this thesis. The upgraded detector is briefly summarised in Section 2.2.12.

A coordinate system within the LHCb detector is assumed in this chapter, and throughout the rest of this thesis. The  $z$ -axis is aligned with the beam-axis passing through the middle of the LHCb detector, and increasing in the direction of the sub-detectors. The  $x$ -axis is parallel to the plane of the LHC ring, increasing moving outwards from the centre of the ring. The  $y$ -axis is oriented perpendicular to the  $x$ - and  $z$ -axes, increasing moving towards the surface from the LHCb cavern. The origin is placed at the centre of the nominal interaction region. The terms ‘upstream’ and ‘downstream’ are used to denote smaller or larger coordinates on the  $z$ -axis, respectively.

### 2.2.1 VERtEX LOcator

The innermost sub-detector of the LHCb experiment is known as the VERtEX LOcator (VELO). The principle function of the VELO is to reconstruct primary vertices

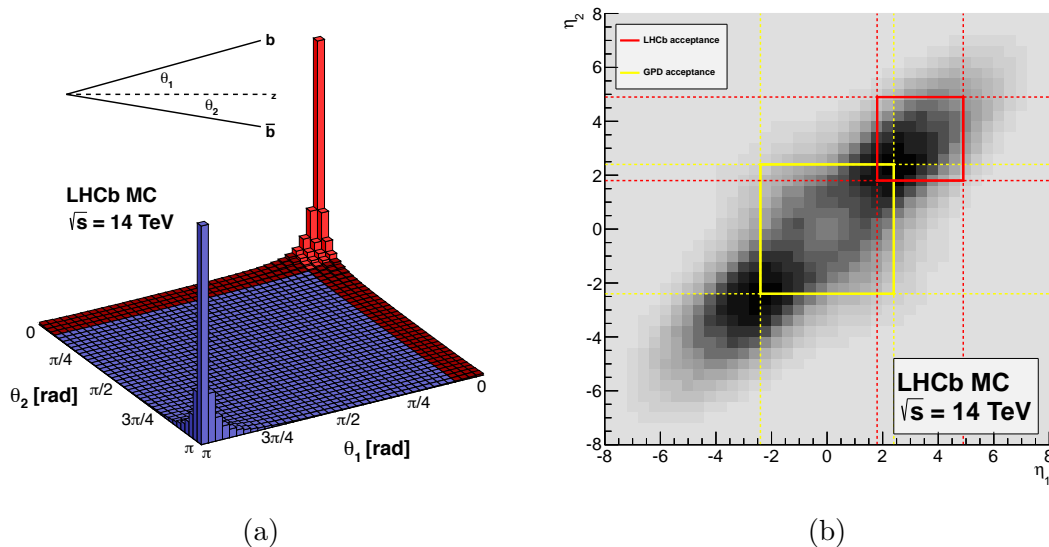


Figure 2.4: Two-dimensional angular distribution of  $b\bar{b}$  pairs produced at the LHC with a centre of mass energy of  $\sqrt{s} = 14$  TeV from simulation. Shown (a) with the LHCb acceptance highlighted in red, and (b) with both the LHCb and approximate ATLAS/CMS acceptances highlighted in red and yellow, respectively [73].

(PVs). The PV is defined as the position of the initial parton interaction in some collision. Weakly decaying  $b$ - and  $c$ -hadrons have lifetimes of  $\mathcal{O}(\text{ps})$ , and their mean flight distance in the LHCb detector is  $\mathcal{O}(1\text{ cm})$ ; thus, they decay well within the VELO which has an overall length of  $\sim 1$  m. The VELO is therefore also crucial for measuring the decay vertex (DV) of long-lived hadrons to allow precise decay-time measurements for time-dependent mixing and  $CP$  violation analyses.

The above physics aims and the conditions at the LHC imposed certain conditions on the construction of the VELO. To improve the vertex resolution, it is beneficial to place the VELO sensors as close as possible to the interaction region, and therefore reduce the distance of extrapolation between tracks in the detector and their origin vertex. However, the LHC requires a minimum clearance between the beams and surrounding hardware such as detectors and the beam-pipe, which is defined in terms of the beam width. Thus, the required clearance is larger at injection than after focusing the beams for collisions. To counteract this, the VELO was designed in two halves to be initially retracted by 3 cm per-half at injection, and then moved into its nominal data-taking position once the LHC declared stable beams. In the nominal position, the innermost radius of the sensors was  $\sim 7$  mm from the LHC beams [74]. Due to the harsh radiation environment close to the

collision point, the design of the VELO elements close to the beam was required to be extremely radiation tolerant.

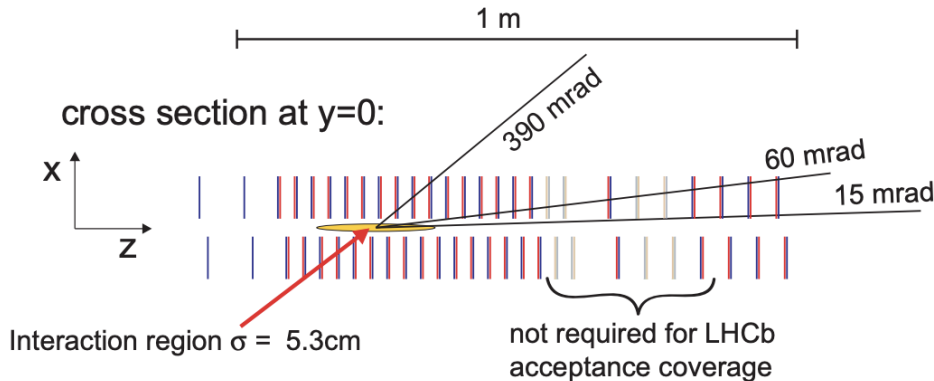


Figure 2.5: Layout of the LHCb VELO modules. Reproduced from [75]. The red (blue) lines indicate a  $\phi$ -sensor ( $r$ -sensor). The grey modules indicate those that were removed from the design in the detector re-optimisation.

Each VELO half was constructed of 21 modules, separated by 3 cm in the  $z$ -axis near the interaction region and by 5 cm further downstream [76]. The two halves were offset by 1.5 cm in the  $z$ -axis relative to one another. Each module held two approximately semi-circular sensors: an  $r$ -sensor, and a  $\phi$ -sensor. Each sensor covered an angular area of slightly greater than  $\pi$  to allow a slight overlap between the VELO halves, which enabled their relative alignment. Each  $r$ -sensor consisted of silicon strips of constant radius to measure the radial position of incident tracks, and each  $\phi$ -sensor was composed of roughly orthogonally-oriented silicon strips to measure the angular position of incident tracks. The ordering of the  $r$ - and  $\phi$ -sensors was switched at each module. The original design of the VELO consisted of 25 modules per-half [77]. In order to reduce the overall material budget of the detector, this was later refined to the final design with 21 modules per-half [75]. The final layout is illustrated in Figure 2.5 together with its differences with respect to the original design. The presence of modules upstream of the interaction region provided additional tracks to improve the PV resolution. Each VELO half contained an additional two modules containing  $r$ -sensors only to estimate the number of PVs in each event and provide a veto for busy events in the first trigger stage. The number of stations and their spacing within the VELO ensured that every track within the LHCb acceptance would pass through at least three VELO modules [78], given constraints imposed on the size of each module for procurement reasons [77].

Each VELO sensor consisted of 2048, 300  $\mu\text{m}$ -thick silicon strips arranged as

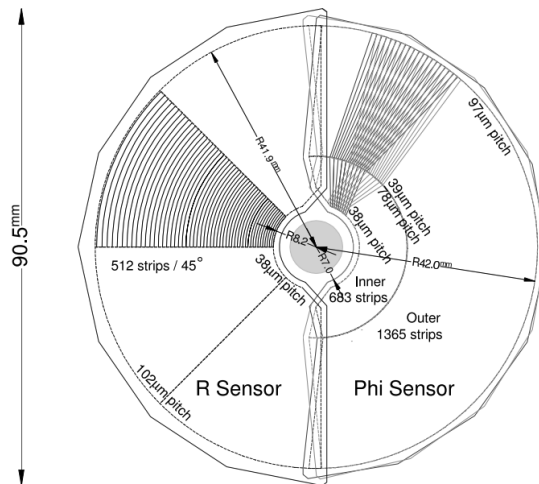


Figure 2.6: Strip layout on a single VELO  $r$ - and  $\phi$ -sensor [78].

shown in Figure 2.6. Each sensor has a radius of 41.9 mm. The  $r$ -sensors consisted of four groups of 512 strips, with each covering an angular region of  $\pi/4$  rad. The strip pitch — the distance between the active sensor elements — linearly increased from  $38\text{ }\mu\text{m}$  for the shortest pair of strips, to  $101.6\text{ }\mu\text{m}$  for the longest pair of strips. The choice to segment the radial strips into four groups was made to reduce the occupancy of each strip and therefore reduce the rate of ghost tracks. Each  $\phi$ -sensor consisted of an inner set of 683 strips and an outer set of 1365 strips. The inner strips were designed with a strip pitch of  $35.5\text{ }\mu\text{m}$  at their innermost point, rising to  $78.3\text{ }\mu\text{m}$  at their outermost point of 17.25 mm. The strip pitch of the outer strips was between  $39.3\text{ }\mu\text{m}$  and  $97\text{ }\mu\text{m}$ . The choice to segment the strips into an inner and outer region was driven partly to avoid a large strip pitch in the outer region, and partly to reduce the occupancy in each strip. The ghost track rate was further reduced by placing the strips on the  $\phi$ -sensors at an angle with respect to the radial. The inner strips were rotated by  $20^\circ$ , while the outer strips were rotated by  $10^\circ$  in the opposite direction. Reversing these angles at every subsequent station then provided some separation power between ghost hits and true hits in each sensor. The average occupancy of the strips in the VELO was  $\sim 1\%$  [78].

The VELO achieved a hit resolution of  $\mathcal{O}(10\text{ }\mu\text{m})$ , depending on the region of the sensor — *i.e.* the strip pitch — and the angle of the track, as illustrated in Figure 2.7 [70]. An improvement over the naïve binary hit resolution — the variance of a uniform distribution with width given by the strip pitch — is achieved by reconstructing clusters rather than hits in individual strips. Clusters were created

starting with the strip producing the largest signal in a region of a VELO sensor, and adding adjacent strips to the cluster as long as they passed a minimum signal threshold. A maximum of four strips were included in each cluster. The position of each hit can therefore be more precisely determined as the mean of the strip positions, weighted by the ADC signal in each strip. The typical hit efficiency in the VELO was  $\sim 99.5\%$  [74]. To determine the hit efficiency and resolution, a set of tracks are fitted with a given sensor excluded. The track is then extrapolated to the sensor under consideration. The presence or lack of a hit determines the efficiency, and the residual between the expected and measured hit determines the resolution.

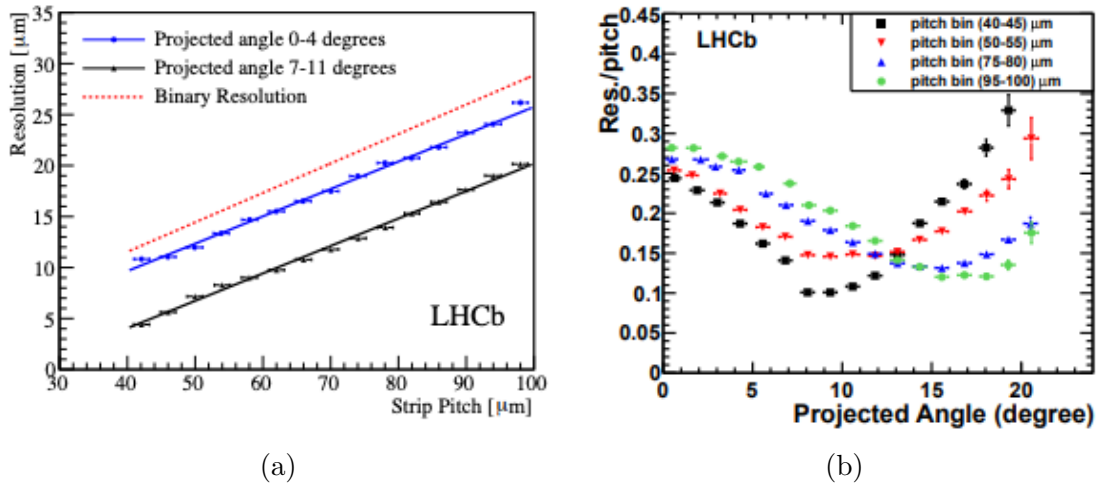


Figure 2.7: VELO hit resolution as a function of (a) strip pitch for two different bins of track incidence angle, and (b) track incidence angle in multiple bins of strip pitch. The red dashed line on the left plot shows the strip pitch divided by  $\sqrt{12}$ , indicative of a binary hit readout. Reproduced from [70].

The bunch crossing rate at the LHC is  $\sim 40$  MHz. In Runs 1 and 2 the LHCb detector operated with a hardware trigger — described in Section 2.2.10.1 — which reduced the rate of events to be retained to  $\sim 1$  MHz. A set of 32 Beetle application-specific integrated circuits (ASICs) [79] were therefore glued to each module. The Beetle chip allowed the sensors on each module to be sampled at a rate of 40 MHz, and the module to be read out at a rate of 1 MHz, with a buffer to allow readout of consecutive events. Each module was then connected through a vacuum-feedthrough system to a pair of 1 MHz ‘TELL1’ readout boards [78,80]. The TELL1 is a custom field-programmable gate array (FPGA) designed to facilitate pre-processing and readout of any LHCb sub-detector at the L0 trigger accept-rate of  $\sim 1.1$  MHz as input to the first high-level trigger.

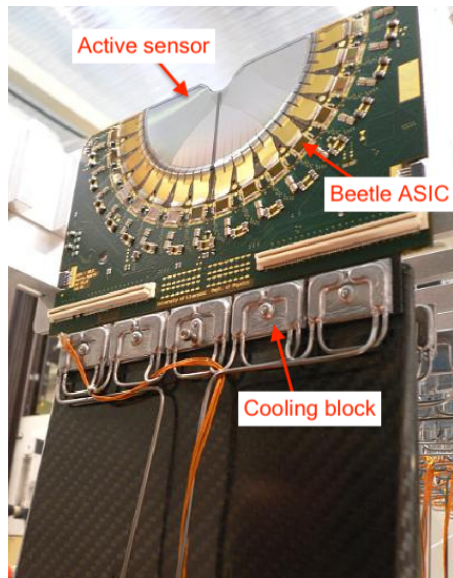


Figure 2.8: Photograph of a single VELO module showing the active sensors, Beetle ASICs, and cooling blocks. Reproduced from Ref. [81] with additional annotations.

Each VELO module also housed five cooling blocks in thermal contact with a set of capillaries to distribute liquid  $\text{CO}_2$  amongst the modules in each VELO half. Each of the sensors were cooled to a target temperature of below  $-5^\circ\text{C}$  to mitigate the impact of radiation damage. Figure 2.8 shows a photograph of a single VELO module with the sensors, Beetle chips, and cooling blocks visible.

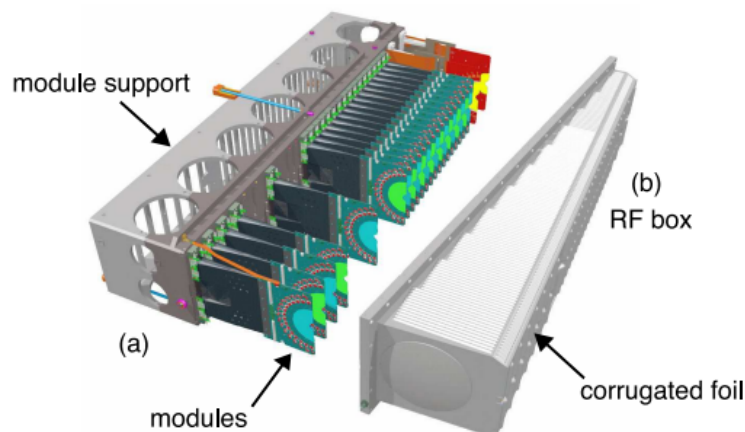


Figure 2.9: Layout of the VELO modules inside the RF box for one VELO half [78].

Each half of the VELO was enclosed in a so-called ‘RF box’ to separate the VELO modules from the primary beam-vacuum of the LHC. The RF box was constructed of 500  $\mu\text{m}$ -thick aluminium walls, with a 300  $\mu\text{m}$ -thick aluminium-magnesium alloy (AlMg3) foil on the side closest to the sensors. The foil was corrugated to fit the

shape of the sensors and allow a complete overlap between the two VELO halves. Operating the VELO modules under vacuum reduces the material budget between the particles produced in each collision and the VELO sensors, since the RF foil does not need to withstand a large pressure difference between the active detector elements and the interaction point. Separating VELO modules in a secondary vacuum also protects the primary LHC vacuum from outgassing of the detector modules, and shields the detector modules from RF fields produced by the LHC beams. The design of the RF box is shown in Figure 2.9.

### 2.2.2 Magnet

The LHCb detector utilises a warm dipole magnet to deflect the trajectories of charged particles and allow precise measurements of their momenta. A warm magnet design, instead of super-conducting, was chosen to reduce both construction time and financial cost. The magnet provides an integrated magnetic field of  $\int B dx \approx 4 \text{ Tm}$  over a track length of  $\sim 10 \text{ m}$ . A diagram of the magnet is shown in Figure 2.10a with the LHCb coordinate system indicated. The magnet provides a magnetic field in the  $y$ -direction such that the trajectories of charged particles traversing the detector are deflected in the  $xz$ -plane. An accurate and precise mapping of the magnetic field for the reconstruction of charged tracks is critical for the physics performance of the LHCb detector, which relies heavily on precise momentum measurements. A detailed mapping of the magnetic field from the interaction point to the RICH2 PID detector, within the LHCb acceptance, has been completed. With  $\mathcal{O}(\text{mm})$  spatial precision, the magnetic field is known to a precision of  $\delta B/B \sim \mathcal{O}(10^{-4})$ . The measured values are generally in excellent agreement with a prior simulation of the expected magnetic field. An additional complication in the magnetic field mapping arises from hysteresis effects. The LHCb magnet is designed to allow the polarity to be reversed frequently during data-taking, which helps to partially cancel detection asymmetries which can bias  $CP$  violation measurements. It has been shown that an equivalent magnetic field of opposite polarity can be achieved at a level that is more precise than the field maps [78]. The magnetic field for each polarity is shown as a function of the  $z$ -position at  $(x, y) = (0, 0)$  in Figure 2.10b.

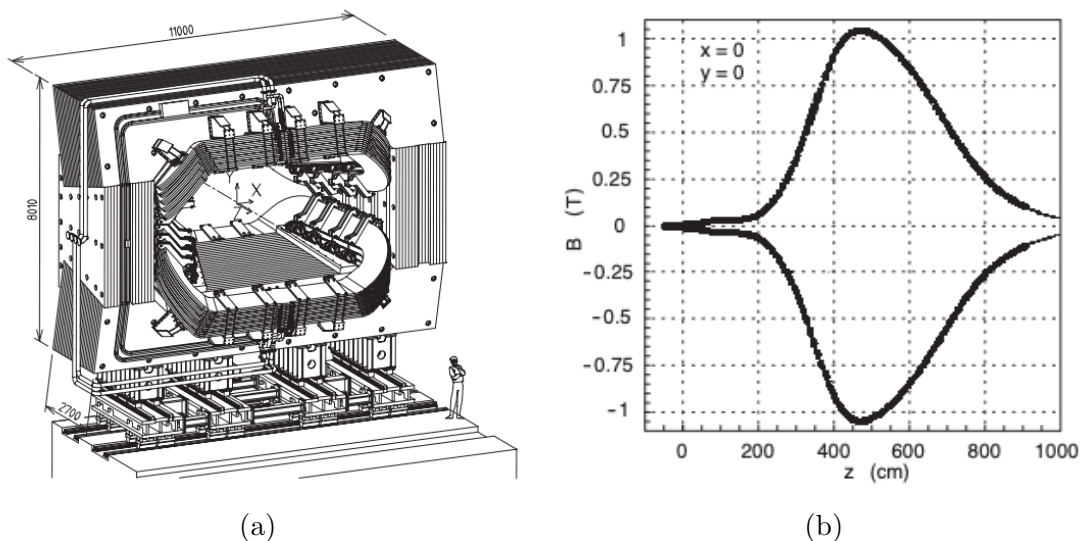


Figure 2.10: (a) Diagram of the LHCb magnet, with the LHCb coordinate system indicated, and (b) magnetic field in the  $y$ -direction,  $B_y$ , as a function of the  $z$ -position at  $x = y = 0$  for both magnet polarities [78].

### 2.2.3 Tracking stations

In addition to the VELO, the LHCb detector contained an additional set of tracking stations upstream and downstream of the magnet known as the Tracker Turicensis (or Trigger Tracker, TT) and tracking stations T1, T2, and T3 (T-stations). The TT was composed of silicon microstrip detectors to provide radiation hardness and lower occupancy per-channel due to its proximity to the interaction region relative to the downstream trackers. The inner regions of the T-stations — known as the Inner Tracker (IT) — were constructed from the same technology as the TT due to the same performance and environmental requirements. The outer regions of the T-stations — known as the Outer Tracker (OT) — were constructed from more cost-effective drift-time sensors. Collectively, the TT and IT were known as the Silicon Tracker (ST).

#### 2.2.3.1 Silicon tracker

The TT consisted of four layers covering a region of approximately 150 cm by 130 cm around 2.5-3 m downstream of the interaction region. The first two layers consisted of seven 14-sensor modules on either side of the beam pipe with two half-modules above and below the beam-pipe. Each 9.64 cm wide and 9.44 cm long sensor contained 512 strip detectors with a pitch of 183  $\mu\text{m}$ . The latter two layers consisted of

a similar design with eight modules on either side of the beam-pipe. The modules in the first and last layers were parallel, while the second and third layers were rotated by  $5^\circ$  in opposite directions. Figure 2.11a shows the structure of the third layer. The first two and last two layers were grouped together, with a gap of 27 cm between the two pairs [78].

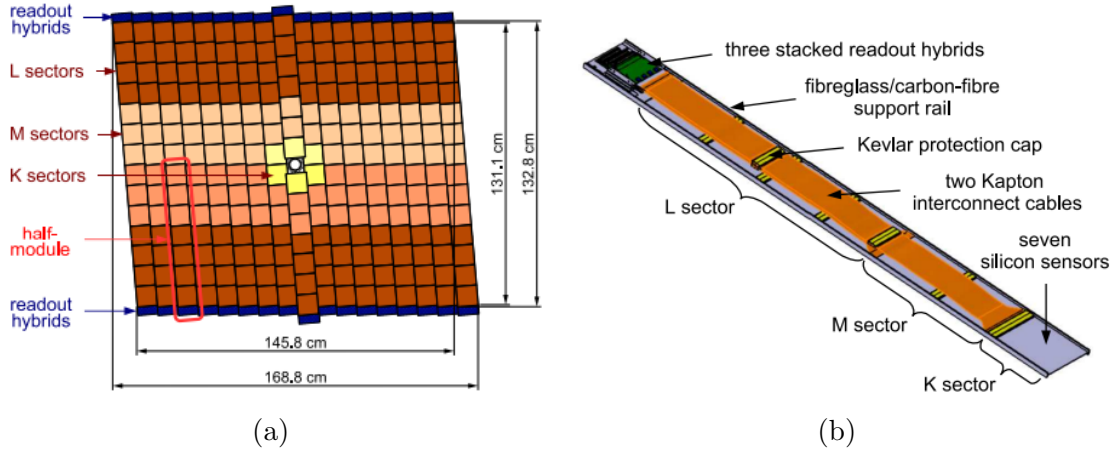


Figure 2.11: Layout of (a) one layer and (b) one half-module of the TT. Reproduced from [78].

Each half-module consisted of either two or three readout groups of sensors. The sensors were bonded together to form longer sensors in groups of between one and four sensors. The half-modules were then constructed from groups of sensors in either a 4-3 configuration, or a 4-2-1 configuration, to provide additional granularity and reduce occupancy in the inner region. The readout groups are indicated by the different coloured sensors on Figure 2.11a, and Figure 2.11b shows the layout of a single 4-2-1 half-module. The readout electronics were located along the top and bottom of each layer. The sensors were oriented such that the strips ran vertically (along the  $y$ -axis in the LHCb coordinate system) and provided the best possible resolution in the  $x$ -axis — given the sensor technology — where charged tracks are deflected by the LHCb magnet. The stereo angle between the layers allowed the  $y$ -position of each hit to be determined [78].

The IT stations of T1-T3 were constructed from layers of modules containing either one or two  $7.6 \times 11 \text{ cm}^2$  silicon sensors containing 384 strips with a  $198 \mu\text{m}$  pitch. The sensors on double-sensor and single-sensor modules were  $410 \mu\text{m}$  and  $320 \mu\text{m}$  thick, respectively, in order to optimise the trade off between single hit efficiencies and the total material budget of the tracking system. Each station

consisted of four layers, with the same  $5^\circ$  rotation structure as the four TT layers to provide the optimal resolution in the  $x$ -direction. The layout of the IT modules in a single layer around the beam-pipe is shown in Figure 2.12 [78].

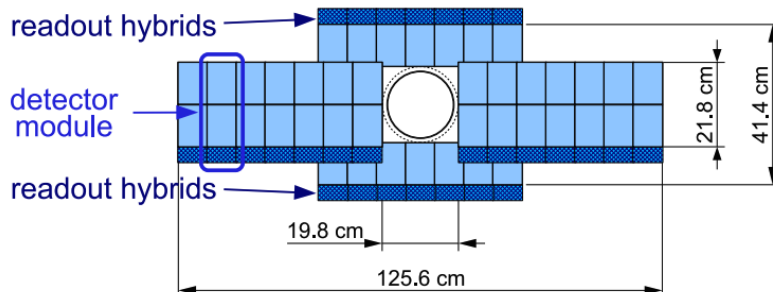


Figure 2.12: Layout of the IT modules in a single layer of a tracking station. Reproduced from [78].

The TT and IT achieved an average hit resolution of  $52.6\ \mu\text{m}$  and  $50.3\ \mu\text{m}$ , respectively. The typical hit efficiencies in both the IT and TT were  $> 99.7\%$ , considering only non-faulty detector channels. The fraction of fully functioning channels in Run 1 was  $\sim 99\%$  [70].

The entire set of ST layers were cooled to a temperature below  $5^\circ\text{C}$  using a liquid  $\text{C}_6\text{F}_{14}$  cooling system during operation. Beetle ASICs were utilised to sample and buffer analogue signals from each sensor at the crossing rate of  $\sim 40\ \text{MHz}$ , and a set of TELL1 boards were used to readout the ST detectors at the L0 accept rate of  $\sim 1.1\ \text{MHz}$ , in a similar fashion to the VELO [78].

### 2.2.3.2 Outer tracker

The OT covered a much larger, lower-occupancy area than the IT. Thus, it was constructed from more cost-effective straw-tube drift-time detectors. The OT regions of each of the T1-T3 tracking stations were composed of four layers with the same vertical orientation as in the ST, with the inner layers rotated from the vertical by  $5^\circ$  in opposite directions. Each layer was constructed from modules denoted  $F$ - and  $S$ -type; the  $F$ -type modules were  $\sim 5\ \text{m}$  long, while the  $S$ -type modules were slightly less than half the length of an  $F$ -type module. The  $F$ -type modules were constructed from two groups of straw tubes around half the module length, with the readout electronics at both ends of each module. The  $S$ -type modules consisted of a single set of straw tubes, and were read out from a single, outer, end. The arrangement of the modules in each layer is shown in Figure 2.13.

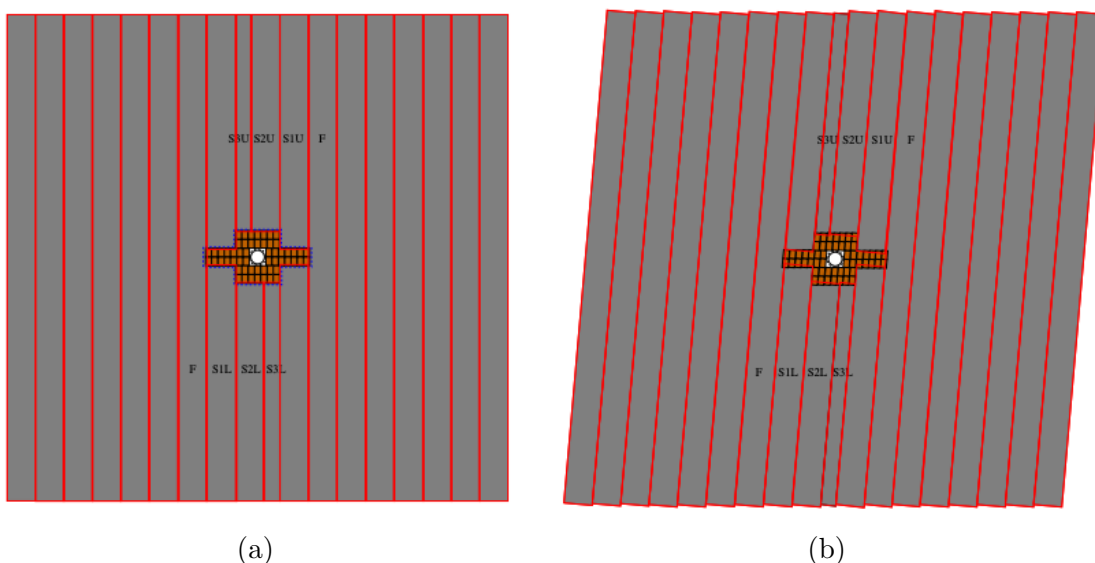


Figure 2.13: Layout of OT modules around the IT. Shown (a) for a vertical layer, and (b) for a layer rotated from the vertical by  $5^\circ$ . Reproduced from [82].

Each module consisted of 128 straw drift tubes divided into two offset layers as illustrated in Figure 2.14a. The straw tubes were constructed from an inner layer of Kapton-XC — a carbon-doped variant of Kapton — which acted as a cathode, and an outer layer of Kapton-Aluminium laminate, as shown in Figure 2.14b. Each tube had a diameter of approximately 5 mm. An anode consisting of a gold-plated tungsten wire was inserted in the centre of each tube. Each tube was filled with a mixture of 70% Ar and 30%  $\text{CO}_2$ . This gas choice ensures a drift time of  $< 50$  ns. The OT was read out using a set of custom front-end (FE) electronics boards which digitised and buffered the drift time — relative to the LHC clock — of each hit. The buffered data was read out to a set of TELL1 boards on each L0 trigger pass. The longest drift times of charges in the OT were  $\sim 35$  ns, which is longer than the length of a single bunch slot (25 ns). To account for this — and other delays such as time-of-flight of the incident particle and signal transmission to the readout electronics — three consecutive bunch crossings were read out on every positive L0 trigger decision.

A hit resolution of  $205\ \mu\text{m}$  was achieved in the OT. The hit efficiency in the OT can be studied as a function of the distance between the position of a predicted hit and the anode. The predicted hit position is based on a track fit with the straw tube under consideration excluded. An example of such a profile is shown in Figure 2.15. The mean hit efficiency in the region of the straw tubes with radius  $< 1.25$  mm was

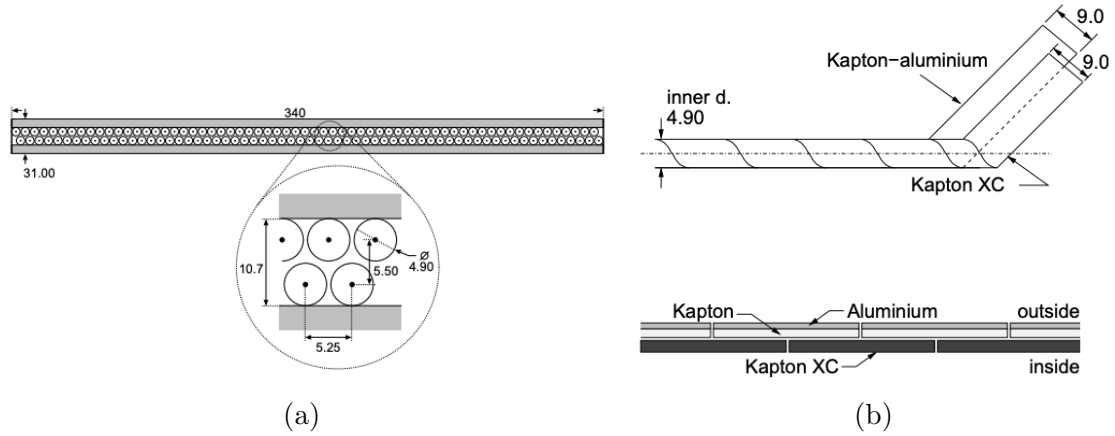


Figure 2.14: (a) Arrangement of straw tubes within a single OT module and (b) composition of a single straw tube. Reproduced from [78].

99.2% [70, 83].

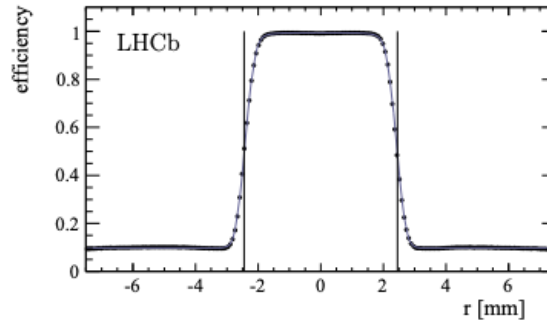


Figure 2.15: Example hit efficiency curve from a single straw tube of the OT. Reproduced from [70].

## 2.2.4 Track reconstruction

Charged tracks in the LHCb detector are fitted using a Kalman filter approach [84]. The Kalman filter approach requires an estimate (seed) of the parameters of a track at a given detector plane, and iteratively adds a sequence of detector hits, updating the track parameters and covariance matrix with each hit that is added. The track seeds can be obtained by applying pattern recognition algorithms to the hits recorded in a single sub-detector in a single bunch crossing. In the VELO, the magnetic field can be neglected and each track forms a straight line. In the TT and T-stations the magnetic field must be taken into account. Each track can be represented by a

state vector given by

$$\vec{x}^T = \left( x, y, \frac{dx}{dz}, \frac{dy}{dz}, \frac{q}{p} \right), \quad (2.1)$$

and its covariance matrix. Here,  $q$  is the charge of the relevant particle,  $p$  is the particle's momentum and  $x, y$  and  $z$  are position coordinates in the LHCb coordinate system. Each state update in the Kalman filter is performed in two steps: prediction and filtering.

In the prediction step, a physical model is applied to the state vector in the first detector layer to predict the state vector (and covariance matrix) in a subsequent detector plane. In the absence of external forces, the coordinates would simply be updated linearly based on their derivatives. In the LHCb detector, the magnetic field is known extremely precisely, as described in Section 2.2.2. The effect of the magnetic field can be incorporated by propagating the track state according to the Lorentz force experienced by a charged particle. The effect of multiple scattering can be incorporated by adding a noise term to the covariance matrix. Since the average energy loss of a charged particle traversing a material can be determined, the effects of energy loss can be incorporated by updating the track momentum in the propagation.

In the filter step, an updated state vector and covariance matrix can be obtained from a least squares fit which minimises the difference between the new state vector and the predicted state vector, given a measured hit in the subsequent detector plane. This updated state is then passed back into the prediction step to propagate the state to the next detector plane. In this manner, the track is iteratively fitted through the entire set of detector layers. This procedure is illustrated in Figure 2.16 with, for example, the  $y$ -direction suppressed.

When the iteration is complete, a measurement of the track state in each detector layer  $i$  exists based on information from all layers  $j < i$ . In order to, for example, reject individual hits which are inconsistent with the overall track, it is desirable to know the track state as precisely as possible in every detector layer. This can be achieved by applying a ‘smoothing’ technique which filters information backwards to earlier stages of the iteration.

Several different track types can be defined in the LHCb detector. The different categories are illustrated in Figure 2.17. VELO tracks are defined as those which leave hits in only the VELO and subsequently lie outside the acceptance of the tracking system. Upstream tracks are those which pass through the VELO and TT,

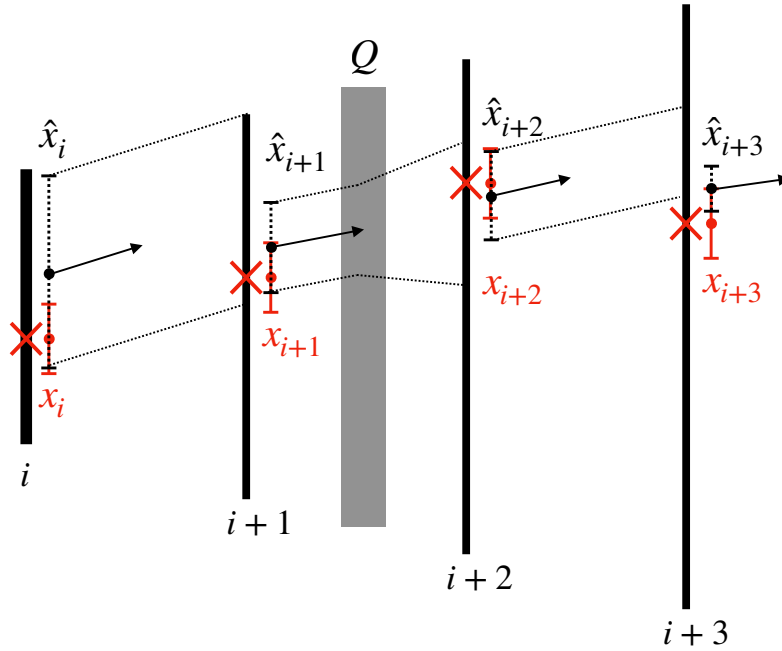


Figure 2.16: Example iterative one-dimensional Kalman fit procedure. At each step,  $x_j$  represents a hit in the detector which is added to the track and  $\hat{x}_j$  represents the updated track state after including  $x_j$ . The dashed lines (loosely) represent the propagation of the track state and covariance to the next detector plane. A noise term  $Q$  is added to the covariance matrix between layers  $i+1$  and  $i+2$  to include the effect of multiple scattering in some material layer.

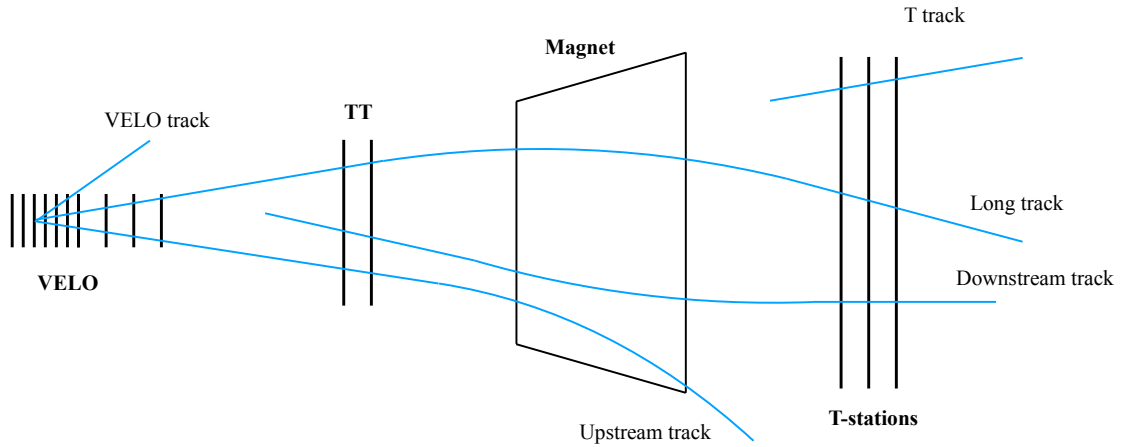


Figure 2.17: Illustration of the different track types defined within the LHCb detector.

but lie outside the T-stations' acceptance; for example, low momentum particles are easily deflected out of the acceptance by the magnet. Long tracks leave hits across the entire tracking system. Finally, downstream tracks and T tracks origi-

nate from decay products of particles which decay downstream of the VELO and TT, respectively. The most precise momentum measurements are available for long tracks. Downstream tracks have a somewhat worse resolution since track directions reconstructed by the VELO are more precise than those from the TT. A rough measurement of the momentum of upstream tracks is possible since there is some small stray magnetic field between the VELO and TT.

The first stage of the LHCb track reconstruction involves identifying groups of hits consistent with originating from a single track in the VELO. Track segments from the VELO are then combined with individual T-station hits to estimate the track momentum and therefore trajectory. Hits in the T-station are projected along the estimated trajectory to a fixed plane at  $z = 8520$  mm (in the T-stations). If the correct pairing between VELO track and T-station hit was made, a peak should be present in the transverse distributions of hits on the projection plane. Otherwise, the projected hit distribution should be uniform. Groups of hits in the T-station consistent with originating from each VELO track are added to the VELO hits to form a potential long track candidate. This approach is known as ‘forward tracking’ [85]. An alternative and complementary approach known as ‘track matching’ also exists [86,87]. In track matching, T-station track segments are projected backwards through the magnetic field to search for consistent VELO segments. Finally, based on the estimated track parameters from VELO and T-station hits, consistent TT hits are added to form a long track candidate. The resulting set of hits from the entire tracking system is then fitted using the Kalman filter approach described above to determine the final measured track parameters. Upstream and downstream track candidates are formed in a similar fashion to the track matching by extrapolating track segments in the VELO and T-stations to the TT, respectively. The final track parameters are again determined using a Kalman fit. Clone tracks are removed based on the number of hits shared by either entire tracks, or track segments in specific tracking stations.

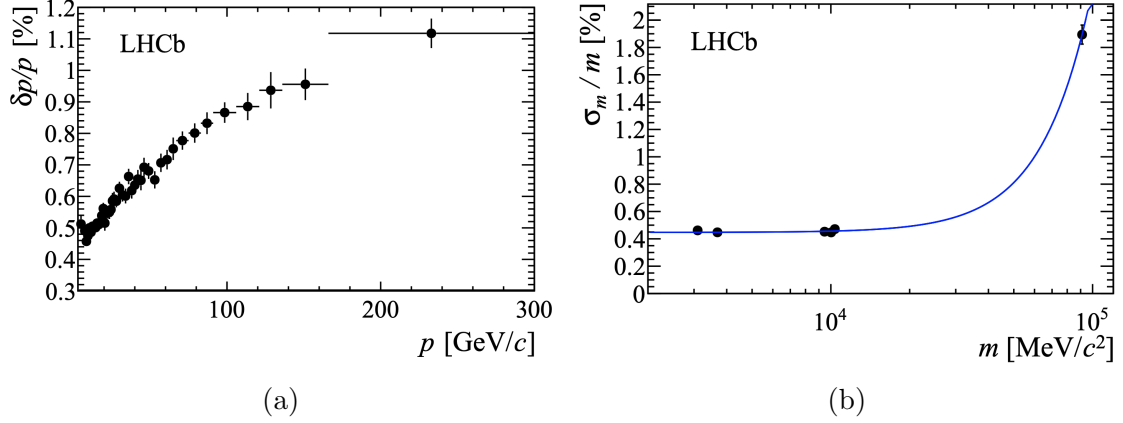


Figure 2.18: (a) Relative momentum resolution measured using  $J/\psi \rightarrow \mu^+\mu^-$  decays and (b) mass resolution determined from dimuon decays of  $J/\psi$ ,  $\psi(2S)$ ,  $\Upsilon(1S)$ ,  $\Upsilon(2S)$ ,  $\Upsilon(3S)$  mesons and  $Z^0$  bosons. Reproduced from [70].

### 2.2.5 Tracking performance

Considering a two-body decay such as  $D^0 \rightarrow \pi^+\pi^-$ , the mass of the parent particle in terms of the decay products' kinematics is given by

$$\begin{aligned} m_{D^0}^2 &= (E_{\pi^+} + E_{\pi^-})^2 - (\vec{p}_{\pi^+} + \vec{p}_{\pi^-})^2 \\ &\approx m_{\pi^+}^2 + m_{\pi^-}^2 + 2|\vec{p}_{\pi^+}||\vec{p}_{\pi^-}|(1 - \cos \theta), \end{aligned} \quad (2.2)$$

where  $\theta$  is the opening angle between the  $\pi^+\pi^-$  pair and the other symbols have their usual meaning. The final approximation holds if  $E_{\pi^+(\pi^-)} \gg m_{\pi^+(\pi^-)}$ . The momentum resolution is therefore typically the limiting factor on the mass resolution in the LHCb detector. For example, reconstructing the decay  $B_s^0 \rightarrow D_s^- \pi^+$  with a mass resolution of  $\sim 10$  MeV equates to a momentum resolution of  $\delta p/p \sim 0.4\%$  for long tracks [78]. An excellent mass resolution is critical to the LHCb physics programme in order to distinguish mis-identified and mis-reconstructed physics backgrounds which peak close to a signal of interest. In addition, an improved mass resolution minimises contamination from combinatorial background around a given signal peak.

The momentum resolution has been determined from a sample of reconstructed  $J/\psi \rightarrow \mu^+\mu^-$  decays. The momentum resolution was determined from the width of a fit to the dimuon invariant mass distribution, and using the fitted muon tracks to subtract the contribution from the uncertainty on the opening angle. The results are shown in Figure 2.18a. The relative momentum resolution ranges from  $\delta p/p \sim 0.5\%$

at momenta of  $\mathcal{O}(\text{GeV})$  to  $\delta p/p \sim 1\%$  at momenta of  $\sim 200 \text{ GeV}$ . Figure 2.18b also shows the relative mass resolutions measured in several dimuon decays. A typical resolution of  $\delta m/m \sim 0.5\%$  is obtained for  $m \lesssim 10 \text{ GeV}$  [70].

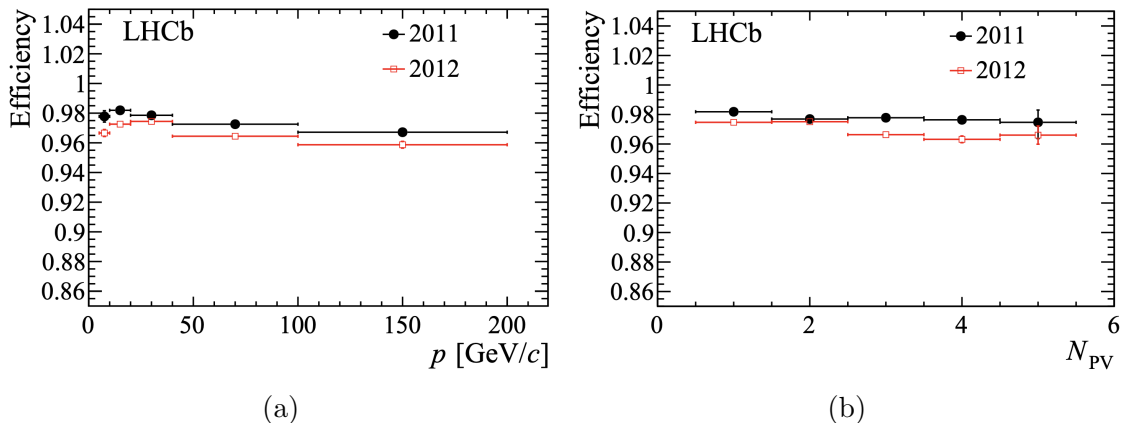


Figure 2.19: Long track reconstruction efficiency measured in 2011 and 2012 data using the tag-and-probe method with  $J/\psi \rightarrow \mu^+ \mu^-$  decays, shown as a function of (a) track momentum and (b) number of tracks in each event. Reproduced from [70].

The reconstruction efficiency of long tracks in the LHCb detector has also been measured in a data-driven way using a ‘tag-and-probe’ method. The decay  $J/\psi \rightarrow \mu^+ \mu^-$  is utilised since a muon will pass through the entire tracking system, provided they do not decay in flight. In addition, hits in the muon station are useful for reconstructing the probe tracks. One of the muons is fully reconstructed as a long track and defined as the ‘tag’ track. The second muon is partially reconstructed using only information from a subset of the tracking detectors, and defined as the ‘probe’. The track reconstruction efficiency is then given by the fraction of probe tracks for which a corresponding long track is found. The probe track and a long track are said to be consistent if they share a number of hits in each sub-detector above a given set of thresholds [88]. The reconstruction efficiency of long tracks varies as a function of the track kinematics and the detector occupancy. Figures 2.19a and 2.19b show the long track reconstruction efficiencies measured using data collected in 2011 and 2012 as a function of track momentum and the number of tracks in each event, respectively. The average long track reconstruction efficiency is  $\sim 96\%$  [70].

For time-dependent analyses such as those presented in this thesis, a precise measurement of the decay time of long-lived hadrons is crucial. This relies on precise measurements of both the PV and displaced DV. The beam-gas imaging

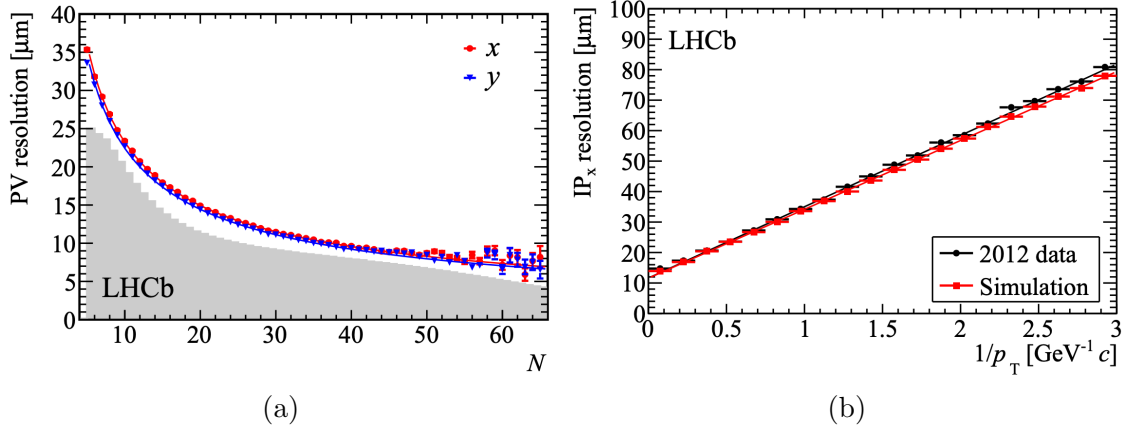


Figure 2.20: (a) Primary vertex resolution and (b) impact parameter resolution measured in Run 1 data with the VELO. The grey filled area on the left plot represents the distribution of the number of tracks in a PV, in arbitrary units. Reproduced from [70].

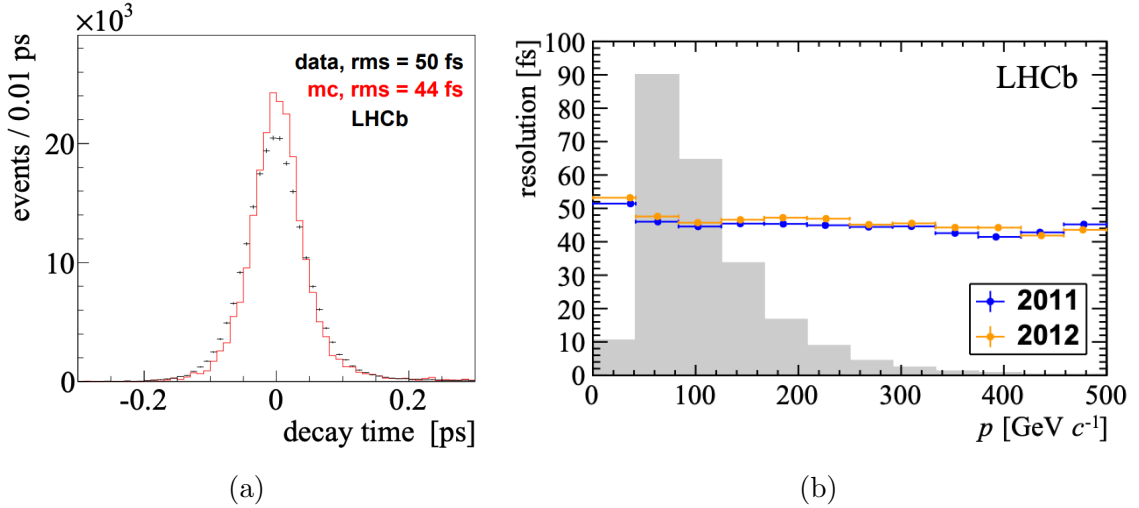


Figure 2.21: (a) Decay time of prompt, fake  $B_s^0 \rightarrow J/\psi\phi$  candidates from data and simulation and (b) decay-time resolution as a function of fake  $B_s^0$  momentum. The grey filled area on the right plot represents the distribution of the fake  $B_s^0$  momentum, in arbitrary units. Reproduced from [74].

luminosity analysis presented in this thesis also relies on precise PV position measurements. In addition, precise measurements of the Impact Parameter (IP) — defined in Section 5.1 — of displaced tracks are required for efficient trigger selections. Figure 2.20a shows the PV resolution achieved by the VELO — typically of  $\mathcal{O}(10 \mu\text{m})$  — parameterised in terms of the number of reconstructed tracks in the PV. Figure 2.20b shows the impact resolution of a single track in terms of  $1/p_T$ . The decay-time resolution of the VELO has been determined using prompt samples

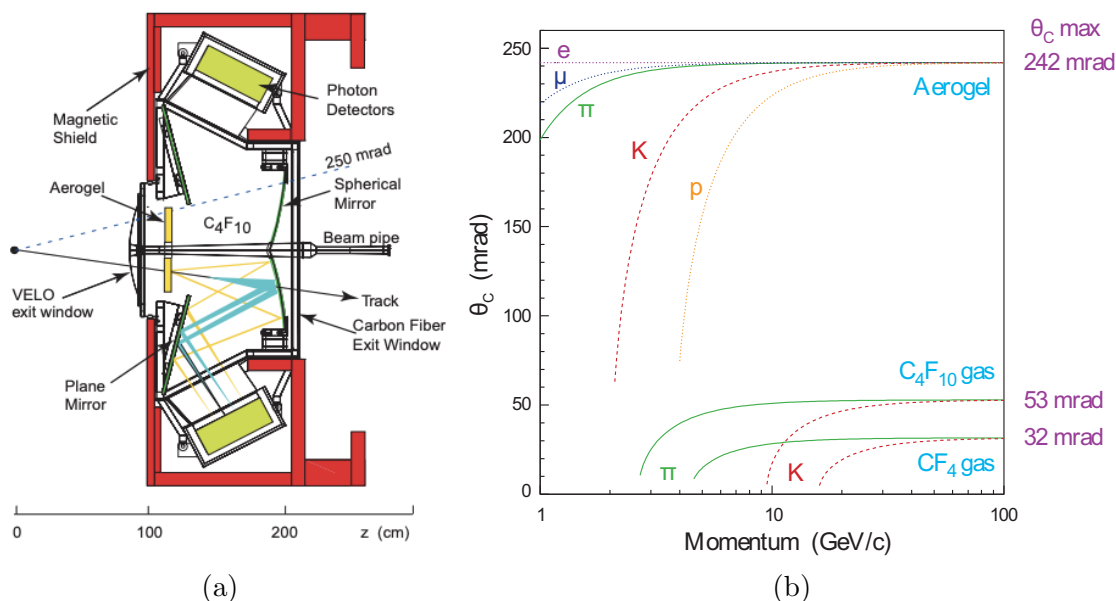


Figure 2.22: (a) Layout of the RICH1 sub-detector and (b) Cherenkov angle versus momentum for various particle species and radiator materials. Reproduced from [78].

of ‘fake’  $B_s^0 \rightarrow J/\psi\phi$  decays (*i.e.* with the same topology, but inconsistent with the  $B_s^0$  mass hypothesis). The decay-time distribution of such candidates should have a mean of zero, since they originate at the PV, and a width given by the decay-time resolution. The results of this study are shown in Figure 2.21. A typical decay-time resolution of  $\sim 50$  fs is obtained, although this value will vary depending on the topology of the decay mode under consideration [74, 89].

## 2.2.6 Ring Imaging Cherenkov detectors

The LHCb detector contains a pair of Ring Imaging Cherenkov (RICH) detectors which provide charged-hadron particle identification (PID). The RICH detectors separate different species of charged hadrons based on the opening angle of the Cherenkov radiation produced as a given particle traverses some medium. RICH1 is situated upstream of the magnet and TT and provides PID for low momentum ( $\sim 1 - 60$  GeV) particles. RICH2 is situated downstream of the magnet and provides complementary PID for higher momentum particles ( $\sim 15 - 150$  GeV).

The RICH1 sub-detector, illustrated in Figure 2.22a, covers the entire LHCb acceptance. A set of optical elements, consisting of spherical and plane mirrors, guided the Cherenkov radiation — produced as charged particles traversed Aerogel

and  $C_4F_{10}$  radiators — outside the acceptance of LHCb. The Aerogel radiator was found to negatively impact the overall PID performance and was consequently removed between Runs 1 and 2 [90]. A set of photon detectors were used to detect the Cherenkov photons; since they are produced at a constant angle from the trajectory of the particle, they form a ring in the detector plane. Placing the photon detectors outside the acceptance reduces the overall material budget within the LHCb acceptance. The opening angle of each ring — which can be determined from the radius — associated with a track with a given measured momentum can be used to identify the particle under consideration, as illustrated in Figure 2.22b. The RICH1 photon detectors were surrounded by a magnetic shield box in order to isolate them from the local stray field of  $\sim 60$  mT from the LHCb magnet.

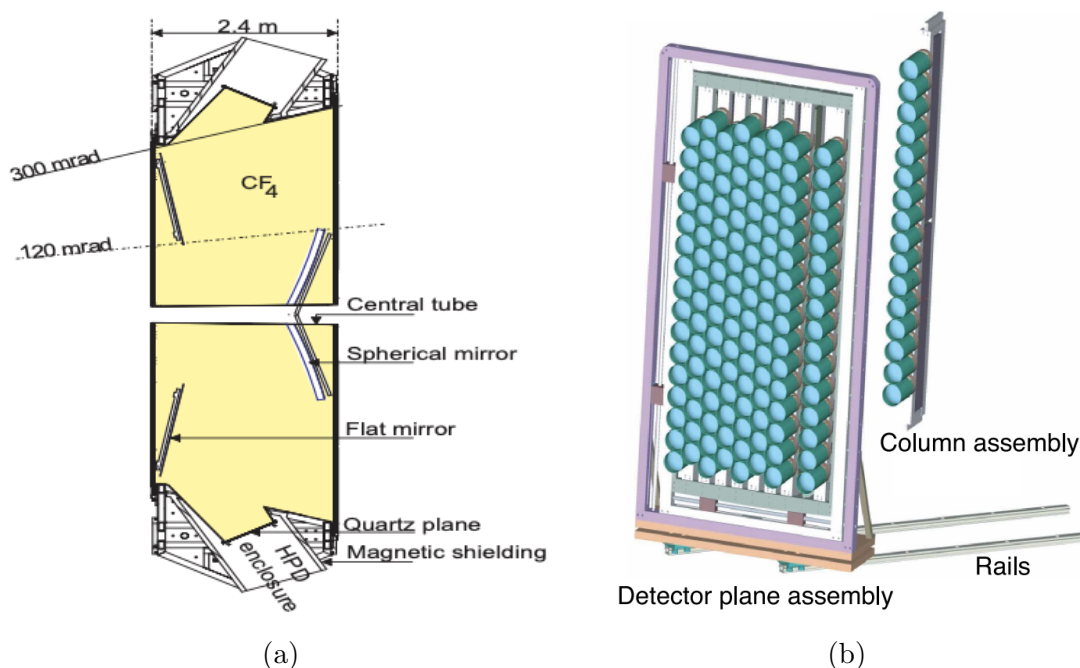


Figure 2.23: Layout of (left) the RICH2 sub-detector optical elements and HPDs, and (right) arrangement of HPDs. Reproduced from [78].

The RICH2 sub-detector is located downstream of the magnet, between the T-stations and the calorimeters, and covers an angular acceptance of  $\sim \pm 15$  mrad to  $\pm 120$  mrad ( $\pm 100$  mrad) in the  $x$ -axis ( $y$ -axis). The reduced coverage is motivated by the fact that higher momentum particles typically lie within this region of the detector, and RICH1 provides PID for lower momentum particles. Similarly to RICH1, the RICH2 photon detectors were surrounded by a magnetic shield to permit efficient operation in the stray magnetic field. The layout of the optical elements

and photon detectors in RICH2 is shown in Figure 2.23.

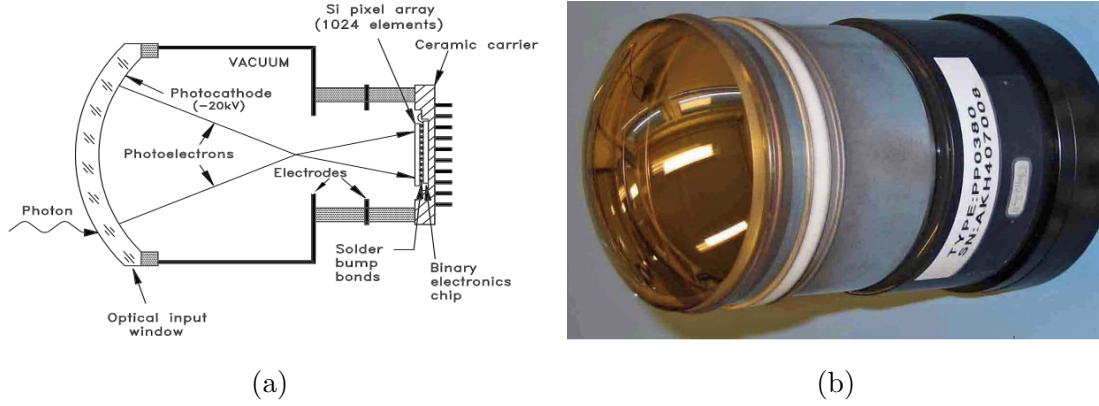


Figure 2.24: (a) Diagram and (b) photograph of a custom pixel-HPD developed for the LHCb RICH detectors. Reproduced from [78].

A custom Hybrid Photon Detector (HPD) was developed for use in the RICH1 and RICH2 sub-detectors. A diagram and photograph of the resulting pixel-HPD are shown in Figures 2.24a and 2.24b, respectively. The pixel-HPD converts incident Cherenkov photons into photoelectrons via an interaction with a photosensitive coating on a quartz entrance window. The photoelectrons are accelerated across a potential difference of 20 kV in a vacuum and focused onto a  $32 \times 32$  array of  $0.5 \text{ mm} \times 0.5 \text{ mm}$  silicon pixels. Each pixel corresponds to an area of  $2.5 \times 2.5 \text{ mm}^2$  on the entrance window. Such a configuration yields several thousand electron-hole pairs per incident photoelectron [78].

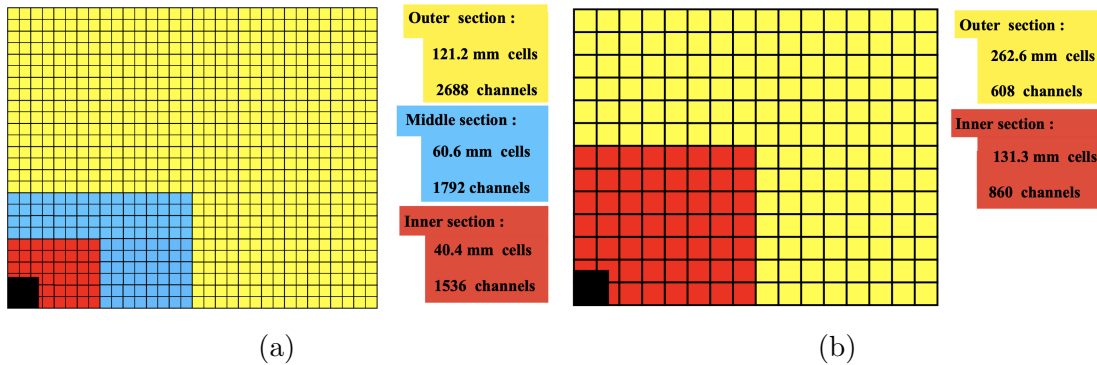


Figure 2.25: Layout of (a) scintillating/absorbing tiles in the SPD, PS and ECAL and (b) modules in the HCAL. Reproduced from [78].

### 2.2.7 Calorimeters

The LHCb calorimeter system is located upstream of the RICH2 sub-detector and covers approximately the full LHCb acceptance. The calorimeter system consisted of a Scintillating Pad Detector (SPD), a PreShower detector (PS), an Electromagnetic CALorimeter (ECAL), and a Hadronic CALorimeter (HCAL). The ECAL and HCAL provide energy, position, and — to some extent — PID measurements of electrons, photons and hadrons. The SPD and PS were introduced in order to improve the selection efficiency for high  $p_T$  electrons, whilst also reducing the level of background contamination. The SPD was sensitive to incident charged particles. A thin piece of lead between the PS and SPD induced electromagnetic showers for incident photons and electrons. Thus, electrons could straightforwardly be distinguished from photons; in particular, those originating from high  $p_T$  neutral pions in the decay  $\pi^0 \rightarrow \gamma\gamma$  produce a significant background. Such a discrimination was particularly useful in the hardware trigger — described in Section 2.2.10.1 — since track reconstruction and association with calorimeter clusters was not available at the required trigger rate.

The PS and SPD layers consisted of scintillating tiles of various sizes, as shown in Figure 2.25a. Smaller cells were utilised closer to the beampipe to keep the occupancy in each channel approximately constant. A 15 mm lead converter — equivalent to 2.5 radiation lengths ( $X_0$ ) — was placed between the PS and SPD. The light produced in each of the scintillating tiles was read out through a set of multianode photomultiplier tubes (MAPMTs) which were optically coupled to the pads by wavelength-shifting (WLS) fibres and clear plastic fibres.

The ECAL is constructed following a sampling (‘shashlik’) design from lead and scintillating tiles. The scintillating tiles and optical readout were broadly similar to the PS and SPD, with the tile structure as illustrated in Figure 2.25a. The tiles are oriented perpendicular to the beam-axis. Each calorimeter module consists of 66 layers of lead and scintillating tiles. The lead tiles are 2 mm thick, while the scintillating tiles are 4 mm thick. The ECAL has a Molière radius of 3.5 cm and an overall radiation length of  $25 X_0$ .

The HCAL is also constructed with a sampling design. The layout of the readout channels is illustrated in Figure 2.25b. The readout regions are composed of modules, each of which is constructed from iron absorber layers and scintillating tiles. Contrary to the PS, SPD and ECAL, however, the absorption and sampling

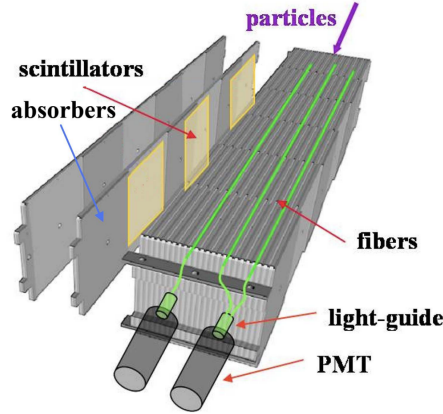


Figure 2.26: Arrangement of absorber and sampling layers in the HCAL. Reproduced from [78].

layers in the HCAL are oriented parallel to the beam-axis in order to maximise light collection from the scintillators. Scintillating tiles are placed between layers of 1 cm thick iron absorber, as illustrated in Figure 2.26. The overall length of the HCAL in the longitudinal direction corresponds to 5.6 hadronic interaction lengths ( $\lambda_I$ ).

The resolution of the ECAL has been determined in a data driven study. Electrons produced in pair production from a photon are identified and their energy as measured in the calorimeter is compared to their momentum measured in the tracking system. The ECAL resolution was determined to be [91]

$$\frac{\sigma_E}{E} = \frac{(13.5 \pm 0.7)\%}{\sqrt{E_{\text{GeV}}}} \oplus (5.2 \pm 1.1)\% \oplus \frac{(320 \pm 30) \text{ MeV}}{E_{\text{GeV}}}. \quad (2.3)$$

The energy resolution of the HCAL has been measured in a test beam. The resolution was found to be given by [92]

$$\frac{\sigma_E}{E} = \frac{(67 \pm 5)\%}{\sqrt{E_{\text{GeV}}}} \oplus (9 \pm 2)\%. \quad (2.4)$$

### 2.2.7.1 Neutral pion reconstruction

In the LHCb reconstruction,  $3 \times 3$  clusters are formed surrounding cells with large energy deposits in the ECAL. If any single cell is shared between two or more clusters, its energy is divided amongst the clusters. Each cluster receives a fraction of the cell energy equal to its fraction of the total energy amongst the clusters. Photon candidates are identified as ECAL clusters with no consistent charged track.

A  $\chi^2$  representing the likelihood a given track and cluster originated from the same particle is computed for each track and cluster combination; only clusters with a minimum  $\chi^2$  above a certain threshold are retained as photon candidates.

Neutral pions have a branching fraction of almost 100% via the decay  $\pi^0 \rightarrow \gamma\gamma$ . If the transverse momentum of the  $\pi^0$  meson is small, then the two photons are separated by a large angle and leave two distinct clusters in the ECAL; such candidates are defined as *resolved*. If the transverse momentum of the  $\pi^0$  meson is large, the opening angle of the diphoton pair is small, and they are detected as a single cluster in the ECAL; such candidates are defined as *merged*. The reconstruction of resolved candidates as a combination of a pair of photon candidates is straightforward. Merged candidates are reconstructed by a dedicated algorithm which divides individual ECAL clusters into a pair of separate, overlapping  $3 \times 3$  clusters of cells. In the overlapping region, the energy of each cell is distributed between the two photon candidates based on a simulated model of the predicted electromagnetic shower shape of a photon incident on the ECAL. Neutral pion mass resolutions of  $\sim 8$  MeV and  $\sim 20$  MeV are obtained for the resolved and merged categories, respectively [91]. Photon and merged  $\pi^0$  candidates are distinguished using a neural network [70].

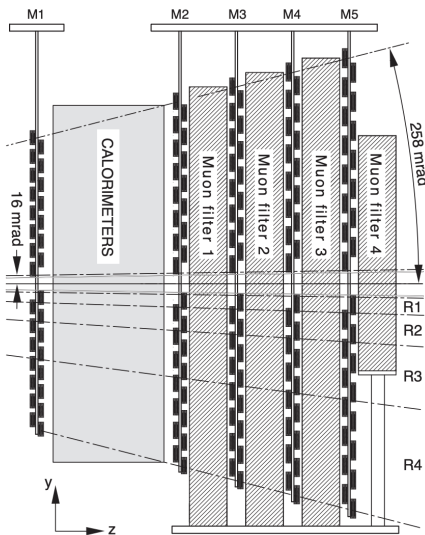


Figure 2.27: Layout of the muon stations and absorbers. Reproduced from [78].

### 2.2.8 Muon stations

The muon stations are the final and furthestmost sub-detector from the interaction point in the LHCb detector. The purpose of the muon stations is to identify and

provide additional tracking measurements for muons. There is a single muon station, M1, located upstream of the calorimeters. The remaining four stations, M2-M5, are situated downstream of the calorimeters. The muon stations cover the angular regions 20-306 mrad and 16-258 mrad in the  $x$ - and  $y$ -directions, respectively. The first station is constructed from Gas Electron Multipliers (GEMs) in the region surrounding the beampipe and Multi-Wire Proportional Chambers (MWPCs) in the outer region. The remaining stations are constructed entirely from MWPCs. Iron absorbers with a thickness of 0.8 m are placed between stations M2-M5 to improve the discrimination between muons and hadrons which are not fully absorbed in the calorimeters. The total hadronic length of the calorimeters and muon absorbers is  $\sim 20\lambda_I$ . The layout of the muon stations is shown in Figure 2.27.

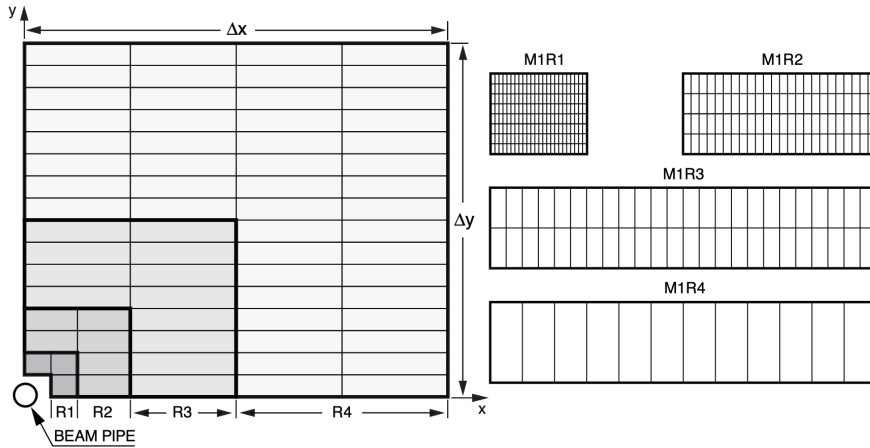


Figure 2.28: (Left) layout of the regions of muon station M1 and (right) layout of sensor pads in each of the regions. Reproduced from [78].

To keep occupancies per channel approximately constant, each station is divided into four regions of various granularities, as illustrated in Figure 2.28 for M1. Relative to M1, the stations M2 and M3 have twice as many sensor pads (cathodes) in the horizontal direction, while stations M4 and M5 have half as many pads in the horizontal direction. The wires (anodes) in each chamber run parallel to the  $y$ -axis. Depending on the region of the detector, the wires and/or pads are read out. The first station is constructed from two active layers, while M2-M5 consist of four active layers. The muon system has a hit efficiency in any given station of  $> 99\%$  [70].

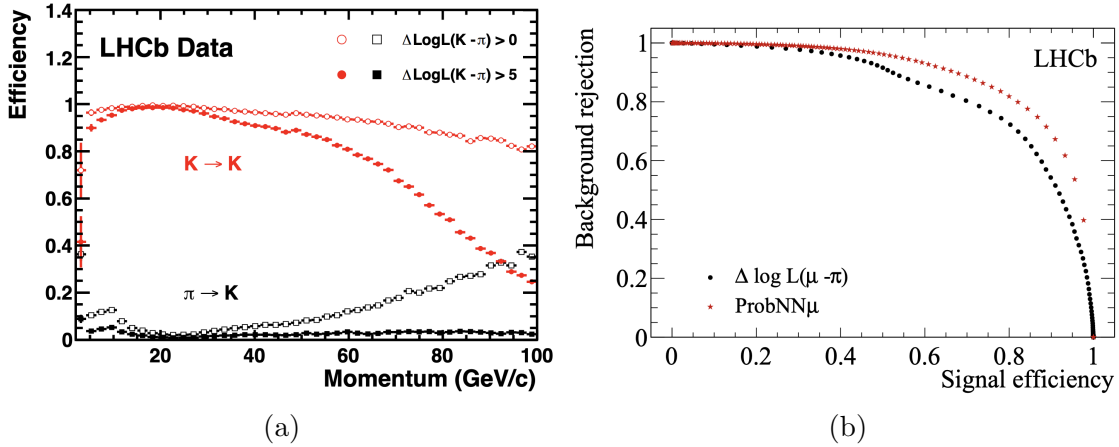


Figure 2.29: (a) Kaon selection efficiency and pion mis-identification rate for different selections applied on the difference in Kaon and pion log-likelihoods. (b) Pion background rejection versus muon signal efficiency for both the difference in log-likelihood and ProbNN methods. Reproduced from [70].

### 2.2.9 Particle identification performance

Two separate methods for combining the PID information from different sub-detectors — RICH, the calorimeter system and the muon stations — have been developed within LHCb. One approach, known as ProbNN [93, 94], makes use of a set of neural networks trained to compute the probability of a given particle hypothesis based on information from various sub-detectors. The second approach computes the likelihood of a given particle hypothesis, relative to the hypothesis that the correct identification is a charged pion. Overall, a selection efficiency of  $\sim 90\%$  of electrons allowing for 5% of  $e \rightarrow h$  mis-identification is obtained. For kaons, a selection efficiency of  $\sim 95\%$  with 5% of  $\pi \rightarrow K$  mis-identification is obtained. Finally, a selection efficiency of  $\sim 97\%$  is obtained for muons, with a mis-identification rate of 1-3% for pions [70, 95]. Figure 2.29a shows an example of the kaon selection efficiency and pion mis-identification probability for the difference in likelihood approach with two different selection requirements. Figure 2.29b shows the pion background rejection rate against muon signal efficiency for both approaches.

### 2.2.10 Trigger

In Runs 1 and 2 the LHCb detector was operated with a three-level trigger. The first, hardware, trigger level operated at the bunch crossing frequency of 40 MHz and is known as the Level-0 (L0) trigger. The latter two stages of the trigger, High

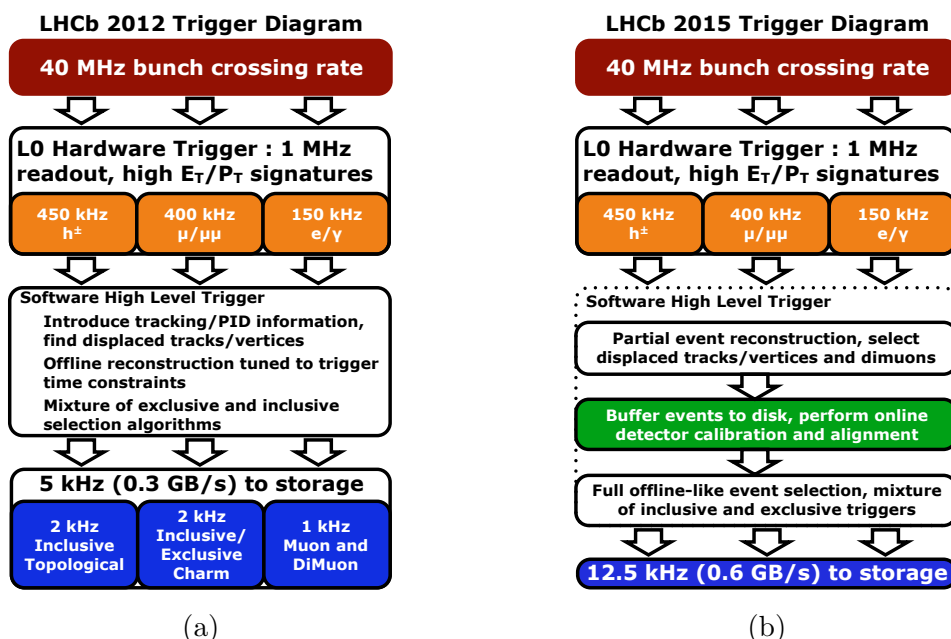


Figure 2.30: Flowchart for the LHCb trigger operation in (a) Run 1 and (b) Run 2 [96].

Level Trigger (HLT) one and two, were implemented in software. An overview of the data flow through the trigger is shown in Figure 2.30. Each of the individual components of the trigger are described in the following sections.

### 2.2.10.1 Level-0 trigger

The L0 hardware trigger was utilised to reduce the event rate from the bunch crossing frequency of 40 MHz to a rate of  $\sim 1.1$  MHz at which the entire LHCb detector could be read out. This requires a trigger decision in an incredibly short window of  $4 \mu\text{s}$ ; thus, a complicated event reconstruction is not possible. The L0 trigger aims to reject extremely busy events for which the reconstruction is complicated and time-consuming, and to select events with high  $p_T$  hadrons, electrons, photons or muons.

The former aim of the L0 trigger is achieved by utilising the upstream  $r$ -only sensors in the VELO. These sensors are known as the pile-up (PU) system, and can provide both a measurement of the backwards track multiplicity and can estimate the longitudinal position — and therefore number — of PVs in each bunch crossing.

The latter aim is achieved based on information from the calorimeters and muon stations. Clusters consisting of  $2 \times 2$  groups of cells are formed in the calorimeters. A simple particle identification is performed based on the energy deposited in each

of the PS, SPD, ECAL and HCAL layers in the region of the cluster, as described in Section 2.2.7. Events which have a particle of sufficient transverse energy,  $E_T$ , are retained by the calorimeter L0 triggers. A rough estimate of the  $p_T$  of muon candidates is possible from information in the muon stations alone. Events with one or more high  $p_T$  muon candidates are retained.

### 2.2.10.2 High-level trigger

The first HLT level, HLT1, a partial event reconstruction is performed to further reduce the data rate. The exact output rate of HLT1 has evolved over time, so no precise number is quoted here; typically the output rate has been around  $\mathcal{O}(10\text{-}100)$  kHz. In HLT1, track segments in the VELO are reconstructed, and an attempt is made to find matching hits in the downstream tracking detectors and muon stations. Events with one or more displaced tracks or vertices (with respect to the PV) satisfying momentum and track/vertex quality requirements are retained. Events with good quality muon tracks of sufficient  $p_T$  are also retained.

The second software trigger level, HLT2, performs a full event reconstruction. HLT2 is implemented as an extremely flexible software package, allowing analysts to — within computing resource limits — implement any selection of interest. Thus, there are an enormous amount of trigger lines implementing a wide variety of criteria. In general, the HLT2 lines can either be classified as *exclusive* — selecting only a single, specific, decay of interest — or *inclusive* — selecting an entire category of decays. The physics analysis in this thesis makes use of both categories, and the specific requirements are described in detail in Section 5.2.1. The output rate of the HLT2 trigger has typically been in the range  $\mathcal{O}(1\text{-}10)$  kHz during Runs 1 and 2 [70].

All events which pass any HLT2 trigger are retained for offline analysis. Only reconstructed objects are stored, in order to reduce the storage volume required. The events are grouped into ‘streams’ based on the particular trigger lines which fired on a given event. A central procedure known as ‘stripping’ is periodically performed on the recorded events in order to apply further selections and build composite decay chains out of the reconstructed objects in each event. The output of the stripping step is available to any member of the LHCb collaboration to perform offline analyses.

### 2.2.11 System for Measuring Overlap with Gas

The primary vacuum of the LHC, where the beams circulate and are brought into collisions in each of the experimental caverns, is maintained in ultra-high vacuum (UHV) conditions at a pressure of  $\sim 10^{-9}$  mbar. The principle motivation for maintaining such a pure vacuum is to maximise the beam lifetimes during each fill. The so-called System for Measuring the Overlap with Gas (SMOG) was conceived and developed at LHCb during the early stages of Run 1 of the LHC [97]. An image of SMOG is shown in Figure 2.31. SMOG facilitated injection of gas (He, Ne or Ar) in a local region of the beam vacuum around the LHCb interaction point, increasing the pressure by around two orders of magnitude. Such a configuration allows a proportional increase in the rate of beam-gas interactions. Beam-gas interactions are simply defined as inelastic collisions between the protons in the LHC beams and the residual gas in the beam pipe. Combined with the excellent PV resolution of the LHCb VELO, this allows for a direct determination of the luminosity by fitting the individual profile of each bunch colliding at LHCb. A detailed description is provided in Chapter 4. In addition to facilitating luminosity measurements, SMOG provided an opportunity to develop a fixed target physics programme at LHCb [98–101].

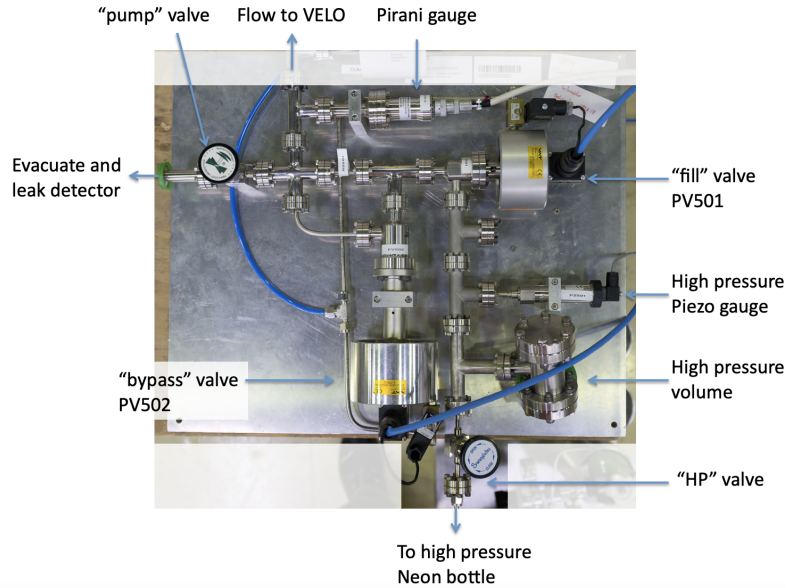


Figure 2.31: Layout of the SMOG system for gas injection around the LHCb interaction region [97].

### 2.2.12 The LHCb upgrade

The LHCb detector has been almost entirely re-built in preparation for Runs 3 and 4 of the LHC [102]. The upgraded detector is shown in Figure 2.32. In Runs 1 and 2 the LHC optics around the LHCb interaction region were tuned such that the average number of visible inelastic  $pp$  collisions per bunch crossing was  $\sim 1$ . In Run 3, the LHCb detector will collect data with  $\sim 5$  visible inelastic  $pp$  collisions per bunch crossing.

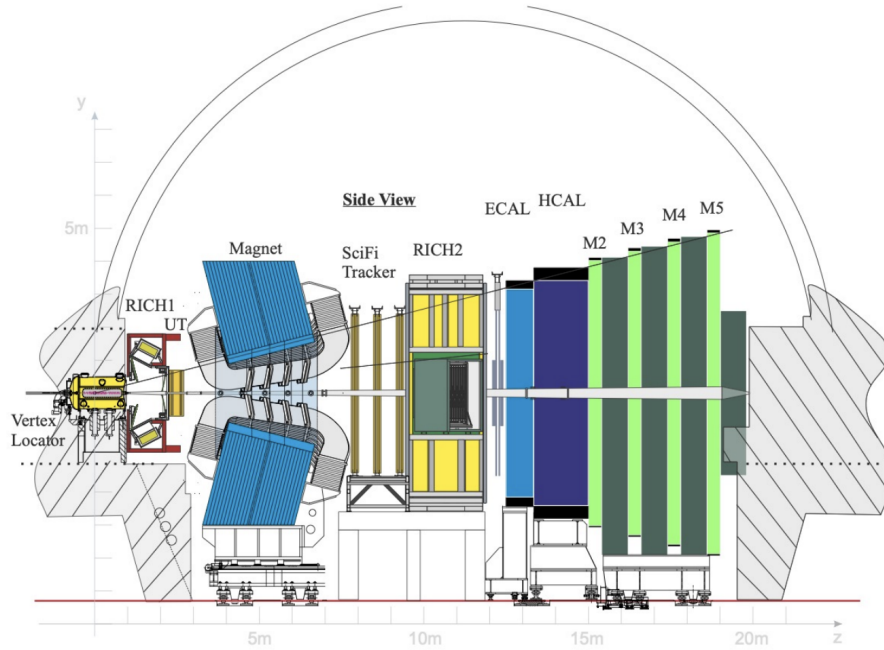


Figure 2.32: Layout of the upgraded LHCb detector. Reproduced from [102].

The VELO has been upgraded to an entirely new silicon-pixel based vertexing detector [103]. The active regions of the upgraded VELO modules are now located just 5.1 mm from the interaction point. The TT has been replaced with a new silicon microstrip tracker known as the Upstream Tracker (UT), which provides a finer granularity. The T-stations have been replaced by a set of SCIntillating Fibre (SCIFI) tracking stations [104]. The optical elements in the RICH detectors have been re-arranged and the HPDs have been replaced with arrays of MAPMTs [105]. The SPD and PS detectors have been removed from in front of the calorimeters. The active regions of the ECAL, HCAL, and muon stations have been retained from the original detector.

The readout electronics for the entire detector — including the sub-detectors

which remain largely unaltered otherwise — have been replaced. This was required since the LHCb detector is now operating with a fully software trigger; thus, the entire detector must be read out at the LHC bunch crossing rate of 40 MHz [106]. The upgraded trigger is implemented in a heterogeneous architecture, with HLT1 running on a large cluster of Graphics Processing Units (GPUs), and HLT2 implemented on a Central Processing Unit (CPU) farm.

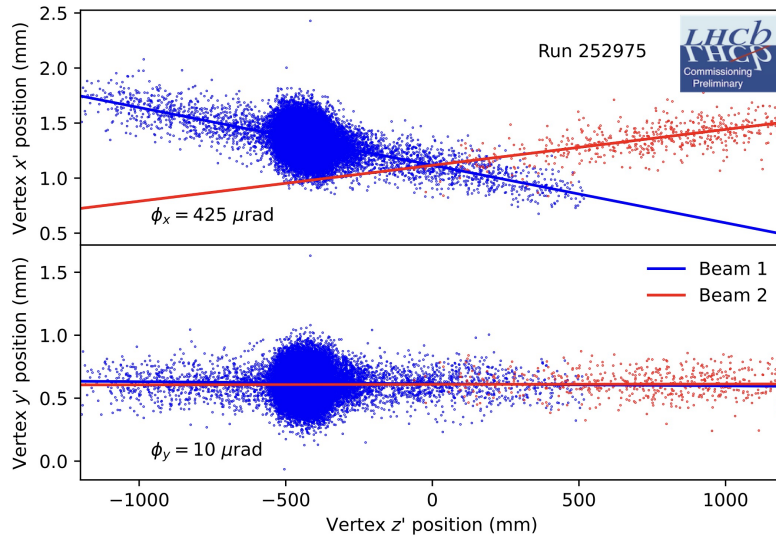


Figure 2.33: Distribution of beam-gas vertices collected with Ar injection in the SMOG2 cell, with a fit to determine the beam crossing angles overlaid.

In addition, SMOG has been replaced with a new injection system based on a gas storage cell design, SMOG2. SMOG2 is a gas storage cell upstream of the VELO which opens and closes with the VELO motion system [107]. The gas cell, contrasted with gas injection throughout the entire VELO vessel using SMOG, allows gas areal densities of at least an order of magnitude higher than SMOG for the same gas flow rate. SMOG2 can inject  $H_2$ ,  $D_2$ , or any noble gas; a successful commissioning programme has taken place involving injections with  $H_2$ , He and Ar to date. Figure 2.33 shows the longitudinal position of a sample of primary vertices reconstructed with SMOG2 active. Besides facilitating higher statistics measurements of the bunch profiles, the SMOG2 system will allow further development of a wide-ranging fixed-target physics programme at LHCb; indeed, improving the fixed-target capabilities of the LHCb experiment was the primary motivation for developing SMOG2 [108].

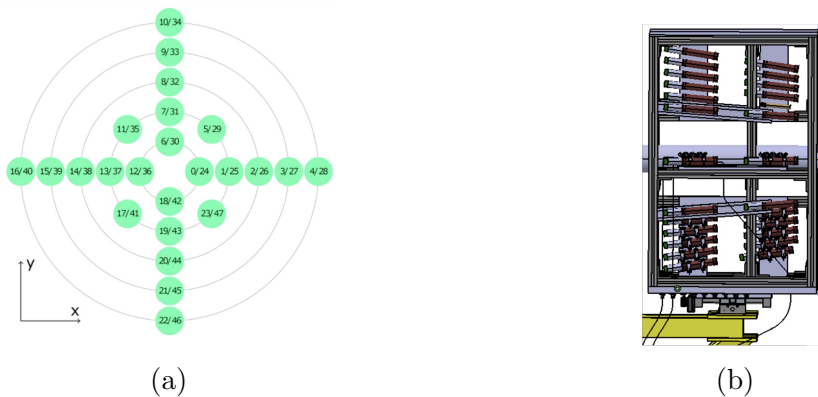


Figure 2.34: Front view (a) and side view (b) of the layout of the PLUME luminometer PMT arrangement. Reproduced from [109].

Finally, a dedicated luminosity sub-detector, Probe for LUMinosity mEasurements (PLUME) has been installed [109]. The primary function of PLUME is to provide online relative luminosity measurements to the LHC with an accuracy of  $\sim 10\%$  and an integration time of  $\sim 3$  s. This function was fulfilled by the hardware trigger level using information from the calorimeters in Runs 1 and 2. PLUME, shown in Figure 2.34, is constructed as a hodoscope of 24 Hamamatsu R760 photo-multiplier tubes (PMT) pairs. Each PMT has a 10 mm diameter photocathode and a 1.2 mm thick quartz entrance window; an additional optically connected 5 mm thick quartz tablet increases production of Cherenkov photons. Two PMT pairs are dedicated to fine timing measurements with a resolution of  $\sim 100$  ps. This will allow for monitoring clock shifts between the LHC and LHCb and for probing the bunch structures of one of the LHC beams. PLUME measurements will also be used for absolute luminosity calibrations. The design is optimised for an occupancy of  $\mathcal{O}(1\%)$  to provide a reliable input to the LogZero method, which is described in Section 3.4.2.

## 2.3 Summary

An overview of the LHC accelerator system and the LHCb detector has been provided. Each of the LHCb sub-detectors and their individual performance has been discussed, along with the overall momentum resolution and PID performance of the entire detector. A particular discussion was provided of charged track and neutral pion reconstruction, which are of particular relevance to this thesis. An overview

of the LHCb trigger in Runs 1 and 2 was provided. Finally, a brief summary of the recently installed upgraded LHCb detector for Runs 3 and 4 of the LHC was presented.

# Luminosity measurements at the LHC

---

LUMINOSITY measurements form a crucial input for any absolute cross section measurement. The integrated luminosity,  $\mathcal{L}$ , can be defined for a single colliding bunch pair in a synchrotron as

$$\mathcal{L} = n \frac{\mu_c}{\sigma_c}, \quad (3.1)$$

where  $n$  is the number of bunch crossings (*i.e.* turns of the bunches in the ring), and  $\mu_c$  and  $\sigma_c$  are the mean number of interactions per bunch crossing and the cross section, respectively, for the process  $c$ . At electron-positron colliders, there exist processes with precisely known cross-sections such as Bhabha scattering ( $e^-e^+ \rightarrow e^-e^+$ ) and dimuon production ( $e^-e^+ \rightarrow \mu^-\mu^+$ ) which are suitable for calibrating the absolute luminosity with a precision below 1% [110–112]. Using such a decay, a measurement of the luminosity requires only a knowledge of the experimental efficiency and the number of events observed, and is given by

$$\mathcal{L} = n \frac{\mu_c^{\text{vis}}}{\varepsilon \sigma_c} = n \frac{\mu_c^{\text{vis}}}{\sigma_c^{\text{vis}}}, \quad (3.2)$$

where:  $\varepsilon$  represents the efficiency of reconstructing and selecting the given final state of interest;  $\mu_c^{\text{vis}}$  represents the number of ‘visible’ interactions per bunch crossing; and  $\sigma_c^{\text{vis}}$  is the visible cross section for that final state. For brevity, the superscript ‘vis’ will be dropped, but is implied throughout Chapters 3 and 4 whenever the cross section or interaction rate are discussed.

At  $pp$  colliders, there exists no such cross section that is theoretically well known

and experimentally clean. Determinations of the luminosity relying on theoretically known cross sections of physical processes are typically affected by uncertainties of several percent [113, 114]. Instead, the luminosity can be determined by first measuring the cross section of some experimentally-defined process,  $\sigma_c$ , during a dedicated luminosity data-taking period. Then, the absolute ‘physics’ luminosity can be determined from Equation 3.1 by combining the measured cross section with a measurement of the interaction rate,  $\mu_c$ , during normal data-taking. In general, the process  $c$  is not constrained to be a physical process such as  $e^-e^+ \rightarrow \mu^-\mu^+$ . Rather, it is typically chosen to be some experimentally clean observable such as the presence of (or lack thereof) a certain reconstructed object in each event, or is based on the occupancy of some sub-detector.

The most well-known approach for determining the calibration cross section is the van der Meer (vdM) method [115–117]. The luminosity can be written in terms of the beam parameters as

$$\mathcal{L} = nN_1N_2K \int \rho_1(\vec{x}, t)\rho_2(\vec{x}, t)d\vec{x}dt = nN_1N_2K\mathcal{O}, \quad (3.3)$$

where:  $K = \sqrt{(\vec{v}_1 - \vec{v}_2)^2 - (\vec{v}_1 \times \vec{v}_2)^2/c^2}$ <sup>1</sup> is a kinematic factor to ensure Lorentz invariance of the integral [118] ( $\vec{v}_i$  is the velocity of the particles in beam  $i$ );  $\rho_i(\vec{x}, t)$  and  $N_i$  are the bunch profile density and population of the colliding bunch in beam  $i$ , respectively; and  $\mathcal{O}$  is the overlap integral. The integration over  $\vec{x}$  runs over all space, while the integration over  $t$  runs over a single bunch crossing. The approximation  $K \approx 2c$  holds in the presence of a small crossing angle when  $|\vec{v}_i| \approx c$ , as is the case at the LHC. If one of the two beams is offset with respect to the other in the transverse plane, Equations 3.1 and 3.3 give

$$\frac{\mu_c(\Delta x, \Delta y)}{\sigma_c} = N_1N_2K\mathcal{O}(\Delta x, \Delta y), \quad (3.4)$$

where  $\mu_c(\Delta x, \Delta y)$  and  $\mathcal{O}(\Delta x, \Delta y)$  represent the interaction rate per bunch crossing and the overlap integral in the displaced configuration. Assuming the beams collide without a crossing angle and that the transverse and longitudinal components

---

<sup>1</sup>Natural units will not be used throughout Chapters 3 and 4.

factorise, the overlap integral can be written as

$$\mathcal{O} = \int \rho_{1,\perp}(x + \Delta x, y + \Delta y) \rho_{2,\perp}(x, y) dx dy \int \rho_{1,\parallel}(z - ct) \rho_{2,\parallel}(z + ct) dz dt = \mathcal{O}_\perp \mathcal{O}_\parallel, \quad (3.5)$$

where  $\mathcal{O}_\perp$  and  $\mathcal{O}_\parallel$  are defined as the transverse and longitudinal parts of the factorised overlap integral, respectively. The transverse part of the overlap integral can be simplified by integrating over the offset parameters as

$$\int \mathcal{O}_\perp d\Delta x d\Delta y = \int \rho_{1,\perp}(x', y') \rho_{2,\perp}(x, y) dx dy dx' dy' = 1 \quad (3.6)$$

where the change of variables  $\Delta x, \Delta y \rightarrow x' = x + \Delta x, y' = y + \Delta y$  has been used in the first equality, and the second equality holds due to the individual normalisations of the transverse bunch profiles. Similarly, using a change of variables  $z, t \rightarrow u = z - ct, v = z + ct$ , the longitudinal part of the overlap integral becomes

$$\mathcal{O}_\parallel = \frac{1}{2c} \int \rho_{1,\parallel}(u) \rho_{2,\parallel}(v) du dv = \frac{1}{2c} \approx \frac{1}{K}. \quad (3.7)$$

Thus, the cross section,  $\sigma_c$ , can be determined by integrating Equation 3.4 over the beam offsets to yield

$$\sigma_c = \int \frac{\mu_c(\Delta x, \Delta y)}{N_1 N_2} d\Delta x d\Delta y. \quad (3.8)$$

A more general derivation can be found, for example, in Ref. [119]. Thus, given measurements of the bunch currents  $N_1$  and  $N_2$ , the vdM method allows the cross section of an arbitrary process,  $c$ , to be determined by making measurements of the interaction rate,  $\mu_c$ , at a number of points as the two beams are swept across one another in both axes of the transverse plane.

An alternative method, known as beam gas-imaging (BGI), has been developed at the LHCb experiment [97, 120–122]. Firstly, the quantities describing the absolute luminosity in terms of the beam parameters as in Equation 3.3 are determined. Measurements of the bunch populations are performed by LHC instrumentation, and corrected to account for erroneous charge outside the nominally filled bunch slots. The excellent primary vertex (PV) resolution of the LHCb VERtEX LOcator (VELO) [74, 77] and increased beam-gas collision rate when injecting gas into the beam volume with the System for Measuring Overlap with Gas (SMOG) [97] allows a determination of the individual bunch profiles in each beam by studying the distribution of vertices from beam-gas collisions. The overlap integral can then be

calculated — analytically, or otherwise — from such measurements of the bunch profiles. A measurement of the relative luminosity,  $\mu_c$ , is obtained by determining the average rate of some process,  $c$ , in each bunch crossing at the LHCb interaction point. Relating Equations 3.1 and 3.3, the cross section  $\sigma_c$  can be calculated from the measured parameters as

$$\sigma_c = \frac{\mu_c}{2cN_1N_2\mathcal{O}}. \quad (3.9)$$

The largest systematic uncertainties affecting the BGI and vdM analyses are largely uncorrelated, and thus their combination can be used to provide a more precise determination of the cross section  $\sigma_c$  [121]. This chapter describes the methods used to determine the parameters common to both analyses, namely the interaction rate and the bunch populations. Chapter 4 presents measurements of the overlap integral, and therefore the calibration cross section, using the BGI method. The final calculation of the absolute luminosity based on the measured value of  $\sigma_c$  is outwith the scope of this thesis. Unless otherwise specified, all measurements presented here refer to  $pp$  collisions at  $\sqrt{s} = 13$  TeV at LHCb in Run 2 of the LHC.

### 3.1 Luminosity calibration fills in Run 2

Luminosity calibration measurements require special beam conditions and therefore must take place in dedicated LHC fills. These fills typically occur once per year, per beam energy and per collision type ( $pp$ ,  $p\text{Pb}$  *etc.*). The fills considered in this analysis are summarised in Table 3.1. We consider only  $pp$  collisions at  $\sqrt{s} = 13$  TeV. Unlike the vdM method which requires a specific programme of beam movements, BGI data can be collected parasitically while the other LHC experiments perform their vdM scans, providing a greater number of datasets for consistency checks of the analysis. The beam width near the interaction point is given by [123]

$$\lambda = \sqrt{\beta(z)\varepsilon}, \quad (3.10)$$

where  $\varepsilon$  is the emittance of the beam and  $\beta(z)$  has the form [123]

$$\beta(z) = \beta^* + \frac{z^2}{\beta^*}. \quad (3.11)$$

Here,  $\beta^*$  is a constant defined by the beam conditions. A value of  $\beta^* = 24$  m at the LHCb interaction point was used for all fills considered in this analysis. Here,  $\lambda$  will

be used throughout instead of the typical ‘ $\sigma$ ’ to denote bunch widths, in order to avoid confusion with the cross section. The measured beam profiles will be given by the convolution of the true profile with the LHCb vertex resolution. Thus, utilising wider bunches than in typical ‘physics’ conditions ( $\beta^* = 3\text{ m}$ ) reduces the impact of the vertex resolution on the precision of BGI measurements. The larger value of  $\beta^*$  also allows the assumption that the  $\beta$  functions of each beam, and therefore the beam widths, are constant within the relevant  $z$ -region of  $\pm 1\text{ m}$ . SMOG allowed the injection of He, Ne or Ar in the beam volume around the LHCb interaction point. A heavier gas is typically preferred to increase the beam-gas interaction cross section and to increase the multiplicity of each collision, which in turn improves the vertex resolution. He and Ne were injected during each of the fills considered in this analysis. While Ne would be preferred for BGI measurements, He was preferred in certain fills for physics studies [98].

Fill	Year	Beam 1/2 bunches	Colliding at LHCb	SMOG gas species
4937	2016	55/51	16	He
4945	2016	56/52	8	He
4954	2016	56/52	8	He
6012	2017	57/56	24	Ne
6016	2017	52/52	8	Ne
6864	2018	70/70	22	He
6868	2018	140/140	23	He

Table 3.1: Summary of fills studied in this analysis.

### 3.1.1 Data taking instabilities

A small subset of the data collected during the fills listed in Table 3.1 is rejected as a result of various instabilities. This section is intended primarily to provide a record of such issues and the affected data to ensure reproducibility of the analysis.

In fill 6012, a large number of bunches experienced a rapid emittance growth. An example of such a bunch is shown in Figure 3.1. The extremely non-Gaussian shape is evident. All bunch crossing IDs (BCIDs) except the following were affected: 895, 2003, 2043, 2083, 2123. All other BCIDs are rejected from this analysis.

Sudden increases of the rate of vertices produced in empty bunch crossings were observed throughout fill 6016 in measurements of the ghost-charge fractions, which are presented in Section 3.2.2. These periods of time followed exactly after resets

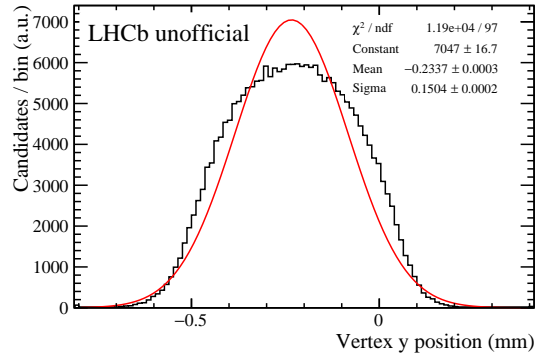


Figure 3.1: Average split vertex position distribution in the  $y$ -direction for beam 2-gas collisions with  $z \in (250, 1000)$  mm in BCID 975 of Fill 6012, Run 195818 with a Gaussian fit overlaid.

to the front-end electronics of the L0 trigger [122]. They appear to be corrected by each run<sup>2</sup> change. To remove such periods, the last 15 minutes (corresponding to one integration period in the determination of the overlap integral) of each run are removed.

## 3.2 Bunch population measurements

Both the vdM and BGI analyses rely on measurements of the bunch populations in the LHC to calibrate the absolute luminosity. A discussion of these measurements is presented in Section 3.2.1. Sections 3.2.2 and 3.2.3 describe corrections to and systematic uncertainties associated with these measurements, respectively.

### 3.2.1 Overview of LHC instrumentation

Measurements of the bunch populations at the LHC are primarily provided by two sets of instruments: the Direct Current Current Transformers (DCCTs) [124] and the Fast Beam-Current Transformers (FBCTs) [125]. The DCCTs provide measurements of the mean current in each beam with a precision of  $\mathcal{O}(0.2\%)$  [126]. The FBCTs have a short integration window to resolve the fraction of charge in each 25 ns bunch slot but provide less accurate measurements than the DCCTs. The

<sup>2</sup>‘Run’ is an internal LHCb term used to define continuous periods of data-taking. Nominally, a new run is automatically started every hour of data-taking. In case of errors reported by any sub-detector, a run change can be manually implemented to reset the detector, resulting in a shorter run. The difference between an LHC and LHCb run should generally be clear from the context.

population of each bunch can be taken as the relative population provided by the FBCTs scaled by the total beam current provided by the DCCTs. For bunch  $j$  in beam  $i$  this is given by

$$N_{i,j} = N_i^{\text{DCCT}} \frac{N_{i,j}^{\text{FBCT}}}{\sum_k N_{i,k}^{\text{FBCT}}}, \quad (3.12)$$

where  $N_j$  represents the population of bunch  $j$  and superscripts denote a measurement from a specific device (for clarity, the index ‘ $j$ ’ will be used to indicate a specific BCID throughout this thesis, while ‘ $i$ ’ will be used to indicate a specific beam). The index  $k$  runs over all filled BCIDs in the LHC for a given fill. The ATLAS Beam Pick-up Timing System (BPTX) [127] also provides sensitivity to the relative bunch populations. This device generally suffers from more noise than the FBCTs, and is therefore utilised for systematic uncertainty studies but not for the nominal measurements.

Both the DCCTs and FBCTs have an identical ‘A’ and ‘B’ set of instrumentation per-beam. The averages of the A and B DCCT measurements are used to define the overall charge scale in each fill, at each time step. The FBCT B system was not available in all of the fills considered here, so measurements from the A system are used. Figure 3.2 shows the DCCT intensity measurements for the A and B systems in each beam throughout each fill considered in this measurement. Figure 3.3 shows the ratio of the A to B DCCT systems for the same measurements. The A and B systems are in excellent agreement to the level of  $\mathcal{O}(10^{-4})$  throughout every fill.

### 3.2.2 Ghost and satellite charge corrections

Both the DCCTs and FBCTs must be corrected from biases originating from erroneously distributed charges in the LHC ring. Contributions to the measurements from each device falling outside nominally filled radio-frequency (RF) buckets are illustrated in Figure 3.4. The DCCTs’ measurements are biased by so-called ‘ghost’ charges while the FBCTs’ measurements are affected by ‘satellite’ charge contributions. Ghost charges are defined as charges which circulate in the LHC ring outside of any nominally filled 25 ns bunch slot. Satellite charges are defined as charges inside a nominally filled bunch slot but outside of the central, filled, 2.5 ns RF bucket.

The ghost-charge contributions to each beam current can be measured by comparing the number of beam-gas vertices produced in empty bunch crossings ( $ee$  and  $eb$  for beam 1, and  $ee$  and  $be$  for beam 2) to that in filled bunch crossings. We

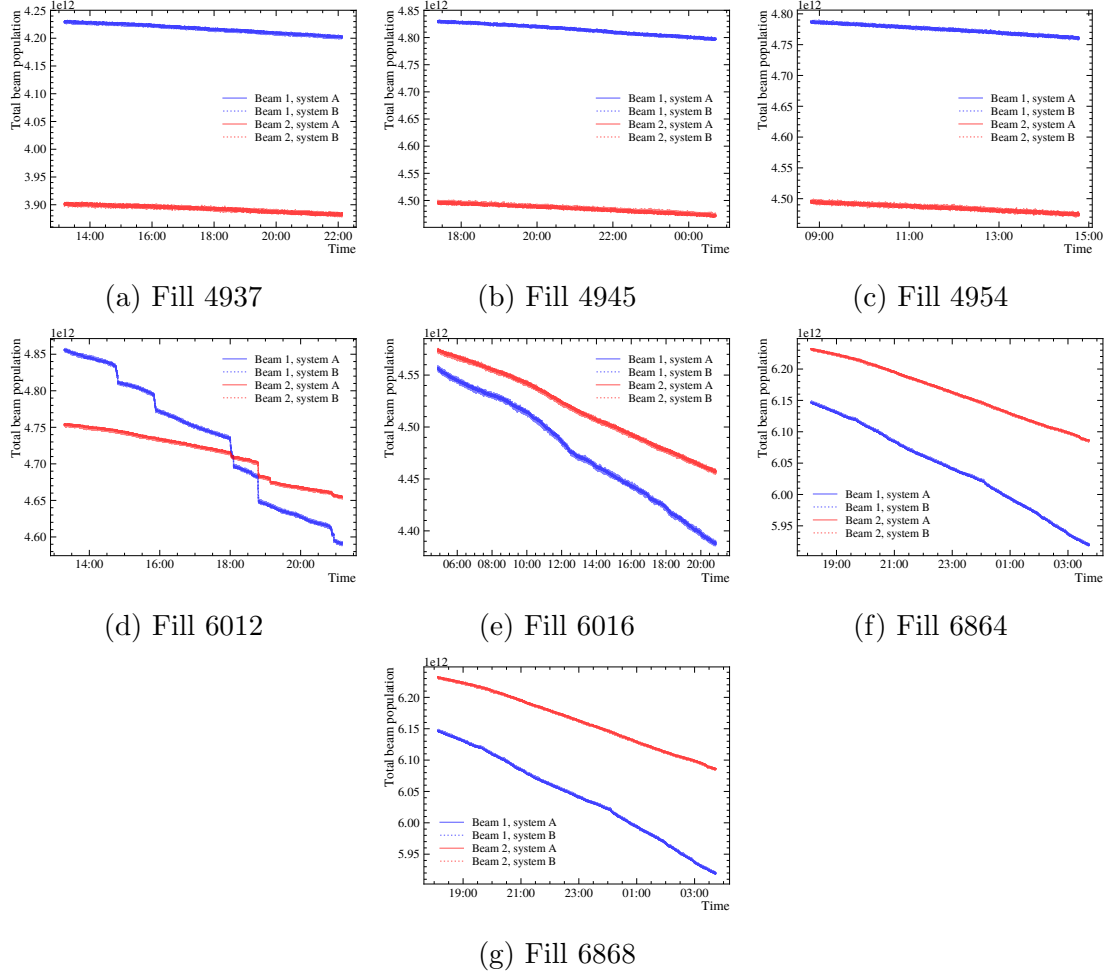


Figure 3.2: DCCT measurements from systems A and B for both beams in each calibration fill. The A and B systems are indistinguishable here in every fill; their difference is better visualised in Figure 3.3.

assume that the number of beam-gas interactions produced per bunch crossing is proportional to the charge of the incident bunch. If the ghost-charge fraction is small it follows that

$$f_{\text{ghost}} = \frac{N_{\text{ghost}}}{N_{\text{filled}} + N_{\text{ghost}}} \approx \frac{N_{\text{ghost}}}{N_{\text{filled}}}, \quad (3.13)$$

where  $N_{\text{ghost}}$  and  $N_{\text{filled}}$  are the total charge contained in (nominally) empty and filled bunch slots, respectively. We can then write for each beam

$$\frac{N_{\text{ghost}}}{N_{\text{filled}}} = \frac{n_{\text{ghost}}}{n_{\text{filled}}}, \quad (3.14)$$

where  $n_{\text{ghost}}$  and  $n_{\text{filled}}$  are the number of reconstructed and selected beam-gas vertices in empty and filled bunch crossings, respectively. We count only vertices in non-

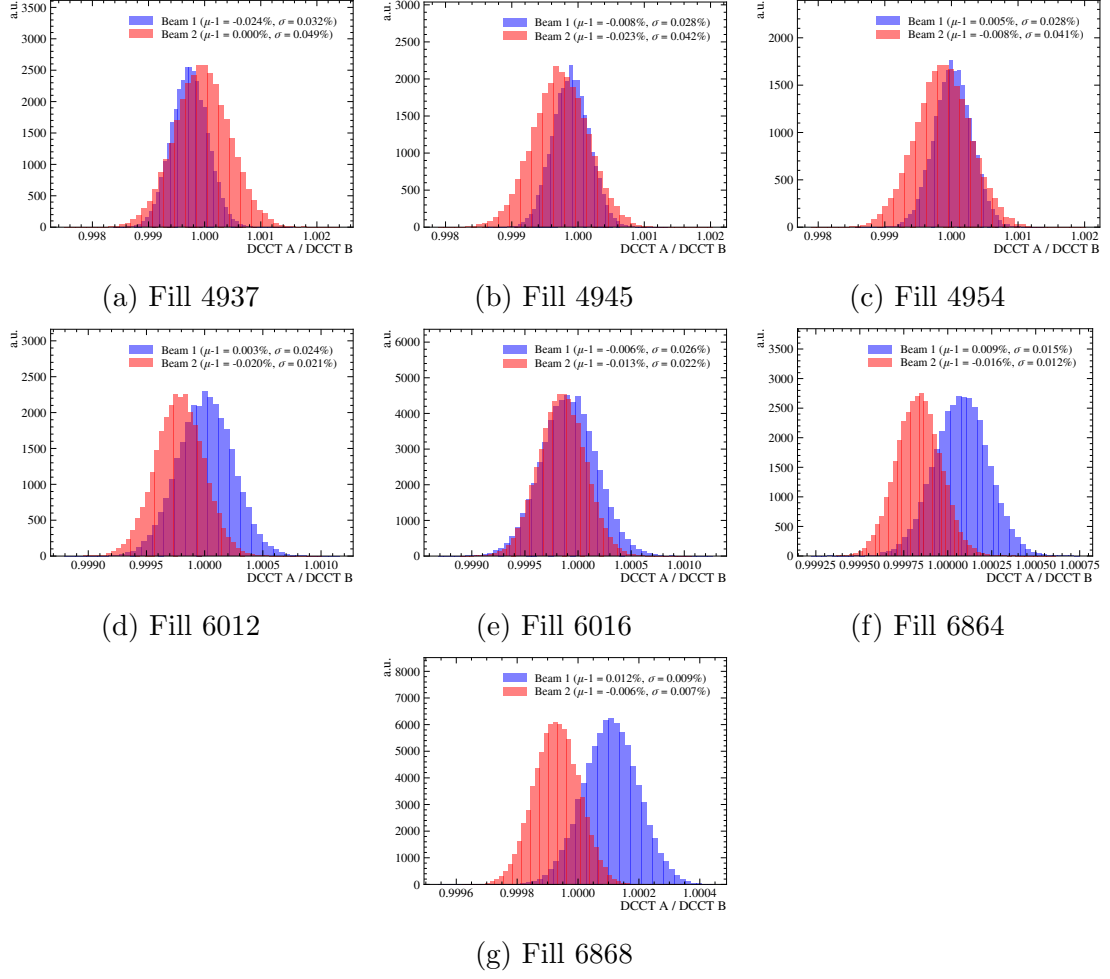


Figure 3.3: Ratio of DCCT system A to system B measurements for both beams in each calibration fill.

colliding bunch crossings and therefore replace  $n_{\text{filled}}$  with  $n_{be(eb)}$  in Equation 3.14; an additional factor is introduced to account for the neglected charge in colliding bunch slots. Primary vertices are selected according to the requirements in Section 4.2.

In addition, the distribution of ghost charges within the empty bunch slots can introduce a difference in reconstruction efficiency between vertices produced from ghost-charge interactions and those produced by the nominally filled bunches. While the particles in nominally filled bunches are contained within the central RF bucket, ghost charges can be distributed in any fashion across the RF buckets in each empty bunch slot. The LHCb trigger clock is optimised such that the trigger efficiency is maximal on the central RF bucket. This is accounted for by applying an efficiency correction factor. The correction factors have been measured by shifting the LHCb clock with respect to the LHC clock and measuring the average efficiency across the

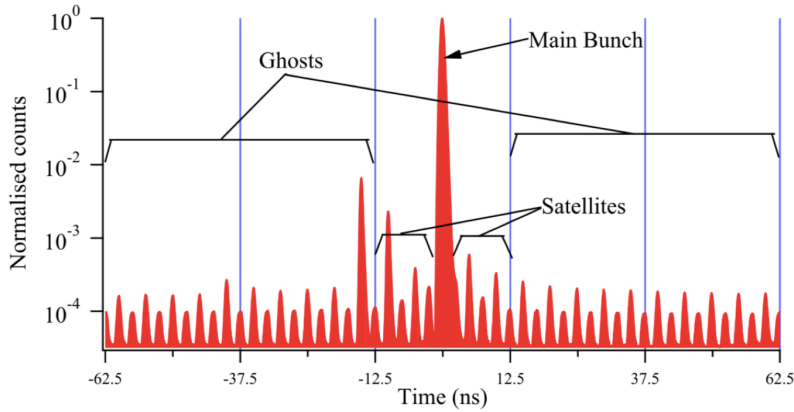


Figure 3.4: Illustration of the definitions of ghost and satellite charges. Reproduced from [128].

bunch slot. Using the average efficiency for this correction implicitly assumes that the ghost charges are uniformly distributed across the RF buckets. This procedure is presented in more detail in Refs. [97, 121]. In addition, ghost-charge interactions can potentially spill between two bunch slots if they are produced by ghost charges near the edge of a bunch slot. Such events can potentially be double-counted. To account for this, the measurement is performed both with and without interactions in consecutive bunch crossings removed. The difference between the two results of the two methods is taken as a systematic uncertainty on the ghost-charge fraction and their average is used as the central value. Table 3.2 shows the correction factors for each beam and counting method. With these corrections, the ghost charge can then be expressed as

$$f_{\text{ghost}}^{1(2)} \approx \frac{N_{\text{ghost}}^{1(2)}}{N_{\text{filled}}^{1(2)}} = \frac{n_{ee+eb(be)}^{1(2)}}{n_{be(eb)}^{1(2)}} \frac{N_{be(eb)}^{1(2)}}{N_{bb+be(eb)}^{1(2)}} \frac{1}{\varepsilon_{\text{trigger}}^{1(2)}}, \quad (3.15)$$

where  $\varepsilon_{\text{trigger}}^{1(2)}$  is the trigger efficiency correction and all other symbols are as previously defined. An additional systematic uncertainty is assigned to each ghost charge measurement based on the uncertainties associated with the efficiency correction factors. Figure 3.5 shows ghost-charge measurements for all of the calibration fills considered in this analysis. The average measured ghost charge, per-beam, in each fill is given in Table 3.3. The statistical error is computed from a constant fit to all measurements in each fill using only their statistical errors. The systematic uncertainty is assumed to be correlated between the measurements within each fill, and therefore averaged across the measurements. The measured ghost-charge fraction is

subtracted from the DCCT measurements to compute the final bunch population scale.

Beam	$\varepsilon_{\text{trigger}}$ , no double counts	$\varepsilon_{\text{trigger}}$ , including double counts
1	$0.93 \pm 0.02$	$1.05 \pm 0.03$
2	$0.86 \pm 0.01$	$0.90 \pm 0.01$

Table 3.2: Bunch timing efficiency correction factors applied in the ghost-charge measurements.

Since fine-timing information within a bunch slot is not generally available with the LHCb detector (although some studies have been carried out, *e.g.* Section 3.2.7 of Ref. [122]), measurements of the satellite charge are not possible. Instead, the satellite charge determination utilises a piece of LHC instrumentation known as either the Beam Synchrotron Radiation Telescope (BSRL) or Longitudinal Density Monitor (LDM) [129, 130]. The BSRL detects synchrotron radiation — produced as the LHC beams are steered by the dipole magnets — with a timing resolution of  $\sim 50$  ps. Table 3.4 shows the average satellite fraction measured for each beam in each calibration fill. Owing to the small size of this effect, the satellite charges are neglected.

### 3.2.3 Systematic uncertainties

A systematic uncertainty related to the bunch population measurements provided by the FBCTs is calculated by repeating the cross section measurement using the relative bunch populations from the BPTX instead. A shift of 0.02% is observed and taken as a systematic uncertainty on the final cross section measurement due to the relative bunch population measurement.

Fill	Beam 1 (%)	Beam 2 (%)
4937	$0.167 \pm 0.001$ (stat) $\pm 0.021$ (syst)	$0.132 \pm 0.001$ (stat) $\pm 0.007$ (syst)
4945	$0.036 \pm 0.001$ (stat) $\pm 0.005$ (syst)	$0.043 \pm 0.001$ (stat) $\pm 0.002$ (syst)
4954	$0.190 \pm 0.001$ (stat) $\pm 0.024$ (syst)	$0.145 \pm 0.001$ (stat) $\pm 0.008$ (syst)
6012	$0.034 \pm 0.000$ (stat) $\pm 0.004$ (syst)	$0.113 \pm 0.001$ (stat) $\pm 0.004$ (syst)
6016	$0.023 \pm 0.000$ (stat) $\pm 0.003$ (syst)	$0.072 \pm 0.001$ (stat) $\pm 0.004$ (syst)
6864	$0.062 \pm 0.001$ (stat) $\pm 0.003$ (syst)	$0.092 \pm 0.001$ (stat) $\pm 0.003$ (syst)
6868	$0.140 \pm 0.001$ (stat) $\pm 0.006$ (syst)	$0.186 \pm 0.001$ (stat) $\pm 0.004$ (syst)

Table 3.3: Average ghost-charge measurements from beam-gas imaging for each beam in each calibration fill.

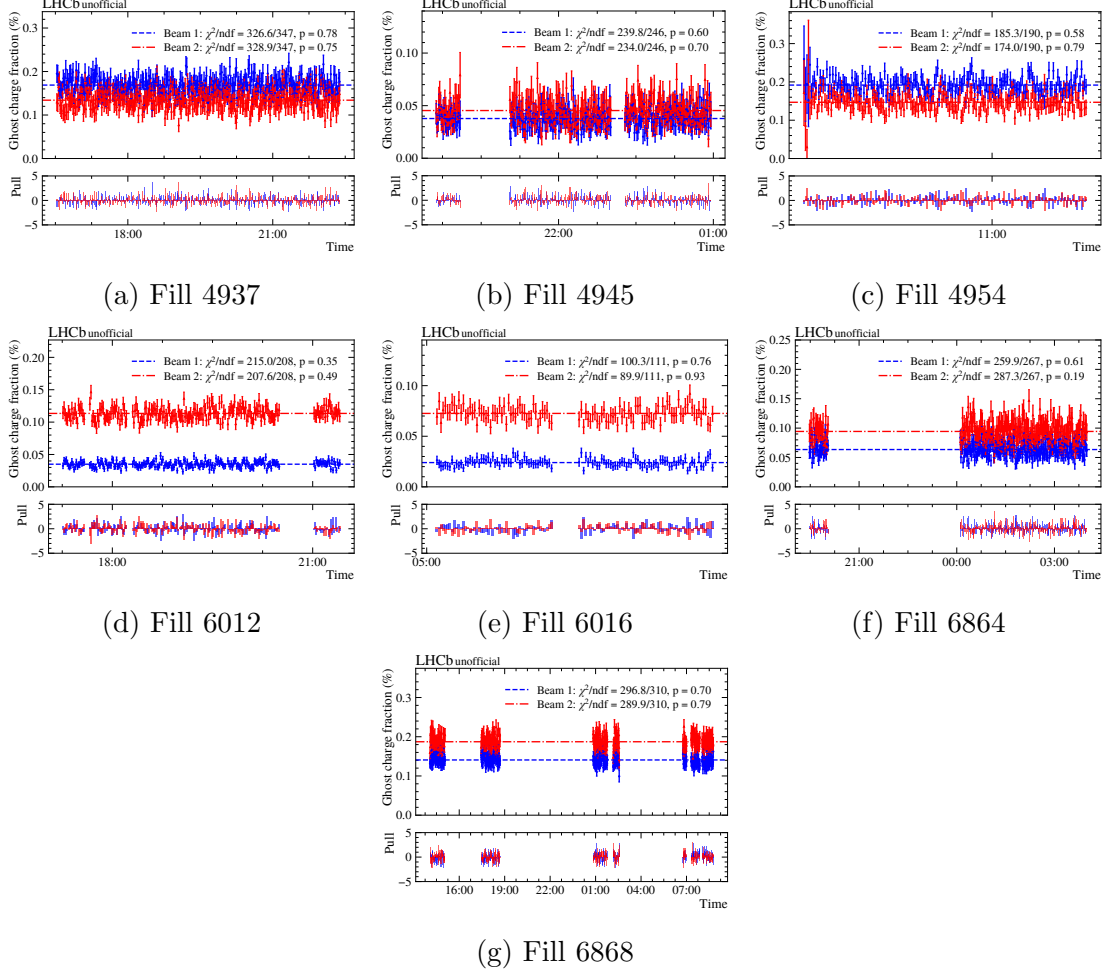


Figure 3.5: Ghost-charge measurements for each calibration fill in this analysis.

Fill	$f_{\text{sat, beam 1}} (10^{-4})$	$f_{\text{sat, beam 2}} (10^{-4})$
4937	1.1	0.7
4945	3.0	2.2
4954	4.4	2.9
6012	0.2	0.8
6016	2.0	1.6
6864	1.7	2.6
6868	5.1	5.8

Table 3.4: Average satellite fraction measured for each beam throughout each calibration fill.

Previous studies of the FBCT and BPTX systems have shown evidence for possible non-linearities in their responses [131]. To correct for this, the relative bunch populations reported by the BPTX are assumed to be locally linear and expanded around their mean value. Measurements from the BPTXs are used for simplicity in

this study. The FBCTs used different integrators for even and odd bunch IDs before 2017, which could in principle contribute different non-linear behaviours. The local expansion of the bunch populations can be written as

$$P_i^j \rightarrow P_i^j + \delta_i^j, \quad (3.16)$$

with  $\delta_i^j = \alpha_i + \beta_i \Delta P_i^j$  and  $\Delta P_i^j = P_i^j - \langle P_i^j \rangle$ . The quantity  $P_i^j$  represents the relative population of BCID  $j$  in beam  $i$ , normalised such that  $\sum_j P_i^j = 1$ . The parameters  $\alpha_i$  and  $\beta_i$  define the expansion for each beam, and  $\langle P_i^j \rangle = 1/n_i$  is the mean relative bunch population, where  $n_i$  is the number of bunches in beam  $i$ . The normalisation of the relative fractions removes one degree of freedom giving

$$\sum_j \delta_i^j = 0 \implies \alpha_i = -\beta_i \sum_j \Delta P_i^j = 0 \quad (3.17)$$

The modified cross section for each bunch with the perturbed population fraction can be written as

$$f(\sigma_j, \beta_1, \beta_2) = \sigma_j \frac{P_1^j}{P_1^j + \delta_1^j} \frac{P_2^j}{P_2^j + \delta_2^j}, \quad (3.18)$$

where  $\sigma_j$  is the average cross section measured for BCID  $j$ . A three-parameter fit is performed where the true cross section,  $\sigma$ , and the gradients of the linear expansion  $\beta_1$  and  $\beta_2$  are floated to minimise the per-bunch spread of the cross section measurements. This corresponds to minimising the  $\chi^2$  given by

$$\chi^2 = \sum_j \frac{(f(\sigma_j, \beta_1, \beta_2) - \sigma)^2}{(\delta\sigma_j)^2}, \quad (3.19)$$

where  $\delta\sigma_j$  represents the statistical error on the average cross section for BCID  $j$ . An overall shift of 0.03% in the final cross section result is observed, which is taken as a systematic uncertainty.

The uncertainty on the measured ghost-charge fraction is propagated to the final cross section by fluctuating the ghost-charge measurements within their uncertainties. Full correlation is assumed between both beams and all fills; this is a conservative choice since the ghost-charge uncertainties are dominated by the statistical error. The central value of each ghost-charge measurement is fluctuated in both directions by its uncertainty. The difference between the two shifted cross sections of  $\sigma_{\text{Vertex}}^+ - \sigma_{\text{Vertex}}^- = 0.04\%$  is taken as a systematic uncertainty.

Fill	Uncertainty (%)
4937	0.22
4945	0.21
4954	0.21
6012	0.21
6016	0.21
6864	0.83
6868	0.50

Table 3.5: DCCT uncertainties affecting the bunch current scale product of both beams in each calibration fill.

A detailed study was performed to characterise possible sources of uncertainty affecting the DCCT bunch current scale measurements in Run 1 of the LHC and can be found in Ref. [126]. The DCCTs were read out in Run 1 using a 12-bit analogue-to-digital converter (ADC), which has since been replaced with an improved 24-bit ADC. Nonetheless, we conservatively apply the same prescription here. The uncertainty on the product of the bunch current scale for both beams in each calibration fill is shown in Table 3.5. The average uncertainty across all fills, 0.34%, is assigned as an uncertainty on the final cross section measurement. The larger uncertainties in fills 6864 and 6868 are dominated by uncertainties calibrated in terms of the least significant bit (LSB) of the 12-bit ADC. Such a procedure almost certainly overestimates the uncertainties associated with the upgraded 24-bit ADC, although currently no prescription exists for calibrating the 24-bit ADC DCCT uncertainties<sup>3</sup>. In addition, a significant contribution to the overall uncertainty arises from a non-linearity in the DCCTs' response which is correlated between the two beams; such an effect has not been observed using the 24-bit ADCs [126].

Since the satellite charge is neglected here, its overall contribution to the bunch currents is taken as a systematic. The relative bias on the population of the bunch current scales is given by  $(1 - f_{\text{sat},1})(1 - f_{\text{sat},2})$ . Averaging this value across all fills gives a systematic uncertainty of 0.05% resulting from the satellite charge fraction.

---

<sup>3</sup>There is currently an external (to LHCb) effort ongoing to better understand the correct way to treat such uncertainties using measurements based on the 24-bit ADC.

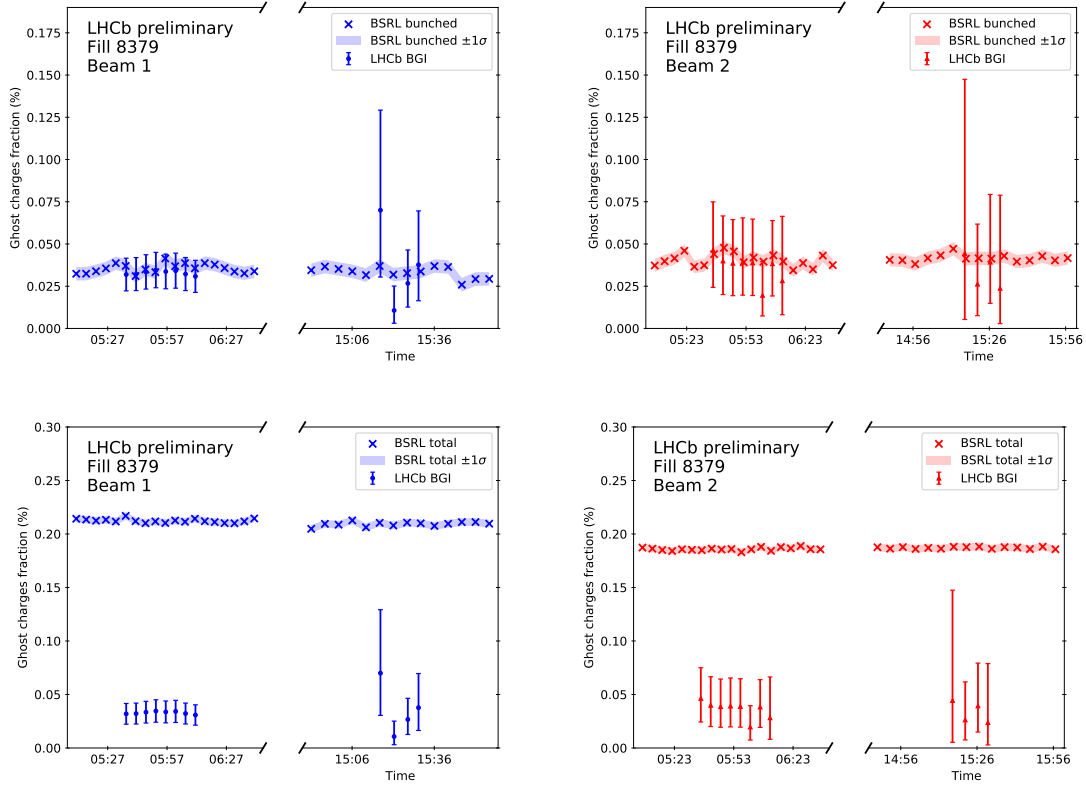


Figure 3.6: Comparison between LHCb and BSRL ghost-charge measurements in fill 8379.

### 3.3 Ghost-charge measurements in 2022

The LHCb detector was almost entirely rebuilt — as described in Section 2.2.12 — in preparation for Run 3 of the LHC, which began in 2022. Throughout 2022 and 2023, the detector has been undergoing an intense commissioning phase. Ghost-charge measurements made in the 2022 luminosity calibration fills — of particular relevance to the ATLAS and CMS experiments to cross-check the BSRL results — were one of the first results published with the upgraded detector [132, 133].

SMOG2 was used to inject Ar gas either into the SMOG2 cell or the VELO vacuum vessel. Events were triggered based on the presence of at least 10 tracks passing through a cylinder around the beamline with a length of 4 m and a radius of 3 mm, centred on the interaction point. The full vertex reconstruction was then performed offline. Beam-gas vertices are highly asymmetric and were therefore required to have at least 10 tracks exclusively towards or away from the LHCb spectrometer, with respect to the position of the interaction point. Material interactions with the

detector and support elements were removed by requiring the radial position of each vertex to lie within 3 mm of the beamline.

Figures 3.6 and 3.7 show the measured ghost charges in calibration fills 8379 and 8381. A comparison with the BSRL measurements is also shown. The ‘bunched’ BSRL measurements are obtained with a baseline subtraction, while the ‘total’ BSRL measurements are obtained without the baseline subtraction. The bunched method is typically preferred, although issues with the baseline subtraction in the presence of de-bunching have been observed in the past [122,128]. The LHCb ghost-charge measurements in fills 8379 and 8381 show good agreement with the BSRL bunched method. Poor agreement is observed between the LHCb and BSRL total method measurements, which is not unexpected due to the absence of the baseline subtraction in the total method.

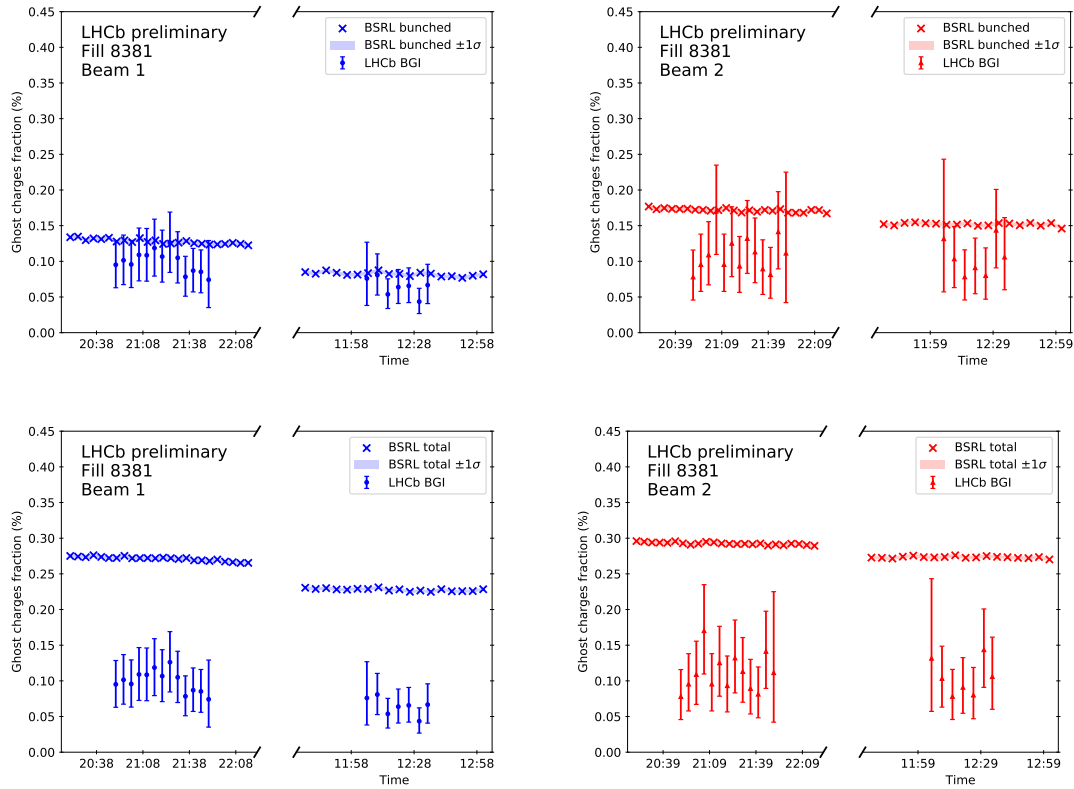


Figure 3.7: Comparison between LHCb and BSRL ghost-charge measurements in fill 8381.

## 3.4 Relative luminosity measurements

The mean number of occurrences of some process  $c$  per bunch crossing,  $\mu_c$ , is proportional to the absolute luminosity and will be referred to here as the relative luminosity. It is related to the cross section of the process  $c$  and the luminosity determined by the bunch profiles as described in Equations 3.1 and 3.3, respectively. Measurements of the relative luminosity allow the cross section to be extracted from measurements of the absolute luminosity per bunch crossing using the BGI method.

### 3.4.1 Counter definitions

The term ‘counter’ is defined to refer to each of the aforementioned processes,  $c$ . A counter can in principle be any physical process or property of each event for which some threshold to distinguish between empty and non-empty events can be defined. There are however several advantageous quantities that a good counter process should possess. It should scale linearly with the absolute luminosity such that the absolute calibration cross section presented in this measurement can be used to extrapolate the luminosity to physics conditions. A ‘reasonable’ fraction of empty events is required to facilitate measurements with the LogZero method described in Section 3.4.2. There should be no dependence on external factors such as the LHC filling scheme. Two empty events in the same bunch crossing should not add together to produce a non-empty event. Finally, the counter should be robust to radiation damage and other effects that could potentially alter its cross section over time. Table 3.6 lists the specific counters used in this measurement. The Vertex counter is used throughout this analysis as it has a relatively small background correction for beam-gas interactions. The Track counter was used in Run 1 to propagate the calibrated luminosity to the physics luminosity as it has a less pronounced efficiency dependence on the shape of the luminous region, which can vary from fill-to-fill. For Run 2, the Vertex counter is used to compute the physics luminosity, although a measurement of the Track cross section is included here for completeness. The Position Of Closest Approach (POCA) used to compute the Track counter is defined as the minimum distance between any point on the extrapolation of each track and the beamline. The PV3D counter — based on a superset of the vertices collected by the Vertex counter — is used to test and assign a systematic on the background subtraction. Events with values of the counter quantity below the listed threshold

are defined as ‘empty’. Having multiple counters to rely on allows the time- and conditions-stability of each counter to be tested by monitoring the ratios of various counters across different fills.

Name	Quantity	Threshold
Vertex	PVs with $ z  < 300$ mm and $x^2 + y^2 < 4$ mm	1
Track	VELO tracks with POCA $ z  < 300$ mm and $x^2 + y^2 < 4$ mm	2
PV3D	PVs	1

Table 3.6: Definitions of selected counters used in this measurement.

### 3.4.2 Measurements of the interaction rate

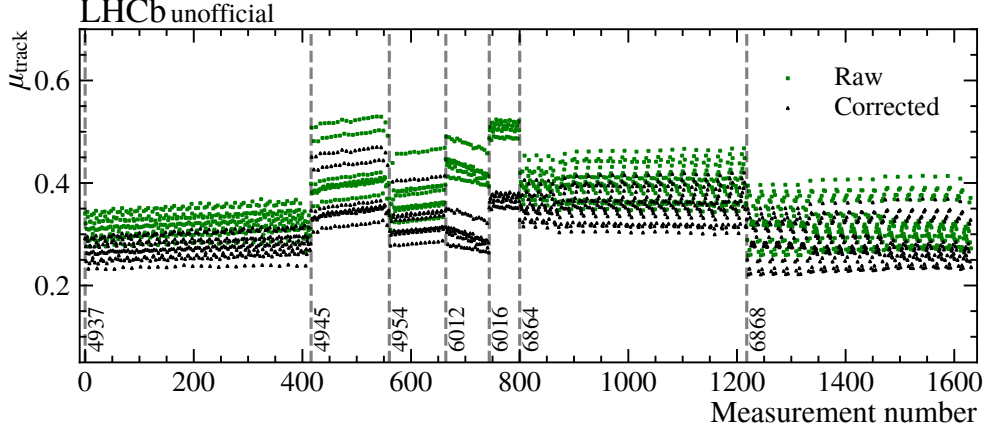
The interaction rate is determined using the ‘LogZero’ method. The LogZero method relates the mean number of interactions per bunch crossing,  $\mu_c$ , to the fraction of empty events for each BCID as

$$\mu_c = -\log(P(0|\mu_c)) = -\log\left(\frac{\mu_c^0 e^{-\mu_c}}{0!}\right) = -\log\left(\frac{n_{\text{empty}}}{n}\right), \quad (3.20)$$

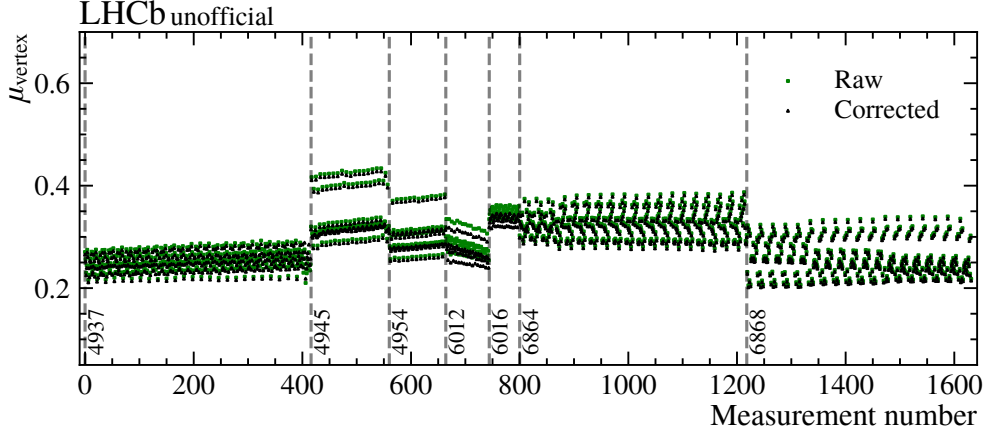
where it is assumed the number of occurrences of process  $c$  per bunch crossing is Poisson distributed with mean  $\mu_c$ . The number of empty events,  $n_{\text{empty}}$ , and the total number of events  $n$ , are determined by randomly triggering on colliding bunch crossings at a rate of 5 kHz. Filled, non-colliding, bunch crossings for each beam are randomly triggered at 2 kHz to allow measurements of the beam-gas background correction. Non-filled bunch crossings are randomly triggered at 0.5 kHz. The LogZero method is robust to loss of events either during data-taking or offline — under the assumption that empty and non-empty events are affected in the same way — since we measure only the fraction of empty events to determine the relative luminosity.

#### 3.4.2.1 Background subtraction

Equation 3.20 assumes that all non-empty events are produced by beam-beam interactions. In practice, some events will be counted as non-empty based on beam-gas interactions alone. We neglect any background originating from empty crossings. To correct for this effect, the beam-gas background must be subtracted from measurements of the interaction rate. We compute the beam-gas background by considering the rate of interactions in non-colliding bunch crossings. The corrected interaction



(a) Track counter



(b) Vertex counter

Figure 3.8: Distribution of interaction rate measurements for the (a) Track and (b) Vertex counters before and after beam-gas background subtraction in each integration period for each BCID. The dashed vertical lines indicate the boundaries between the different fills included in this measurement.

rate can then be written as

$$\mu_c = \mu_c^{\text{raw}} - N_1 \langle \nu_{c,1} \rangle - N_2 \langle \nu_{c,2} \rangle, \quad (3.21)$$

where  $\mu_c^{\text{raw}}$  is the raw interaction rate determined using Equation 3.20,  $N_i$  is the population of the relevant bunch in beam  $i$  and  $\langle \nu_{c,i} \rangle$  is the average specific rate of interactions observed in all filled, non-colliding bunches of beam  $i$ . The interaction rates  $\mu_c$  and  $\mu_c^{\text{raw}}$  refer to a single bunch,  $j$ , in beam  $i$ , although these indices are suppressed for brevity. The specific rate of interactions is defined for each BCID  $j$

as

$$\nu_{c,i}^j \equiv \frac{\mu_{c,i}^j}{N}, \quad (3.22)$$

where  $N$  is the relevant bunch population.

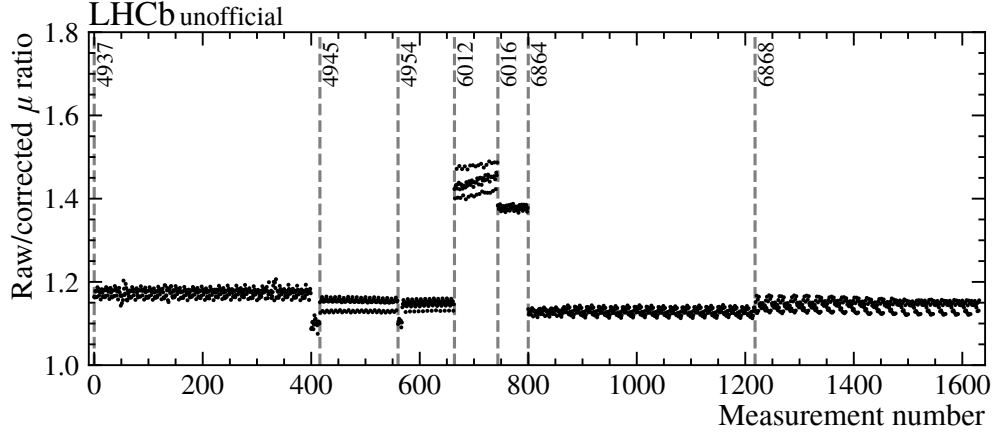
Figure 3.8 shows the distribution of the Track and Vertex counters' interaction rate measurements before and after the background subtraction. Figure 3.9 shows the ratio of the measurements before and after the correction. Note the different scales for the two counters. The beam-gas background correction for the Track counter is significantly larger than for the Vertex counter, and thus the Vertex counter is chosen as the nominal counter for this analysis. The increased beam-gas background evident in fills 6012 and 6016 is due to the larger beam-gas cross section for Ne compared to He, which was injected in all other fills (see Table 3.1).

#### 3.4.2.2 Efficiency correction

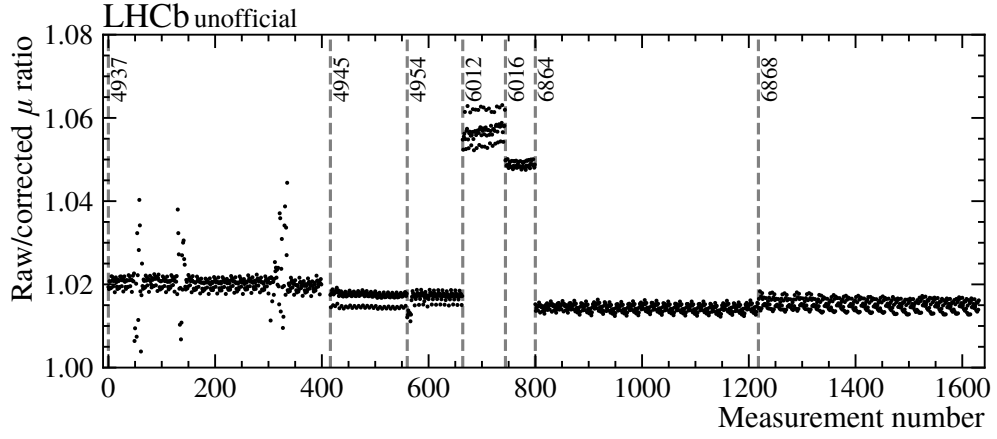
The probability of reconstructing both tracks and vertices changes as a function of the longitudinal position,  $z$ . Therefore, both the Track and Vertex counters exhibit some dependence on the width and position of the luminous region. To correct for this, the measured values of each counter are normalised to the reference point  $\mu_{zl} = 0$ ,  $\sigma_{zl} = 50$  mm using a correction factor. The procedure for determining the correction factors is described in detail in Ref. [97]. The efficiency has been evaluated as a function of the longitudinal position from simulation. Assuming the luminous region follows a Gaussian distribution in the longitudinal region, this efficiency map is used to derive an efficiency correction factor which normalises each measurement to the interaction rate which would have been measured with the above reference parameters. The efficiency correction as a function of the position of the luminous region, assuming a width of  $\sigma_{zl} = 50$  mm, is shown in Figure 3.10 for the Track and Vertex counters. By definition, the correction is unity at  $z = 0$ . The variation in efficiency, and therefore the difference of the correction factors from unity, is significantly larger for the Vertex counter than for the Track counter.

#### 3.4.3 Systematic uncertainties

Potential systematic effects affecting the counter background subtraction are assessed by comparing the Vertex and PV3D counters. The PV3D counter uses the same sample of vertices as the Vertex counter, but places no requirement on their



(a) Track counter



(b) Vertex counter

Figure 3.9: Ratio of interaction rate measurements for the (a) Track and (b) Vertex counters before and after beam-gas background subtraction in each integration period for each BCID. The dashed vertical lines indicate the boundaries between the different fills included in this measurement.

position. Thus, it is more sensitive to beam-gas background and has a larger background correction due to its increased acceptance outside the luminous region. Figure 3.11 shows the ratio of the raw to background corrected PV3D counter to highlight the larger background correction required with respect to the Vertex counter. Figure 3.12b shows the ratio of the PV3D and Vertex counters after background correction. The deviation of the average value from unity, 0.01%, is taken as a systematic uncertainty arising from the counter background subtraction.

The average ratio of the Track and Vertex counters is used to convert the measured Vertex cross section to a measurement of the Track cross section for propaga-

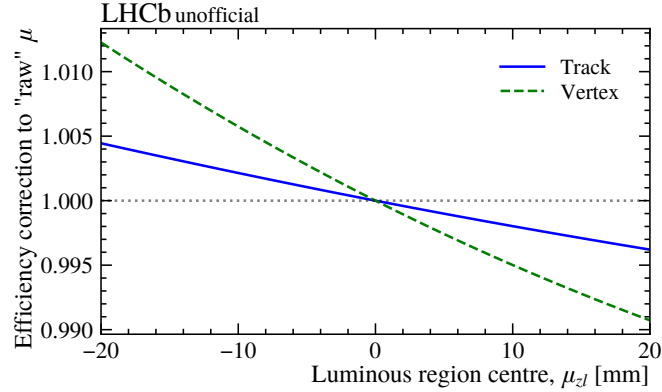


Figure 3.10: Efficiency of interactions for the Track and Vertex counters as a function of luminous region center, assuming  $\sigma_{zl} = 50$  mm.

tion to the physics luminosity. Figure 3.12a shows this ratio for all measurements of the cross section performed in this analysis. A mean value of  $\mu_{\text{Track}}/\mu_{\text{Vertex}} = 1.099$  is obtained. Each data point corresponds to one BCID and one integration period. The relative standard deviation of the ratio, 0.22%, is taken as a systematic uncertainty on the measured cross section.

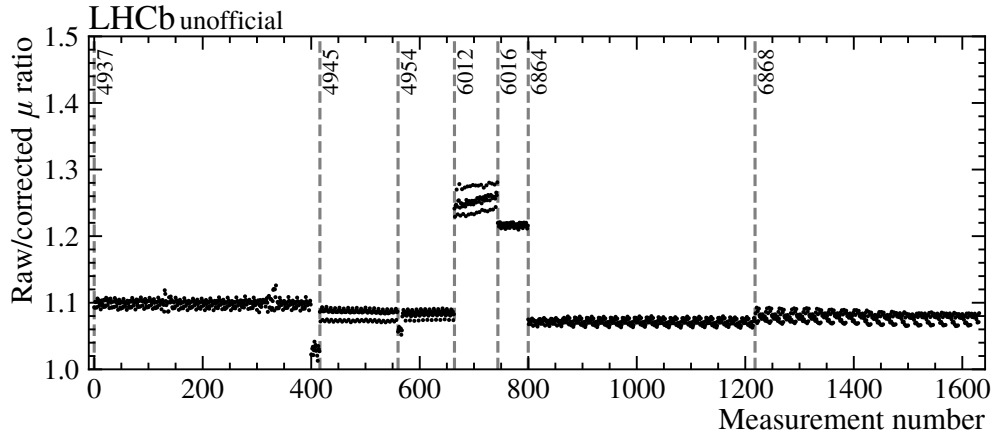
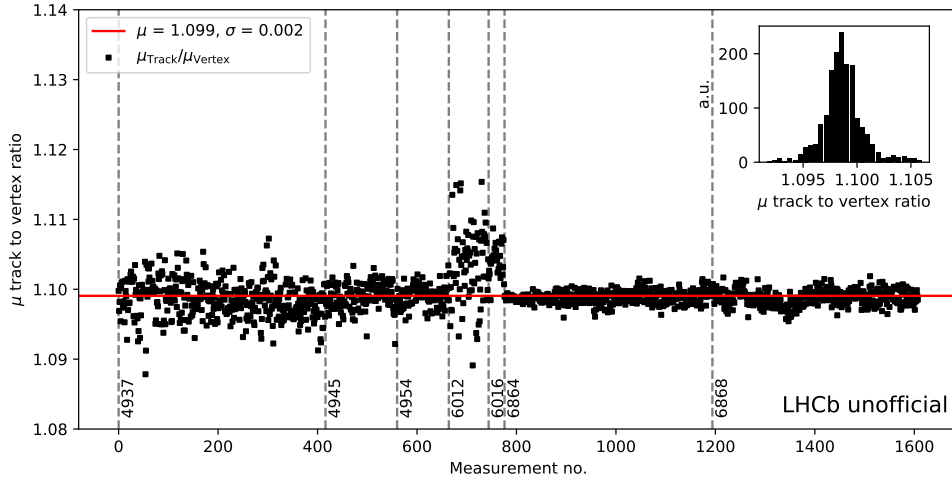
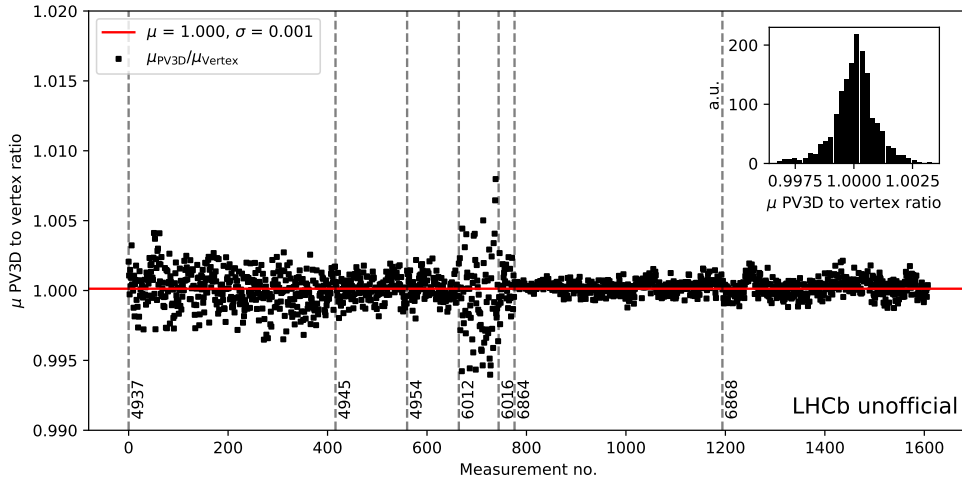


Figure 3.11: Ratio of interaction rate measurements for the PV3D counter before and after beam-gas background subtraction in each integration period for each BCID. The dashed vertical lines indicate the boundaries between the different fills included in this measurement.



(a) Track-to-vertex ratio



(b) PV3D-to-vertex ratio

Figure 3.12: Ratio of the (a) Track to Vertex and (b) PV3D to Vertex counters for all calibration measurements in this analysis. The dashed vertical lines indicate the boundaries between the different fills included in this measurement.

### 3.5 Summary

An overview of luminosity determination at the LHC has been presented. The vdM method, used by all of the LHC experiments to calibrate the absolute luminosity, was briefly presented. A brief discussion of the BGI method, which is unique to LHCb, was also presented. The LHC instrumentation responsible for providing measurements of the bunch currents was described. Corrections for ghost and satel-

lite charges were presented, including measurements made in both Runs 2 and 3 of the LHC. Finally, the relative luminosity counters used to propagate the absolute luminosity to physics conditions were described, and measurements of the relative luminosity were presented. Systematic uncertainties studies affecting each of the bunch current and relative luminosity measurements were described.

# Absolute luminosity determination at LHCb

---

THE LHCb experiment has the unique capability of calibrating the luminosity by directly reconstructing the individual beam profiles using the BGI method, as introduced in Chapter 3. The results of the BGI analysis applied to the Run 2  $pp$  collision calibration fills, at a centre of mass energy of  $\sqrt{s} = 13$  TeV, are presented in this chapter.

## 4.1 Useful definitions

By convention, the beam travelling towards the LHCb spectrometer at the interaction point is denoted beam 1; the other beam is denoted beam 2. The forwards and backwards directions are defined with respect to the direction of beam 1, *i.e.* forwards points into the LHCb spectrometer from the interaction point. The term ‘beam-gas interaction’ will typically be used to refer to an inelastic collision between a proton in one of the LHC beams and a gas molecule in the beam-pipe that produces a PV. The radio-frequency (RF) cavities which accelerate the bunches in the LHC operate at a frequency of 401 MHz. Combined with the circumference of the ring, this gives 35,640 2.5 ns-long windows defined as ‘RF buckets’. The buckets are further grouped into 25 ns long periods defined as ‘bunch slots’. Only one of the central RF buckets in each bunch slot is nominally filled, as illustrated previously in Figure 3.4. In each bunch crossing at LHCb, there are four possible configurations depending on whether the bunch slot in each beam is filled or empty. Crossings where both beams are filled are denoted  $bb$ . Crossings where only beam 1 (2) is filled are denoted  $be$  ( $eb$ ). Crossings where both beams are empty are denoted  $ee$ .

## 4.2 Primary vertex selections

Table 4.1 lists the L0 selections utilised for the BGI analysis in the luminosity calibration fills throughout Run 2;  $\sum E_T^{\text{CALO}}$  is the total transverse energy deposited in the calorimeters, and  $N_{\text{PU}}$  and  $N_{\text{SPD}}$  are the number of hits in the PU and SPD sub-detectors which were introduced in Chapter 2, respectively. The hardware trigger requirements were updated in 2017 to reduce the impact of spillover (remnant activity in one or more sub-detectors from the previous bunch crossing) for the B1gas line, and to increase the acceptance rate for B2gas. Table 4.2 lists the HLT1 trigger selections applied to each primary vertex. Each of the HLT1 lines requires that either of the beam-gas L0 triggers fire. All HLT1 lines additionally require that the vertex has a radial position that satisfies  $\sqrt{x^2 + y^2} < 4$  mm. No selections are applied at the HLT2 stage. Offline, a tighter radial cut of  $\sqrt{x^2 + y^2} < 3$  mm is imposed to further suppress material interactions and vertices are required to lie in the longitudinal region  $[-1000, 1000]$  mm. Beam-gas vertices are distinguished by requiring each vertex originating from beam 1 (2) to have no backwards (forwards) tracks.

L0 line	Requirements
B1gas (2015-16)	$N_{\text{SPD}} > 2$ hits
B2gas (2015-16)	$N_{\text{PU}} > 9$ hits
B1gas (2017-18)	$\sum E_T^{\text{CALO}}$ and $N_{\text{SPD}} > 30$ hits
B2gas (2017-18)	$N_{\text{PU}} > 6$ hits

Table 4.1: L0 selections utilised for the BGI analysis in Run 2.

HLT1 line	Prescale	Crossing type	Longitudinal region (mm)	Track multiplicity
BeamGasNoBeam	1	<i>ee</i>	$[-2000, 2000]$	$> 9$
BeamGasBeam1	1	<i>be</i>	$[-2000, 2000]$	$> 9$
BeamGasBeam2	1	<i>eb</i>	$[-2000, 2000]$	$> 9$
BeamGasCrossingForcedReco	1	<i>bb</i>	$[-2000, 2000]$	$> 9$
BeamGasCrossingFullZLowNTracks	0.25	<i>bb</i>	$[-2000, -250] \cup [250, 2000]$	$> 9$
BeamGasCrossingForcedRecoFullZ	1	<i>bb</i>	$[-2000, 2000]$	$> 27$

Table 4.2: HLT1 selections utilised for the BGI analysis in Run 2.

### 4.3 Overlap integral measurements

The overlap integral is determined by fitting the distribution of vertices produced in beam-gas and beam-beam interactions in three stages. Firstly, the crossing angle is determined once for each data-taking run. The individual bunch profiles (separately for each colliding bunch pair) are then extracted from a fit to vertices collected in nominally 15 minute integration periods. Some measurements are taken over shorter periods due to short runs or run lengths which differ from a multiple of 15 minutes; such measurements are nonetheless included in the analysis. Finally, the longitudinal bunch distributions are determined from a fit to the sample of beam-beam interactions collected during the same integration windows. This procedure assumes that the bunch densities can be factorised into transverse and longitudinal components — *i.e.*  $\rho_i(\vec{x}) = \rho_i^\perp(x, y)\rho_i^\parallel(z)$  — but not that the transverse distributions are factorisable.

#### 4.3.1 Overlap integral in the case of Gaussian beams

The beam-gas imaging method involves directly reconstructing the individual bunch profiles from beam-gas interactions to calculate the overlap integral. The overlap integral is defined as

$$\mathcal{O} \equiv \int \rho_1(\vec{x}, t) \rho_2(\vec{x}, t) d\vec{x} dt, \quad (4.1)$$

where  $\rho_i(\vec{x}, t)$  is the probability density function describing the distribution of protons in a single bunch in beam  $i$ . If the bunch densities follow a Gaussian distribution in the transverse spatial directions it can be shown that

$$\mathcal{O} = \frac{1}{4\pi c \lambda_x \lambda_y}, \quad (4.2)$$

assuming the beams collide head-on without any crossing angle. In this approximation the overlap integral does not depend on the bunch shapes in the longitudinal direction. The parameters  $\lambda_x$  and  $\lambda_y$  are the convolved bunch widths<sup>1</sup>, *i.e.*  $\lambda_x^2 = \lambda_{x,1}^2 + \lambda_{x,2}^2$ , in each of the transverse directions. In the presence of a crossing angle and an offset between the beams the expression for the overlap integral

---

<sup>1</sup>The convention used to define the convolved bunch widths in Ref. [134] differs by a factor of two, however the final overlap integral expanded in terms of single bunch widths agrees between the two conventions. The convention in this thesis is preferred to align with the actual code implementation of the analysis.

becomes [134]

$$\mathcal{O} = \frac{e^{\frac{-\Delta_x^2}{2\Sigma_x^2}} e^{\frac{-\Delta_y^2}{2\Sigma_y^2}}}{4\pi c \Sigma_x \Sigma_y}. \quad (4.3)$$

The parameters  $\Delta x$ ,  $\Delta y$  are the offsets between the beam centres at the crossing point,  $z_{RF}$  (defined in Section 4.3.5). The modified bunch widths,  $\Sigma_x$  and  $\Sigma_y$  are defined as

$$\begin{aligned} \Sigma_x^2 &\approx \lambda_x^2 + \phi_x^2 \lambda_z^2 \\ \Sigma_y^2 &\approx \lambda_y^2 + \phi_y^2 \lambda_z^2 \approx \lambda_y^2, \end{aligned} \quad (4.4)$$

where  $\phi_x$ ,  $\phi_y$  are the half-crossing angles between the beams and  $\lambda_z$  is the convolved longitudinal bunch length. The final approximation is valid in the conditions of all calibration fills described in this measurement, where  $\phi_y \sim 0$ . In typical luminosity calibration conditions at the LHCb interaction point —  $\lambda_{x,i} \sim 0.1$  mm,  $\lambda_{z,l} \sim 50$  mm (defined in Section 4.3.5) and  $\phi_x = 450 \mu\text{rad}$  — the overlap integral differs from Equation 4.2 by around 3%. This change is dominated by the modification of the bunch widths.

In order to extract the beam profiles from the vertex distributions, the vertex resolution must be known. Given some function describing the vertex resolution,  $R(x)$ , the observed bunch profile,  $P_i(x)$ , is given by

$$P_i(x) = R(x) * \rho_i(x), \quad (4.5)$$

where the bunch profile is reduced to a single dimension for simplicity. If both the resolution model and the bunch profile have a Gaussian shape, the convolution will also follow a Gaussian distribution. The mean position of the bunch profile will be unaltered in the convolution assuming the resolution is unbiased. The measured bunch width of beam  $i$ ,  $\lambda_i$ , will be given by

$$\lambda_i^2 = (\lambda_i^{\text{true}})^2 + \tau^2, \quad (4.6)$$

where  $\lambda_i^{\text{true}}$  is the true bunch width and  $\tau$  is the width of the resolution function.

A single Gaussian model does not in practice adequately model either the vertex resolution or the bunch profiles. In particular, non-factorisability of the transverse axes is not allowed by such a simple model and vertices with different track multiplicities are combined in a single sample for each fit but are affected by different resolutions. Since the analytic expressions for the convolution and overlap integral

in terms of Gaussian distributions are known, more flexible models are constructed simply from a sum of multiple Gaussian components. The observed transverse bunch profile densities can then be written generally for a single bunch  $j$  (in one of the two beams) as

$$\begin{aligned}
 P_j(x, y) &= \sum_{a,b,c,d} w_{a,b} f_c^x f_d^y [g(x | 0, \tau_c^x) * g(x | \mu_a^x, \lambda_a^x)] [g(y | 0, \tau_d^y) * g(y | \mu_b^y, \lambda_b^y)] \\
 &= \sum_{a,b,c,d} w_{a,b} f_c^x f_d^y g\left(x | \mu_a^x, \sqrt{(\lambda_a^x)^2 + (\tau_c^x)^2}\right) g\left(y | \mu_b^y, \sqrt{(\lambda_b^y)^2 + (\tau_d^y)^2}\right) \quad (4.7)
 \end{aligned}$$

where:  $g$  represents a Gaussian distribution;  $w_{a,b}$  is a weight parameter of the bunch profile model with  $\sum_{a,b} w_{a,b} = 1$ ;  $f_{c(d)}^{x(y)}$  is a weight parameter of the resolution model with  $\sum_c f_c^x = \sum_d f_d^y = 1$ ;  $\tau_{c(d)}^{x(y)}$  and  $\lambda_{a(b)}^{x(y)}$  are the widths of the resolution and bunch profile components respectively; and  $\mu_{a(b)}^{x(y)}$  is the mean position of a bunch profile component. The indices  $a$  and  $b$  run over the bunch profile components, while the indices  $c$  and  $d$  run over the resolution components. The bunch profiles can therefore be determined as follows: the set of resolution parameters  $\{f_{c(d)}^{x(y)}\}$  and  $\{\tau_{c(d)}^{x(y)}\}$  are measured and then used to construct the observed bunch profile models in terms of the true bunch profile parameters  $\{w_{a,b}\}$ ,  $\{\mu_{a(b)}^{x(y)}\}$ , and  $\{\lambda_{a(b)}^{x(y)}\}$ . The total overlap integral then becomes

$$\mathcal{O} = \sum_{a,b,\alpha,\beta} (w_{a,b}^1 w_{\alpha,\beta}^2 \mathcal{O}_{a,b,\alpha,\beta}), \quad (4.8)$$

where the weights are as in Equation 4.7 with an additional superscript indicating the beam from which each component originates, and  $\mathcal{O}_{a,b,\alpha,\beta}$  represents the partial overlap integral for each combination of components from both beams and both axes (with  $a, b \rightarrow \alpha, \beta$  in Equation 4.7 for beam 2).

### 4.3.2 Crossing angle measurements

The directions of the two beams in each of the transverse axes can be measured by fitting a linear slope to some sample of beam-gas vertices, as illustrated in Figure 4.1. The lever arm of the fit is increased by integrating the sample of vertices across all bunches from all crossing types. We choose the sample of vertices for each fit to correspond to a single run of data-taking. The half crossing angle is defined as

$$\phi_a = \frac{\arctan(m_{2,a}) - \arctan(m_{1,a})}{2} \approx \frac{m_{2,a} - m_{1,a}}{2}, \quad (4.9)$$

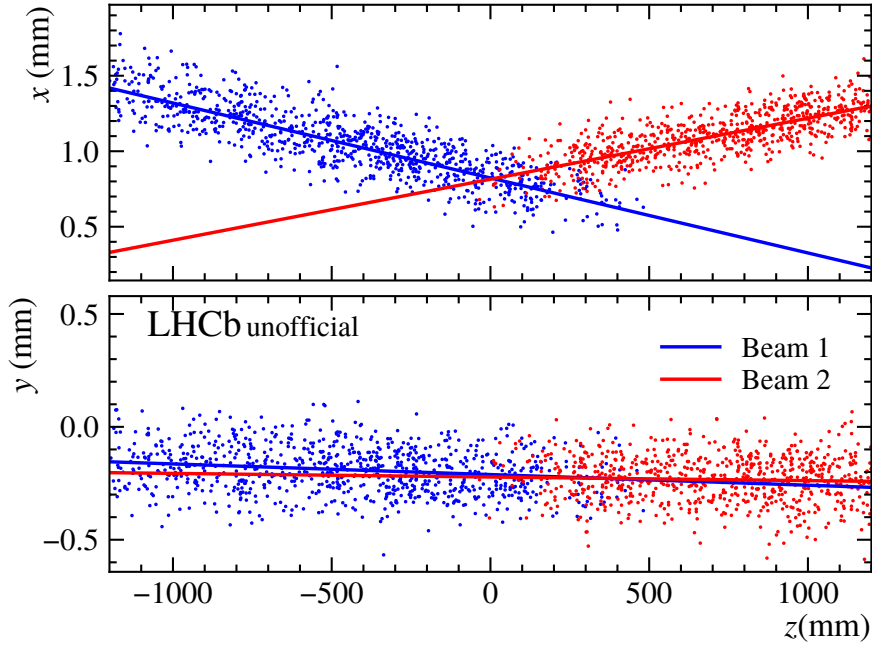


Figure 4.1: Example crossing angle measurement from Fill 4937, Run 174627.

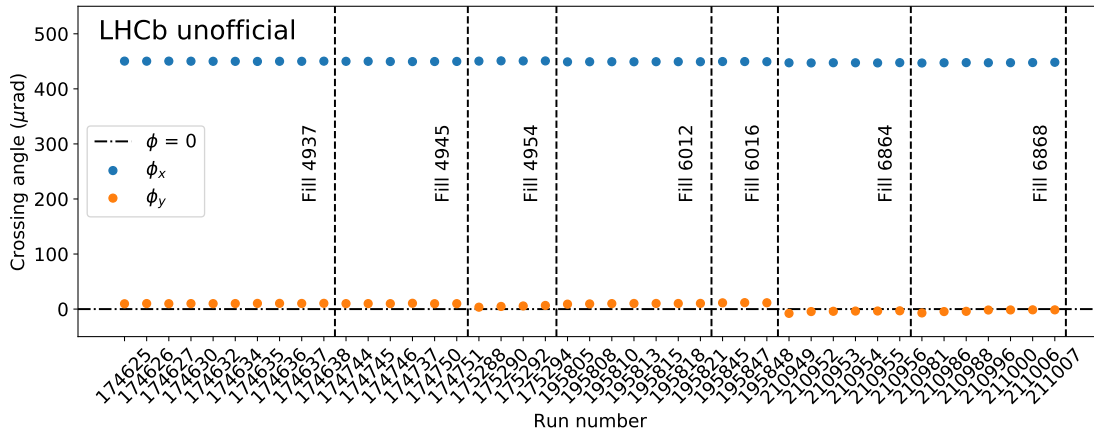


Figure 4.2: Half-crossing angle measurements for each run considered in this measurement.

where  $m_{i,a}$  is the slope of beam  $i$  in axis  $a$ . The half crossing angle provided by the LHC was nominally  $450 \mu\text{rad}$  in the  $x$ -axis and zero in the  $y$ -axis at LHCb for all of the calibration fills used in this measurement. The measured crossing angles for each run are shown in Figure 4.2. The average crossing angles measured in each fill are shown in Table 4.3.

Fill	$\phi_x$ ( $\mu\text{rad}$ )	$\phi_y$ ( $\mu\text{rad}$ )
4937	450.1	10.1
4945	449.8	10.0
4954	450.7	5.1
6012	449.2	9.9
6016	449.5	11.5
6846	447.3	-4.4
6868	447.6	-3.1

Table 4.3: Average crossing angles measured in each calibration fill.

### 4.3.3 Vertex resolution measurements

Knowledge of the vertex resolution is a critical element for determining the bunch profiles. The methodology for including the resolution in the fit models was given in Section 4.3.1. The procedure for determining the resolution models is described here. Vertex resolution models are determined separately in each of the  $x$ - and  $y$ -directions, applying a data-driven procedure directly to each sub-sample of the data (*i.e.* one bunch over one integration period).

#### 4.3.3.1 Determination with the split-vertex method

The vertex resolution is determined by a data-driven process known as the ‘split-vertex’ method. The tracks from each vertex are randomly divided into two subsets and a new ‘split’ vertex is fitted from each subset. An equal composition of tracks in each split vertex and from the A- and C-sides of the VELO is enforced at the splitting stage, up to possible differences when splitting an odd numbers of tracks. The split vertices’ positions can be written as

$$\begin{aligned} x_1 &= x_{\text{true}} + \delta_1 \\ x_2 &= x_{\text{true}} + \delta_2, \end{aligned} \tag{4.10}$$

where  $x_i$  and  $\delta_i$  are the measured position and offset from the true vertex,  $x_{\text{true}}$ , of vertex  $i$ . The resolution affecting each of the split vertices can be determined from the difference in their positions which has variance given by

$$\text{Var} \left( \frac{x_1 - x_2}{2} \right) = \text{Var} \left( \frac{\delta_1 - \delta_2}{2} \right). \tag{4.11}$$

The bunch profile can be fitted from the average position of the split vertices, which has variance

$$\begin{aligned} \text{Var} \left( \frac{x_1 + x_2}{2} \right) &= \text{Var} (x_{\text{true}}) + \text{Var} \left( \frac{\delta_1 + \delta_2}{2} \right) + 2 \text{Cov} \left( x_{\text{true}}, \frac{\delta_1 + \delta_2}{2} \right) \\ &\approx \text{Var} (x_{\text{true}}) + \text{Var} \left( \frac{\delta_1 + \delta_2}{2} \right). \end{aligned} \quad (4.12)$$

The last approximation assumes the split vertex offsets are independent of the true vertex position. The relationship between the resolution affecting the average position and that measured by the split-vertex method is given by

$$\text{Var} \left( \frac{\delta_1 + \delta_2}{2} \right) = \text{Var} \left( \frac{\delta_1 - \delta_2}{2} \right) + \text{Cov} (\delta_1, \delta_2). \quad (4.13)$$

The resolution measured from the difference between the split vertices can therefore be used to determine the bunch profiles under the assumption that the correlation between the split vertices can be neglected. Effects such as detector mis-alignments could induce possible correlations that break this assumption; corrections for such effects are discussed in Section 4.3.3.3. The distribution of average split vertex positions will have the same bunch profile as the fully reconstructed vertex positions, albeit convoluted with a different resolution distribution.

Figure 4.3 shows an example parameterisation of the beam-gas vertex resolution determined with the split-vertex method for each of the beams. The resolution affecting each of the split vertices is modelled in terms of the number of tracks entering each of the split vertices,  $n_{\text{Tr}}$ , as

$$R(n_{\text{Tr}}) = \frac{a}{n_{\text{Tr}}^b} + c. \quad (4.14)$$

The primary factor influencing the resolution is the number of tracks entering the vertex fit. There is also some dependence on the  $z$ -position of the vertex. These parameterisation fits are for illustration only, and are not used in the actual measurement.

The transverse vertex resolution is instead determined directly on each sub-sample of beam-gas vertices per colliding bunch pair, integration period and longitudinal bin (defined in Section 4.3.4). The resolution distribution is modelled using a triple-Gaussian sum in each axis. An example fit is shown in Figure 4.4. The

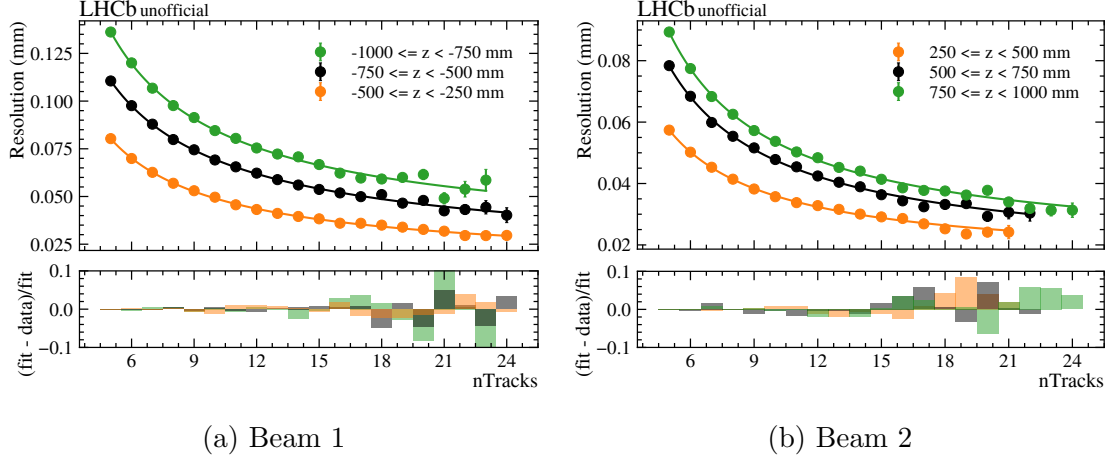


Figure 4.3: Beam-gas vertex resolution parameterisation in the  $x$ -axis for (a) beam 1 and (b) beam 2 for fill 4937, run 174630.

fitted width and weight parameters are then used as an input to the bunch profile fits as described in Equation 4.7. The vertex resolution in the longitudinal direction is neglected since the typical width of the luminous region is  $\mathcal{O}(40\text{-}50\text{ mm})$  while the width of the resolution distribution is  $\sim 0.1\text{ mm}$ .

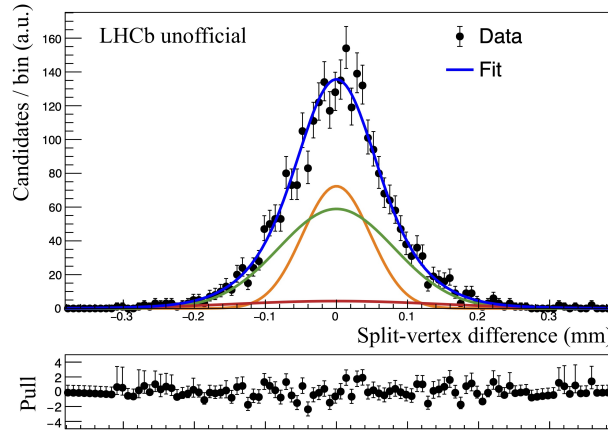


Figure 4.4: Example resolution fit from Fill 6868, Run 211007, BCID 1433 for a single  $z$ -bin in the  $y$ -axis. The fit model is composed of a sum of three Gaussian distributions, which are shown individually as the green, orange, and red curves. The total fit model is shown in blue.

#### 4.3.3.2 Differences with respect to previous measurements

The approach to parameterising the vertex resolution here differs from previous BGI measurements [97]. In previous measurements the resolution was parameterised in

terms of the number of tracks in each vertex using the split-vertex method, as shown in Figure 4.3. A set of correction factors was then computed to take into account variations of the resolution with longitudinal position within each bin. The assumption that the resolution was absolutely correct at the arbitrary point  $z = 0$  (in the LHCb co-ordinate system) was made at an intermediate step when deriving these correction factors. Based on the parameterisation and correction factors, a resolution was calculated for each vertex and a distribution of resolution values was created for each colliding bunch pair and integration period. A triple-Gaussian resolution model was constructed by binning this distribution and taking the fraction of events in each bin as that component's weight, with its width given by the average resolution of the vertices in the bin. A significant variation of the measured cross section with the beam-beam vertex resolution was observed. Combined with systematic uncertainties affecting the beam-gas resolution, the vertex resolution was the single largest uncertainty in the BGI Run 1 luminosity calibration with a value of 1.08% [121].

#### 4.3.3.3 Global correction factor on the vertex resolution

As mentioned in Section 4.3.3.1 the split-vertex method relies on the assumption that correlations between the offsets of the split vertices from the true vertex position can be neglected. If such correlations cannot be neglected we would expect to observe a dependence of the measured cross section on the vertex resolution. Practically this can be tested by binning the vertices in the longitudinal direction. The vertices are divided into 3 bins, defined by  $|z| \in [250, 500), [500, 750), [750, 1000)$  mm, for each beam. The innermost, middle and outermost sets of vertices from each beam are paired together. Vertices at large  $|z|$  typically suffer from worse resolution than those closer to the interaction region. Figure 4.5 shows a linear fit to the Vertex cross section as a function of the beam-gas vertex resolution in each fill, along with a comparison of the gradients measured in each fill. The calculation of the cross section is described in Section 4.4. The quality of some of the fits shown in Figure 4.5 is poor; the procedures and results presented here are a work in progress, and should thus be considered preliminary. A non-zero gradient is unambiguously observed, which indicates a bias in the split-vertex determination of the vertex resolution; such a bias is most likely attributable to the neglected correlations between the split-vertex offsets. In particular, the sign of the gradient indicates that the resolution is

underestimated.

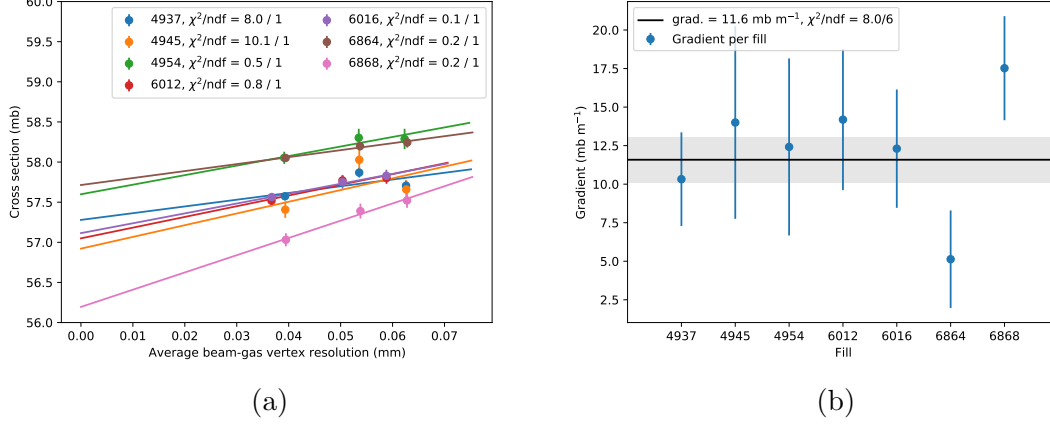


Figure 4.5: (a) Linear fit to the dependence of the Vertex cross section on the beam-gas vertex resolution in each fill, and (b) fit to the measured gradient across all fills.

As an additional test of the hypothesis that the beam-gas vertex resolution is underestimated we can compare the true resolution in a simulated sample with that measured by the split-vertex method. The true resolution is defined by the distribution of differences between the average split-vertex position and the true vertex position. The variance of the true resolution is given by

$$\text{Var} \left( \frac{x_1 + x_2}{2} - x_{\text{true}} \right) = \text{Var} \left( \frac{\delta_1 + \delta_2}{2} \right). \quad (4.15)$$

The split-vertex resolution is defined as in Equation 4.11. While simulation is generally not trusted to accurately reproduce absolute values of the vertex resolution, observing the same effect would nonetheless provide stronger evidence that an underestimate of the vertex resolution from the split-vertex method is indeed the cause of the variation of the cross section with the resolution. Figure 4.6 shows the split-vertex resolution versus the true resolution from simulation in each of the transverse axes. The split-vertex method is found to underestimate the resolution, in agreement with the effect observed in data. The simulated sample consists of minimum bias  $p\text{He}$  collisions originating from beam 1 (travelling towards the LHCb detector at the interaction point) with a beam energy of 6.5 TeV produced in 2016 *MagDown* conditions. No suitable simulation samples are available for beam 2. Since the simulation is intended only to confirm the effect observed in data without reproducing

the absolute correction, no attempt has been made to generate a suitable sample.

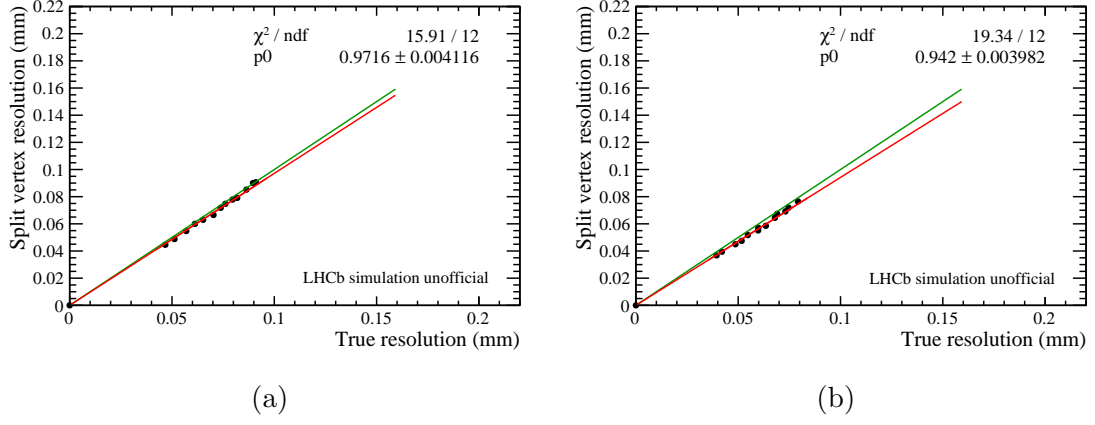


Figure 4.6: Split-vertex resolution versus true vertex resolution on a simulated 2016 pHe beam 1 sample for the (a)  $x$ -axis and (b)  $y$ -axis. The green line has a slope of unity and the slope of the red line is fitted to the measured values. Both lines pass through the origin.

To correct for the underestimation of the vertex resolution, we multiply each of the width parameters fitted using the split-vertex method by a single global scale factor. Figure 4.7 shows the gradient per-fill after applying this correction procedure, and the combined gradient across all fills with different correction factors. On the right plot, the first and last data point represent no correction and the smaller of the two corrections from simulation motivated by the gradients observed in Figure 4.6, respectively. The middle point represents a data-driven choice of correction factor such that the cross section is compatible with no dependence on the beam-gas vertex resolution. The final value of the correction factor is chosen to be 1.012, indicating that correlations between the split vertex offsets may induce a bias on the split-vertex method up to the percent level. One should note that the resulting bias on the beam widths — and thus the cross section — without this correction is below the percent level since the resolution enters as a convolution with the true beam profile.

#### 4.3.4 Transverse bunch profile fits

The transverse bunch profiles are fitted per-bunch in each integration period using the resolution measurements described in Section 4.3.3 as an input. For each beam the profile is determined by a simultaneous fit to beam-gas vertices with reconstructed longitudinal position in three bins defined by  $|z| \in$

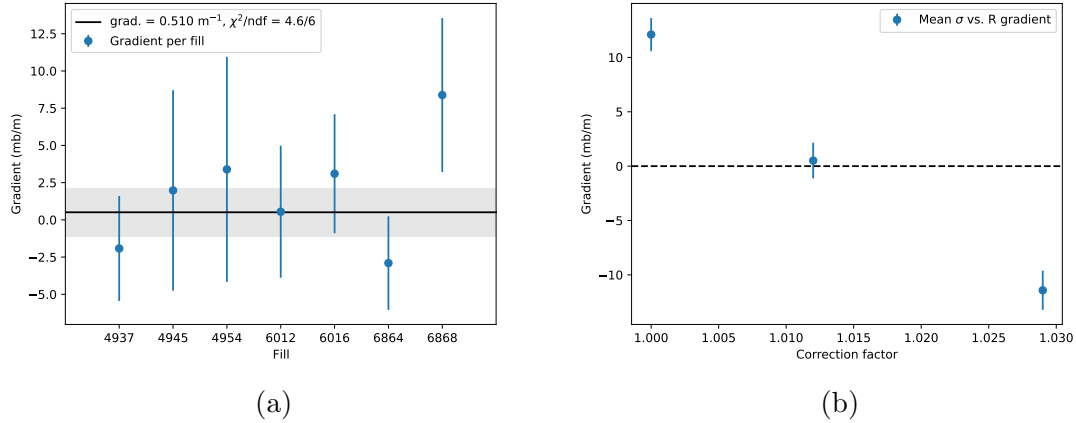


Figure 4.7: (a) Vertex cross section versus beam-gas resolution gradients after correction and (b) dependence of the combined gradient on the global resolution correction factor. On the right plot, the first and last data point represent no correction and the smaller of the two corrections from simulation motivated by the gradients observed in Figure 4.6, respectively. The middle point (also visible as the per-fill averaged grey band on the left plot) represents a data-driven choice of correction factor such that the cross section is compatible with no dependence on the beam-gas vertex resolution.

[250, 500), [500, 750), [750, 1000) mm. The transverse reconstructed co-ordinates of each vertex are projected to the central  $z$ -position in each bin using the beam slopes fitted for the crossing angle measurements; henceforth any discussion of the transverse co-ordinates refers to such projected values. The simultaneous fit in multiple regions reduces the impact of extrapolation errors by projecting all vertices to some central point. All fits are implemented as unbinned maximum likelihood fits using RooFIT [135].

#### 4.3.4.1 One-dimensional description of the bunch profiles

The simplest possible model constructed only of Gaussian components is a single Gaussian profile in each of the transverse axes. Such a model has no freedom to model correlations between the  $x$  and  $y$  co-ordinates of the bunch profiles. Figure 4.8 shows the overlap integral evaluated using a single Gaussian model for each colliding bunch pair and integration window. The measurement number index used throughout from here is sorted by time and then BCID. Variations of the overlap integral throughout each fill are observed and indicate an evolution of the bunch profiles in time.

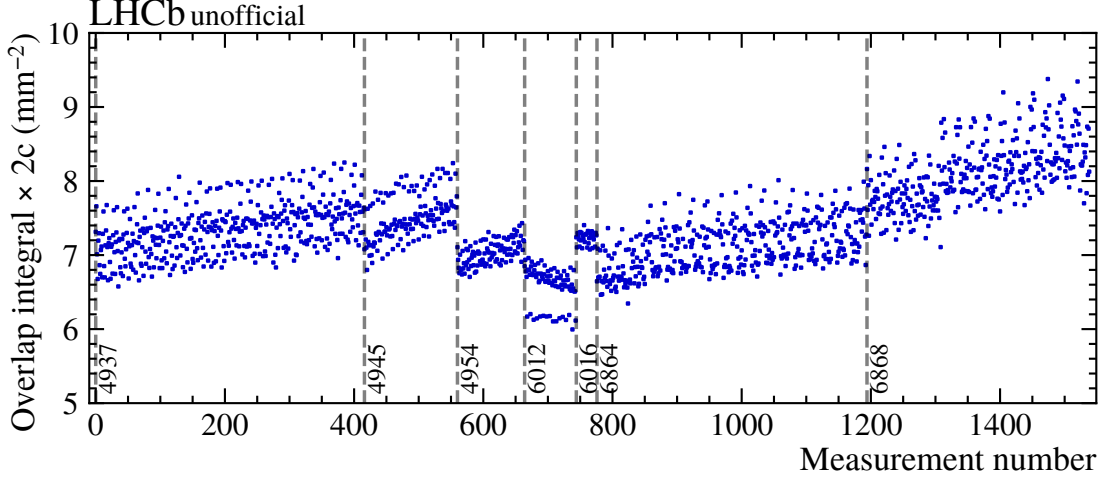


Figure 4.8: Overlap integral measurements assuming single Gaussian bunch profiles across all calibration fills per-BCID and integration period.

#### 4.3.4.2 Non-factorisable description of the bunch profiles

More generally the bunch profiles can be fitted using a two-dimensional parameterisation which allows for non-factorisability of the transverse axes. The bunch profiles are modelled using a Gaussian sum which can be written as

$$\rho(x, y) = \sum_{a=0}^n w_a g(x | \mu_a^x, \lambda_a^x) g(y | \mu_a^y, \lambda_a^y), \quad (4.16)$$

where all of the parameters have the same meanings as in Equation 4.7. This is equivalent to reducing the bunch profile component indices in Equation 4.7 to a single index. Such a model is non-factorisable by construction — so long as there is more than one non-zero weight and non-degenerate width — since cross terms between the different components in each axis are ignored. A triple-Gaussian model is used for the nominal analysis procedure. The effect of choosing a different model is studied in Section 4.3.6. The mean positions are parameterised as the mean of the bunch density at  $z = 0$ . In each of the bins,  $b$ , used in the fit the mean positions are calculated as (suppressing the axis superscript)

$$\mu'_b = \mu_b + m_i \langle z \rangle_b, \quad (4.17)$$

to account for the beam slopes, where  $m_i$  represents the gradient of beam  $i$  in the relevant axis against  $z$ , and  $\langle z \rangle_b$  is the centre of the bin in  $z$ . Each component

of the model has a separate mean parameter which allows more freedom to model correlations between the axes than a model with a single mean parameter per-axis. A total of 14 parameters are floated in each fit: 2 weights, 3 widths per-axis and 3 means per-axis. Figure 4.9 shows the overlap integral measured using this more general model. Figure 4.10 shows the ratio of overlap integrals measured with the single Gaussian model and the non-factorisable triple Gaussian model. The significant deviations of the ratio from unity highlight the importance of the non-factorisable description of the bunch profiles.

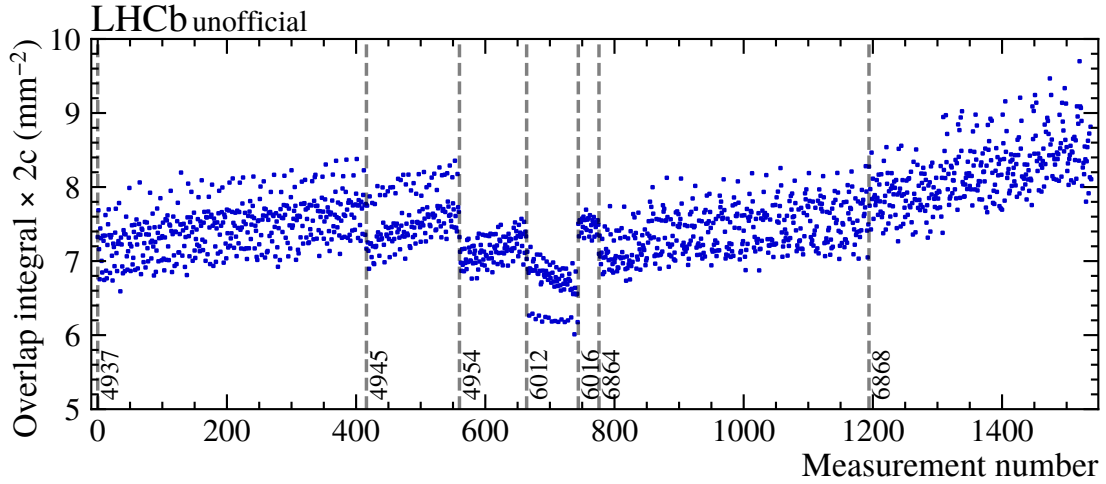


Figure 4.9: Overlap integral measurements assuming triple Gaussian bunch profiles across all calibration fills per-BCID and integration period.

### 4.3.5 Longitudinal bunch profile fits

No fine timing information is available on vertices reconstructed in the LHCb detector and therefore beam-gas vertices provide no sensitivity to the longitudinal bunch profiles. The longitudinal distribution of the luminous region is however related to the longitudinal profiles of the individual bunches and thus provides sensitivity to their convolved bunch lengths. Figure 4.11 illustrates the geometry of two colliding beams in the  $xz$ -plane. The crossing point,  $z_{RF}$ , is defined as the longitudinal position at which the longitudinal beam centres meet. This can be displaced from the centre of the luminous region,  $\mu_{z,l}$ , in the presence of an offset of the beams in either transverse plane. A temporal offset of the bunches will produce an equivalent effect to such a spatial offset. Assuming Gaussian bunch profiles in both the longitudinal

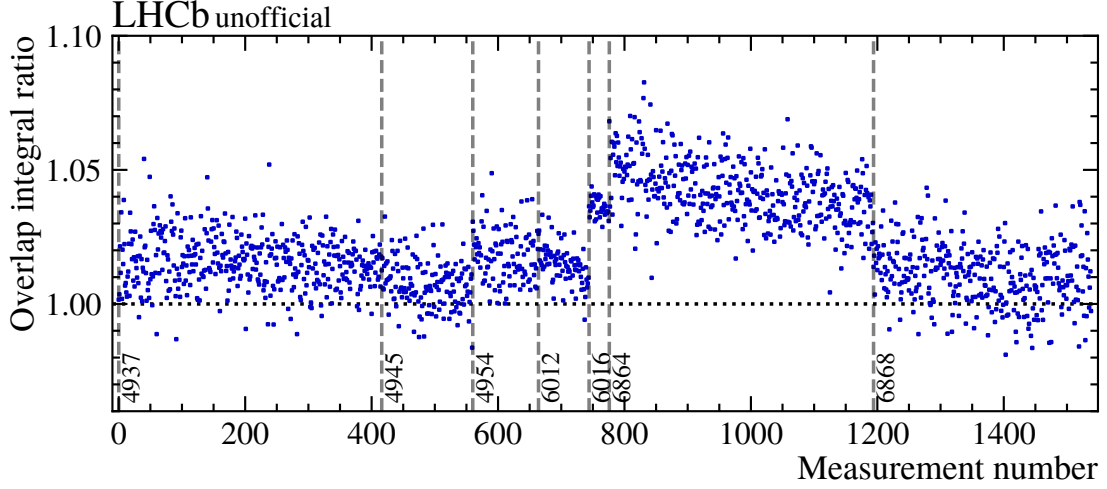


Figure 4.10: Ratio of overlap integral measurements assuming single Gaussian and triple Gaussian bunch profiles across all calibration fills per-BCID and integration period.

and transverse directions the mean position of the luminous region can be written as [134]

$$\mu_{zl} \approx z_{RF} - \frac{\lambda_z^2 - \lambda_x^2}{2\Sigma_x^2} \phi_x \Delta x. \quad (4.18)$$

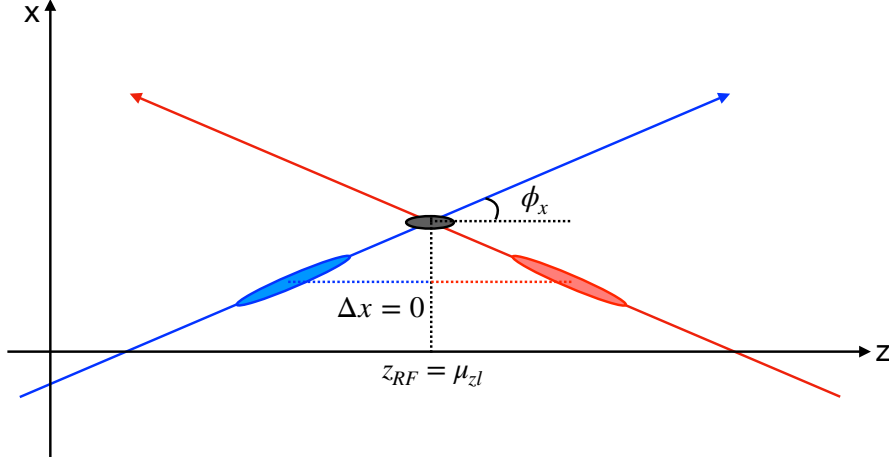
The above expression assumes no crossing angle in the  $y$ -direction and that the individual bunch widths in the  $x$ -direction are approximately equal. The width of the luminous region,  $\lambda_{zl}$ , can be written as [134]

$$\lambda_{zl} \approx \left( \frac{4}{\lambda_z^2} + \frac{\lambda_x^2 \phi_x^2}{\lambda_{x,1}^2 \lambda_{x,2}^2} \right)^{-\frac{1}{2}}, \quad (4.19)$$

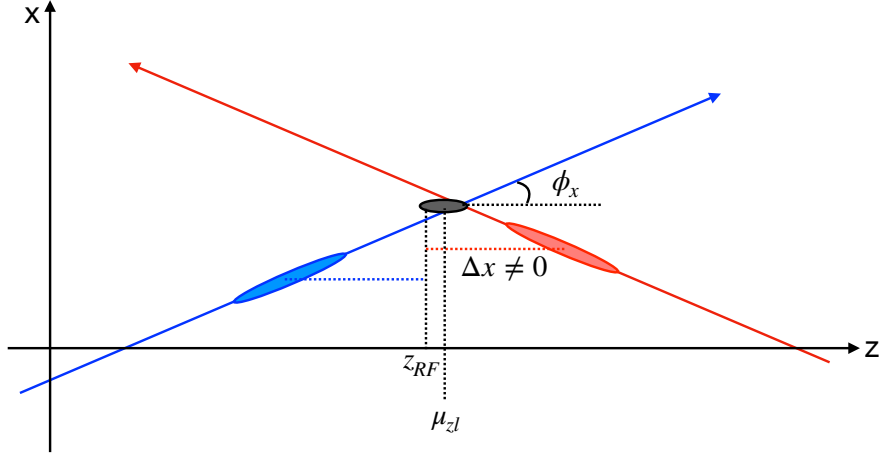
where the absence of a crossing angle in the  $y$ -direction is assumed.

A single Gaussian distribution is not sufficient to describe the transverse bunch profiles, as detailed in Section 4.3.4. Assuming factorisation of the longitudinal and transverse directions, the luminous region distribution can be constructed from all possible combinations of the individual Gaussian components for each beam and axis. The weight of each individual component is proportional to the contribution to the total overlap integral (or equivalently, the luminosity) which it provides (see Equation 4.8). This can be written as

$$\rho_{bb}(z) = \sum_{a,b,\alpha,\beta} w_{a,b}^1 w_{\alpha,\beta}^2 \mathcal{O}_{a,b,\alpha,\beta} g_{a,b,\alpha,\beta}(z), \quad (4.20)$$



(a) Luminous region geometry with head-on beams.



(b) Luminous region geometry with offset beams.

 Figure 4.11: Illustration of the luminous region geometry for beams colliding (a) without and (b) with an offset in the  $x$ -direction.

where the indices  $a, b$  ( $\alpha, \beta$ ) run over the  $x$ - and  $y$ -axis components of beam 1 (2), respectively. The term  $g_{a,b,\alpha,\beta}(z)$  represents a Gaussian distribution with mean and width given by Equations 4.18 and 4.19, respectively, taking the transverse parameters from the relevant single Gaussian components.

The acceptance of the LHCb VELO — and therefore the primary vertex reconstruction efficiency — is not constant in  $z$ . To account for this, each vertex is weighted in the fit by the inverse of its relative reconstruction efficiency. The reconstruction efficiency has been determined from simulation [97] and is shown in Figure 4.12 along with a linear interpolation between each pair of consecutive points used to determine the per-vertex weights. The efficiency map is scaled such that the maximum efficiency is unity to ensure all weights are  $\mathcal{O}(1)$ . No requirements

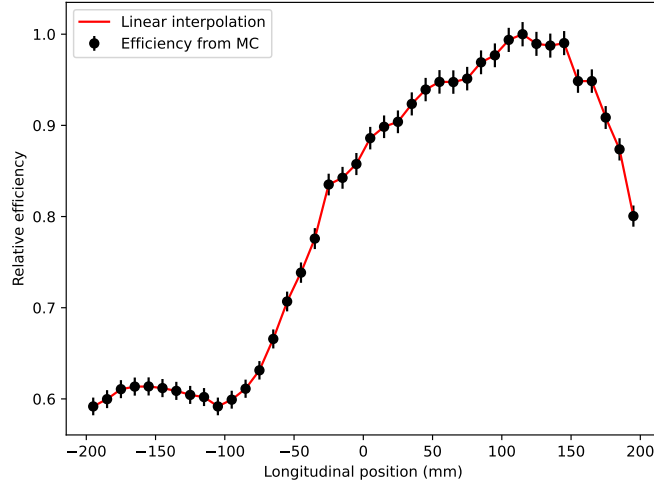


Figure 4.12: Relative vertex reconstruction efficiency as a function of longitudinal position from simulation [97].

are placed on the direction of tracks originating from each vertex; this avoids the efficiency falling to zero at large  $z$ . Figure 4.13 shows an example fit to the longitudinal luminous region shape. The split-vertex residual distribution, with a width of 0.076 mm, is also shown to motivate the assumption that the longitudinal resolution can be neglected. A small beam-gas background is potentially present below the peak due to the lack of a track-direction based selection. Such a background is negligible compared to the number of beam-beam vertices and thus ignored in the fit.

#### 4.3.6 Systematic uncertainties on the overlap integral

The detector alignment was found to induce a systematic uncertainty on the measurement of the crossing angle in the Run 1 BGI calibration [97, 121]. The effect of a biased crossing angle on the overlap integral is quantified by

$$\frac{d\mathcal{O}}{d\phi_x} \approx \frac{1}{4\pi c\Sigma_y} \left( \frac{d}{d\phi_x} \frac{1}{\Sigma_x} \right) = \frac{1}{4\pi c\Sigma_x\Sigma_y} \left( \frac{-\phi_x\lambda_z^2}{\Sigma_x^2} \right), \quad (4.21)$$

where all of the parameters are as defined in Section 4.3.1 and the effect of offset beams has been ignored. We neglect here also any effect of the crossing angle in the  $y$ -direction. It follows that the relative uncertainty on the overlap integral — and

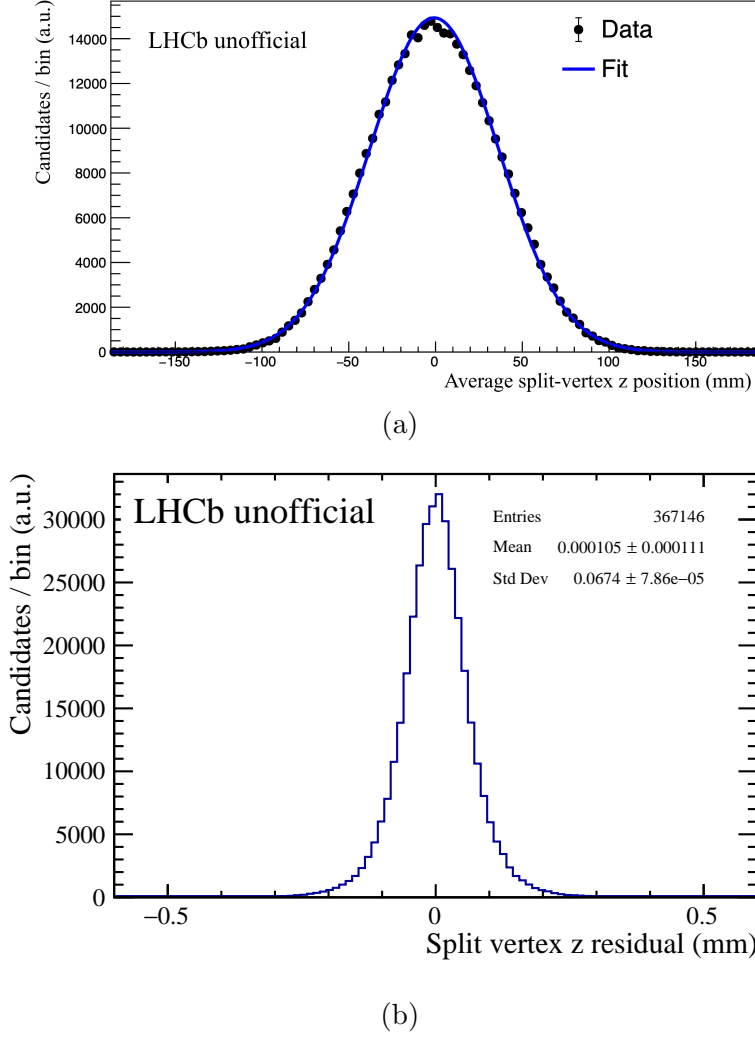


Figure 4.13: (a) Example fit to the luminous region vertex distribution and (b) split-vertex residual distribution for fill 4937, run 174626, BCID 222.

thus the cross section — is given by

$$\left| \frac{d\mathcal{O}}{\mathcal{O}} \right| \approx \left| \frac{\phi_x \lambda_z^2}{\Sigma_x^2} \right| d\phi_x. \quad (4.22)$$

The uncertainty on the half crossing angle,  $d\phi_x$ , is taken as the standard deviation of the measurements for each run. We find that  $d\phi_x = 1.2 \mu\text{rad}$  and  $d\phi_y = 6.4 \mu\text{rad}$ . Conservatively, we use the larger of the two values to compute the systematic uncertainty. The other parameters are taken as the average across all measurements. This results in a relative systematic uncertainty of 0.08%.

Statistical uncertainties on the vertex resolution are covered by the overall treatment of the statistical uncertainty on this measurement. The only other source of

uncertainty arises from the assumptions of the split-vertex method and the correction factor procedure. We repeat the correction procedure by adding an offset to each width — instead of multiplying by a scale factor — to test the assumption that the beam-gas vertex resolution should be corrected by a global scale factor. Figure 4.14 shows, as a function of the correction offset, the gradient of the cross section versus beam-gas vertex resolution. A value of  $1.2 \times 10^{-3}$  mm is chosen as the correction value. A shift of 0.50% in the Vertex cross section is observed compared to the correction using a scale factor and is taken as a systematic uncertainty due to the vertex resolution.

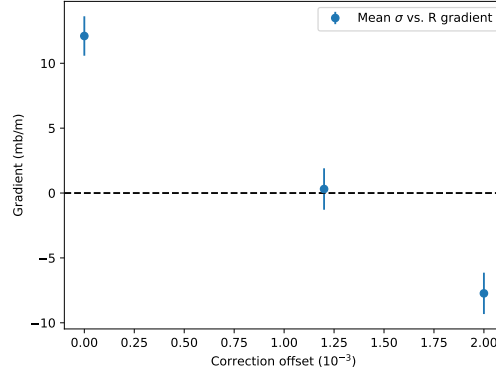


Figure 4.14: Dependence of the combined Vertex cross section versus beam-gas vertex resolution gradient across all fills on the resolution correction offset.

A systematic uncertainty on the fit model is assessed from the shift observed in the Vertex cross section when a different bunch profile model is assumed. We use the same model as in the nominal measurement — described in Equation 4.16 — taking  $w_2 = 0$ , *i.e.* reducing to a double Gaussian shape. A shift of 0.06 mb is observed, corresponding to a relative systematic uncertainty of 0.10%.

The measurement of the longitudinal bunch profiles only enters into the calculation of the overlap integral through the presence of either a crossing angle or offset beams. The effect of mis-modelling in the longitudinal direction on the overlap integral measurement is therefore heavily suppressed with respect to mis-modelling in the transverse directions. A conservative systematic uncertainty related to the longitudinal efficiency map is assigned by repeating the longitudinal fits with no efficiency applied. Shifts of  $\sim 5\%$  are observed in the convolved bunch length. The overall cross section measurement shifts by 0.12%, which is assigned as a systematic uncertainty.

The BGI method assumes that the bunch profiles and beam positions are stable over each integration window. Any drift of the beams during this time will artificially inflate the measured bunch widths. If the mean position of each beam drifts throughout a given integration period with some standard deviation,  $\lambda_{\text{drift}}$ , then the modification of the bunch width will be approximately given by

$$\lambda_{\text{obs}}^2 = \lambda_{\text{true}}^2 + \lambda_{\text{drift}}^2, \quad (4.23)$$

where  $\lambda_{\text{obs}}$  is the observed bunch width,  $\lambda_{\text{true}}$  is the true bunch width and a single Gaussian profile is assumed. The relative bias can then be estimated as

$$1 - \frac{\lambda_{\text{obs}}}{\lambda_{\text{true}}} = 1 - \sqrt{1 + \frac{\lambda_{\text{drift}}^2}{\lambda_{\text{true}}^2}} \approx -\frac{\lambda_{\text{drift}}^2}{2\lambda_{\text{true}}^2}. \quad (4.24)$$

To evaluate the size of the effect, the mean position of each beam in each axis is measured in 30 s time intervals throughout each run, integrated across all filled BCIDs. Figure 4.15 shows an example of such a measurement for a single run. To indicate the size of this effect, both plots show the same data but the length of the vertical axis on the right plot corresponds to around half of the bunch widths. Each run lasts up to 1 hr, *i.e.* 4 full integration periods, so this is viewed as a conservative choice. The average drift across each beam, axis and run is found to be  $4.1 \mu\text{m}$ . Assuming a beam width of  $0.10 \text{ mm}$ — the average over  $x$  and  $y$  of bunch width across all single Gaussian bunch profile measurements — results in a relative bias of  $0.09\%$ . Since a beam drift will only increase the measured beam widths, this is correlated between the two beams. A systematic uncertainty on the final cross section is therefore taken as the resulting bias — given this correlation — on the product of two beam widths, which is calculated to be  $0.18\%$ . No attempt is made to subtract the expected spread from statistical fluctuations alone, which is again a conservative choice.

The electromagnetic interactions between protons from opposite colliding bunch pairs contributes one of the largest systematic uncertainties in the vdM analysis [121]. Changes in the beam-beam force due to movements of the beams at any interaction point on the LHC ring can dynamically modify the bunch profiles and therefore bias the BGI measurement. To evaluate the importance of this effect, the cross section is measured with BCIDs split into four categories depending on at which interaction points they collide. This is shown in Figure 4.16. The results

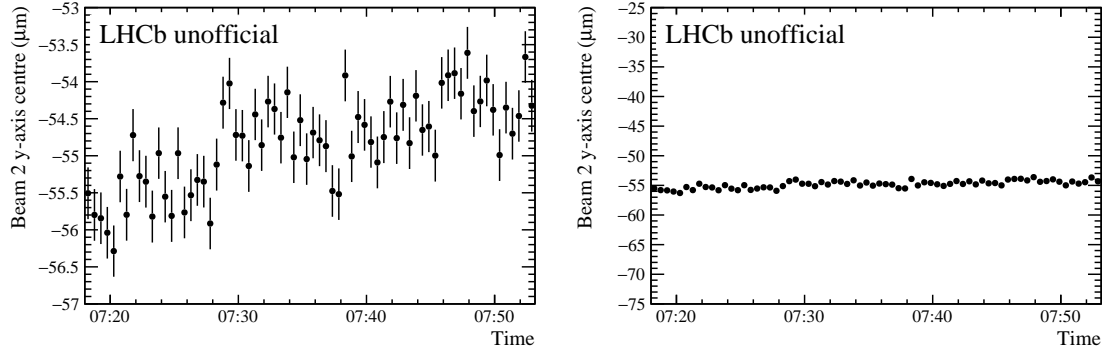


Figure 4.15: Example beam drift measurement for the  $y$ -axis of beam 2 in fill 6868, run 211007, integrated across all BCIDs. The same data is shown on both plots, however the length of the  $y$ -axis scale on the right plot corresponds to around half the transverse bunch widths during luminosity calibration fills to indicate the size of this effect.

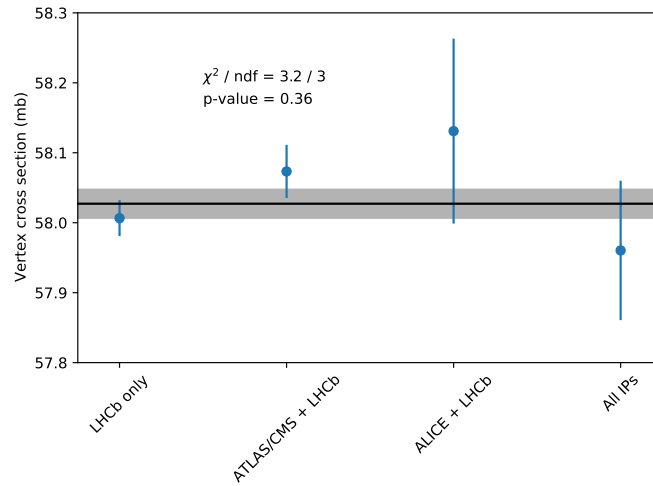


Figure 4.16: Cross section measurements split by interaction points at which each BCID collides.

across all samples are statistically compatible. Therefore, no systematic uncertainty is assigned.

## 4.4 Final cross section determination

The cross section is determined per bunch and integration periods based on the results of the previous sections. The cross section is given by

$$\sigma_c = \frac{\mu_c}{2cN_1N_2\mathcal{O}}, \quad (4.25)$$

where all parameters are as defined in Chapter 3. A total cross section for each BCID is obtained from a weighted average of the individual integration periods. The weighted average used the length of each integration period as a weight; this implicitly assumes the rate of beam-gas vertices is stable throughout each fill. Figure 4.17 shows an example of the beam-gas trigger rate throughout fill 4937 for each beam; good stability is observed. A total cross section per-fill is obtained by averaging the cross section measured per-BCID. This assumes that the beam-gas rates for each individual BCID are equal. Figure 4.18 shows the number of selected vertices integrated over 5 minute periods for each colliding BCID throughout an example run, normalised to the average value. While not a perfect assumption, the rate of vertices per-BCID is generally stable with a spread of a few percent. The final measured cross section is obtained from a least squares fit to the per-fill cross section using the standard statistical error only. Figure 4.19 shows the results for each individual measurement and the final combination across all fills. A final measurement of

$$\sigma_{\text{Vertex}} = 58.00 \pm 0.02 \text{ mb}$$

is obtained, where the error is statistical only. The individual fill measurements are not statistically compatible, and a systematic uncertainty to account for this is detailed below. Figure 4.20 shows each individual cross section measurement per BCID and per integration period. Figure 4.21 shows the evolution of the BCID-averages of all of the quantities entering into the cross section calculation throughout each of the calibration fills. Good stability of the measured cross section is observed throughout each fill. Figure 4.22 shows the individual cross section measurements using the single Gaussian model to again highlight the importance of modelling the non-factorisability of the bunch shapes. Significant differences are observed between the different fills, along with instabilities in time within each fill.

Table 4.4 summarises the uncertainties affecting this measurement. Most of

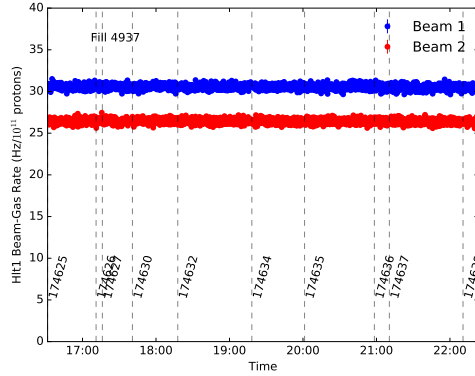


Figure 4.17: Rate of positive trigger decisions for the Hlt1BeamGasBeam{1,2} trigger lines throughout fill 4937 per  $10^{11}$  protons in each beam (roughly corresponding to one bunch).

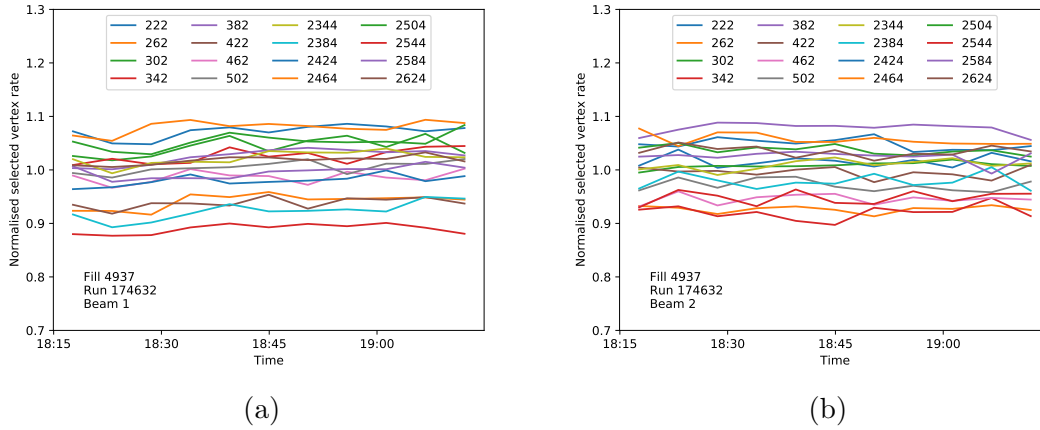


Figure 4.18: Example rate of selected beam-gas vertices integrated over 5 minutes for each BCID colliding at LHCb over an example run. Plots (a) and (b) show the rate of vertices for beams 1 and 2, respectively.

these have already been discussed in Sections 3.2.3, 3.4.3 and 4.3.6. The column labelled ‘Contribution’ indicates the reduction in the total uncertainty if the relevant component is removed. The measurements of the cross section are not statistically compatible between all of the calibration fills. This is believed to be due to mis-modelling of the bunch profiles by assuming only combinations of Gaussian distributions. An additional systematic uncertainty is assigned based upon the spread of the measurements. The value is taken as the largest standard deviation when the measurements are combined per-fill (0.29%), per-run (0.29%) and per-BCID (0.45%); the latter two are illustrated in Figure 4.23. The standard deviations are calculated from an unbinned maximum likelihood fit of a Gaussian distribution to

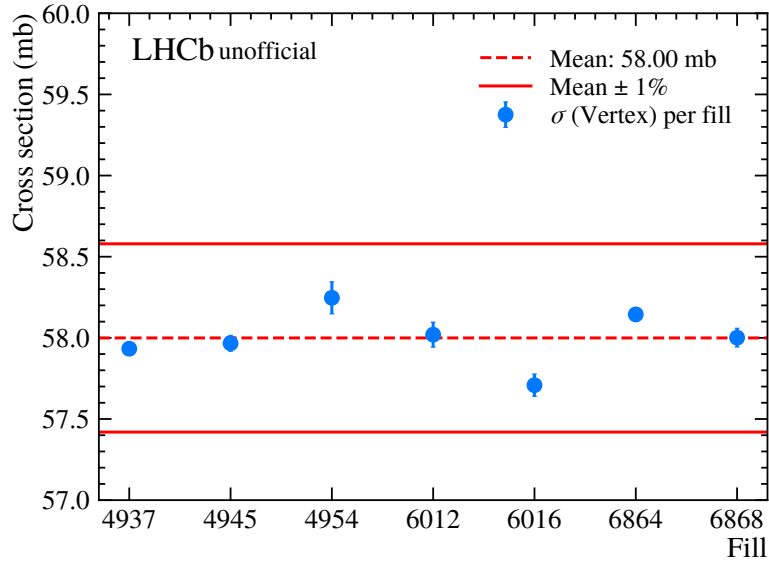


Figure 4.19: Measured cross section per-fill with statistical uncertainties only.

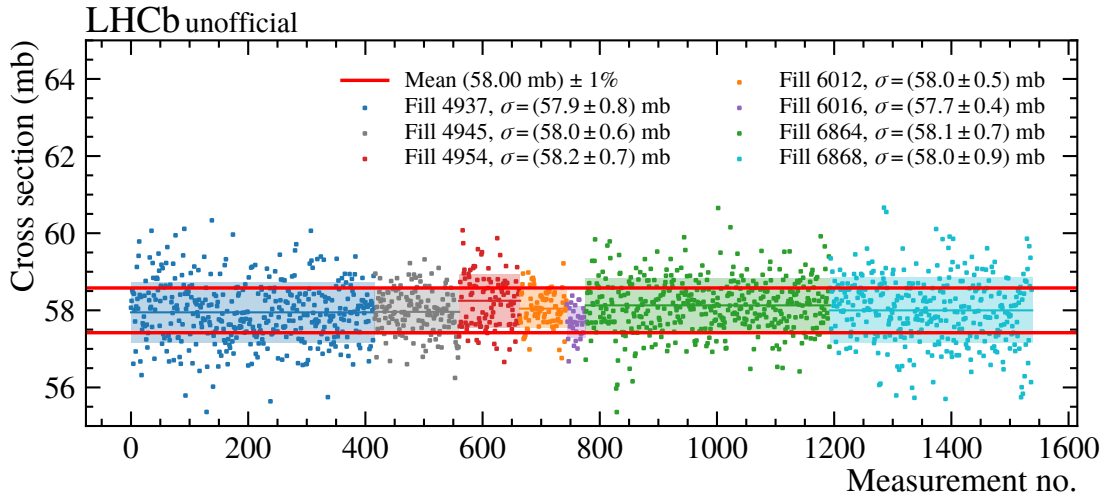
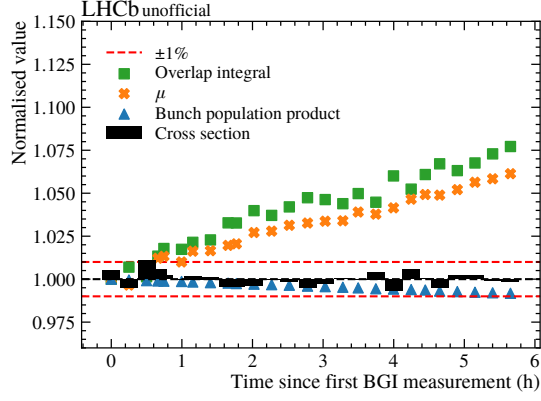
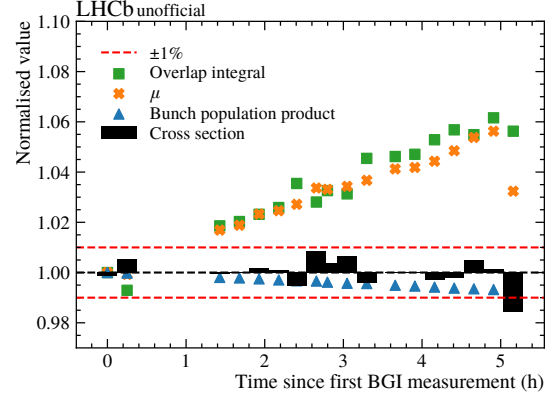


Figure 4.20: All cross section measurements using the triple Gaussian bunch profile model.

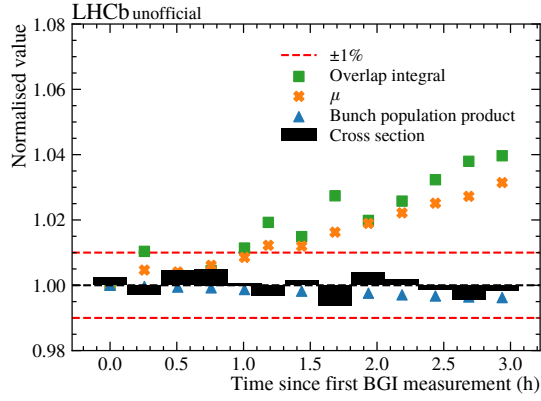
each set of cross section measurements. Uncertainties due to a possible pressure gradient within the beam volume and absolute scale errors arising from the VELO are taken from Ref. [121].



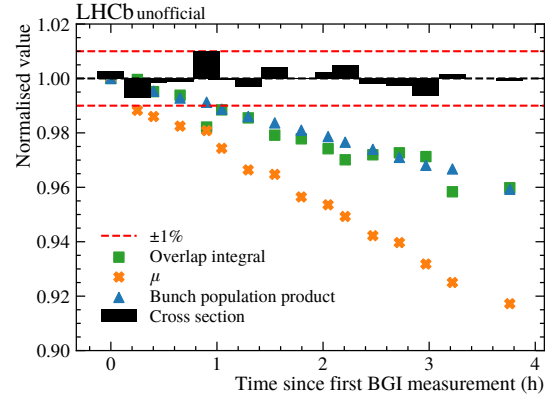
(a) Fill 4937



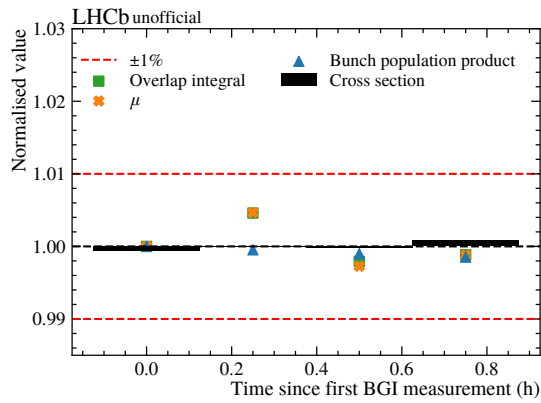
(b) Fill 4945



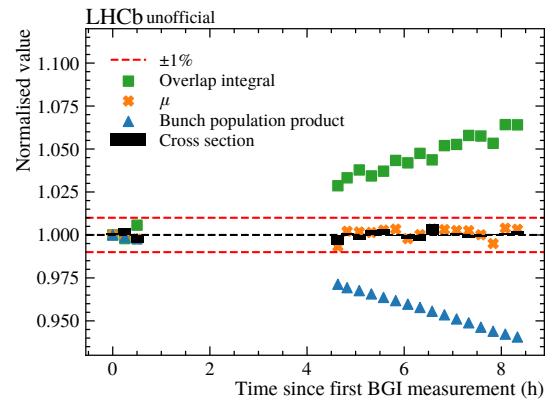
(c) Fill 4954



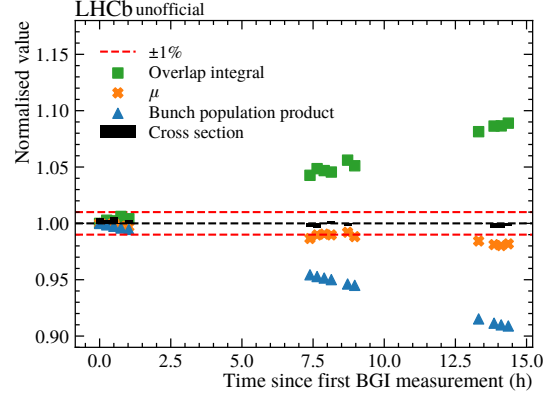
(d) Fill 6012



(e) Fill 6016



(f) Fill 6864



(g) Fill 6868

Figure 4.21: Time evolution of quantities entering the cross section calculation for each fill, averaged over all BCIDs. The cross section values are normalised to their mean value; all other quantities are normalised to their first value.

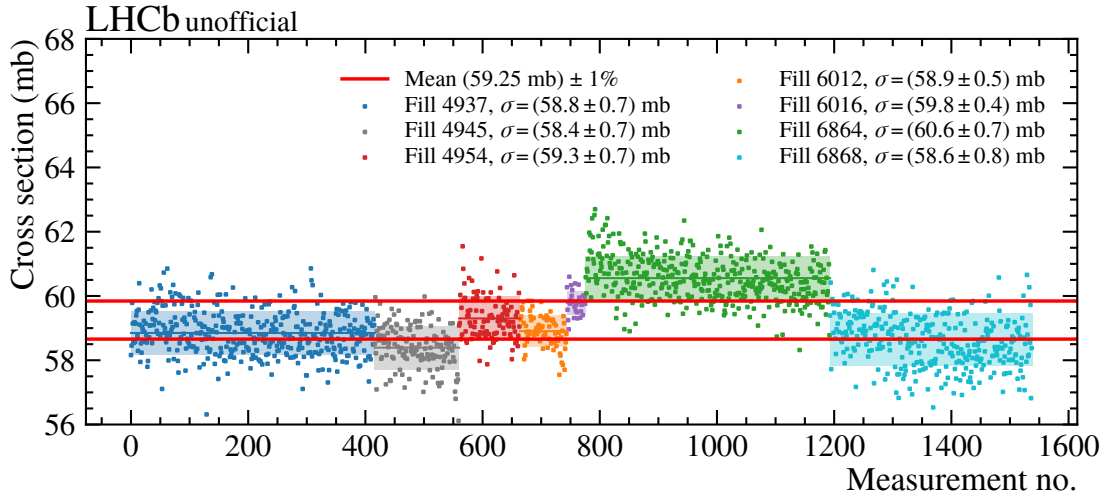
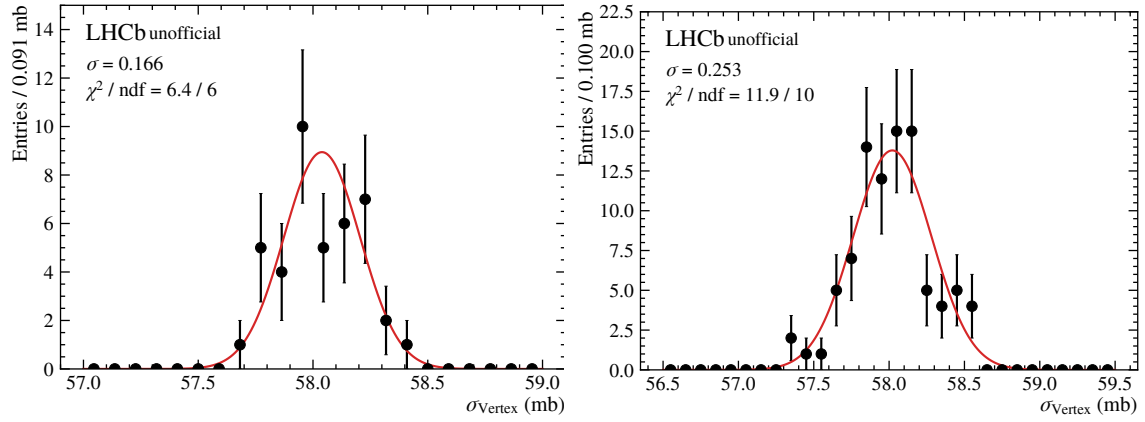


Figure 4.22: All cross section measurements using the single Gaussian bunch profile model.



(a) Cross section spread per-run.

(b) Cross section spread per-BCID.

Figure 4.23: Measurement spread of the cross section averaged across (a) individual runs and (b) individual bunches.

Source	Relative uncertainty (%)	Contribution (%)
Vertex resolution	0.50	20.2
Measurement spread	0.45	16.0
DCCT uncertainty	0.34	8.8
Track/Vertex ratio	0.22	3.6
Beam drift	0.18	2.4
Longitudinal efficiency	0.12	1.1
Fit model	0.10	0.8
Crossing angle	0.08	0.5
Satellite charge	0.05	0.2
VELO transverse scale	0.05	0.2
Ghost charge	0.04	0.1
Pressure gradient	0.03	0.07
Statistical	0.03	0.07
FBCT non-linearity	0.03	0.07
FBCT/BPTX difference	0.02	0.03
Counter background subtraction	0.01	0.01
Total	0.83	-

Table 4.4: Summary of the relative size of uncertainties affecting the absolute BGI calibration. The column labelled ‘Contribution’ indicates the reduction in the total uncertainty if the relevant component is removed

## 4.5 Summary

An absolute luminosity calibration of the LHCb Track and Vertex counters has been presented. A final result of

$$\sigma_{\text{Vertex}} = 58.00 \pm 0.02 (\text{stat}) \pm 0.48 (\text{syst}) \text{ mb}$$

is obtained. Combined with the measured ratio of the background-corrected Track to Vertex counters,  $1.099 \pm 0.002$ , this gives a cross section for the Track counter of

$$\sigma_{\text{Track}} = 63.74 \pm 0.02 (\text{stat}) \pm 0.53 (\text{syst}) \text{ mb}.$$

The final relative precision of this measurement is 0.83%. The dominant systematic uncertainties arise from the vertex resolution corrections, measurement spread — believed to be related to mis-modelling of the transverse beam profiles — and bunch current measurements. The dominant part of the uncertainty is entirely uncorrelated from the vdM method, and thus the precision can be further improved through a combination of the two analyses.

# Selection of $D^0 \rightarrow h^- \pi^+ \pi^0$ candidates

---

SEPARATING candidates of the signal decay of interest from any potential sources of background is an important aspect of any particle physics measurement. This chapter will describe the specific selection requirements applied to the 2012 and 2015–18 LHCb datasets to retain as many signal candidates in the  $D^0 \rightarrow h^- \pi^+ \pi^0$  decays as possible, while suppressing both physics and combinatorial backgrounds. ‘Physics’ backgrounds are defined as those originating from a similar physical process which mimics the decay of interest in some fashion, while ‘combinatorial’ background is comprised of random combinations of particles produced in potentially many separate decays which mimic the decay of interest. A number of kinematic variables which are commonly used within the LHCb collaboration to distinguish signal decays from any relevant backgrounds are defined in Section 5.1. The remainder of the chapter is dedicated to describing the specific requirements imposed for this analysis.

## 5.1 Definitions of kinematic variables

In addition to the standard kinematic variables such as mass,  $m$ , momentum,  $p$ , and energy,  $E$  (and the transverse components,  $p_T$  and  $E_T$ ), it is useful here to introduce some variables which are widely used within LHCb analyses.

The impact parameter ( $IP^1$ ) is defined as the minimum distance of closest approach (DOCA) of an extrapolated track to some point, most commonly the ‘best’ PV. For particles with no track, such as an indirectly measured  $D^0$  candidate, the

---

<sup>1</sup>The initialism is shared with ‘interaction point’, but the distinction should be clear from context.

IP is calculated from the kinematics of the daughter particles. A related variable,  $\chi_{\text{IP}}^2$ , is defined as the difference in the vertex fit  $\chi^2$ ,  $\chi_{\text{vtx}}^2$ , of the best PV fit with and without a given track or particle included in the fit. The best PV is typically defined as the PV with the smallest  $\chi_{\text{IP}}^2$  for a given track or particle. The flight distance (FD) of a particle is defined as the distance between its decay and production vertices. The parameter  $\chi_{\text{FD}}^2$  represents the  $\chi^2$  of the hypothesis that a given particle has no flight distance, *i.e.* decays at its production vertex. Each of these quantities are particularly useful for selecting displaced vertices originating from  $b$ - and  $c$ -hadron decays.

Another key selection requirement is enhancing the rate of ‘real’ tracks with respect to ghost tracks or real tracks with incorrect matching upstream and downstream of the magnet. The quality of the track fit is typically defined in terms of a  $\chi^2$  value,  $\chi_{\text{track}}^2$ . A ‘ghost probability’ for each track is defined based on the output of a neural network. The neural network takes as input various parameters of the track, its constituent hits, and the tracking detectors’ occupancies [136].

Physical backgrounds from mis-identified backgrounds are suppressed using the PID techniques described in Section 2.2.9. The difference in log-likelihood approach defines a set of variables expressed as  $\text{PID}x$ , where  $x$  is the particle hypothesis under consideration. A  $\pi^0$  candidate confidence level (CL) is defined based on particle-identification neural-networks and the presence of, or lack thereof, a track compatible with the calorimeter cluster(s).

Finally, some variables which are useful to suppress combinatorial backgrounds can be defined. The output of a MatrixNet classifier — taking as input kinematic and vertex quality variables — is used to select two-track vertices where both tracks truly originated in the same decay. The direction angle (DIRA) of a particle is defined as the angle between its momentum and the vector relating its production and decay vertices. In partially reconstructed decays, a corrected mass can be defined as  $m_{\text{corr}} = \sqrt{m^2 + p_{\perp, \text{miss}}^2} + |p_{\perp, \text{miss}}|$ , where  $m$  is the invariant mass of the reconstructed decay products, and  $p_{\perp, \text{miss}}$  is the missing momentum of the decay products perpendicular to the parent particle’s flight direction. The parameter  $\chi_{\text{DOCA}}^2$  is the  $\chi^2$  value of the hypothesis that two tracks or particles originate from the same vertex.

## 5.2 Event selection and reconstruction

For this analysis, events where a  $D^0$  candidate is reconstructed in either of the decays  $D^0 \rightarrow \pi^+ \pi^- \pi^0$  or  $D^0 \rightarrow K^- \pi^+ \pi^0$  are selected. The  $D^0$  meson is required to originate from the strong decay  $D^*(2010)^+ \rightarrow D^0 \pi_{\text{tag}}^+$ , where the  $D^{*\pm}$  meson is produced promptly, *i.e.* in the initial  $pp$  collision. The charge of the tagging pion is used to infer the flavour of the  $D^0$  meson at production. The data sample is divided into two categories based on the reconstruction of the  $\pi^0 \rightarrow \gamma\gamma$  decay in the final state: resolved events are defined as those in which the photons are detected as independent ECAL clusters, while merged events are defined as those in which the photon clusters overlap and cannot be completely disentangled. Photons are reconstructed by the LHCb detector by considering  $3 \times 3$  clusters of ECAL cells, centred on local maxima of deposited energy, as described in Section 2.2.7.1. Data collected in 2012, and between 2015 and 2018 by the LHCb experiment is analysed. A suitable HLT2 trigger line for the decay modes studied here in Run 1 was not implemented until 2012, and so data from 2011 is not analysed.

Year(s)	HLT1 line(s)
2012	D_Hlt1TrackAllL0
2015-18	D_Hlt1TrackMVA
	D_Hlt1TwoTrackMVA

Table 5.1: HLT1 lines used in this analysis.

Year(s)	HLT2 line(s)
2012	Dstr_Hlt2CharmHadD02HHXDst_hhX
2015-18	Dstr_Hlt2CharmHadInclDst2PiD02HHXBDT
	Dstr_Hlt2CharmHadDstp2D0Pip_D02(PimPipPi0/KmPipPi0)_Pi0(M/R)

Table 5.2: HLT2 lines used in this analysis.

### 5.2.1 Trigger selection

No explicit requirements are imposed at the L0 trigger level. It was shown in a previous analysis that all available lines provide some contribution for the decay modes studied here [137]. The HLT requirements applied are listed in Tables 5.1 and 5.2. Where multiple lines are listed for a given trigger level and period,

events are only required to pass at least one of the lines. In all cases a positive triggered-on-signal (TOS) decision is required. For data collected in 2012, the trigger line Hlt1TrackAllL0 selects a daughter of the  $D^0$  meson with a track which is displaced from the primary vertex (PV), has high  $p_T$ , and a good quality track fit. For data collected in Run 2, the trigger line Hlt1TrackMVA essentially replaces the Hlt1TrackAllL0 line. In addition to requirements on track quality, the Hlt1TrackMVA line requires that each track satisfies the expression (using  $p_T$  in units of GeV/ $c$ )

$$[(p_T > 25) \text{ AND } (\chi_{\text{IP}}^2 > 7.4)] \text{ OR } [(1 < p_T < 25) \text{ AND } (\chi_{\text{IP}}^2 > F(p_T; \lambda))], \quad (5.1)$$

where

$$F(p_T; \lambda) = \ln(7.4) + \frac{1}{(p_T - 1)^2} + \lambda \left(1 - \frac{p_T}{25}\right). \quad (5.2)$$

The parameter  $\lambda$  took on different values in the range (1.1,2.3) during Run 2, depending on the trigger configuration. The Hlt1TwoTrackMVA line allows for the single track requirements to be loosened, and additional requirements on a vertex fit to the pair of charged tracks from candidate  $D^0$  meson decays are imposed. A detailed list of the requirements imposed by each trigger line is provided in Table 5.3. Where multiple cut values are given, the trigger requirements fluctuated depending on the trigger configuration. The MatrixNet variable used by the Hlt1TwoTrackMVA line is a classifier trained to identify signal-like events based on vertex quality and  $p_T$  information [138].

For data collected in 2012, candidates are required to pass the Dstr\_Hlt2CharmHadD02HHXDst\_hhX trigger line at HLT2 level. This line partially reconstructs the  $D^{*\pm}$  meson by combining two charged hadrons from a candidate  $D^0$  decay with a candidate tagging pion. Trigger lines for exclusively selecting the final states considered here were not implemented in Run 1. The requirements of this trigger line are listed in Table 5.4. Here and throughout the following, selections on particles denoted  $h^\pm$  apply only to the  $D^0$  meson decay products and not the tagging pion. As before, an entry with multiple cut values indicates that the trigger configuration changed over time. In Run 2, candidates must pass either the inclusive Dstr\_Hlt2CharmHadInclDst2PiD02HHXBDT trigger line, or one of the exclusive Dstr\_Hlt2CharmHadDstp2D0Pip\_D02(PimPipPi0/KmPipPi0)\_Pi0(M/R) trigger lines, where the latter depends on the final state and  $\pi^0$  reconstruction

Trigger	Object	Quantity	Requirement
Hlt1TrackAllL0	Track	VELO hits	$> 9$
		VELO missing hits	$< 3$
		$\chi^2/\text{ndf}$	$< 1.5, 2$
		$p$	$> 3, 10 \text{ GeV}/c$
		$p_T$	$> 1.6, 1.7 \text{ GeV}/c$
		$\chi_{\text{IP}}^2$	$> 16$
Hlt1TrackMVA	Track	$p_T, \chi_{\text{IP}}^2$	see Equations 5.1 and 5.2
		$\chi^2/\text{ndf}$	$< 2.5$
		ghost probability	$< 0.2, 0.4$
		$p$	$> 3, 5 \text{ GeV}/c$
		$\chi^2/\text{ndf}$	$< 2.5$
Hlt1TwoTrackMVA	Both tracks	ghost probability	$< 0.2, 0.4$
		$p$	$> 3, 5 \text{ GeV}/c$
		$p_T$	$> 0.5, 0.6 \text{ GeV}/c$
		$\chi_{\text{IP}}^2$	$> 4$
		$\eta$	$\in [2, 5]$
	Vertex	$m_{\text{corr}}$	$> 1 \text{ GeV}/c$
		MatrixNet	$> 0.95, 0.97$
		$p_T$	$> 2 \text{ GeV}/c$
		$\chi_{\text{vtx}}^2$	$< 10$
		DIRA	$< \pi/2$

Table 5.3: Selection requirements for the HLT1 lines used in this analysis.

category under consideration. The former line is based upon a bonsai-BDT classifier, which is an efficient BDT implementation that takes discrete inputs given by coarsely binning the input variables [139]. The bonsai-BDT takes as input the following variables: the  $D^0$  meson's flight distance and  $\chi_{\text{vtx}}^2$ , the  $D^*$  meson's flight distance (2015 only) and direction angle (DIRA), the  $p_T$  and helicity angle,  $\cos(\theta)$ , of the tagging pion, and the sum of the charged  $D^0$  daughters'  $p_T$ . The exclusive trigger line fully reconstructs the decay chain, and its requirements are given in Table 5.5.

### 5.2.2 Stripping selection

The stripping lines used for both the Run 1 and Run 2 samples are listed in Table 5.6. The stripping selections are identical for both sets of lines, and are listed in Table 5.7. The selections for the signal and control channels are identical, with the exception of cuts on the PID variables. Each event is also required to have fewer than 180 long tracks.

Particle(s)	Quantity	Requirement
$h^\pm$	track $\chi^2/\text{ndf}$	$< 3$
	$p_T$	$> 0.3 \text{ GeV}/c$
	$p$	$> 3 \text{ GeV}/c$
	$\chi_{\text{IP}}^2$	$> 6$
	$m$	$< 2.1 \text{ GeV}/c^2$
$h^+ h^-$ combination	$\sum p_T$	$> 0 \text{ GeV}/c$
	DOCA	$< 0.1 \text{ mm}$
	FD	$> 0 \text{ mm}$
	$m_{\text{corr}}$	$< 3.5 \text{ GeV}/c$
	$\chi_{\text{FD}}^2$	$> 100$
	DIRA	$> 0.99$
	$\chi_{\text{vtx}}^2/\text{ndf}$	$< 10$
	track $\chi^2/\text{ndf}$	$< 2.25$
$h^+$ or $h^-$	$\chi_{\text{IP}}^2$	$> 36$
	track $\chi^2/\text{ndf}$	$< 2.25$
	$p_T$	$> 0.3 \text{ GeV}/c$
	$p$	$> 3 \text{ GeV}/c$
$\pi_{\text{tag}}^\pm$	$\chi_{\text{IP}}^2$	$< 9$
	$h^+ h^- \pi_{\text{tag}}^\pm$ combination	DOCA $< 100 \text{ mm}$
	$D^{*\pm}$	$p_T > 3500, 3750, 3850 \text{ GeV}/c$
$h^+, h^-, \pi_{\text{tag}}$	$m_{hh\pi_{\text{tag}}} - m_{hh}$	$\in [0, 250], [0, 285] \text{ MeV}/c^2$

Table 5.4: Selection requirements for the Dstr.Hlt2CharmHadD02HHXDst.hhX trigger line.

### 5.2.3 Offline selection and reconstruction

For events which pass the trigger and stripping selections, the DECAYTREEFITTER (DTF) algorithm [140] is used to reconstruct each event with the following constraints: the  $\pi^0$  meson's mass is taken as equal to its known value from the Particle Data Group (PDG), and the  $D^{*\pm}$  meson must be produced exactly at the PV. In particular, this procedure significantly improves the resolution of the  $D^0$  and  $D^{*\pm}$  masses, their difference  $\Delta m \equiv m(D^{*+}) - m(D^0)$ , and the  $D^0$  decay time. This is illustrated for the latter two variables in Figure 5.1.

We impose a simple offline pre-selection which is described in Table 5.8. Separate selections are imposed for merged and resolved candidates due to their differing kinematics. The same pre-selection is used for both the signal and control channels. Requirements on the  $\chi_{\text{IP}}^2$  of the  $D^0$  meson and the  $\chi_{\text{FD}}^2$  of the  $D^{*\pm}$  meson reduce contamination from decays where the  $D^{*\pm}$  is produced in the decay of a  $B$  meson, rather than in the initial  $pp$  collision. Such events are known as secondary decays.

Particle(s)	Quantity	Requirement
$h^+ h^-$ combination	DOCA	$< 0.08$ mm
	$m$	$< 1.9$ GeV/ $c$
	$\chi_{\text{vtx}}^2$	$< 20$
	$\chi_{\text{IP}}^2$ w.r.t. best PV	$> 25$
	$\chi_{\text{IP}}^2$	$> 36$
	$\sum p_{\text{T}}$	$> 1.9$ GeV/ $c$
$\pi^0$	$p_{\text{T}}$	$> 1.7$ GeV/ $c$
	$\chi_{\text{IP}}^2$	$> 36$
$D^0$	$\chi_{\text{vtx}}^2/\text{ndf}$	$< 20$
	$p_{\text{T}}$	$> 1.4$ GeV/ $c$
	$m_{\pi\pi\pi}$	$\in [1700, 2020]$ MeV/ $c^2$
	$m_{D^0}$	$\in [1745, 1985]$ MeV/ $c^2$
	$\chi_{\text{IP}}^2$ w.r.t. best PV	$< 50$
	DIRA	$> 0.9995$
	$\tau$	$> 0.2$ ps
$D^*$	$m_{D^*} - m_{D^0} - m_{\pi_{\text{tag}}}$	$\in [-999, 45.43]$ MeV/ $c^2$
	$\chi_{\text{vtx}}^2/\text{ndf}$	$< 10$
	$m_{h^+ h^- \pi^0 \pi_{\text{tag}}} - m_{h^+ h^- \pi^0} - m_{\pi_{\text{tag}}}$	$\in [-999, 55.43]$ MeV/ $c^2$

 Table 5.5: Selection requirements for the  $D^0 \rightarrow h^+ h^- \pi^0$  decays' exclusive HLT2 trigger lines in Run 2.

Year(s)	Stripping line
2012	StrippingDstarToHHPi0_(pipipi0/Kpipi0)_(M/R)_Line
2015-18	StrippingDstarD0ToHHPi0_(pipipi0/Kpipi0)_(M/R)_Line

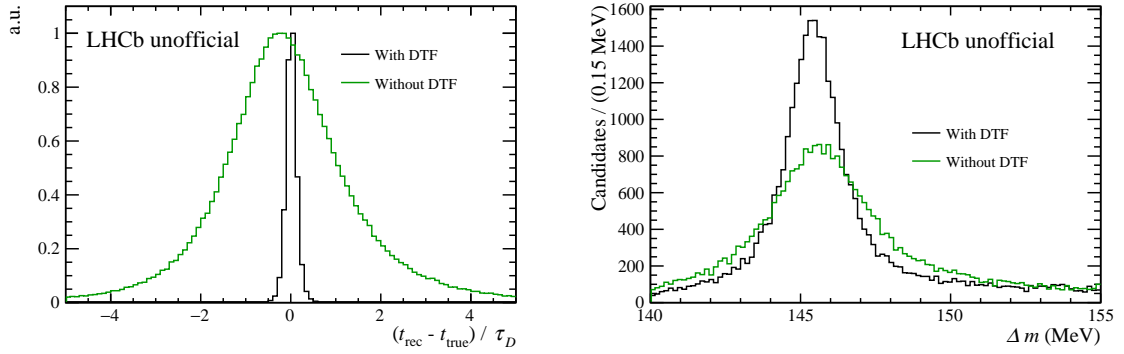
Table 5.6: Stripping lines used in this analysis.

The cut on the combined mass of the final state charged hadrons removes contamination from  $D^0 \rightarrow K_S^0 (\rightarrow \pi^+ \pi^-) \pi^0$  decays, and is only applied to the signal channel. This removes  $\sim 1-2\%$  of candidates. The cut on the quality of the DTF fit,  $\chi_{\text{DTF}}^2$ , removes events where the constrained reconstruction fit fails. The asymmetric cut around the  $D^0$  meson mass for merged candidates is chosen to suppress contamination from  $D^0 \rightarrow K^- \pi^+ \pi^0$  decays where the kaon is mis-identified as a pion, which will peak in the lower  $m_{D^0}$  sideband.

In addition to the previous cut-based selections, a multivariate analysis strategy is employed to further reduce combinatorial background. Separate BDTs [141] are trained for the merged and resolved samples, and for the Run 1 and Run 2 data-taking periods. A simple sideband subtraction procedure based on a fit to the  $\Delta m$  distribution is applied to define the signal and background training samples. A

Particle	Quantity	Requirement (merged)	Requirement (resolved)
$D^{*\pm}$	$\chi_{DOCA}^2(D^0, \pi_{\text{tag}}^\pm)$	$< 20$	$< 20$
	$m_{D^{*\pm}} - m_{D^0}$	$< 180 \text{ MeV}/c^2$	$< 180 \text{ MeV}/c^2$
	$\chi_{\text{vtx}}^2/\text{ndf}$	$< 9$	$< 9$
$D^0$	$p_T$	$> 1.4 \text{ GeV}/c$	$> 1.4 \text{ GeV}/c$
	$ m_{D^0} - 1864.83 $	$< 150 \text{ MeV}/c^2$	$< 150 \text{ MeV}/c^2$
	$\chi_{\text{vtx}}^2/\text{ndf}$	$< 20$	$< 20$
$\pi_{\text{tag}}^\pm$	$p_T$	$> 300 \text{ MeV}/c$	$> 300 \text{ MeV}/c$
	Track ghost probability	$< 0.35$	$< 0.35$
	PIDe	$< 5$	$< 5$
	$\min(\chi_{\text{IP}}^2 \text{ w.r.t. each PV})$	$< 9$	$< 9$
$h^\pm$	$p_T$	$> 500 \text{ MeV}/c$	$> 500 \text{ MeV}/c$
	Track ghost probability	$< 0.35$	$< 0.35$
	PIDK	$< 0(\pi^\pm) / > 7(K^\pm)$	$< 0(\pi^\pm) / > 7(K^\pm)$
$h^+$ or $h^-$	$p_T$	$> 1.7 \text{ GeV}/c$	$> 1.7 \text{ GeV}/c$
	$\chi_{\text{IP}}^2 \text{ w.r.t. best PV}$	$> 36$	$> 36$
$h^+$ and $h^-$	$m_{h^+h^-}$	$< 1850 \text{ MeV}/c^2$	$< 1850 \text{ MeV}/c^2$
	$\chi_{DOCA}^2(h^+, h^-)$	$< 15$	$< 15$
$\pi^0$	$p_T$	$> 500 \text{ MeV}/c$	$> 500 \text{ MeV}/c$
	$ m_{\pi^0} - 135 $	-	$< 15 \text{ MeV}/c^2$

Table 5.7: Stripping selection requirements.



(a) Decay time residuals in units of  $\tau_{D^0}$  from truth-matched, merged- $\pi^0$  simulated data before and after DTF reconstruction. (b)  $\Delta m$  distribution in the 2015 *MagUp* merged signal channel sample before and after DTF reconstruction.

Figure 5.1: Illustration of the effect of the DTF reconstruction on the  $\Delta m$  and decay-time resolutions.

signal region is defined as  $\pm 2\sigma$  around the  $\Delta m$  peak and a background region is defined in the upper sideband. Candidates lying in the signal region are assigned a weight of unity, and candidates in the background region are assigned a (single) negative weight based on the ratio of the integrals of the background PDF from the

Particle	Quantity	Requirement (merged)	Requirement (resolved)
$D^0$	$m_{D^0} - 1865$	$\in (-60, 120) \text{ MeV}/c^2$	$\in (-60, 60) \text{ MeV}/c^2$
	$\log(\chi_{\text{IP}}^2)$	$< 2$	$< 2$
$D^{*\pm}$	$\log(\chi_{\text{FD}}^2)$	$< 4$	$< 4$
	$\chi_{\text{DTF}}^2$	$> 0$	$> 0$
$\pi^+$ and $\pi^-$	$ m_{\pi^+\pi^-} - 497.6 $	$> 10 \text{ MeV}/c^2$	$> 10 \text{ MeV}/c^2$

Table 5.8: Offline cut-based selection requirements.

Variable	Importance (%)	Variable	Importance (%)
$\pi^0 \cos(\theta)$	16	$p_{\text{T}} (\pi^0)$	19
$p_{\text{T}} (\pi^0)$	16	$\pi^0 \cos(\theta)$	18
$D^0 \cos(\theta)$	15	$p_{\text{T}} (D^0)$	16
$D^0 \text{ DIRA}$	13	$p_{\text{T}} (D^*)$	12
$p_{\text{T}} (h^+) + p_{\text{T}} (h^-)$	11	$D^0 \text{ DIRA}$	12
$m_{\pi^0}$	9	$\pi^0 \text{ CL}$	10
$p_{\text{T}} (D^0)$	9	$D^0 \cos(\theta)$	9
$p_{\text{T}} (D^*)$	7	$p_{\text{T}} (h^+) + p_{\text{T}} (h^-)$	4
$\pi^0 \text{ CL}$	6		

Table 5.9: Variables used by the offline merged (left) and resolved (right) BDTs for Run 1.

fit in the two regions. Tables 5.9 and 5.10 show the variables used in each BDT, along with their relative importances as computed by TMVA [142]. The kinematics of the tagging pion are not used in the BDT to avoid introducing any additional nuisance asymmetry effects.

Figures 5.2 and 5.3 show the output distributions of each BDT. Appendix A contains additional plots to illustrate the performance of each BDT. As a test of overtraining, a  $\chi^2$  value is computed between the output distributions for the training sample and an independent testing sample. In all cases, the output distributions are found to be compatible. The BDTs are trained using the 2012 *MagUp* and 2017 *MagUp* real data samples for Run 1 and Run 2, respectively. Half of the data in each sub-sample is used for training, and the remaining half is used to perform the overtraining test. The training and testing samples each correspond to around 25% (6%) of the events in the 2012 (2015–18) datasets. The cut applied to the output of each BDT is optimised based on a binned maximum likelihood fit to the  $\Delta m$  distribution using the metric  $S/\sigma_S$ , where  $S$  represents the number of signal candidates, and  $\sigma_S$  its uncertainty. The same BDTs are used for the signal and control channels, however the cuts to their output are optimised separately. Plots of the optimisation

Variable	Importance (%)	Variable	Importance (%)
$D^0$ DIRA	16	$p_T(\pi^0)$	20
$p_T(\pi^0)$	15	$D^0$ DIRA	15
$D^0 \cos(\theta)$	14	$\pi^0 \cos(\theta)$	14
$\pi^0 \cos(\theta)$	14	$p_T(D^0)$	13
$p_T(D^*)$	10	$p_T(D^*)$	12
$p_T(h^+) + p_T(h^-)$	10	$D^0 \cos(\theta)$	11
$m_{\pi^0}$	8	$\pi^0$ CL	10
$p_T(D^0)$	8	$p_T(h^+) + p_T(h^-)$	4
$\pi^0$ CL	6		

Table 5.10: Variables used by the offline merged (left) and resolved (right) BDTs for Run 2.

metric for the 2012 signal channel datasets, using the same data samples used to train the BDTs, are shown in Figure 5.4, and the remaining plots for all other data samples can be found in Appendix A. Table 5.11 shows the chosen cut for each category of the data.

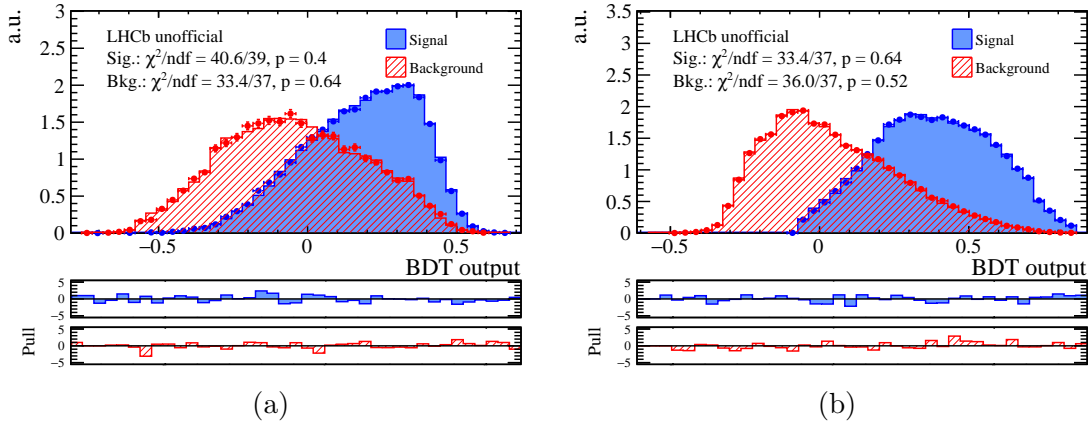


Figure 5.2: Output distributions for (a) merged and (b) resolved Run 1 BDTs.

Finally, for events where more than one candidate remains after the full selection, a single candidate is randomly selected to be kept and all others are removed. This is implemented in two stages. Firstly, the merged and resolved samples are treated independently and the removal procedure is applied. Then, for any events where a candidate remains in both the merged and resolved sample, one candidate is randomly rejected. Removing such candidates avoids double counting, since *e.g.* the same pair of charged tracks could be combined with two different  $\pi^0$  candidates to form two  $D^0$  candidates from a single decay. Table 5.12 shows the fraction of events removed from each sub-sample of the data. Figures 5.5 and 5.6 show the  $\Delta m$

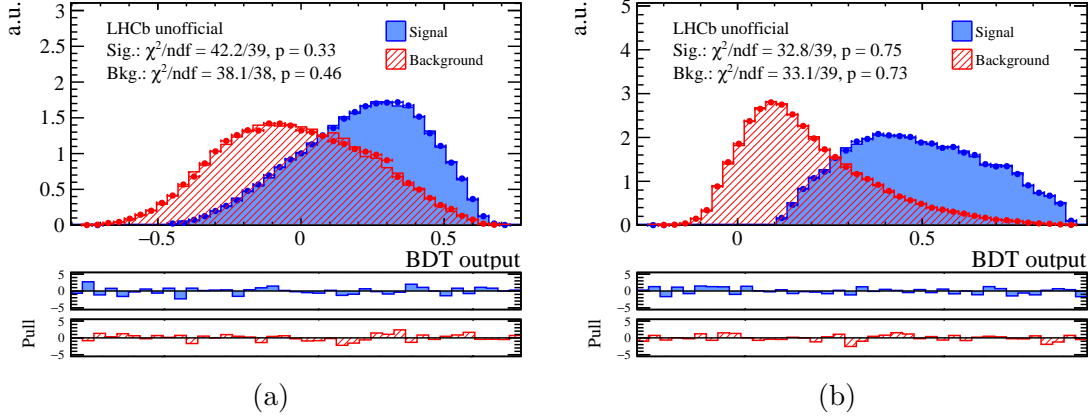


Figure 5.3: Output distributions for (a) merged and (b) resolved Run 2 BDTs.

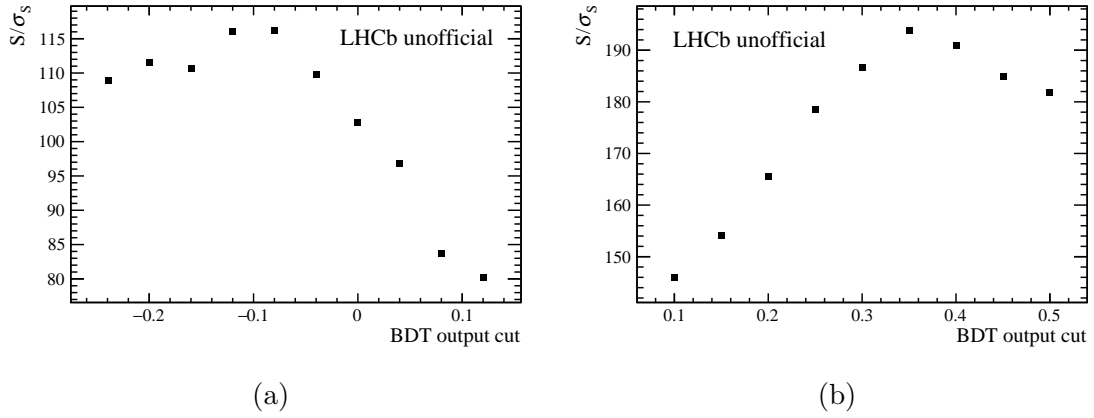


Figure 5.4: Optimisation metric as a function of BDT cut for the (a) merged and (b) resolved 2012 signal channel data.

distributions for the 2016 *MagUp* merged and resolved signal channel samples, respectively, after the initial trigger and stripping selections, and after the full selection procedure. Figure 5.7 shows the corresponding  $m(D^0)$  distributions for candidates within  $\pm 2\sigma$  of the  $\Delta m$  peak for the same sub-samples, after the full selection.

#### 5.2.4 Mis-identified and mis-reconstructed backgrounds

Since other decay modes can be affected by different asymmetries than the signal mode under consideration here, contamination from real physics processes which are mis-reconstructed or mis-identified can bias the measured  $\Delta Y$ . To study this, the fraction of contamination in the signal channel is estimated for a range of possible sources by estimating PID and  $m(D^0)$  selection efficiencies, assuming all other selection efficiencies are the same for signal decays and the background under considera-

Data sample	BDT output requirement
2012 $D^0 \rightarrow \pi^+ \pi^- \pi^0$ , merged	$> -0.08$
2012 $D^0 \rightarrow \pi^+ \pi^- \pi^0$ , resolved	$> 0.35$
Run 2 $D^0 \rightarrow \pi^+ \pi^- \pi^0$ , merged	$> 0$
Run 2 $D^0 \rightarrow \pi^+ \pi^- \pi^0$ , resolved	$> 0.585$
2012 $D^0 \rightarrow K^- \pi^+ \pi^0$ , merged	$> -0.35$
2012 $D^0 \rightarrow K^- \pi^+ \pi^0$ , resolved	$> 0.35$
Run 2 $D^0 \rightarrow K^- \pi^+ \pi^0$ , merged	$> -0.25$
Run 2 $D^0 \rightarrow K^- \pi^+ \pi^0$ , resolved	$> 0.48$

Table 5.11: Offline BDT selection requirements.

Dataset	$\pi^+ \pi^- \pi^0$		$K^- \pi^+ \pi^0$	
	Merged (%)	Resolved (%)	Merged (%)	Resolved (%)
12 <i>MagUp</i>	3.7	13.6	2.3	13.0
12 <i>MagDown</i>	3.4	13.7	2.3	13.1
15 <i>MagUp</i>	4.8	12.4	2.7	15.1
15 <i>MagDown</i>	4.2	12.4	2.7	15.4
16 <i>MagUp</i>	7.3	11.1	4.3	13.2
16 <i>MagDown</i>	7.2	10.6	4.2	12.7
17 <i>MagUp</i>	6.3	10.0	4.3	12.0
17 <i>MagDown</i>	7.3	9.8	4.3	11.9
18 <i>MagUp</i>	6.7	10.3	4.5	11.9
18 <i>MagDown</i>	6.7	10.3	4.5	11.9

Table 5.12: Fraction of candidates rejected by the multiple candidate selections in each sub-sample of the control and signal channel datasets.

tion, and taking branching fractions from the PDG [143]. Under these assumptions, the fraction of a single background component present in the sample is given by

$$f_B = \frac{B}{S+B} = \left( \frac{S}{B} + 1 \right)^{-1} = \left( \frac{\mathcal{B}_S}{\mathcal{B}_B} \times \frac{\varepsilon_{\text{PID}}^S}{\varepsilon_{\text{PID}}^B} \times \frac{\varepsilon_{m(D)}^S}{\varepsilon_{m(D)}^B} + 1 \right)^{-1}, \quad (5.3)$$

where  $\varepsilon_{\text{PID}}^{S(B)}$  and  $\varepsilon_{m(D)}^{S(B)}$  are the signal (background) PID and  $m(D^0)$  selection efficiencies, respectively, and  $\mathcal{B}_{S(B)}$  are the branching fractions. The PID efficiencies are measured in bins of  $p_T$  and  $\eta$  for a given charged particle using PIDCALIB2 [144], and then a weighted average of this efficiency map is taken using the distribution of candidates in the  $(p_T, \eta)$ -space from simulated data. For potential backgrounds where both pions are mis-identified, the total PID efficiency is assumed to be the product of the efficiencies from the individual pions. Efficiencies for the  $m(D^0)$  mass window selection are computed using the RAPIDSIM package [145], where the

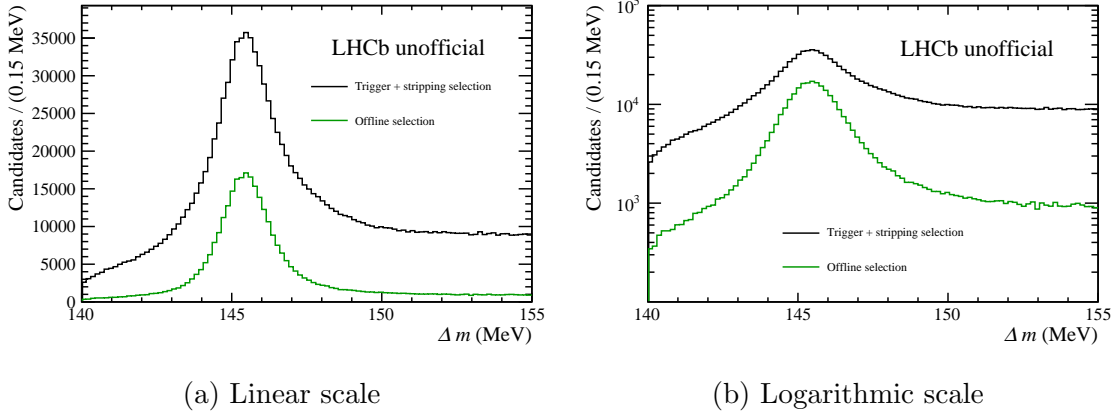


Figure 5.5: Comparison of the  $\Delta m$  distributions for the 2016 *MagUp* merged signal channel sample after trigger and stripping selection, and full offline selection.

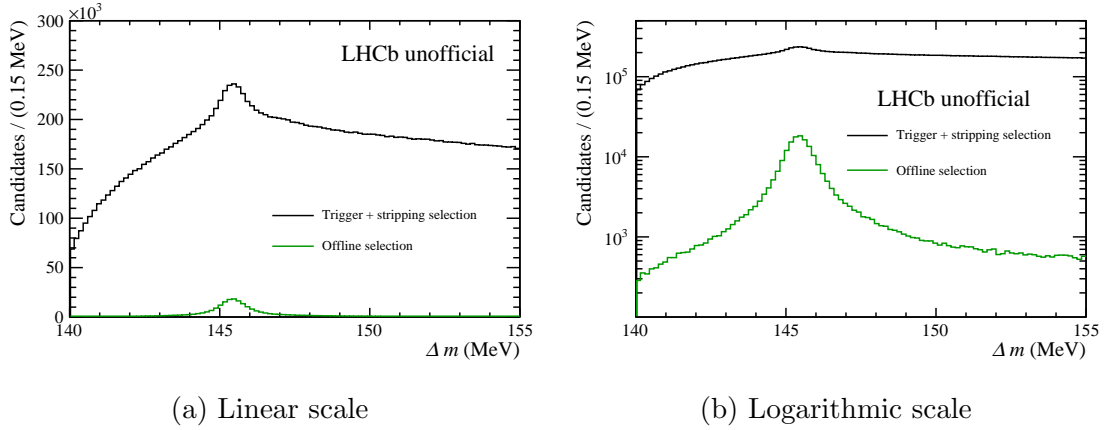


Figure 5.6: Comparison of the  $\Delta m$  distributions for the 2016 *MagUp* resolved signal channel sample after trigger and stripping selection, and full offline selection.

resolution smearing of the  $\pi^0$  mass has been tuned so that the mass resolution of the reconstructed  $D^0$  meson in the decay  $D^0 \rightarrow \pi^+ \pi^- \pi^0$  matches that of the full LHCb simulation, separately for the merged and resolved  $\pi^0$  categories; for other particles, the default RAPIDSIM smearing is used. Potential mis-identified or mis-reconstructed backgrounds which have been studied here are listed in Table 5.13. All are found to be negligible ( $\ll 1\%$ ) except for the Cabibbo-favoured control mode used in this analysis,  $D^0 \rightarrow K^- \pi^+ \pi^0$ , where the kaon can be mis-identified as a pion. The contamination from this mode is estimated to be 0.7% and 0.8% in the merged and resolved samples, respectively. An estimate of the potential bias on the measured time-dependent asymmetry from this residual  $D^0 \rightarrow K^- \pi^+ \pi^0$  contamination is provided in Appendix B. The list of decays considered here is restricted to real  $D^0$  meson decays with mis-identification or mis-reconstruction of the final state,

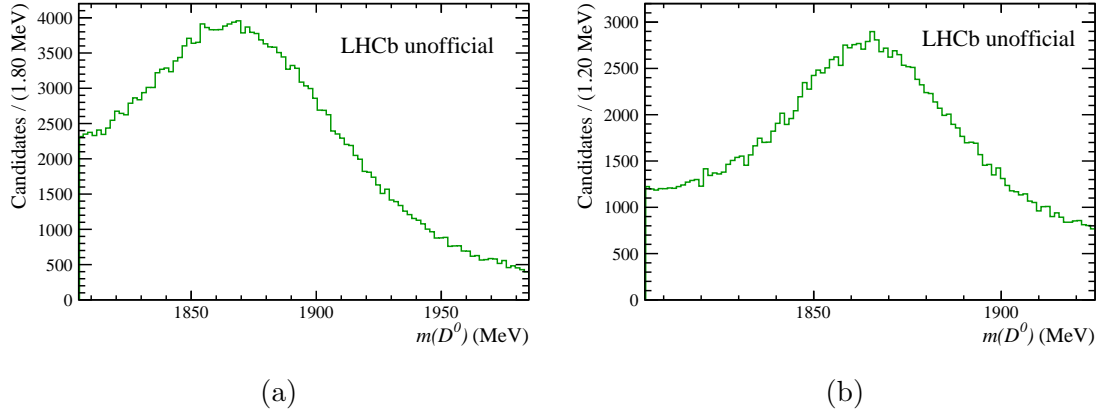


Figure 5.7: Distributions of  $m(D^0)$  for the 2016 *MagUp* (a) merged and (b) resolved signal channel sample after the full offline selection.

since other potential background sources will not peak in the  $\Delta m$  distribution and therefore will not be included in the signal component.

Background source	Comments
$D^0 \rightarrow K^- \pi^+ \pi^0$	$K^-$ mis-identified as $\pi^-$
$D^0 \rightarrow \pi^- \pi^0 e^+ \nu_e$	$\nu_e$ not reconstructed, $e^+$ mis-identified as $\pi^+$
$D^0 \rightarrow K^- \pi^0 e^+ \nu_e$	$\nu_e$ not reconstructed, $e^+$ mis-identified as $\pi^+$ , $K^-$ mis-identified as $\pi^-$
$D^0 \rightarrow \omega(\rightarrow \pi^+ \pi^- \pi^0) \gamma$	$\gamma$ not reconstructed
$D^0 \rightarrow K_S^0 \pi^+ \pi^- \pi^0$	$K_S^0$ not reconstructed
$D^0 \rightarrow K^- \pi^+ \eta$	$K^-$ mis-identified as $\pi^-$ , $\eta$ mis-identified as $\pi^0$
$D^0 \rightarrow \pi^+ \pi^- \pi^0 \pi^0$	One $\pi^0$ not reconstructed

Table 5.13: List of potential mis-identified or mis-reconstructed background sources.

### 5.2.5 Final signal yields

Figures 5.8 and 5.9 show fits to the  $\Delta m$  distributions of all selected candidates, for both the signal and control channels and both merged and resolved  $\pi^0$  categories. The fit models are described in Section 6.2. In the signal channel, the final signal yields are approximately 2.26M and 1.51M candidates, with a purity of around 87% in both  $\pi^0$  categories. In the control channel, final samples of around 18.0M and 20.3M decays, with purities of approximately 96% and 93%, are obtained in the merged and resolved  $\pi^0$  categories, respectively. These yields are computed from the fits to the  $\Delta m$  distribution, by counting the number of candidates within  $2\sigma$  of the mean value of the signal peak. Tables 5.14 and 5.15 list the fractions of selected

candidates which pass each trigger selection at HLT1 and HLT2 level, respectively. By definition, the respective relative efficiencies for the 2012 sample are always 100% since only a single trigger line is utilised at both HLT1 and HLT2.

$\pi^0$ category	Dataset	$\pi^+ \pi^- \pi^0$		$K^- \pi^+ \pi^0$	
		Track (%)	TwoTrack (%)	Track (%)	TwoTrack (%)
Merged	15 <i>MagUp</i>	99.7	85.5	99.7	85.5
	15 <i>MagDown</i>	100	85.8	100	86.2
	16 <i>MagUp</i>	93.3	81.6	91.8	81.8
	16 <i>MagDown</i>	97.4	79.5	97.0	80.0
	17 <i>MagUp</i>	98.3	78.5	98.2	79.1
	17 <i>MagDown</i>	98.3	79.1	98.2	79.2
	18 <i>MagUp</i>	97.9	77.4	97.8	77.8
	18 <i>MagDown</i>	97.9	77.4	97.8	77.8
Resolved	15 <i>MagUp</i>	99.9	86.2	99.8	86.9
	15 <i>MagDown</i>	100	87.1	100	87.7
	16 <i>MagUp</i>	98.6	84.2	97.8	85.6
	16 <i>MagDown</i>	99.6	83.4	99.3	84.7
	17 <i>MagUp</i>	99.8	84.2	97.8	85.6
	17 <i>MagDown</i>	99.8	82.8	99.6	84.5
	18 <i>MagUp</i>	99.7	81.6	99.5	83.4
	18 <i>MagDown</i>	99.7	81.5	99.5	83.3

Table 5.14: Fraction of selected candidates passing each HLT1 selection in each sub-sample of the control and signal channel datasets. ‘Track’ refers to the requirement that the  $D^0$  candidate fires TOS on the HLT1TrackMVA line, and ‘TwoTrack’ refers to the same requirement on the HLT1TwoTrackMVA line.

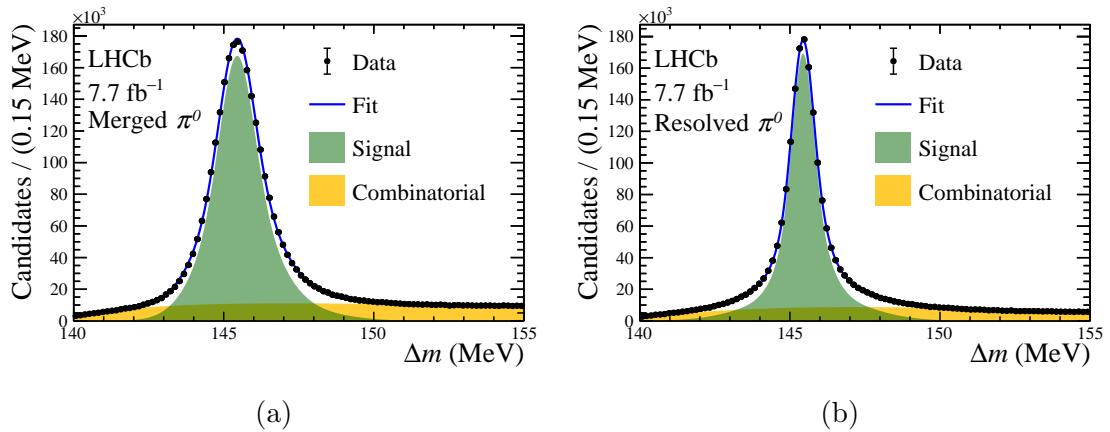


Figure 5.8: Fits to the  $\Delta m$  distributions of selected  $D^{*+} \rightarrow D^0 \pi_{\text{tag}}^+$  candidates in the (a) merged and (b) resolved  $\pi^0$  categories for the signal channel [146].

$\pi^0$ category	Dataset	$\pi^+ \pi^- \pi^0$		$K^- \pi^+ \pi^0$	
		Exclusive (%)	Inclusive (%)	Exclusive (%)	Inclusive (%)
Merged	15 <i>MagUp</i>	15.2	87.6	11.0	91.5
	15 <i>MagDown</i>	1.2	99.0	0.84	99.4
	16 <i>MagUp</i>	76.0	35.2	74.0	39.5
	16 <i>MagDown</i>	72.9	36.3	69.0	43.1
	17 <i>MagUp</i>	78.5	32.3	75.3	38.8
	17 <i>MagDown</i>	79.8	31.1	75.6	38.6
	18 <i>MagUp</i>	92.8	20.1	90.8	26.2
	18 <i>MagDown</i>	93.0	20.0	90.9	26.2
Resolved	15 <i>MagUp</i>	18.1	88.6	15.4	89.6
	15 <i>MagDown</i>	1.4	99.1	1.1	99.3
	16 <i>MagUp</i>	31.9	76.9	24.6	82.4
	16 <i>MagDown</i>	34.5	74.6	25.0	82.3
	17 <i>MagUp</i>	40.7	69.8	27.5	80.9
	17 <i>MagDown</i>	41.5	69.3	27.8	80.8
	18 <i>MagUp</i>	58.9	56.6	42.6	70.6
	18 <i>MagDown</i>	59.3	56.2	42.8	70.4

Table 5.15: Fraction of selected candidates passing each HLT2 selection in each subsample of the control and signal channel datasets. ‘Exclusive’ and ‘Inclusive’ refer to the requirements that the  $D^*$  candidate fires TOS on the exclusive and inclusive lines, respectively, given in Table 5.2.

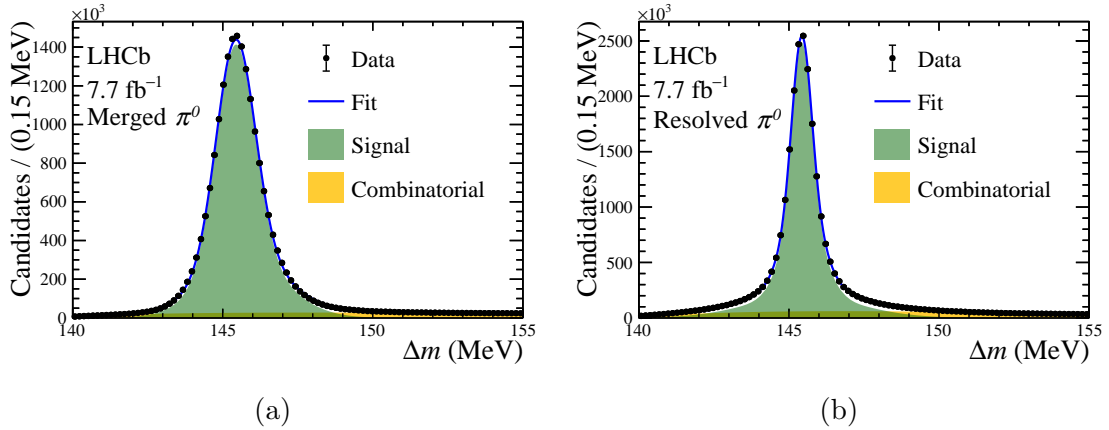


Figure 5.9: Fits to the  $\Delta m$  distributions of selected  $D^{*+} \rightarrow D^0 \pi_{\text{tag}}^+$  candidates in the (a) merged and (b) resolved  $\pi^0$  categories for the control channel [146].

### 5.3 Summary

The selection procedure applied to the 2012 and 2015-18 LHCb datasets to select  $D^0 \rightarrow h^- \pi^+ \pi^0$  decays has been described in detail. Events were triggered at the first software level based on the charged  $D^0$  daughter tracks, or their combined

vertex. At the second software level, events were triggered based on either a partial or full reconstruction of the  $D^0$  candidate. Offline, a selection of cuts were applied to remove secondary decays and other physics backgrounds. A set of multivariate classifiers were trained in order to further suppress combinatorial backgrounds. Final signal yields of  $\sim 3.8\text{M}$  and  $\sim 38\text{M}$  are obtained in the signal and control channels, respectively.

# Measurement of $\Delta Y$

---

EXPERIMENTALLY, the decay rates cannot be directly probed in order to make a measurement of the time-dependent asymmetry. Rather, the raw asymmetry is measured as a function of decay time, which potentially contains unwanted asymmetries in addition to the  $CP$  asymmetries given in Equation 1.62. This measurable quantity can be expressed as

$$\mathcal{A}_{\text{raw},f}(t) = \frac{N_{D^0 \rightarrow f}(t) - N_{\bar{D}^0 \rightarrow f}(t)}{N_{D^0 \rightarrow f}(t) + N_{\bar{D}^0 \rightarrow f}(t)} \approx \mathcal{A}_f^{CP}(t) + \mathcal{A}_{\text{det}}(t) + \mathcal{A}_{\text{prod}}(t), \quad (6.1)$$

where  $\mathcal{A}_{\text{det}}(t)$  and  $\mathcal{A}_{\text{prod}}$  are detection and production asymmetries respectively. The detection asymmetry may carry a time dependence and mimic a time-dependent  $CP$  asymmetry. Corrections to account for these false asymmetries are detailed in Section 6.1. The procedure used to determine  $\Delta Y_{\pi\pi\pi}^{\text{eff}}$  ( $\Delta Y_{K\pi\pi}$ ) from the signal (control) data is described in Section 6.2. The data is analysed independently per-year, per-polarity, and per- $\pi^0$  category, and subsequently a weighted least squares fit is used to extract a combined value of  $\Delta Y_{\pi\pi\pi}^{\text{eff}}$  ( $\Delta Y_{K\pi\pi}$ ) across the sub-samples.

## 6.1 Origin and correction of detection asymmetries

### 6.1.1 Origin of detection asymmetries

*A priori*, the decay time of each  $D^0$  candidate is completely uncorrelated with the kinematics of the event. However, certain selection requirements that are necessary to suppress the significant levels of combinatorial backgrounds can introduce corre-

lations between the  $D^0$  decay time and different kinematic variables; asymmetries in these kinematic variables due to detector effects can then in turn induce false asymmetries in the data, which must be carefully accounted for. In particular, when a particle is reconstructed in the LHCb detector its decay time is calculated as:

$$t = \frac{md}{p}, \quad (6.2)$$

where  $m$ ,  $d$  and  $p$  are the measured mass, flight distance and momentum, respectively, of the particle. Correlations of the  $D^0$  meson decay time and its momentum can arise, for example, from the minimum requirement on the  $\chi^2_{\text{IP}}$  of at least one of the final-state charged hadrons in Table 5.7. This requires the  $D^0$  decay vertex to be displaced from the PV, and so degrades the selection efficiency at low decay times since only  $D^0$  candidates with large enough momentum will have a sufficiently large flight distance. This does not directly introduce a time-dependent asymmetry, however it can have an indirect effect. Oppositely charged tagging pions are deflected in opposite directions by the LHCb magnet, and thus any asymmetry in the response of the LHCb detector along the bending axis of the magnet can induce a kinematic asymmetry. Despite the magnet polarity being reversed frequently during data taking, averaging over both polarities does not guarantee complete correction of these asymmetries for several reasons: the beams crossing angle lies in the magnet's bending plane; the condition of the detector changes over time; the material placement is not entirely symmetrical about the bending direction.

### 6.1.2 Correction of detection asymmetries

To correct for such detection asymmetries, it is sufficient to weight the time-integrated kinematic distributions of  $D^0$  and  $\bar{D}^0$  candidates so that they agree. The tagging pion contributes most significantly to these detection asymmetries since it typically has low momentum and thus significant track curvature, so the first step of the weighting equalises its kinematic distributions. Using three orthogonal kinematic variables would allow the kinematics to be fully constrained, but due to low statistics in the smaller datasets this step of the weighting is performed in several 2D stages. The variables used for the weighting are:

$$\theta_x(\pi_{\text{tag}}^\pm) = \pm \text{atan} \left( \frac{p_x}{p_z} \right); \quad \theta_y(\pi_{\text{tag}}^\pm) = \text{atan} \left( \frac{p_y}{p_z} \right); \quad k(\pi_{\text{tag}}^\pm) = \frac{1}{\sqrt{p_x^2 + p_z^2}}. \quad (6.3)$$

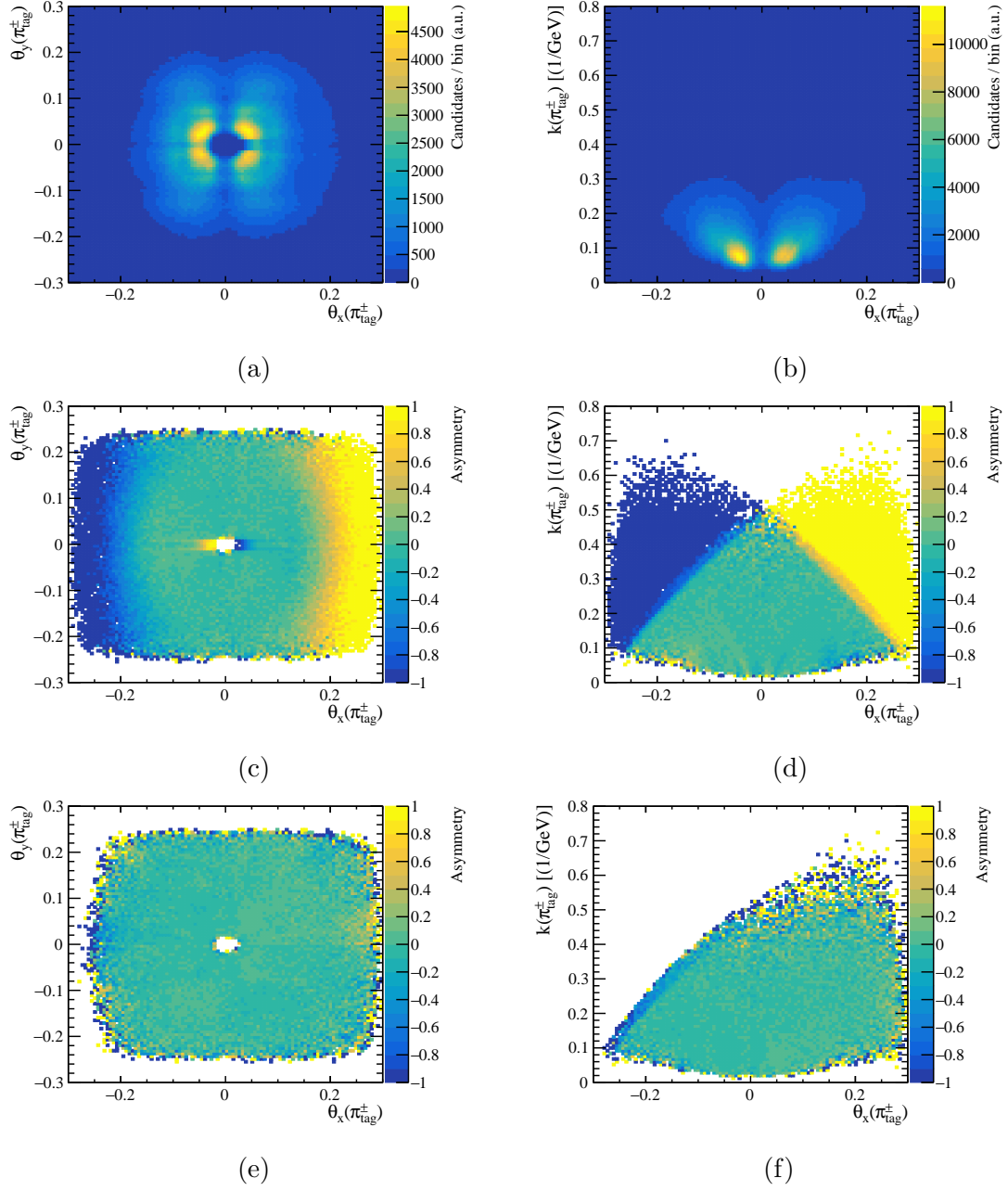


Figure 6.1: Example background-subtracted distributions and asymmetries in the (left)  $(\theta_x, \theta_y)$  and (right)  $(\theta_x, k)$  planes for tag pions from the 2018 *MagUp* resolved control channel dataset. The three plots in each plane correspond to the (top) sum, (centre) asymmetry and (bottom) asymmetry with the sign flip on  $\theta_x$  of the  $\pi_{\text{tag}}^+$  and  $\pi_{\text{tag}}^-$  distributions.

The variable  $k$  is a measure of the track curvature of the particle in the LHCb magnetic field. The sign flip in  $\theta_x$  for  $\bar{D}^0$  mesons arises since the LHCb magnet bends oppositely charged particles in opposite directions in the  $x$ -direction; thus positively

charged particles will be directed out of the LHCb acceptance at one extreme of the detector, while negatively charged particles will be directed further into the acceptance and vice versa at the opposite extreme. A similar effect also occurs around the beam pipe. Figure 6.1 shows some example distributions showing such asymmetries observed in the data. Consequently, it is expected that, if no detection asymmetries were present, the momentum distributions in the  $x$ -direction for  $\pi_{\text{tag}}^{\pm}$  mesons would agree only after a sign flip. Weights calculated from first equalising the  $(\theta_x, k)$ -space and then the  $(\theta_y, k)$ -space are found to factorise, and thus these combinations are used. The signal distributions used to compute the weights are created by subtracting the background in the signal region based on a fit to the  $\Delta m$  distribution. Weighting either the  $D^0$  meson events or the  $\bar{D}^0$  meson events to agree with the other has been found to induce a bias; thus, both distributions are weighted to some mean value [147]. Both the geometric and arithmetic mean have been considered, however the geometric mean is chosen since it is found to remove the detection asymmetries while requiring a less granular binning of events. To avoid large weights, a weight of zero is applied in any bin where the size of the uncorrected asymmetry is larger than 20%, or where there are fewer than 20 events of either flavour. The binning scheme consists of 42 bins for  $\theta_x$  in the range  $[-0.3, 0.3]$ , 28 bins for  $\theta_y$  in the range  $[-0.3, 0.3]$  and in both cases 12 bins for  $k$  in the range  $[0.0, 0.55]$  c/GeV. For each variable the bins are of equal widths. The binning schemes are chosen as the minimal number of bins such that across all datasets, the p-values computed from a  $\chi^2$  comparison of the weighted flavour-tagged distributions are  $\gtrsim 20\%$  for all variables.

The above procedure will — if the assumption that the tag pion kinematic weighting can be factorised into two steps holds — fully correct any detection asymmetries arising from tag pion kinematic asymmetries. However, asymmetries in the  $D^0$  meson kinematics are possible in the control channel since the final states for  $D^0$  and  $\bar{D}^0$  mesons are different. At this stage the  $p_T(D^0)$ ,  $\eta(D^0)$  and  $\eta(\pi_{\text{tag}}^{\pm})$  distributions are equalised. Again, a two-stage 2D procedure is employed where the  $(\eta(D^0), \eta(\pi_{\text{tag}}^{\pm}))$ -space is weighted first followed by the  $(p_T(D^0), \eta(\pi_{\text{tag}}^{\pm}))$ -space. The  $\eta(D^0)$  distribution is divided into 25 bins in the range  $[1.7, 4.5]$ , the  $p_T(D^0)$  distribution is divided into 25 bins in the range  $[0, 35]$  GeV/c and in both cases 15 bins are used for the  $\eta(\pi_{\text{tag}}^{\pm})$  distribution in the range  $[1.7, 4.5]$ . Figures 6.2 and 6.3 show example distributions of all variables used in the weighting procedure before the equalisation, and after the full procedure. Additional plots showing example kinematic distribu-

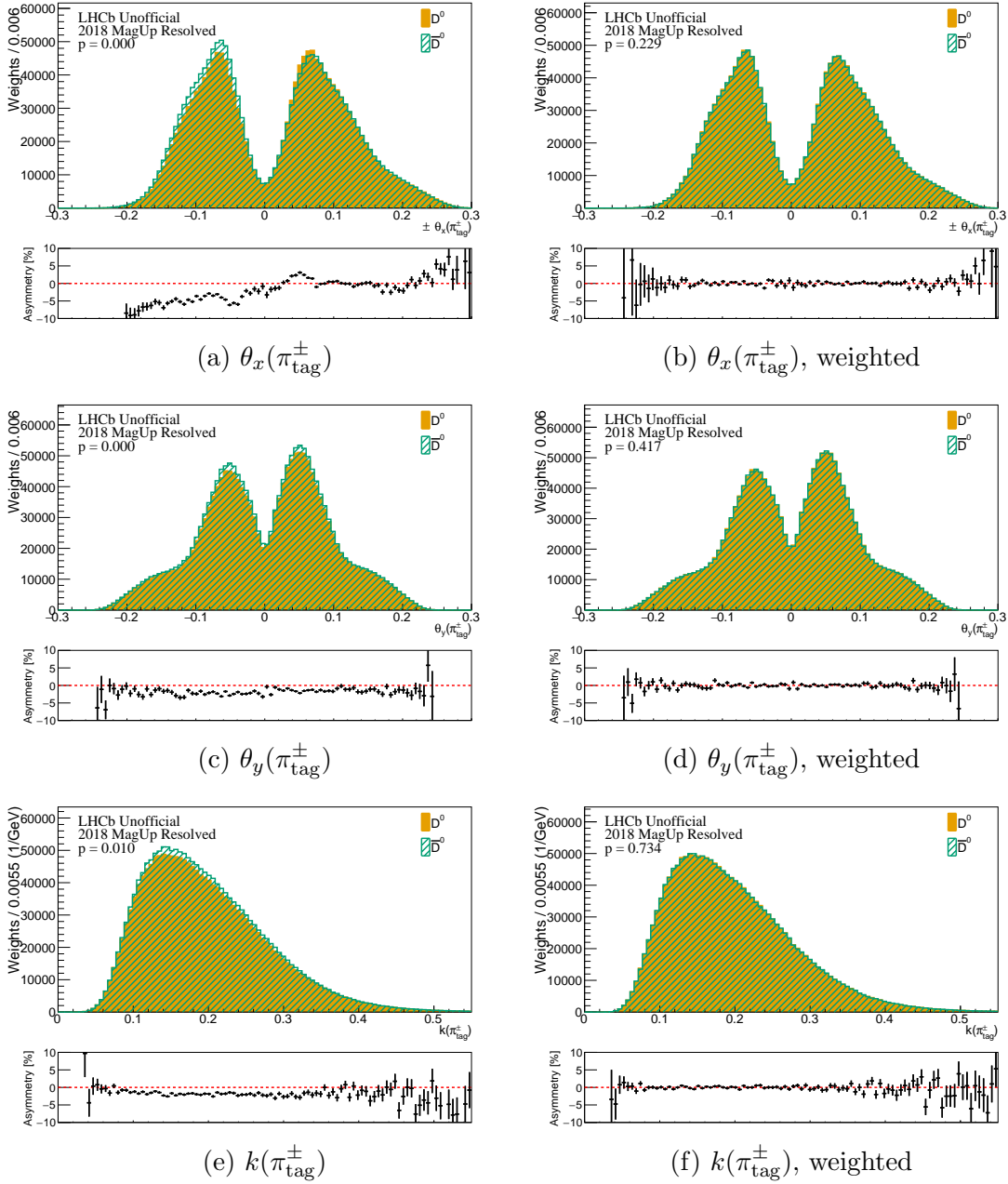


Figure 6.2: 2018 *MagUp* resolved control channel tagging pion kinematic distributions before (left) and after (right) kinematic weighting.

tions at an intermediate stage of the kinematic weighting, for a merged sub-sample of the data and for sub-samples of the signal data can be found in Appendix C. Further studies of potential detection asymmetries in terms of the  $D^0$  daughter kinematics can be found in Section 7.9.

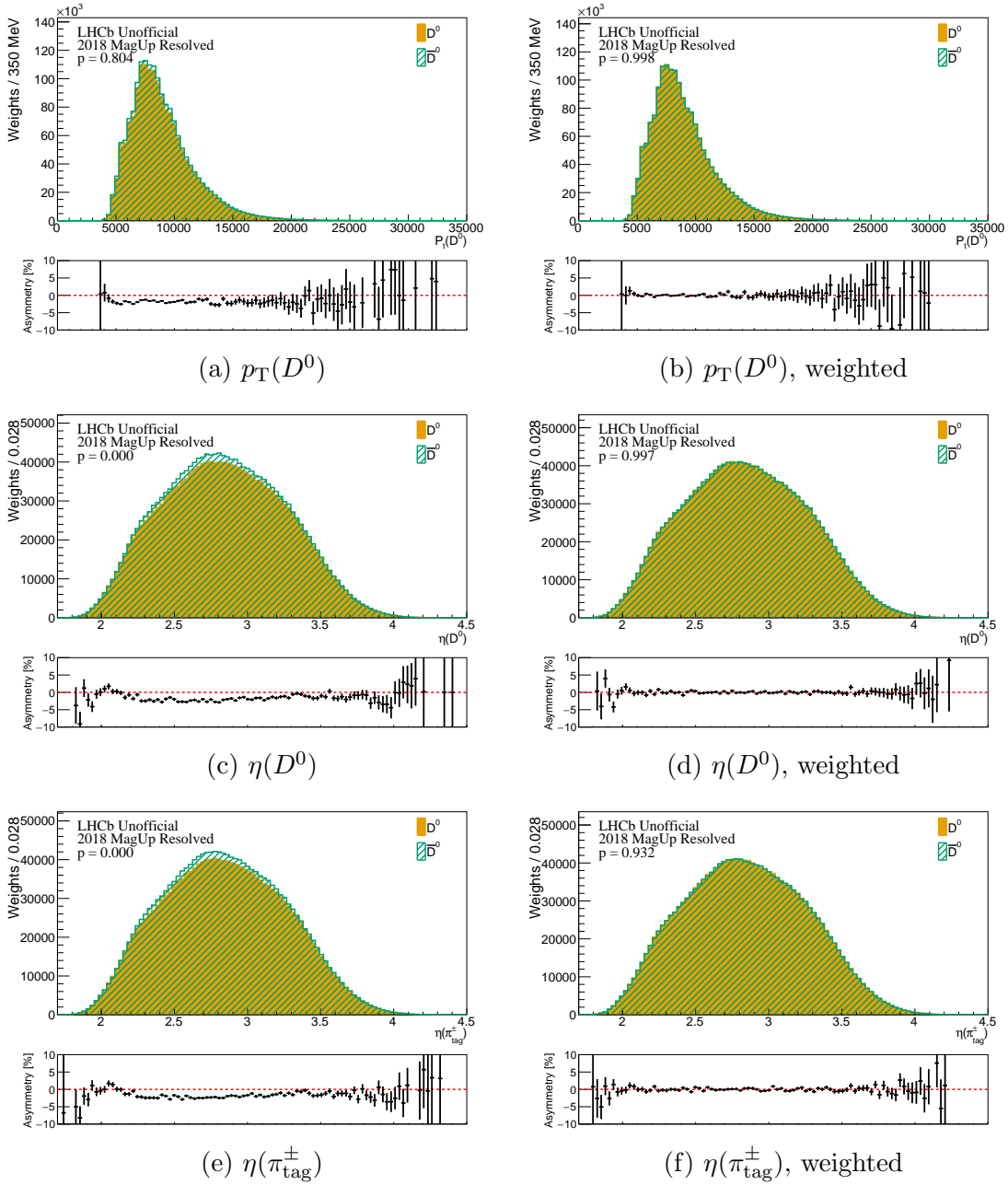


Figure 6.3: 2018 *MagUp* resolved control channel  $D^0$  and tagging pion kinematic distributions before (left) and after (right) kinematic weighting.

### 6.1.3 Dilution of measured $\Delta Y$ due to kinematic weighting

Since a true time-dependent asymmetry and correlation of the kinematics with decay time would introduce a kinematic asymmetry, the kinematic weighting procedure will dilute slightly any true asymmetry. This effect is corrected by injecting several known asymmetries into the data, and then re-performing the nominal analysis

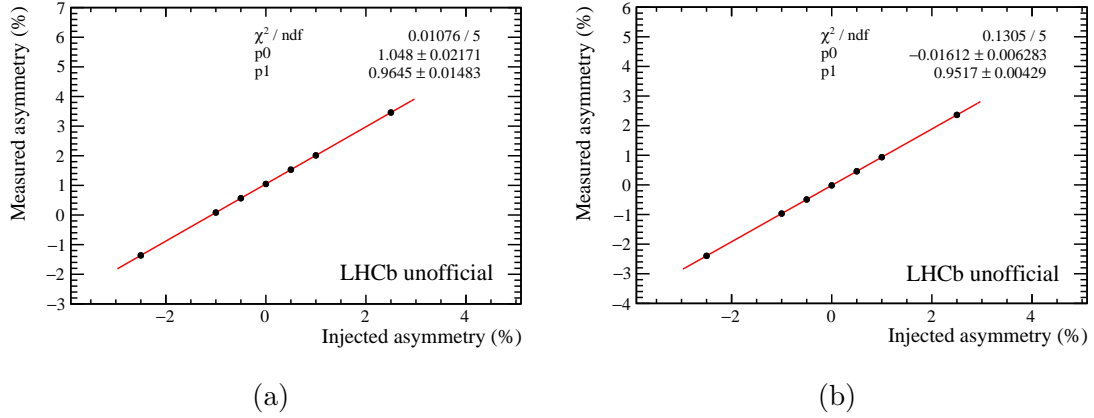


Figure 6.4: Measured vs. injected asymmetries from the study to investigate the dilution due to the kinematic weighting, for both the (blinded) (a) signal and (b) control channels using real flavour tags.

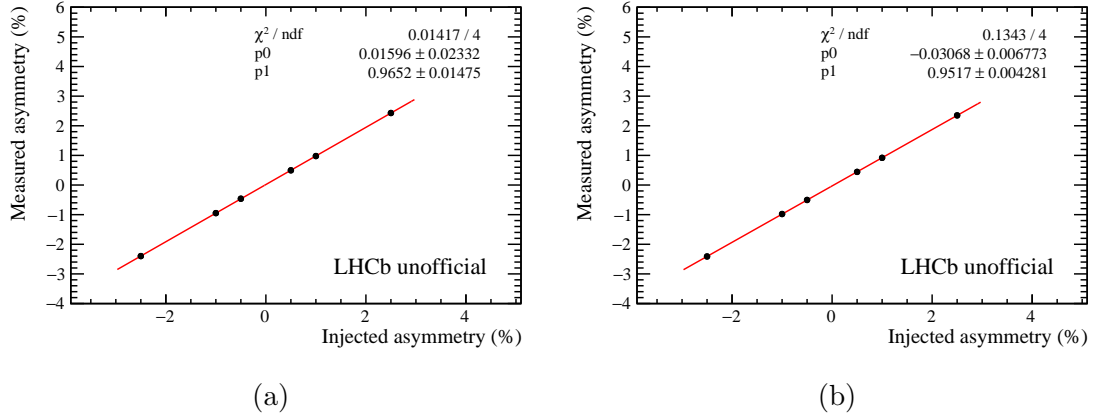


Figure 6.5: Measured vs. injected asymmetries from the study to investigate the dilution due to the kinematic weighting, for both the (a) signal and (b) control channels using random flavour tags.

sequence for each, including the kinematic weighting. This study has been performed with two different configurations; firstly, using the real flavour tag for each candidate, and secondly with each candidate assigned a random flavour tag. The random flavour tags serve to remove any existing asymmetries in the sample, and remove the need for blinding the signal data. Then, a correction factor, computed as the inverse of the gradient from a plot of measured asymmetry against injected asymmetry, is applied to the measured value of  $\Delta Y_{\pi\pi\pi}^{\text{eff}}$ . Asymmetries are injected into the data by applying a time-dependent efficiency to each event, separately for  $D^0$  and  $\bar{D}^0$ , such

that the yields are transformed as

$$\begin{aligned} N(t) &\rightarrow \varepsilon(t)N(t) = \left(1 + A_{\text{inj}}\frac{t}{\tau}\right) N(t), \\ \bar{N}(t) &\rightarrow \bar{\varepsilon}(t)\bar{N}(t) = \left(1 - A_{\text{inj}}\frac{t}{\tau}\right) \bar{N}(t), \end{aligned} \tag{6.4}$$

where  $A_{\text{inj}}$  is the injected asymmetry gradient. Plots of measured against injected asymmetry are shown in Figures 6.4 and 6.5; the correction factors are found to be 1.036 (1.037) and 1.051 (1.051) for the signal and control channels, respectively, by taking the inverse of the gradient in each case and using random (real) flavour tags. For the corrections to the measured asymmetries the values computed using random flavour tags are used. In both cases there appears to be a bias on the fitted intercept in the control channel. Since the same data samples with different injected time-dependent asymmetries are used at each stage, the statistical uncertainty on the intercept of the linear fit is underestimated; such biases are therefore not significant. These studies were performed before the analysis was unblinded, and therefore the offset from zero of the intercept in Figure 6.4a corresponds to the blinding offset on  $\Delta Y_{\pi\pi\pi}^{\text{eff}}$ .

## 6.2 Measurement of $\Delta Y$

The value of  $\Delta Y_{\pi\pi\pi}^{\text{eff}}$  ( $\Delta Y_{K\pi\pi}$ ) for each subset is extracted by performing a linear fit to the asymmetry measured in 21 bins of decay-time in the range  $[0.6, 8.0]\tau_{D^0}$ . The decay time binning scheme is chosen so that signal candidates are approximately evenly distributed across the bins. The centre of each bin,  $i$ , for the linear fit is computed as

$$\langle t/\tau_{D^0} \rangle_i = \frac{\sum_i (w_i t_i / \tau_{D^0})}{\sum_i w_i}, \tag{6.5}$$

where the per-event weights  $w_i$  are computed from a flavour-integrated fit to the  $\Delta m$  distribution in each decay time bin in order to subtract the combinatorial background in the signal region. In the linear fit, the bin centres are assumed to have no error.

The asymmetry is measured in each decay time bin from a simultaneous binned maximum likelihood fit to the  $\Delta m$  distributions for  $D^0$  and  $\bar{D}^0$  candidates. The signal probability density function (PDF) is parameterised as a sum of three

Gaussian distributions, and the background PDF is modelled using the empirical RooDstD0BG shape from the RooFIT package [135, 148]. The RooDstD0BG PDF is defined as

$$P(\Delta m) = \frac{\theta(\Delta m - \Delta m_0)}{N} \left[ (1 - e^{-(\Delta m - \Delta m_0)/c}) \left( \frac{\Delta m}{\Delta m_0} \right)^a + b \left( \frac{\Delta m}{\Delta m_0} - 1 \right) \right], \quad (6.6)$$

where  $a, b, c$  and  $\Delta m_0$  are empirically determined parameters,  $\theta$  is the Heaviside function, and  $N$  is a normalisation factor. All shape parameters are shared between the  $D^0$  and  $\bar{D}^0$  distributions to reduce any possible biases from the choice of fit model. An example of such a fit is shown in Figure 6.6. Several shape parameters are fixed in the time-dependent fits from a time- and flavour-integrated fit to improve fit stability. For the background, all shape parameters except  $b$  ( $b$  and  $\Delta m_0$ ) are fixed for the merged (resolved) datasets. The background yields are floated separately for  $D^0$  and  $\bar{D}^0$ . For the signal shape, the first (narrowest) width and the mean values of the Gaussian distributions are free to float. The ratio of widths of the wider components to the narrowest component are fixed. The use of identical  $\Delta m$  distribution shapes for  $D^0$  and  $\bar{D}^0$  candidates is justified by the consistency of the nominal measurements with the measurements from the cross-check described in Section 7.10.3. The fits are performed in bins of decay time — instead of using a time-integrated fit and applying a background subtraction within each bin — due to variations in the  $\Delta m$  shapes as a function of decay time; Figure 6.7 illustrates this for the signal  $\Delta m$  shape.

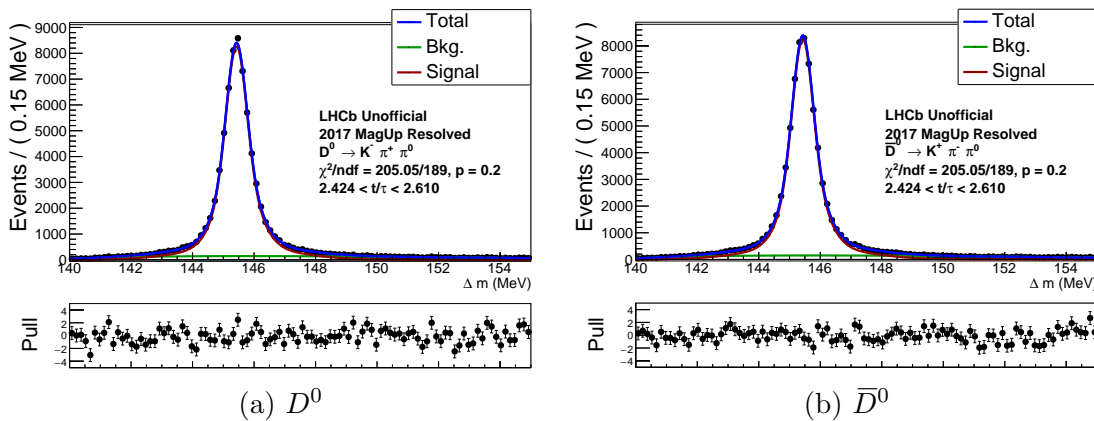


Figure 6.6: Example flavour-tagged fit to the  $\Delta m$  distribution used in the asymmetry measurement. Shown (a) for  $D^0$  and (b) for  $\bar{D}^0$  decays in the 2017 *MagUp* resolved control channel dataset.

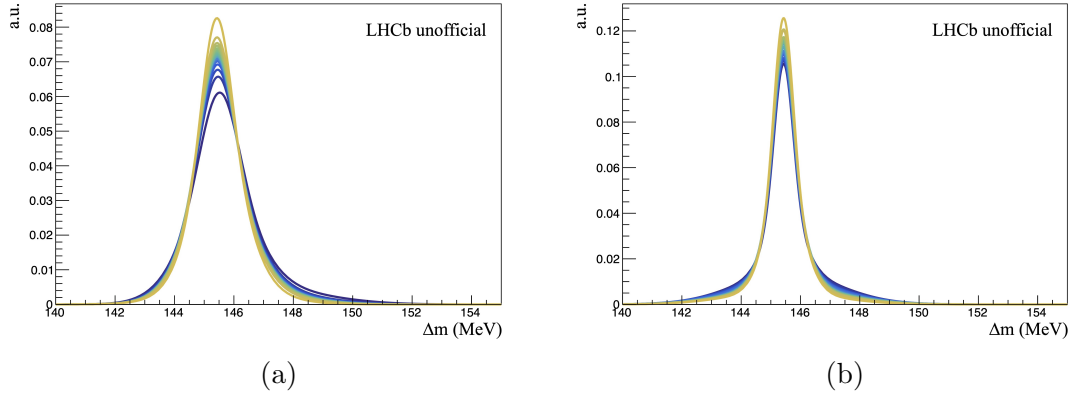


Figure 6.7: Example decay-time evolution of the  $\Delta m$  signal shape in (a) merged and (b) resolved sub-samples of the control channel data. The lowest decay-time bin is in dark blue, trending towards yellow in the highest decay-time bin.

### 6.2.1 Blinding strategy

The minimal blinding strategy for this analysis would involve simply adding an unknown gradient to the measured asymmetries to keep the true gradient blind. However, the procedure described in Section 6.1.2 will remove any total time-integrated asymmetry. Thus, a non-zero intercept in the linear fit for  $\Delta Y$  would provide an indication of the value of the gradient. Consequently, the measured asymmetries were blinded in the following way:

$$\mathcal{A}_{\text{blind}}(t) = \mathcal{A}_{\text{meas}}(t) + a_1 + a_2 \frac{t}{\tau_{D^0}}, \quad (6.7)$$

where  $\mathcal{A}_{\text{meas}}(t)$  is the asymmetry measured in the data after any corrections have been applied,  $\mathcal{A}_{\text{blind}}(t)$  is the value visible to the analyst, and  $a_1, a_2$  are two unknown blinding parameters. These parameters were randomly sampled from a Gaussian distribution with  $\mu = 0$  and  $\sigma = 0.01$ . The values of the blinding parameters,  $a_1$  and  $a_2$ , were only examined after the full analysis procedure was finalised.

## 6.3 Final results

Figures 6.8 and 6.9 show the combination of measured  $\Delta Y_{\pi\pi\pi}^{\text{eff}}$  and  $\Delta Y_{K\pi\pi}$  values across all the sub-samples for the signal and control channels, respectively, at each stage of the kinematic weighting. The effect of the kinematic weighting in the control channel is clear:  $\Delta Y_{K\pi\pi}$  is around  $2.5\sigma$  from zero before the weighting, and

is compatible with zero at the level of around  $1\sigma$  after the weighting. The linear fits to obtain the measured values used in these combinations are shown in Figures 6.10 and 6.11 for the merged and resolved sub-samples of the signal channel, respectively, and in Figures 6.12 and 6.13 for the merged and resolved sub-samples of the control channel, respectively. After unblinding, a final result of  $\Delta Y_{\pi\pi\pi}^{\text{eff}} = (-1.2 \pm 6.0) \times 10^{-4}$  is obtained [146], where the uncertainty is statistical only. In the control channel, a measurement of  $\Delta Y_{K\pi\pi} = (-1.7 \pm 1.8) \times 10^{-4}$  is obtained [146], again with only a statistical uncertainty. The associated systematic uncertainties are discussed in Chapter 7. Correction factors for the dilutions due to the kinematic weighting procedure and finite decay time resolution, described in Sections 6.1.3 and 7.8, respectively, have been applied here after combining the results from the individual sub-samples.

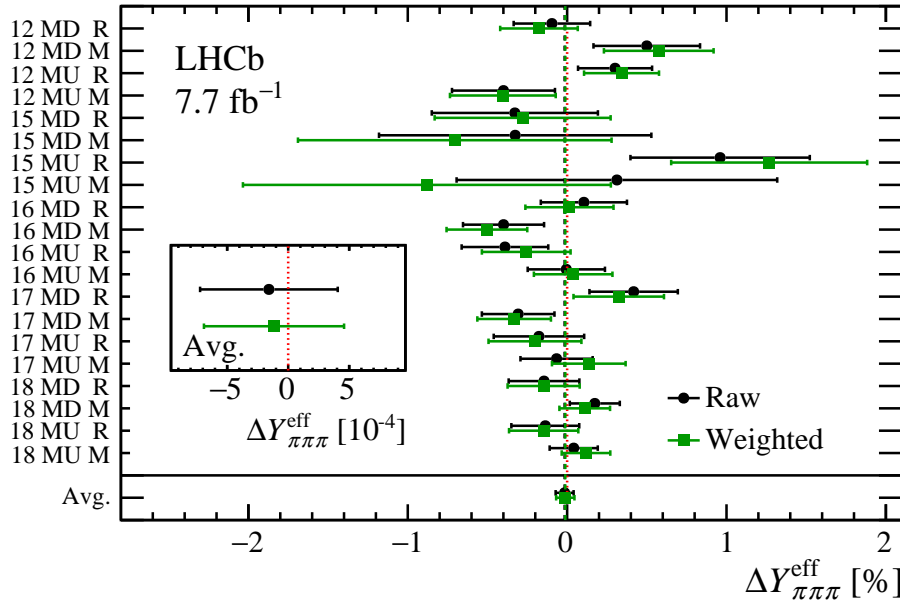


Figure 6.8: Combination of  $\Delta Y_{\pi\pi\pi}^{\text{eff}}$  values for the signal channel across all sub-samples [146].

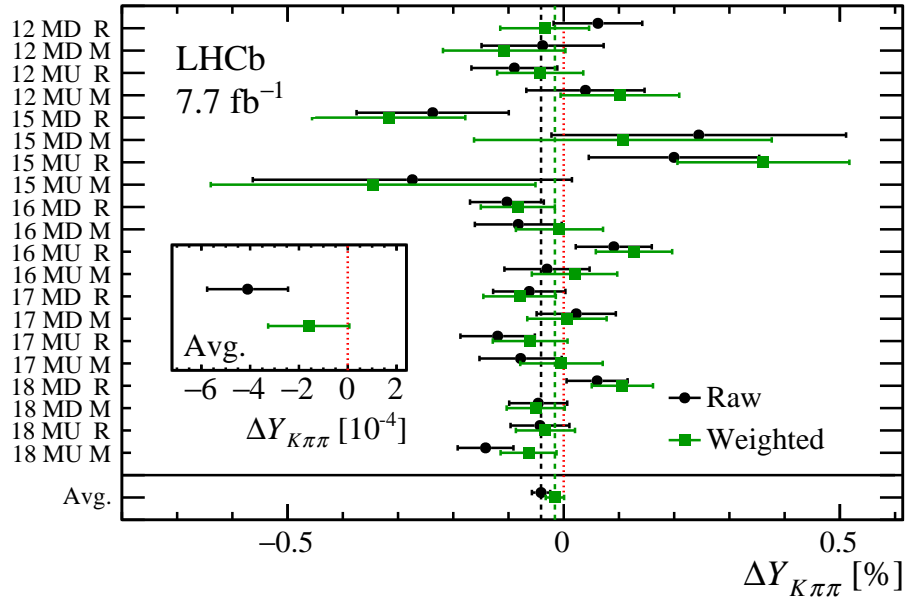


Figure 6.9: Combination of  $\Delta Y_{K\pi\pi}$  values for the control channel across all subsamples [146].

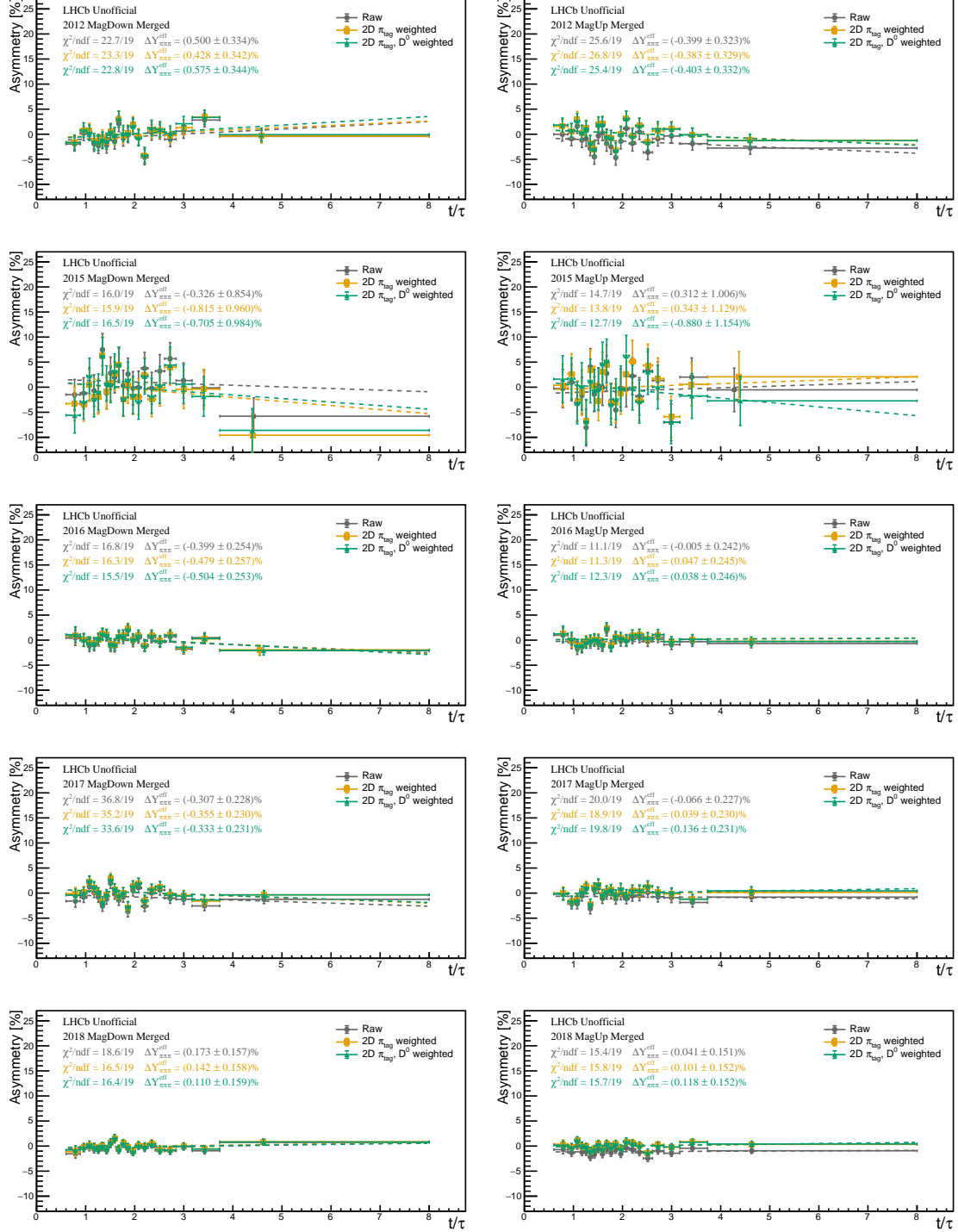


Figure 6.10: Linear fits to measured  $\mathcal{A}_f^{CP}(t)$  at each stage of the weighting procedure for the merged  $D^0 \rightarrow \pi^+ \pi^- \pi^0$  sub-samples.

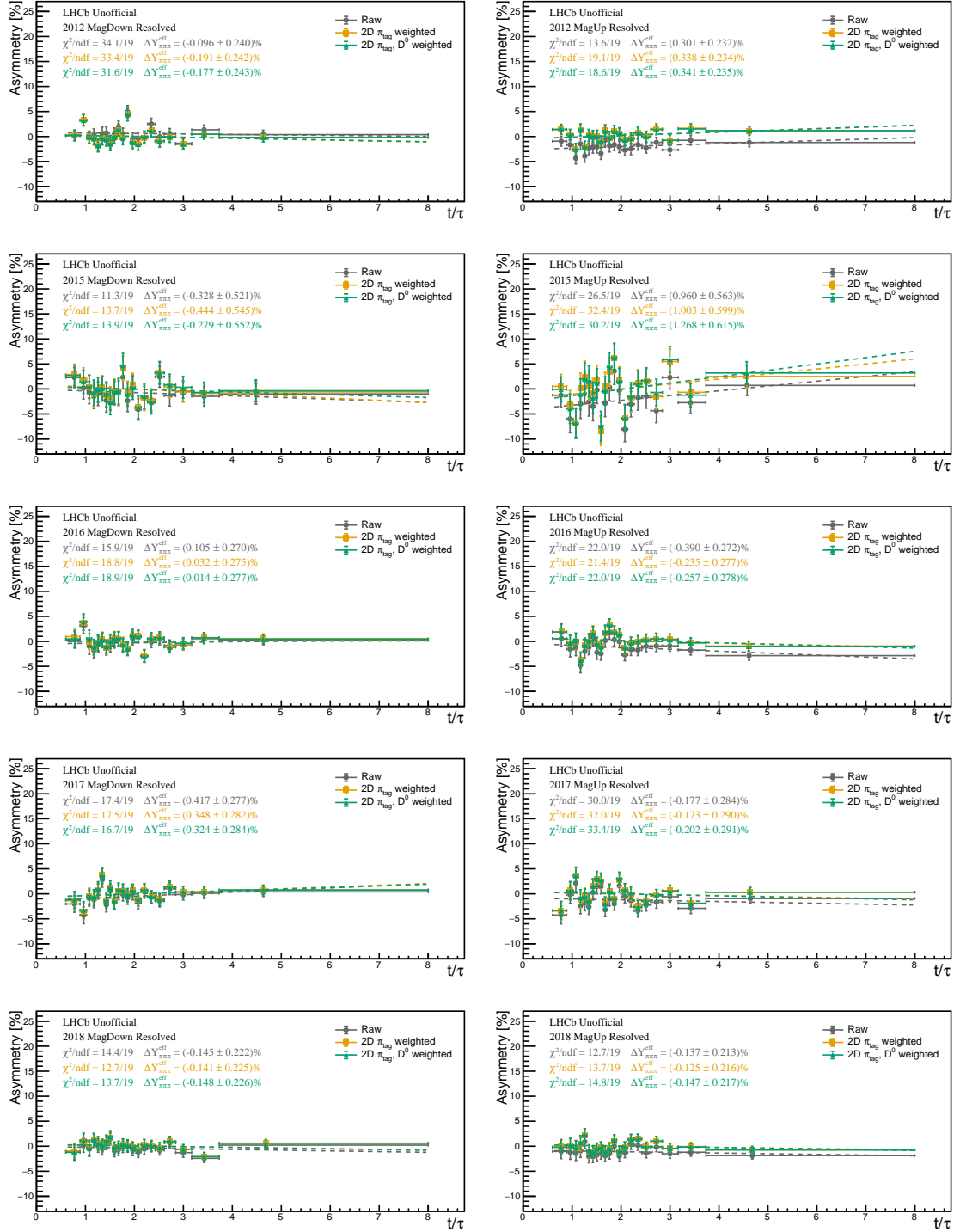


Figure 6.11: Linear fits to measured  $\mathcal{A}_f^{CP}(t)$  at each stage of the weighting procedure for the resolved  $D^0 \rightarrow \pi^+ \pi^- \pi^0$  sub-samples.

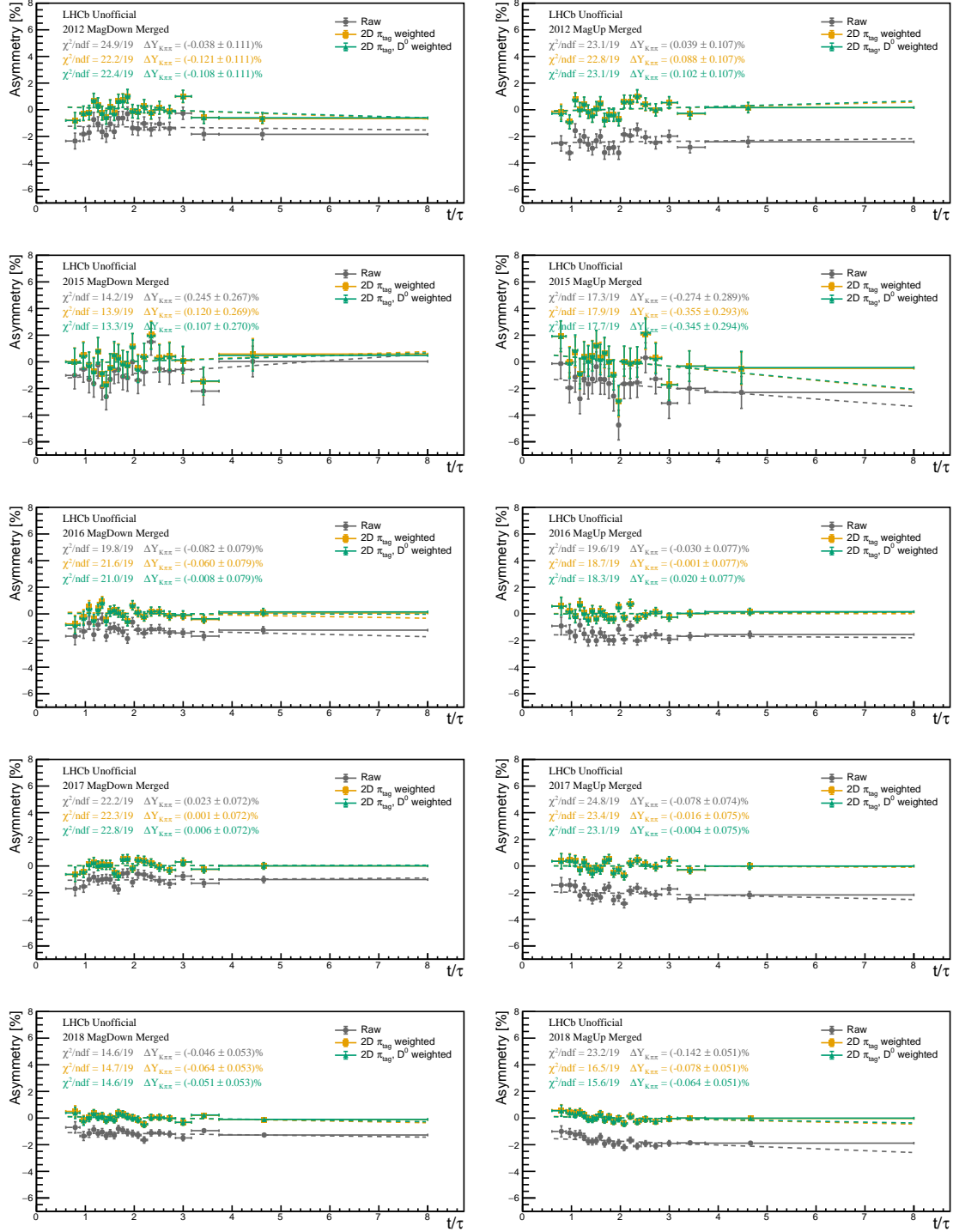


Figure 6.12: Linear fits to measured  $\mathcal{A}_f^{CP}(t)$  at each stage of the weighting procedure for the merged  $D^0 \rightarrow K^- \pi^+ \pi^0$  sub-samples.

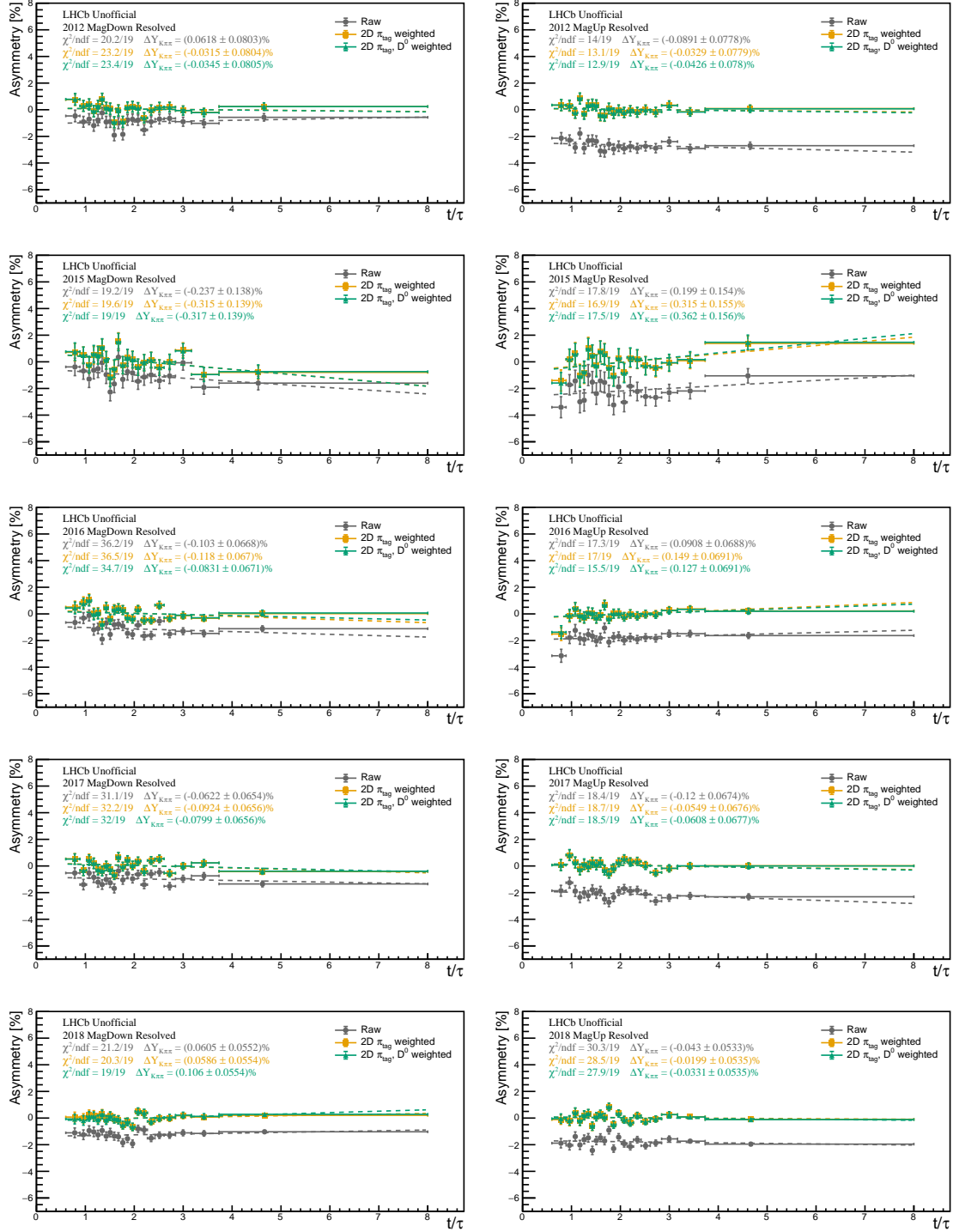


Figure 6.13: Linear fits to measured  $\mathcal{A}_f^{CP}(t)$  at each stage of the weighting procedure for the resolved  $D^0 \rightarrow K^- \pi^+ \pi^0$  sub-samples.

# Systematic uncertainties and stability checks

---

THE analysis methods used to determine  $\Delta Y$  were presented in Chapter 6, along with the final results which were obtained. This chapter will present the results of studies performed to determine the systematic uncertainties associated with those results, alongside some additional cross-checks performed to validate the analysis procedure.

## 7.1 Choice of $\Delta m$ fit model

Since the choice of PDF to model the  $\Delta m$  distributions in the analysis is somewhat arbitrary, it is possible that it introduces some bias into the measured asymmetries. While this effect is expected to be small since the  $D^0$  and  $\bar{D}^0$  candidates are fitted with identical shape parameters, it is nonetheless evaluated with two studies.

### 7.1.1 Test of underestimation of $\sigma_{\text{stat}}$

Firstly, a toy study was performed to evaluate a possible underestimation of the statistical error from the nominal fit model, which is described in Section 6.2. For each sub-sample of the data, a set of toy datasets (pseudoexperiments) are generated according to a 2D  $\Delta m$  and  $t/\tau_{D^0}$  PDF fitted to the data, separately for signal and background events and separately for  $D^0$  and  $\bar{D}^0$  events. The background decay-time shape is fitted to data from the upper  $\Delta m$  sideband, and the signal decay-time shape is fitted from a background subtracted  $t/\tau_{D^0}$  distribution in the  $\Delta m$  signal region. No artificial asymmetries are injected into the toy data. The nominal fitting

procedure is then applied to each toy dataset, keeping the first 5000 toy datasets where all fits converge. A systematic uncertainty given by  $\sqrt{\sigma_{\text{pull}}^2 - 1} \times \sigma_{\text{stat}}$  is assigned, where  $\sigma_{\text{pull}}$  is the width of a Gaussian fit to the pull distribution of measured  $\Delta Y$  values in the toy datasets. This procedure is justified briefly in Appendix D. If the width of the original pull distribution is smaller than unity, indicating an overestimate of the statistical uncertainty, no additional systematic uncertainty is applied. The pull distributions from this study are shown in Figure 7.1. For the signal channel, this results in a systematic uncertainty of  $0.64 \times 10^{-4}$ . In the control channel, the pull width is less than unity, so no systematic uncertainty is applied. Both pull distributions are also found to be unbiased.

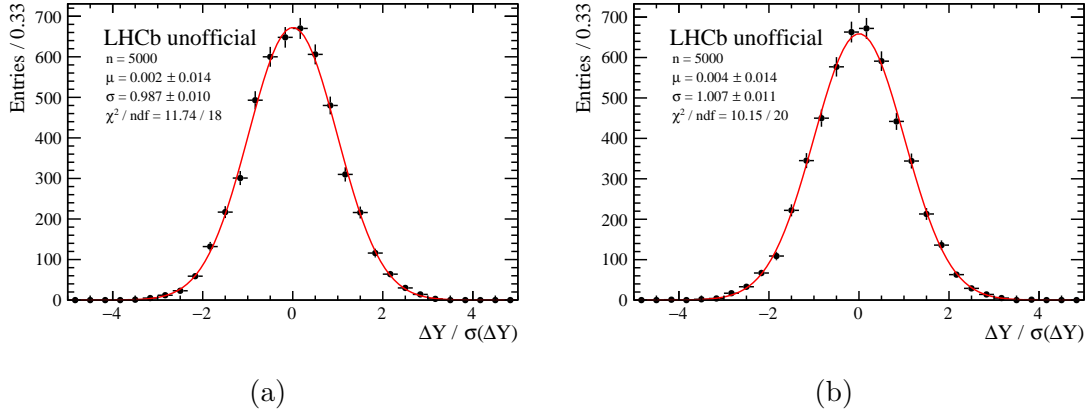


Figure 7.1:  $\Delta Y$  pull distributions from the  $\Delta m$  fit model toy studies in the (a) control channel and (b) signal channel.

### 7.1.2 Test of bias from $\Delta m$ fit model

To test for possible biases arising from the choice of  $\Delta m$  model, a toy study is performed. Toy datasets are generated and fitted in a similar manner to that described in Section 7.1.1. At the generation stage, an alternative  $\Delta m$  model is used, and the nominal model is used in the fitting stage. The alternative model is comprised of the sum of a Gaussian PDF and a Johnson- $S_U$  PDF [149] to model the signal shape, and a 3rd-order Chebychev polynomial to model the background shape. The resulting pull distributions for the measured time-dependent asymmetry are shown in Figure 7.2 for both the control and signal channels. A systematic uncertainty is assigned from the product of the central value of the mean of the pull distribution and the statistical uncertainty in each channel. This is equivalent to the bias on the

distribution of measured values for  $\Delta Y$  for each toy dataset. Systematic uncertainties of  $0.08 \times 10^{-4}$  and  $0.4 \times 10^{-4}$  are assigned in the control and signal channels, respectively.

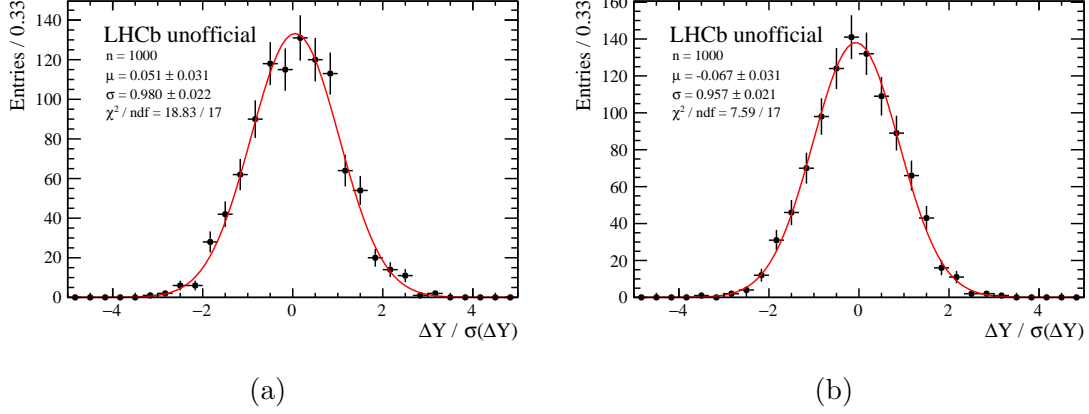


Figure 7.2:  $\Delta Y$  pull distributions from the alternative  $\Delta m$  fit model toy studies in the (a) control channel and (b) signal channel.

## 7.2 Contamination from secondary decays

In Section 1.3.3, when deriving the time-dependent asymmetry, it is implicitly assumed that a pure sample of prompt decays is being studied. However, in practice there will be some contamination from secondary decays where the  $D^{*\pm}$  meson is produced away from the PV in the decay of some long-lived  $b$ -hadron. Such decays are subject to different production and detection asymmetries than prompt decays. In addition, the fraction of secondary decays is expected to increase as a function of decay-time since the typical lifetime of  $b$ -hadrons contributing to secondary decays is much larger than the  $D^0$  lifetime [143]. Thus, even a constant difference in the asymmetries affecting prompt and secondary decays can give rise to a time-dependent asymmetry which will bias the measurement of  $\Delta Y$ . For a sample consisting of a mixture of prompt and secondary decays, the asymmetry measured as in Section 6.2 can be expressed as

$$\mathcal{A}_{\text{meas}}(t) = (1 - f_{\text{sec}}(t))\mathcal{A}_{\text{prompt}}(t) + f_{\text{sec}}(t)\mathcal{A}_{\text{sec}}(t). \quad (7.1)$$

Here,  $\mathcal{A}_{\text{prompt}}(t)$  and  $\mathcal{A}_{\text{sec}}(t)$  are the asymmetries in the prompt and secondary decays respectively,  $f_{\text{sec}}(t)$  is the fraction of the sample made up of secondary decays, and

$\mathcal{A}_{\text{meas}}(t)$  is the asymmetry measured in the data after the kinematic weighting. Thus, in order to disentangle the effect of such contamination, both the fraction of secondary decays in the sample as a function of decay-time, and their asymmetry must be measured. Both quantities are measured here using data from the control channel, and it is assumed that the effects are the same in the signal channel.

### 7.2.1 Measurement of the secondary fraction

Since secondary decays originate from the decay of long-lived  $b$ -hadrons, the production vertex of the  $D^{*\pm}$  meson is typically displaced from the PV. Thus, prompt and secondary decays can be distinguished by considering variables such as the Impact Parameter (IP) or  $\chi_{\text{IP}}^2$  of the  $D^0$  meson. The secondary fractions are determined here by fitting the  $\log(\chi_{\text{IP}}^2(D^0))$  distribution. To aid with stability and convergence in the fits, the prompt and secondary shapes are fitted from a simulated sample of mixed prompt and secondary  $D^0 \rightarrow \pi^+\pi^-\pi^0$  decays. Both the prompt and secondary PDF shapes are modelled using a Johnson- $S_U$  function. Comparisons of the results of these fits in the simulated samples with the known secondary fractions as a function of decay-time bin number are shown in Figure 7.3 for both the merged and resolved samples.

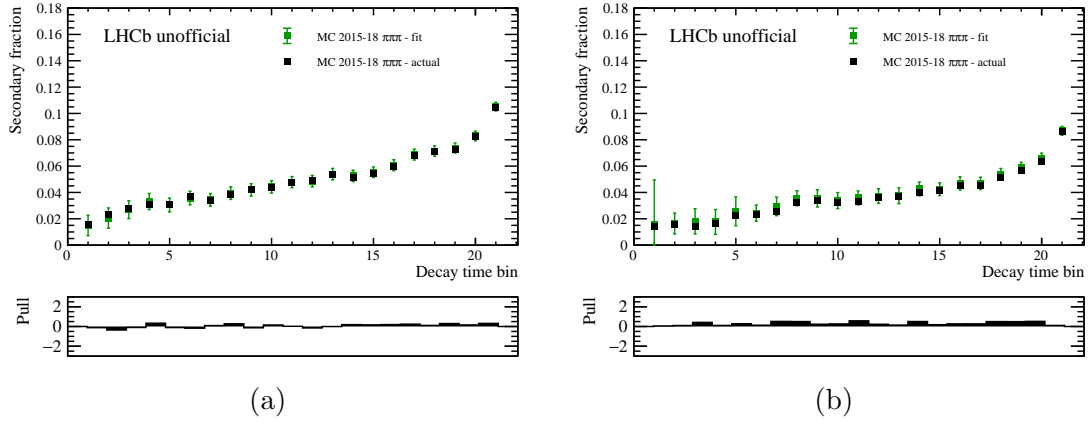


Figure 7.3: Comparison of measured and actual secondary fractions from simulated data for (a) merged and (b) resolved samples.

The secondary fractions in real data are fitted from the 2012 and 2017 sub-samples. The same secondary fractions as 2017 are assumed for the other years in Run 2. For these fits, the prompt and secondary PDF shapes from the simulated data fits are combined with an estimate of the shape of the  $\log(\chi_{\text{IP}}^2(D^0))$  combinatorial

background distribution under the  $\Delta m$  signal peak. Such an estimate is obtained simply by interpolating the binned  $\log(\chi_{\text{IP}}^2(D^0))$  distribution from the lower and upper  $\Delta m$  sidebands. Due to limited statistics in the simulated sample, the prompt shape parameters are allowed to float in the fits, with a Gaussian constraint on each of the parameters in the likelihood. The secondary shape parameters are completely fixed. The mean positions of both the prompt and secondary distributions are allowed to float, since it is known that simulated data does not accurately reproduce absolute values of  $\chi_{\text{IP}}^2$ . The combinatorial background fraction is fixed from a fit to the  $\Delta m$  distribution in each decay-time bin, and thus this component has no freedom. Examples of these fits are shown in Figures 7.4 and 7.5 for the merged and resolved samples, respectively.

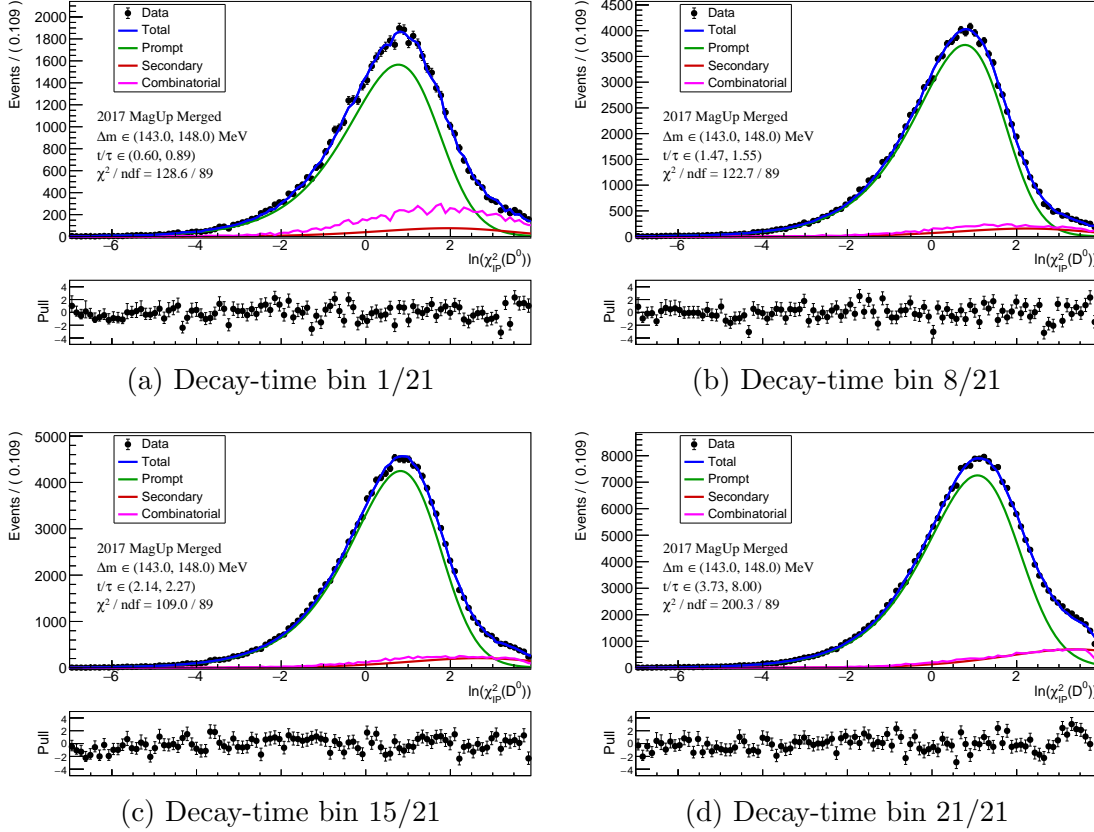


Figure 7.4: Example secondary fraction fits to the 2017 *MagUp* merged control channel sample.

The uncertainties on the secondary fractions from such fits appear to be underestimated, as the *MagUp* and *MagDown* distributions for merged sample show disagreements that are larger than the statistical uncertainties. This is assumed to be due

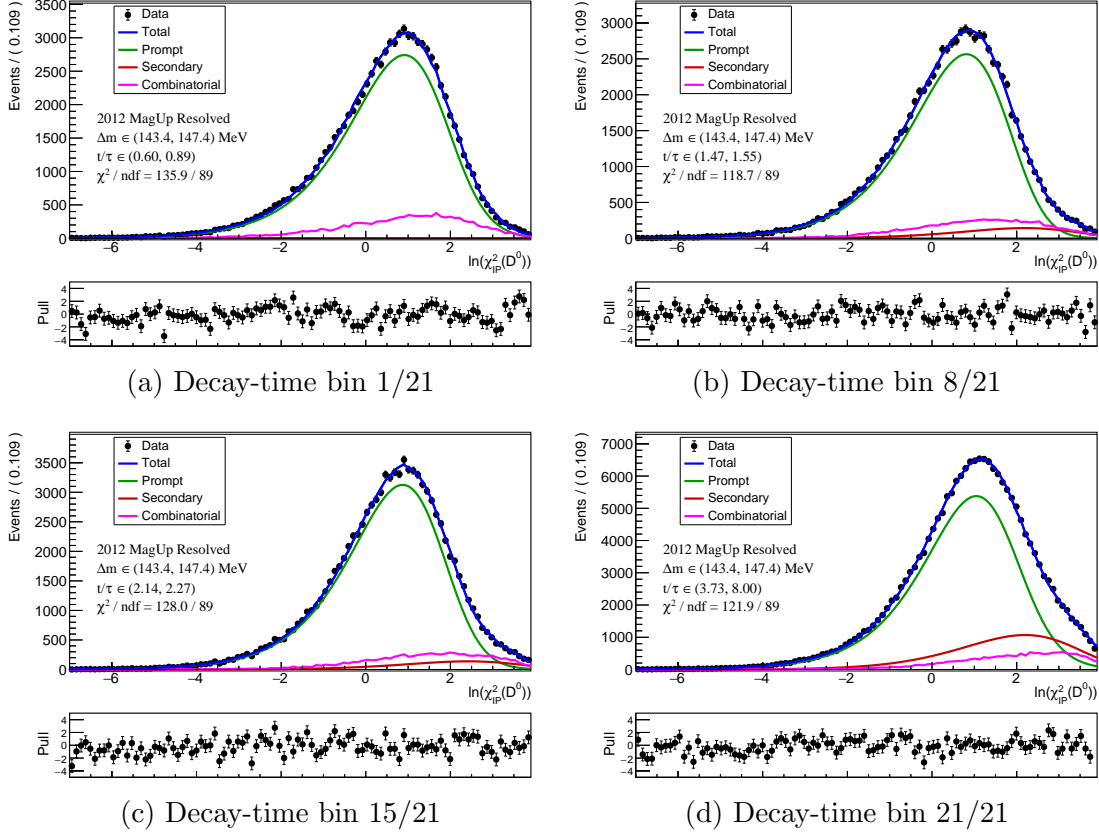


Figure 7.5: Example secondary fraction fits to the 2012 *MagUp* resolved control channel sample.

to uncertainties on the shapes of the secondary and combinatorial background components which have no freedom in the fits. Thus, the final values of the secondary fractions for the merged and resolved samples are computed by averaging the secondary fractions across the *MagUp* and *MagDown* samples for each category. The statistical uncertainties on the secondary fractions are obtained by taking the average of the uncertainties from the *MagUp* and *MagDown* samples in each decay-time bin. An additional systematic uncertainty is calculated as the standard deviation of the differences between the secondary fractions measured using the *MagUp* and *MagDown* samples across all decay-time bins. These values are plotted in Figure 7.6 for both the merged and resolved samples. Differences between the secondary fractions measured in Run 1 and Run 2 are not fully understood, although due to the significantly different triggers utilised in the two periods, such differences are not unexpected.

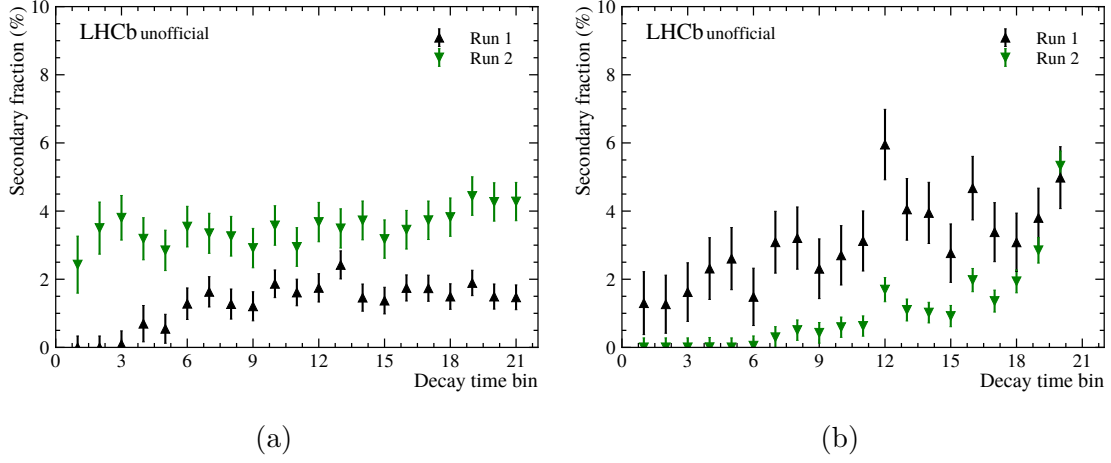


Figure 7.6: Secondary fractions used for the final systematic calculation for the (a) merged and (b) resolved samples.

### 7.2.2 Measurement of the secondary asymmetry

The secondary asymmetry is fitted for each of the control channel sub-samples based on a simultaneous flavour-tagged fit to the  $\log(\chi^2_{\text{IP}}(D^0))$  distribution in each decay-time bin, with the prompt, secondary and combinatorial PDF shapes entirely fixed. Within each sub-sample, the secondary fractions are assumed from the fits described in the previous section, and the shape parameters are first fitted from the flavour-integrated distributions in each decay-time bin. Then, the flavour-tagged fits are performed, where the only floating parameters are the secondary and prompt asymmetries in each decay-time bin. The combinatorial background asymmetry is taken from a flavour-tagged fit to the  $\Delta m$  distribution. No significant shift in the measured asymmetries is observed if the combinatorial background is constrained to have no asymmetry. Finally, the secondary asymmetry is assumed to carry no time dependence and a constant is fitted to the values across the decay-time bins. The time dependence on  $\mathcal{A}_{\text{sec}}$  will therefore be dropped in the following. Figure 7.7 shows the distribution of secondary asymmetries across all the sub-samples, before and after the kinematic weighting procedure. The sub-samples are found to be consistent with one another, and after the weighting an asymmetry affecting the secondary decays around the percent level remains.

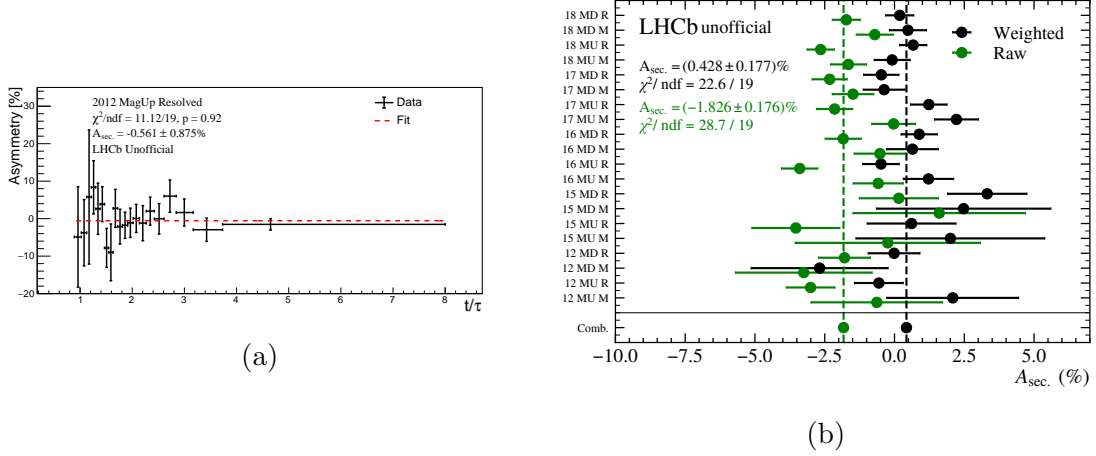


Figure 7.7: (a) Example fit to the secondary asymmetry of a single sub-sample of the data, and (b) combination of the secondary asymmetries across all sub-samples before the weighting (labelled raw) and after the weighting (labelled weighted), in the control channel.

### 7.2.3 Final secondary contamination systematic

A simple toy study is used to compute the final systematic uncertainty from the contamination of secondary decays. In each control channel sub-sample, the measured asymmetries are corrected by re-arranging Equation 7.1 in terms of the prompt asymmetry as

$$\mathcal{A}_{\text{prompt}}(t) = \frac{1}{1 - f_{\text{sec}}(t)} [\mathcal{A}_{\text{meas}}(t) - f_{\text{sec}}(t)\mathcal{A}_{\text{sec}}]. \quad (7.2)$$

Using this correction,  $\Delta Y_{\text{meas}}$  is defined as the gradient obtained from a linear fit to the  $\mathcal{A}_{\text{meas}}(t)$  values, while  $\Delta Y_{\text{prompt}}$  is the gradient obtained from a linear fit to the values corrected for secondary contamination,  $\mathcal{A}_{\text{prompt}}(t)$ . The secondary fractions are taken from the fits described in Section 7.2.1, while the secondary asymmetries are taken from each of the sub-samples themselves. Then, three contributions to the systematic are considered. Firstly, the measured asymmetries,  $\mathcal{A}_{\text{meas}}(t)$ , are varied 1000 times within their (assumed to be Gaussian) uncertainties to build a distribution of the difference  $\Delta \equiv \Delta Y_{\text{meas}} - \Delta Y_{\text{prompt}}$ . The values of  $\Delta Y_{\text{meas}}$  and  $\Delta Y_{\text{prompt}}$  are taken from a least-squares fit of a constant to all sub-samples, as in the real analysis. Then, the values of  $f_{\text{sec}}(t)$  in each decay-time bin and  $\mathcal{A}_{\text{sec}}$  are similarly varied within their uncertainties to give separate distributions of  $\Delta$ . Gaussian fits to each of these distributions are shown in Figure 7.8. The final systematic is taken as

the sum in quadrature of the mean and width of the fits for the toy where the  $\mathcal{A}_{\text{meas}}(t)$  values are varied, and the widths of the fits to the toy datasets where the  $\mathcal{A}_{\text{sec}}$  and  $f_{\text{sec}}(t)$  values are varied. Table 7.1 shows these individual contributions, along with the final systematic uncertainty. This is found to be  $0.84 \times 10^{-4}$  for the control channel. The same value is assumed for the signal channel. As an additional test, this toy study is also performed assuming 100% correlation between the secondary fractions in each decay time bin, and then again assuming 100% correlation between the secondary fractions across the decay time bins and also all of the subsets of the data. In both cases, the value of the systematic uncertainty does not change at the quoted precision. To test that the final systematic uncertainty is not significantly underestimated, a cross check where the data is split into two equally populated bins of  $\log(\chi^2_{\text{IP}}(D^0))$  and the time-dependent asymmetry is compared between these two sub-samples can be found in Appendix F.

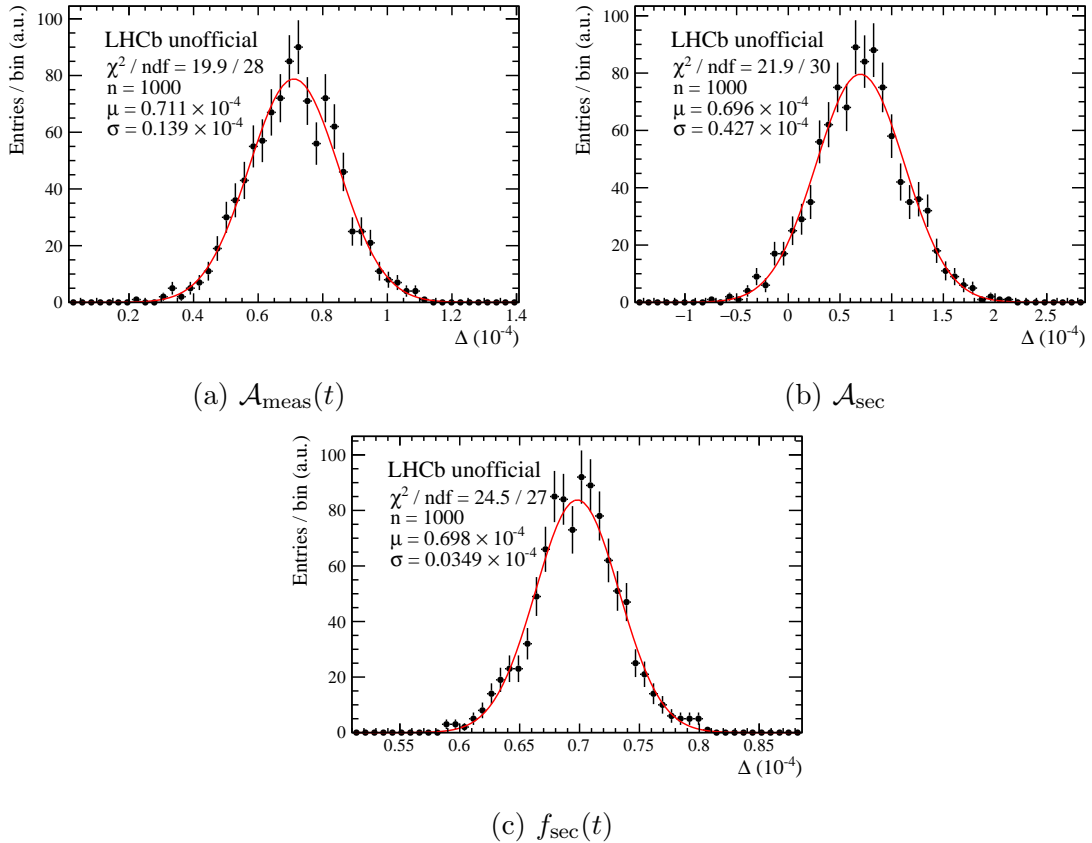


Figure 7.8:  $\Delta$  distributions from varying  $\mathcal{A}_{\text{meas}}(t)$ ,  $f_{\text{sec}}(t)$  and  $\mathcal{A}_{\text{sec}}$ . A Gaussian fit is overlaid in red.

Source	Value ( $10^{-4}$ )
$\mu\mathcal{A}_{\text{meas}}$	0.71
$\sigma\mathcal{A}_{\text{meas}}$	0.14
$\sigma\mathcal{A}_{\text{sec}}$	0.43
$\sigma f_{\text{sec}}$	0.03
$\sigma_{\text{sec}}^{\text{syst}}$	0.84

Table 7.1: Contributions to the final secondary contamination systematic.

### 7.2.4 Potential bias on the mean decay times

Since secondary decays are true  $D^{*+} \rightarrow D^0(\rightarrow \pi^+\pi^-\pi^0)\pi^+$  decays, their contribution will peak in the  $\Delta m$  distribution and be included in the signal component of the  $\Delta m$  fits used to extract the time-dependent asymmetries. Since the mean decay time in each bin is computed based on a background subtraction from these fits, it will potentially be biased towards larger values due to the larger average lifetime of secondary decays; this could in turn cause a bias of the measured  $\Delta Y$ . To check for this, the measurement is re-performed using a mean decay time in each bin taken from prompt, truth-matched simulation passing the full selection. The simulation is integrated across data taking periods and magnet polarities due to relatively low statistics compared to the data. When performing the measurement using these alternative mean decay times, the results are shifted (in absolute terms) by  $0.74 \times 10^{-4}$  and  $0.01 \times 10^{-4}$  in the signal and control channels, respectively, from the nominal results. Figure 7.9 shows the ratio of mean decay times computed from data to that from the simulation. No clear trend is observed towards the mean decay times from data being larger than those from simulation, and in general the values agree to within  $\mathcal{O}(1\%)$ . Based on these studies, it is concluded that no systematic uncertainty should be assigned here.

## 7.3 Choice of decay-time binning scheme

A systematic uncertainty is assigned for the choice of decay-time binning scheme by re-computing the bin edges with varying numbers of bins, and repeating the analysis on both the (blinded) signal channel and the control channel. Since the nominal number of bins is 21, a range of bin numbers which encompasses half and double this value are used. The results are shown in Figure 7.10, with the nominal results highlighted in red. The value of the systematic uncertainty is taken as the standard

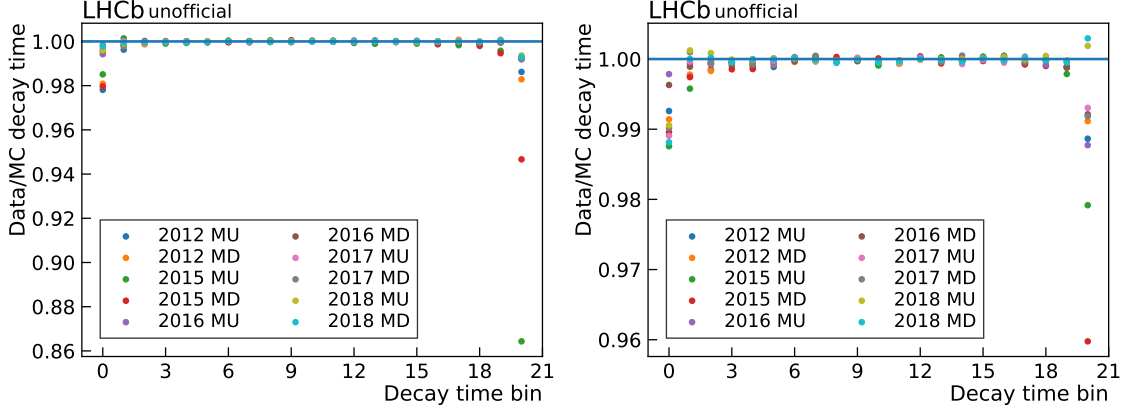


Figure 7.9: Ratio of mean decay-times measured from data and simulation, for the (a) merged and (b) resolved  $\pi^0$  categories in the signal channel. MU and MD represent *MagUp* and *MagDown*, respectively.

deviation of the measured values of  $\Delta Y_{\pi\pi\pi}^{\text{eff}}$  ( $\Delta Y_{K\pi\pi}$ ). This results in systematic uncertainties of  $1.04 \times 10^{-4}$  for the signal channel, and  $0.14 \times 10^{-4}$  for the control channel.

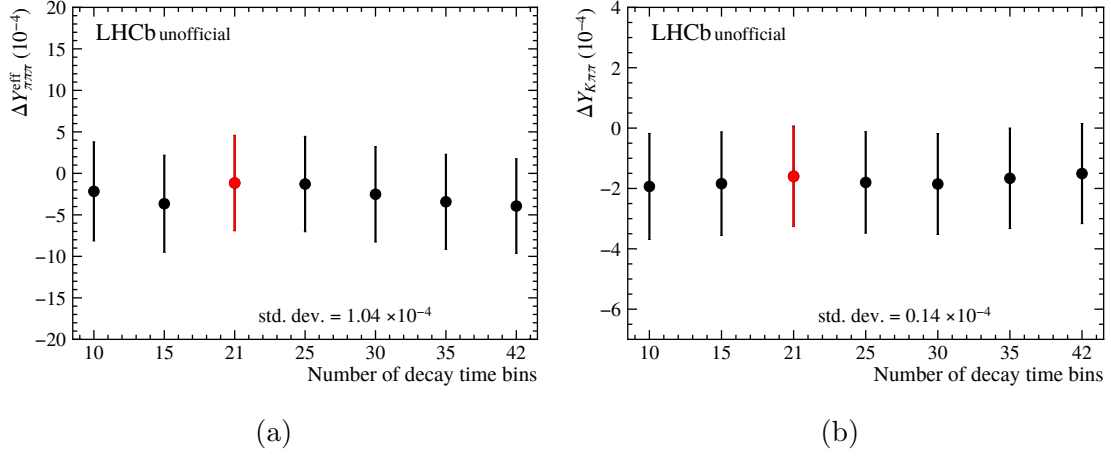


Figure 7.10: Results of decay-time binning study for the (a) signal channel and (b) control channel. The nominal binning scheme is highlighted in red.

## 7.4 Choice of kinematic weighting binning scheme

The effect of the nominal choice of binning scheme for the kinematic weighting is assessed by varying the total number of bins by a factor,  $f$ , in the range  $\frac{1}{4}$  to 4,

corresponding to halving and doubling the number of bins used along each axis. The factors used are:  $\frac{1}{4}$ ,  $\frac{1}{3}$ ,  $\frac{1}{2}$ , 1, 2, 3, and 4. For each factor, the number of bins along a given axis is computed by rounding  $\sqrt{f} \times n$  to the nearest integer, where  $n$  is the number of bins for a given variable and weighting stage in the nominal scheme described in Section 6.1.2. To ensure an identical sample of events is analysed for each factor, only the events retained by the finest binning scheme are used throughout. The results of this study are presented in Figure 7.11. A systematic uncertainty is assigned as the standard deviation of the measured values of  $\Delta Y_{K\pi\pi}$  across the range of factors. This study is not repeated on the signal channel due to a lack of statistics for the finest binning scheme. This results in a systematic uncertainty of  $0.22 \times 10^{-4}$  for both the signal and control channels.

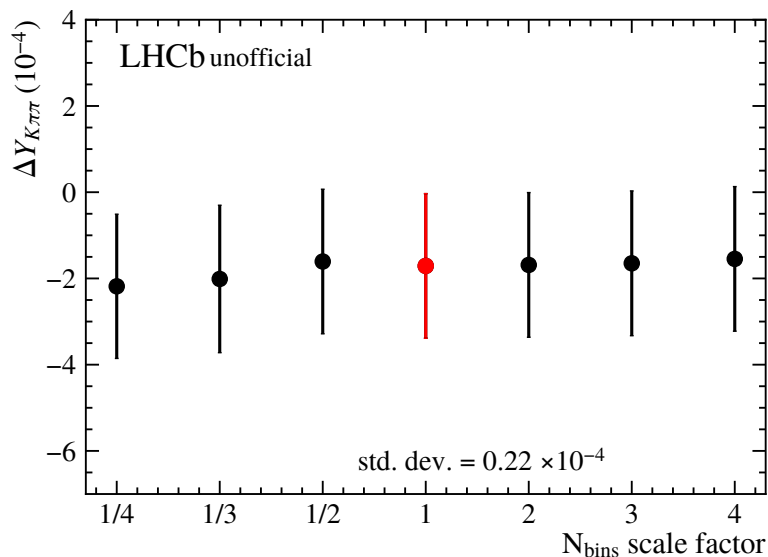


Figure 7.11: Results of kinematic weighting binning study in the control channel. The nominal binning scheme is highlighted in red.

## 7.5 Effect of phase-space efficiency on the $CP$ -even fraction

A non-uniform efficiency across the phase-space could bias the effective value of the  $CP$ -even fraction, and thus the measured  $\Delta Y$ . The efficiency variations across the phase-space are studied using simulated data. The numerator of the efficiency is taken from a sample of full MC data. Events in the MC sample must satisfy

the same selection requirements as candidates in the real data, and a set of truth-matching requirements. The denominator is taken from a sample of particle-gun simulated data generated with the same phase-space model as the full MC data, with no selection requirements applied. Truth level variables are used for both samples. Two different representations of the efficiency are then considered. The first uses an adaptive binning scheme across the Dalitz plot to form a histogram representation of the efficiency. The second utilises a 5th-order two-dimensional polynomial which is fitted to an efficiency histogram with uniform bin areas. The efficiency maps across the Dalitz plot for both methods are shown in Figure 7.12. Since different samples are used for the numerator and denominator, the  $z$ -scale is arbitrary. Figures 7.13 and 7.14 show the corresponding plots when the data is split by  $\pi^0$  category; one can see that the efficiencies for the different  $\pi^0$  categories are significantly different.

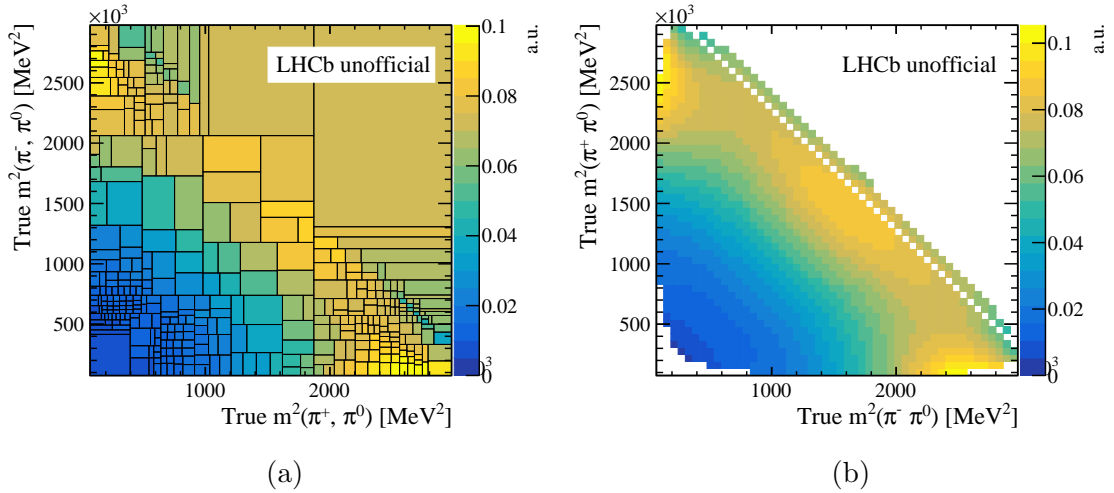


Figure 7.12: Efficiency variation across the Dalitz plot from simulation for both  $\pi^0$  categories using (a) a histogram representation and (b) a polynomial parameterisation.

The effect of these efficiency maps on the  $CP$ -even fraction is studied by calculating the  $CP$ -even fraction, using an amplitude model measured by BaBar [53], as

$$F_+ = \frac{\int |A_+|^2 ds_{13} ds_{23}}{\int (|A_+|^2 + |A_-|^2) ds_{13} ds_{23}}, \quad (7.3)$$

where  $A_{+(-)}(s_{13}, s_{23})$  is the amplitude for the  $CP$ -even (odd) combination of  $D^0$  and  $\bar{D}^0$ . The definitions  $s_{13} \equiv s(\pi^+, \pi^0)$  and  $s_{23} \equiv s(\pi^-, \pi^0)$  for  $D^0$  candidates are made here, with the pion charges swapped for  $\bar{D}^0$ . The integral is performed numerically

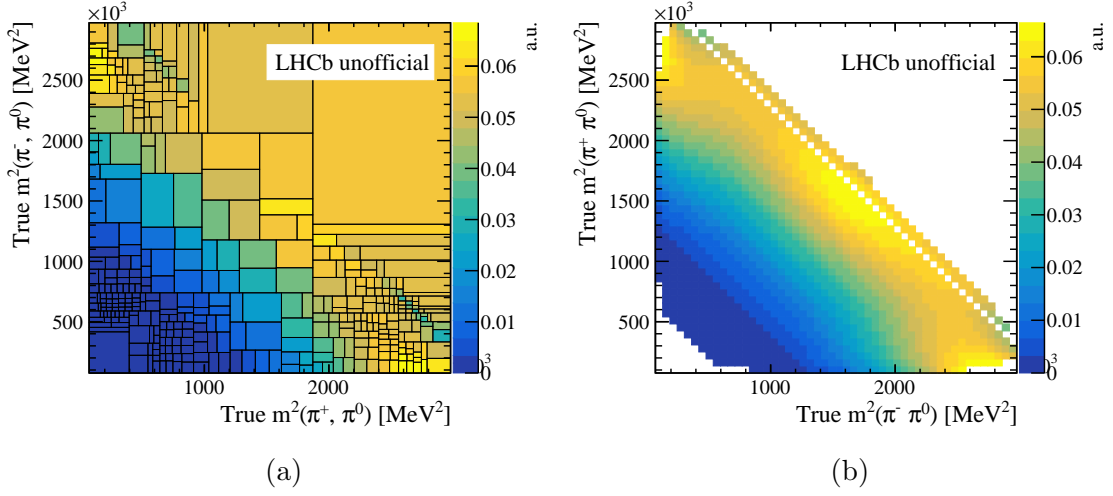


Figure 7.13: Efficiency variation across the Dalitz plot from simulation for the merged  $\pi^0$  category using (a) a histogram representation and (b) a polynomial parameterisation.

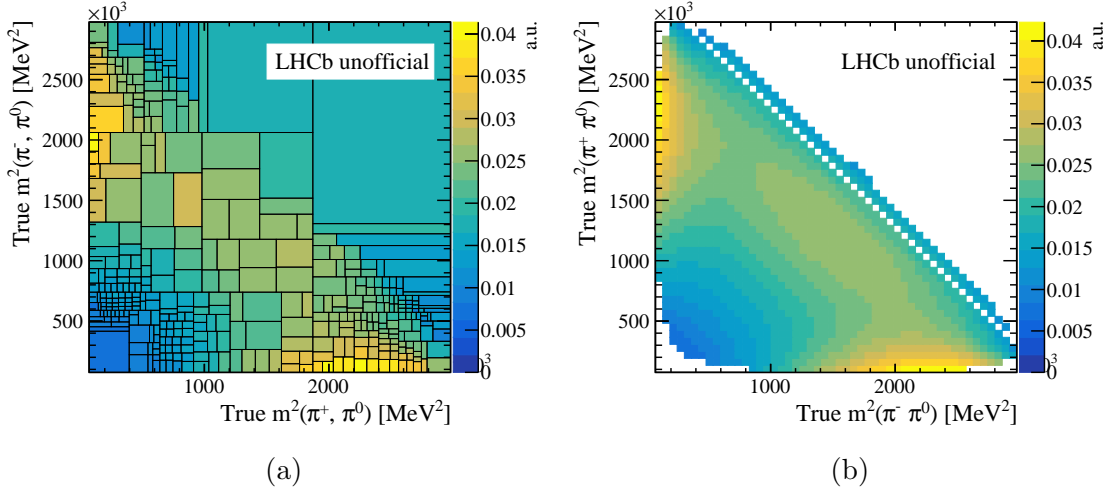


Figure 7.14: Efficiency variation across the Dalitz plot from simulation for the resolved  $\pi^0$  category using (a) a histogram representation and (b) a polynomial parameterisation.

with a Monte Carlo procedure. The amplitude model is implemented using the EvtGen package. Figure 7.15 shows the Dalitz distribution and a sample of toy computations of  $F_+$ , without applying any efficiency effects. The estimated value of  $F_+ \approx 0.945$  is in reasonable agreement with the model-independent measurement given in Equation 1.83 ( $F_+ = 0.973 \pm 0.017$  [62]). To reduce — and understand the size of — the effect of statistical fluctuations in the numerical integration, 1000 toy datasets are generated, with  $F_+$  computed with and without the efficiency model in each. This is repeated for both the histogram and polynomial representations,

$\pi^0$ category	$\Delta F_+$ , histogram efficiency (%)	$\Delta F_+$ , polynomial efficiency (%)
Resolved	-0.02	+0.01
Merged	+1.66	+1.68
Both	+1.00	+1.00
Merged/resolved average	+0.99	+1.00

Table 7.2: Shifts in  $F_+$  for each  $\pi^0$  category and efficiency representation.

and for the merged, resolved and combined efficiencies. Examples of the results of such a toy study, in terms of the shift in the  $CP$ -even fraction by applying the efficiency model, are shown in Figure 7.16 for both efficiency representations using the combined merged and resolved simulated sample. The differences obtained in  $F_+$  with and without applying the efficiencies are given in Table 7.2 for all possible configurations. The statistical uncertainties on each of the shifts are an order of magnitude smaller than the precision to which they are reported. The ‘merged/resolved average’ row of the table represents an average of the merged and resolved shifts, weighted by their yields in real data. These values are in excellent agreement with the shift measured using the combined efficiency map from simulation. Both efficiency representations are in good agreement. Based on these studies, an additional uncertainty on  $F_+$  of 1% is assigned. The resulting systematic uncertainty is then computed using Equation 7.5. This results in a systematic uncertainty of  $0.021|\Delta Y|$  in the signal channel. The simulated data used for this study are not corrected to match real data; due to the negligible size of this systematic the impact of this choice is also expected to be negligible.

## 7.6 Uncertainty on the $CP$ -even fraction

After  $\Delta Y_{\pi\pi\pi}^{\text{eff}}$  is measured, the value of  $\Delta Y$  is computed from Equation 1.82 as

$$\Delta Y = \frac{\Delta Y_{\pi\pi\pi}^{\text{eff}}}{|2F_+ - 1|}. \quad (7.4)$$

Using the value of  $F_+^{\pi\pi\pi}$  and its uncertainty from Equation 1.83, the uncertainty on  $|\Delta Y|$  associated with the uncertainty on  $F_+$  is thus given by

$$\sigma(\Delta Y)_{F_+} = \left| \frac{\partial \Delta Y}{\partial F_+} \right| \sigma_{F_+} = \frac{2\sigma_{F_+}}{|2F_+ - 1|^2} |\Delta Y_{\pi\pi\pi}^{\text{eff}}| = \frac{2\sigma_{F_+}}{|2F_+ - 1|} |\Delta Y| = 0.036|\Delta Y|. \quad (7.5)$$

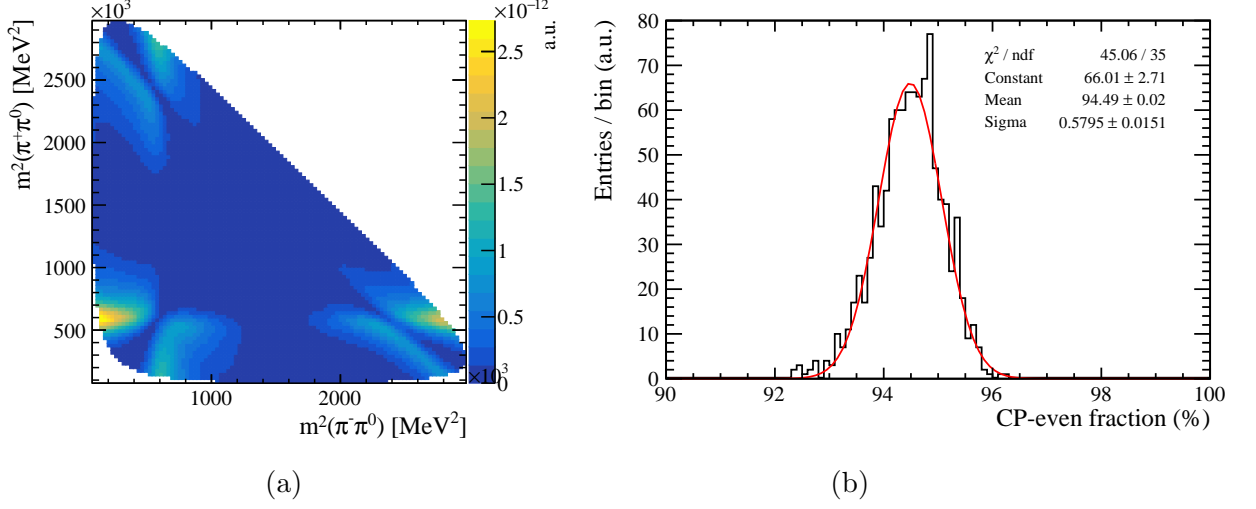


Figure 7.15: (a) Dalitz distribution and (b) CP-even fraction toy results using the BaBar-2016 model [53] in EvtGen.

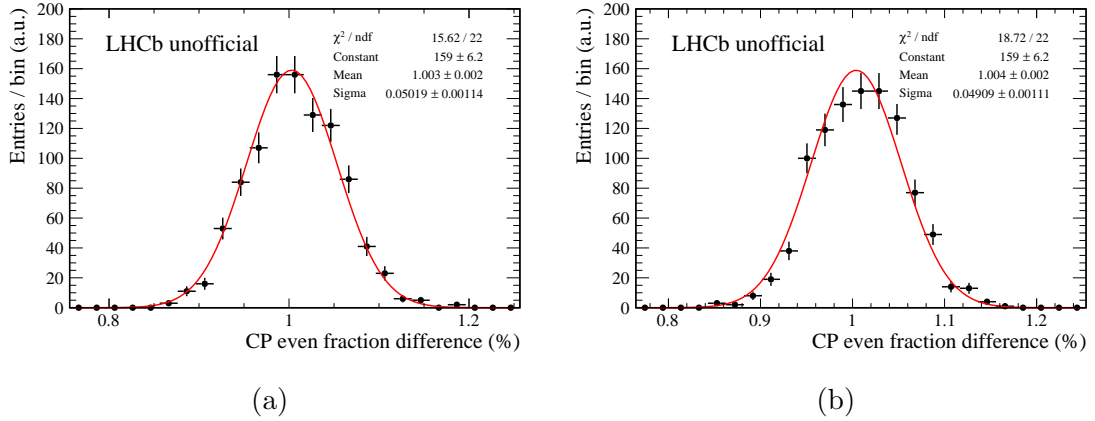


Figure 7.16: Example output of a toy study to investigate the effect of the phase-space efficiency on the  $CP$ -even fraction, using the (a) histogram efficiency model and (b) polynomial efficiency parameterisation with the combined resolved and merged simulated samples.

## 7.7 Uncertainty on the $D^0$ meson lifetime

The current world average of the  $D^0$  lifetime from the PDG is  $0.4103 \pm 0.0010$  ps [8]. The measurement of  $\Delta Y_{\pi\pi\pi}^{\text{eff}}$  is obtained here from a linear fit to the time-dependent asymmetry, which can be written (up to a constant offset) as

$$A_{CP}(t) \sim \Delta Y_{\pi\pi\pi}^{\text{eff}} \frac{t}{\tau_{D^0}} = at, \quad (7.6)$$

where  $a$  is defined as the gradient of the asymmetry. The uncertainty on  $\Delta Y$  due

to the uncertainty on  $\tau_{D^0}$  is given by

$$\sigma(\Delta Y_{\pi\pi\pi}^{\text{eff}})_{\tau_{D^0}} = \left| \frac{\partial \Delta Y_{\pi\pi\pi}^{\text{eff}}}{\partial \tau_{D^0}} \right| \sigma_{\tau_{D^0}} = \frac{\sigma_{\tau_{D^0}}}{\tau_{D^0}} |\Delta Y_{\pi\pi\pi}^{\text{eff}}| = 0.0024 |\Delta Y_{\pi\pi\pi}^{\text{eff}}|, \quad (7.7)$$

since  $|\partial \Delta Y_{\pi\pi\pi}^{\text{eff}} / \partial \tau_{D^0}| = |a|$ .

## 7.8 Decay-time resolution

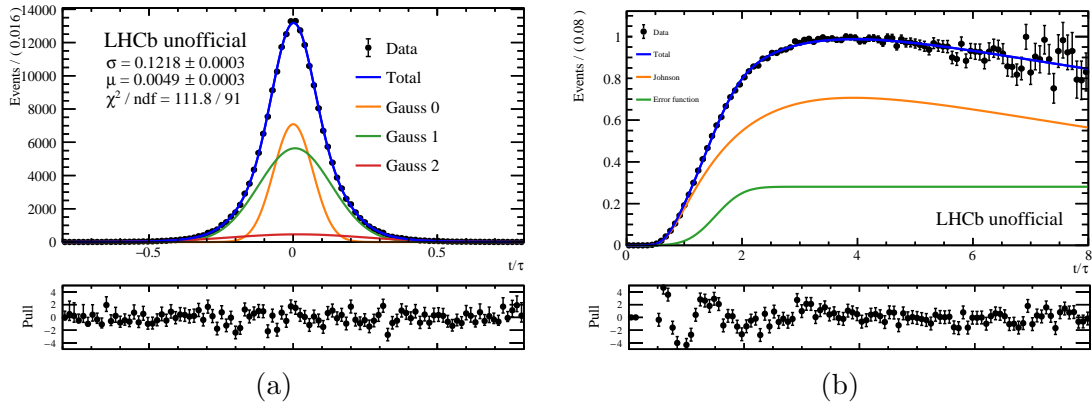


Figure 7.17: (a) Example decay-time resolution and (b) acceptance fits for the resolved  $\pi^0$  category.

A finite decay time resolution will cause a dilution of the measured time-dependent asymmetry. The effect of this is assessed by generating and fitting a set of 1000 toy datasets with an injected, non-zero, time-dependent asymmetry. For each of the toy datasets, descriptions of the  $\Delta m$  and decay time distributions are required for both signal and background. The  $\Delta m$  distribution shapes are fitted from the integrated  $\Delta m$  distributions across all sub-samples, separately for merged and resolved candidates. The decay time shapes are modelled as a resolution function convolved with an exponential of the form  $\exp(-t/\tau_{D^0})$ , where  $\tau_{D^0}$  is taken as its PDG value [143], and multiplied by an acceptance function. The resolution function is modelled as the sum of three Gaussian distributions, and fitted from simulated data. The acceptance is modelled as the sum of an error function and Johnson- $S_U$  distribution and fitted to background-subtracted data divided by the convolution of the exponential and resolution functions. The combinatorial background decay time distribution is fitted in a similar manner, using data from the  $\Delta m$  sideband. Example resolution and acceptance fits are shown in Figure 7.17. Correlations between  $\Delta m$  and the de-

cay time are neglected in the toy generation. The number of candidates generated for each of the signal and background components for each toy are taken from the integrated fits.

The injected values of  $\Delta Y_{\pi\pi\pi}^{\text{eff}}$  are chosen as  $[\pm 3, \pm 5, \pm 7] \times \sigma_{\text{stat}}^{\pi\pi\pi}$ . The dilution due to the decay-time resolution is calculated by fitting a linear slope to the measured against injected values, as shown in Figure 7.18. The measured value of  $\Delta Y_{\pi\pi\pi}^{\text{eff}}$  is corrected by multiplying with the inverse of this gradient. A systematic uncertainty is assigned as the difference between the corrected and uncorrected values, corresponding to  $0.003 \times |\Delta Y_{\pi\pi\pi}^{\text{eff}}|$ . A dilution of the same magnitude is assumed in the control channel. These results rely on a sample of simulated data which has not been corrected to match real data, but, due to the size of this systematic, the effect of this choice is expected to be negligible.

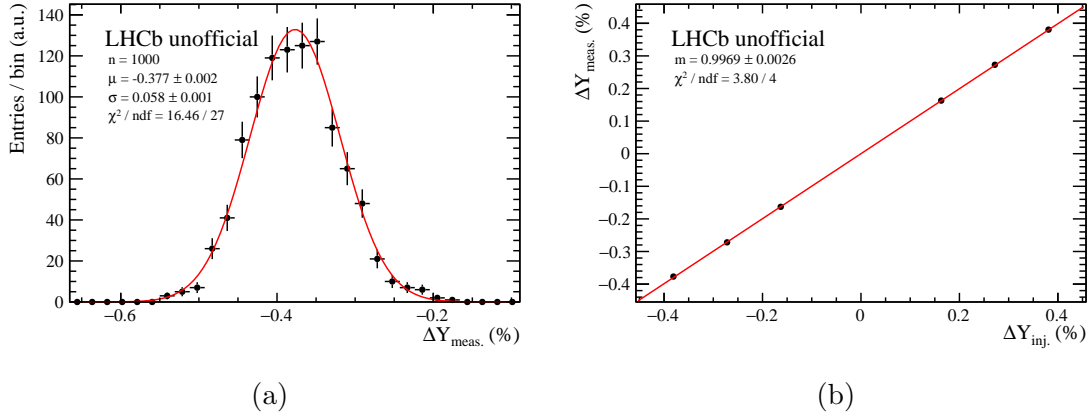


Figure 7.18: (a) Example individual toy-study results for an injected gradient of  $-3.81 \times 10^{-4}$ , and (b) dilution gradient fit for the decay-time resolution studies.

## 7.9 Phase-space dependent detection asymmetries

A detection asymmetry which varies across the phase-space could bias the measured  $\Delta Y$  if either the phase-space efficiency or the asymmetry itself vary with decay-time. Such an asymmetry could arise, for example, due to a kinematic-dependent asymmetry between oppositely charged kaons (in the control channel) or pions (in both channels). For example, the largest contribution to the decay  $D^0 \rightarrow \pi^+\pi^-\pi^0$  arises from the resonance  $D^0 \rightarrow \rho^+\pi^-$ , while the  $\bar{D}^0$  decay is dominated by the

component  $\bar{D}^0 \rightarrow \rho^- \pi^+$ . The kinematic distributions of the oppositely charged pions — but, crucially, not of the same-sign pions — between  $D^0$  and  $\bar{D}^0$  decays should therefore agree. A kinematic-dependent  $\pi^+ \pi^-$  detection asymmetry will therefore lead to a time-dependent asymmetry in the presence of correlations between the kinematics and decay time.

### 7.9.1 Procedure for determining the detection asymmetry

Such detection asymmetries are determined using samples of  $D_{(s)}^+ \rightarrow 3h$  decays and a similar approach to that employed in previous analyses [45, 46]. To determine the relevant detection asymmetries the cancellation of all other detection asymmetries based on the topologically similar 2-body decay  $D_{(s)}^+ \rightarrow \phi(\rightarrow K^- K^+) \pi^+$  is relied upon. All of the decays considered are currently experimentally compatible with no CP asymmetry [8]. Using this approach, the relevant detection asymmetries can be written as

$$\begin{aligned} A_{\text{det}}^{\pi\pi} &= A(D_{(s)}^+ \rightarrow \pi^+ \pi^+ \pi^-) - A(D_{(s)}^+ \rightarrow \phi(\rightarrow K^- K^+) \pi^+) \\ A_{\text{det}}^{K\pi} &= A(D^+ \rightarrow K^- \pi^+ \pi^+) - A(D^+ \rightarrow \phi(\rightarrow K^- K^+) \pi^+). \end{aligned} \quad (7.8)$$

One of the same-sign pions for each  $D_{(s)}^+ \rightarrow \pi^+ \pi^+ \pi^-$  candidate is randomly chosen to correspond to the pion from the  $D^+ \rightarrow \phi \pi^+$  decay, henceforth referred to as the ‘bachelor’ pion,  $\pi^+_{\text{b}}$ .

The selections are aligned to the signal and control channels as closely as possible. The trigger lines used to select each category of  $D_{(s)}^+ \rightarrow 3h$  candidates are shown in Table 7.3. The kinematic and PID selections listed in Table 5.7 are applied as far as possible. Kinematic selections on the  $\pi^0$  are applied to the bachelor pion. No attempt is made to align the trigger selections or the BDT selections due to complications arising from their dependence on variables for which no equivalent exists in the  $D_{(s)}^+$  decays (e.g.  $\pi^0$  CL) or kinematic variables which do not exist in the nTuples and are non-trivial to compute without re-processing the samples (e.g.  $\chi^2_{\text{IP}}$  selections on the  $h^+ h^-$  combination), and handling the interplay of the two HLT2 lines utilised in Run 2. Kinematic selections on the  $\pi^0$  are applied to the bachelor pion.

The phase-space is defined in terms of the helicity angle,  $\theta_{\pi\pi}$  ( $\theta_{K\pi}$ ), and the invariant mass of the two charged hadrons of interest,  $m^2(\pi^+, \pi^-)$  ( $m^2(K^-, \pi^+)$ ).

Decay	HLT2 line
$D^+ \rightarrow \pi^+ \pi^+ \pi^-$	Hlt2CharmHadDpToPimPipPipTurbo
$D_s^+ \rightarrow \pi^+ \pi^+ \pi^-$	Hlt2CharmHadDspToPimPipPipTurbo
$D^+ \rightarrow K^- \pi^+ \pi^+$	Hlt2CharmHadDpToKmPipPipTurbo
$D^+ \rightarrow \phi \pi$	Hlt2CharmHadDpToKmKpPipTurbo
$D_s^+ \rightarrow \phi \pi$	Hlt2CharmHadDspToKmKpPipTurbo

 Table 7.3: HLT2 lines used to select  $D_{(s)}^+ \rightarrow 3h$  candidates.

The phase-space is divided into 30 bins, and in each bin a kinematic weighting procedure to match the kinematics of the calibration samples and the signal and control datasets using GBReweighter from hep\_ml [150] is performed. The two-body  $D_{(s)}^+$  samples are shared by every bin of the phase space, with different weights applied in each bin. The weighting is performed in three stages:

1. Match the azimuth angle,  $\varphi$ , distributions of  $\pi^+, \pi^-$  ( $K^-, \pi^+$ ) in  $D_{(s)}^+ \rightarrow \pi^+ \pi^+ \pi^-$  ( $D^+ \rightarrow K^- \pi^+ \pi^+$ ) to  $D^0 \rightarrow \pi^+ \pi^- \pi^0$  ( $D^0 \rightarrow K^- \pi^+ \pi^0$ )
2. Match the  $p_T, \eta$  distributions of  $\pi^+, \pi^-$  ( $K^-, \pi^+$ ) in  $D_{(s)}^+ \rightarrow \pi^+ \pi^+ \pi^-$  ( $D^+ \rightarrow K^- \pi^+ \pi^+$ ) to  $D^0 \rightarrow \pi^+ \pi^- \pi^0$  ( $D^0 \rightarrow K^- \pi^+ \pi^0$ )
3. Match the  $p_T, \eta$  distributions of  $D_{(s)}^+, \pi_b^+$  in  $D_{(s)}^+ \rightarrow \phi(\rightarrow K^- K^+) \pi_b^+$  to  $D_{(s)}^+, \pi_b^+ D_{(s)}^+ \rightarrow \pi^+ \pi^+ \pi^-$  ( $D^+ \rightarrow K^- \pi^+ \pi^+$ )

A time-dependence in the measured asymmetry is allowed by binning in  $\theta_{\pi\pi}$  ( $\theta_{K\pi}$ ) and decay-time, again repeating the weighting procedure in each bin. For the case of  $D_{(s)}^+ \rightarrow \pi^+ \pi^+ \pi^-$  decays, the detection asymmetry is then determined by fitting the  $D_{(s)}^+$  mass distribution in each bin, simultaneously for  $D_{(s)}^+$  and  $D_{(s)}^-$  candidates with shared signal and background shapes. The sample of  $D^+ \rightarrow K^- \pi^+ \pi^+$  candidates has a very high purity after selection, so for simplicity in this mode the number of  $D^+$  and  $D^-$  candidates are simply counted within  $\pm 2\sigma$  of the  $D^\pm$  mass peak. The entire procedure is repeated twice in both cases, weighting separately to the merged and resolved samples of the signal and control datasets.

### 7.9.2 Results and toy studies for $D^0 \rightarrow \pi^+ \pi^- \pi^0$

To study the  $\pi^+ \pi^-$  asymmetry potentially affecting the signal mode, the entire 2016–18 sample of  $D_{(s)}^+ \rightarrow \pi^+ \pi^+ \pi^-$  decays is utilised. The 2015 dataset is neglected

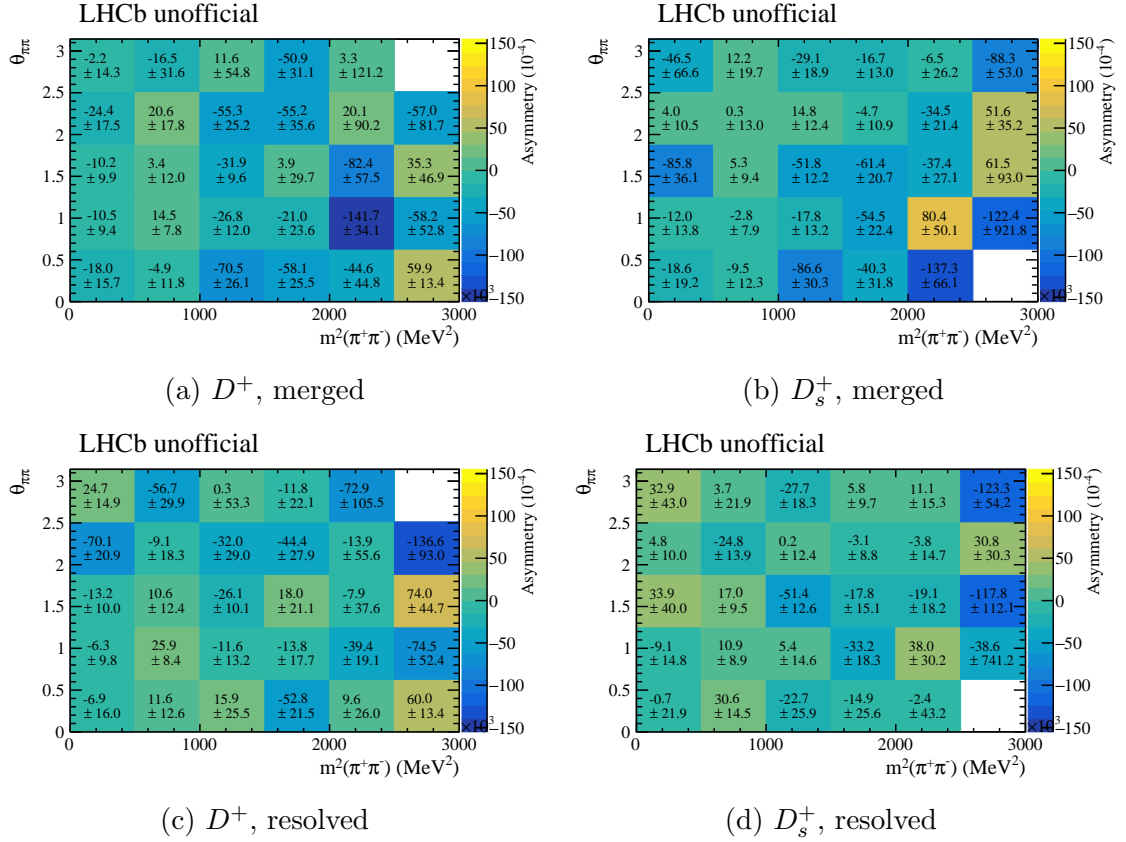


Figure 7.19:  $\pi^+\pi^-$  detection asymmetry maps split by parent particle and  $\pi^0$  reconstruction category.

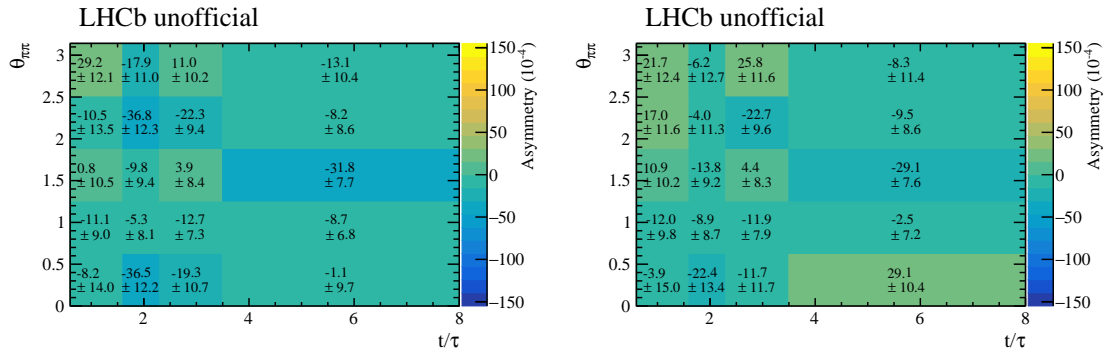


Figure 7.20:  $\pi^+\pi^-$  detection asymmetry maps in the  $(\theta_{\pi\pi}, t/\tau_{D^0})$ -plane for the merged (left) and resolved (right) categories.

due to the smaller statistics and negligible impact on the overall results, and 2012 is neglected due to the lack of currently available nTuples. Each year and polarity combination is treated separately with respect to the kinematic weighting and determination of the asymmetry, and finally in each bin of the phase-space the overall

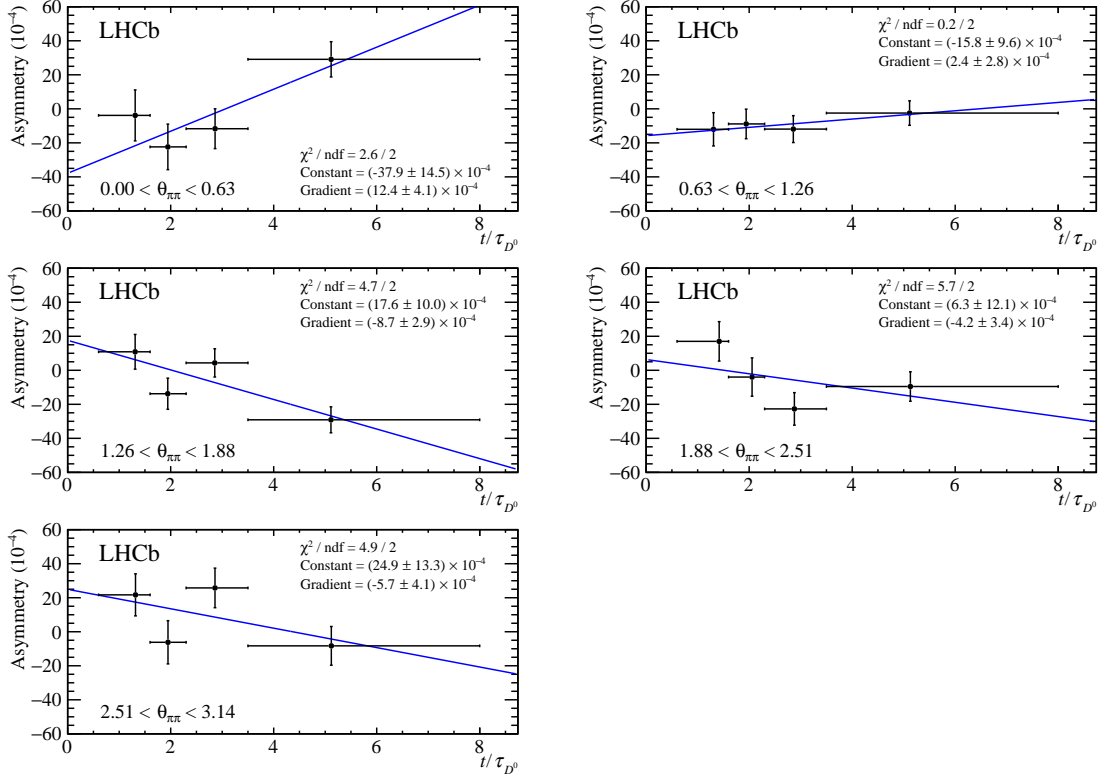


Figure 7.21: Linear fit to the time-dependent asymmetry in each  $\theta_{\pi\pi}$  bin for the resolved category [146].

value is extracted from a least squares fit across the sub-samples. Integrating across year and polarity gives the asymmetry maps shown in Figure 7.19, separately for merged and resolved and  $D_s^+$  and  $D^+$ . The blank bins have virtually no events, and so are assigned an asymmetry of 0 for this plot to avoid saturating the scale due to large fluctuations in their central values. A  $\chi^2$  test between the asymmetry maps computed from  $D_s^+$  and  $D^+$  gives p-values of 4%, 6% for the merged and resolved cases, respectively. For the remainder of this study the maps from  $D_s^+$  and  $D^+$  are combined.

Performing the same study in bins of  $\theta_{\pi\pi}$  and decay-time yields the asymmetry maps shown in Figure 7.20. Figure 7.21 shows a linear fit to the gradient in each  $\theta_{\pi\pi}$  bin for the resolved category. The decay-time variable is normalised to the  $D^0$  lifetime to match that used in the nominal analysis procedure.

A toy study is performed to consider the potential impact of these asymmetries on the measured  $\Delta Y$ . Toy datasets are generated according to a kernel-density model in each decay-time bin used in the nominal analysis from simulation, integrated across 2015–18 and separately for the merged and resolved  $\pi^0$  categories, to represent

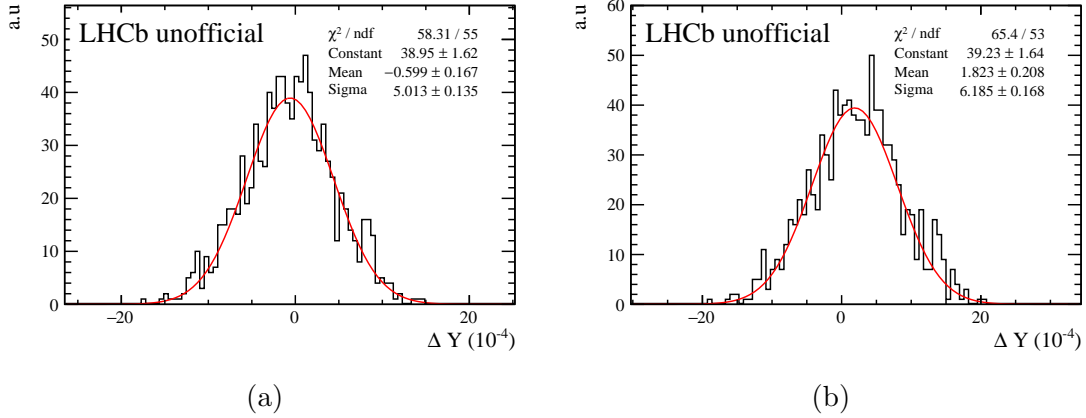


Figure 7.22:  $A_{\text{det}}^{\pi\pi}$  toy studies without time-dependence in the asymmetry maps for (a) merged and (b) resolved  $\pi^0$  categories.

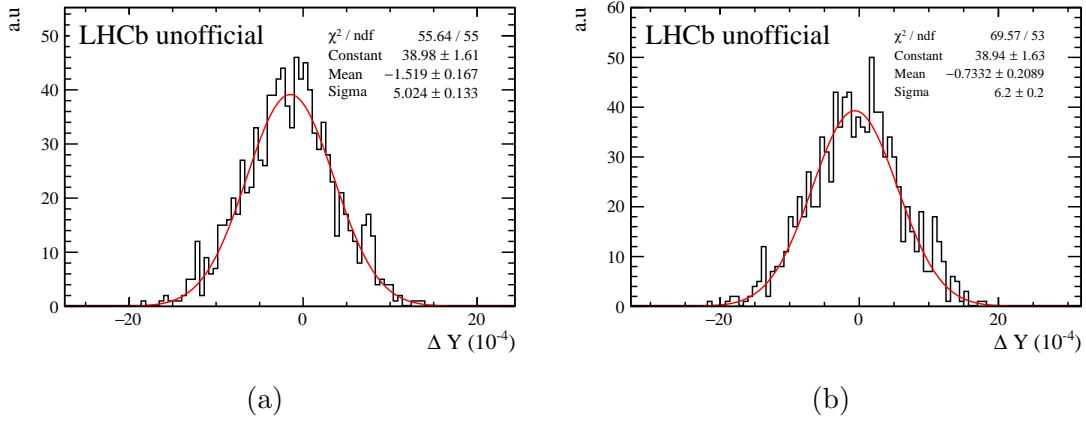


Figure 7.23:  $A_{\text{det}}^{\pi\pi}$  toy studies with time-dependence in the asymmetry maps for the (a) merged and (b) resolved  $\pi^0$  categories.

both the underlying amplitude model and phase-space efficiency. The asymmetry is applied to each toy dataset as an efficiency across the phase space. To include the time-dependence, the gradient in each  $\theta_{\pi\pi}$  bin is added to the asymmetry maps in the  $(\theta_{\pi\pi}, m^2(\pi^+, \pi^-))$ -space, keeping the average value equal to that measured in the time-integrated maps and producing an asymmetry map in each of the decay-time bins used in the nominal analysis. The toy datasets are then passed into the nominal fitting procedure for  $\Delta Y$ . Figures 7.22 and 7.23 show the results of a sample of toy datasets with and without the time-dependence, respectively. In all cases a bias of  $\sim 10^{-4}$  is present. Finally, the impact of uncertainties on the asymmetry maps on this bias is considered. The central values of the asymmetry maps and gradients are fluctuated assuming Gaussian errors and using a single representative toy dataset. Correlations between the asymmetries in different bins — which will exist due to

the shared, but differently weighted,  $D_{(s)}^+ \rightarrow \phi\pi$  samples — are neglected since it is highly non-trivial to include these. The results of such a set of toy datasets are shown in Figure 7.24. The spread on these results is of a similar size to the bias observed in the earlier toy studies, indicating the bias is potentially caused by statistical fluctuations of the central values on the asymmetry maps.

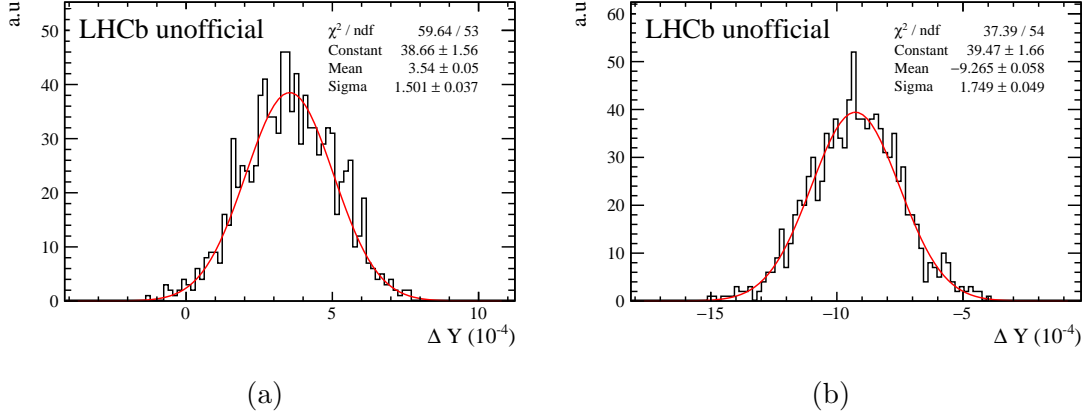


Figure 7.24:  $A_{\text{det}}^{\pi\pi}$  toy studies, with time-dependence, using a single toy dataset and fluctuating the asymmetry maps for the (a) merged and (b) resolved  $\pi^0$  categories.

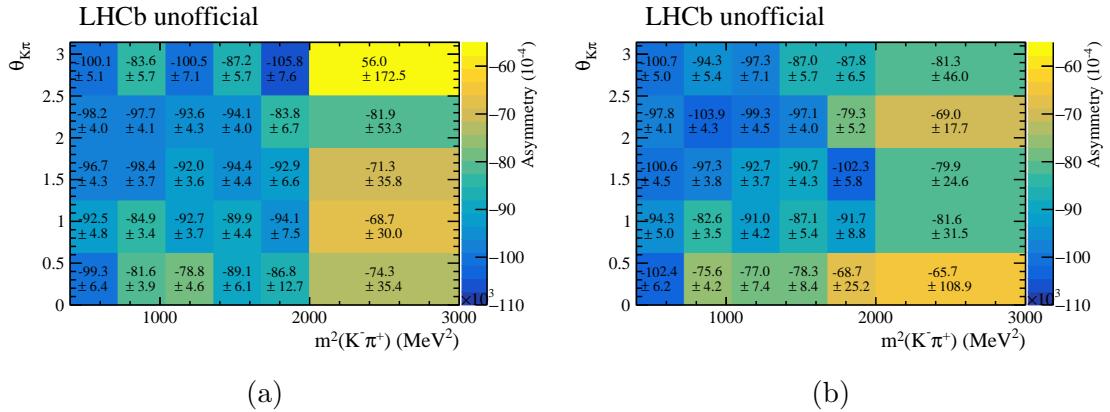


Figure 7.25:  $K\pi$  detection asymmetry maps for the (a) merged and (b) resolved  $\pi^0$  reconstruction categories.

### 7.9.3 Results and toy studies for $D^0 \rightarrow K^-\pi^+\pi^0$

A similar study is repeated using  $D^+ \rightarrow K^-\pi^+\pi^+$  decays to determine the potential asymmetry affecting the  $D^0 \rightarrow K^-\pi^+\pi^0$  sample. Due to the much larger statistics available, only the 2018 dataset is utilised. Figure 7.25 shows the time- and

polarity-integrated asymmetry maps for both the merged and resolved categories. The general size of the asymmetries,  $\mathcal{O}(-1\%)$ , is in good agreement with previous studies of  $K\pi$  detection asymmetries [151, 152]. Figure 7.26 shows the asymmetry maps, allowing for a time-dependence. Figure 7.27 shows a linear fit to the gradient in each  $\theta_{K\pi}$  bin.

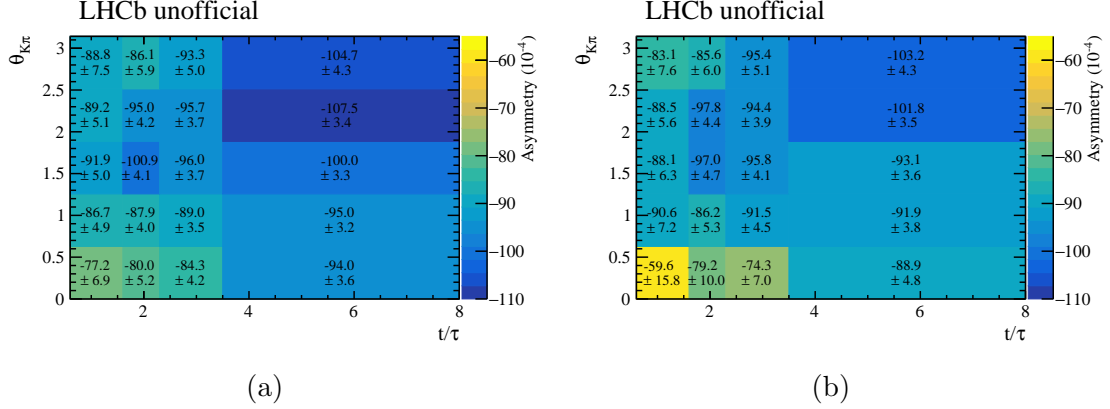


Figure 7.26:  $K\pi$  detection asymmetry maps for the (a) merged and (b) resolved  $\pi^0$  reconstruction categories, allowing for a time-dependence.

Again, a toy study is performed to assess the impact on the measured  $\Delta Y_{K\pi\pi}$ . The phase-space map used to generate the toy datasets is taken from the 2018  $D^0 \rightarrow K^- \pi^+ \pi^0$  data, integrated across magnet polarities and  $D^0$  flavour. The results of the toy studies with and without a time-dependence are shown in Figures 7.28 and 7.29, respectively. A bias of  $\sim -3 \times 10^{-4}$  is observed when allowing for a time-dependence. Again, the impact of uncertainties on the asymmetry maps is assessed by sampling the value in each bin assuming Gaussian errors, and neglecting correlations between bins. The results of this study are shown in Figure 7.30. Here, particularly in the merged case, the spread is much smaller than the bias on the previous toy datasets, indicating this bias is a real effect and not a fluctuation.

#### 7.9.4 Final detection asymmetry systematic uncertainties

The final systematic uncertainty is calculated as a weighted average of the biases found in the merged and resolved toy studies, with the weights given by the yield in real data of each category. A conservative choice is made to use the largest bias for each  $\pi^0$  category, ignoring any cancellation due to opposite signs. Thus, for the control channel, the results of the toy datasets allowing for a time-dependence of

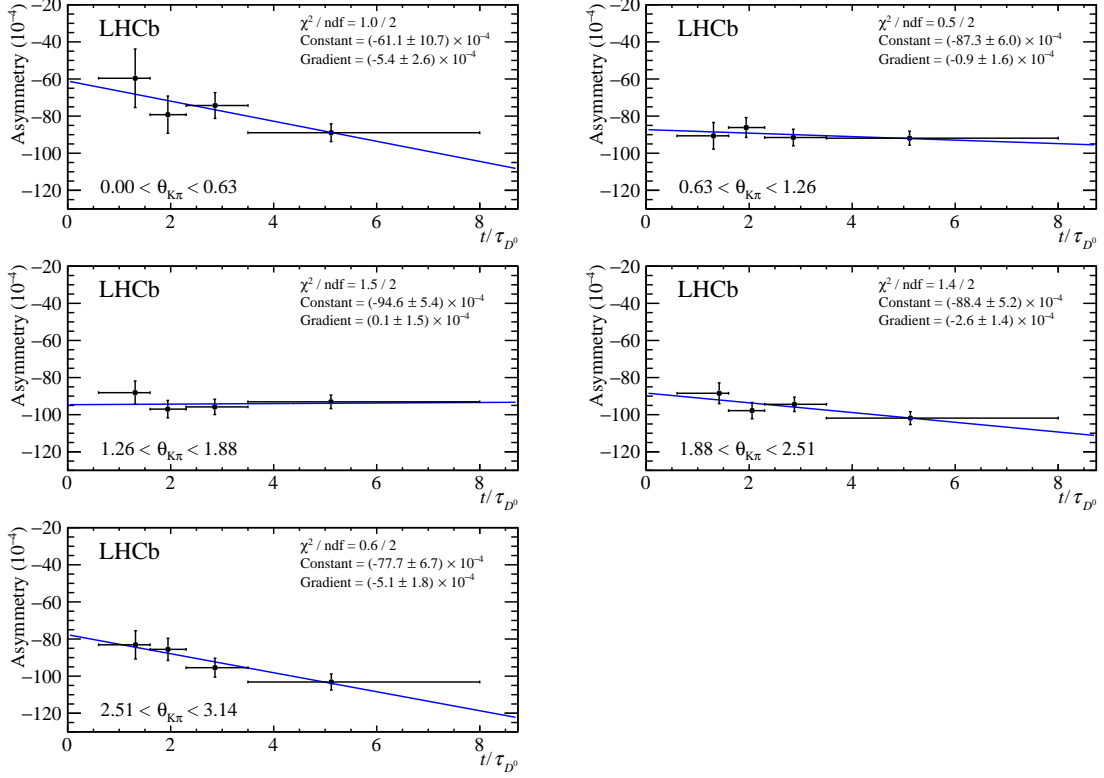


Figure 7.27: Linear fit to the time-dependent asymmetry in each  $\theta_{K\pi}$  bin for the resolved category [146].

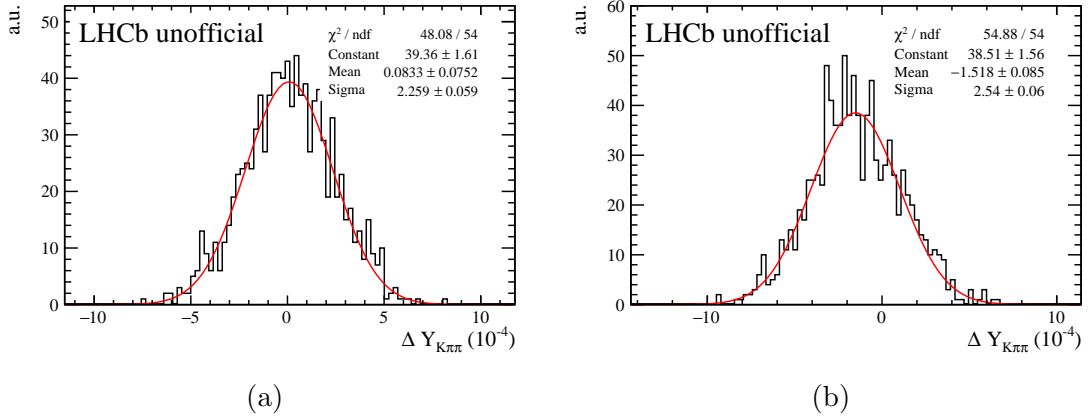


Figure 7.28:  $A_{\text{det}}^{K\pi}$  toy studies without time-dependence in the asymmetry maps for the (a) merged and (b) resolved  $\pi^0$  categories.

the asymmetry are used, which gives a systematic uncertainty of  $3.4 \times 10^{-4}$ . For the signal channel, the absolute biases without a time-dependence for the resolved sample, and with a time-dependence for the merged sample are taken, giving a systematic uncertainty of  $1.6 \times 10^{-4}$ . No additional systematic error due to the uncertainty on the asymmetry maps is assigned. Some additional figures related to

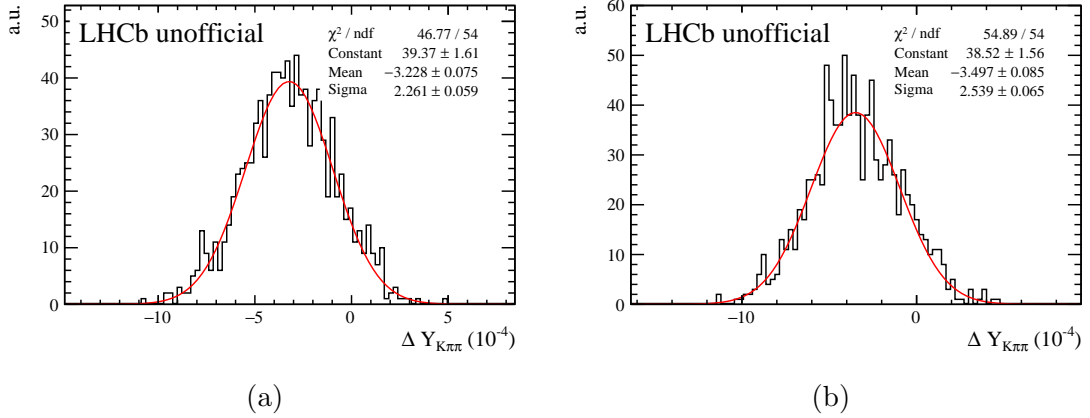


Figure 7.29:  $A_{\text{det}}^{K\pi}$  toy studies with time-dependence in asymmetry maps for the (a) merged and (b) resolved  $\pi^0$  categories.

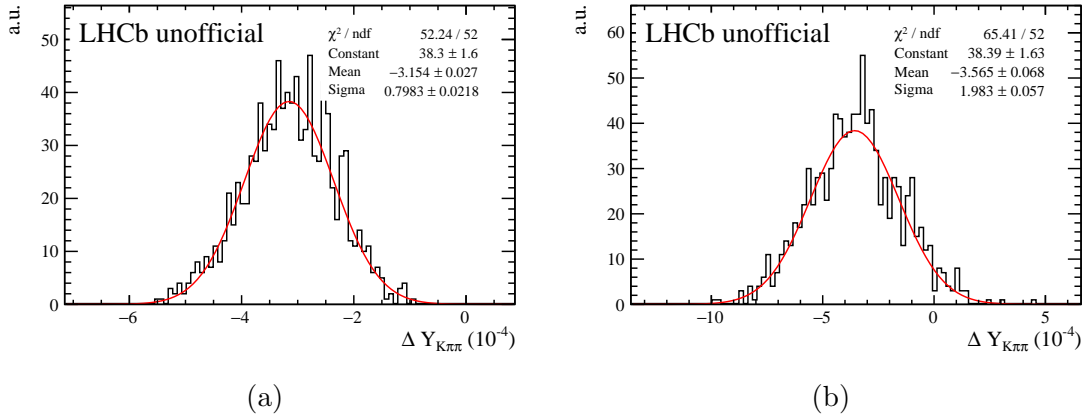


Figure 7.30:  $A_{\text{det}}^{K\pi}$  toy studies, with time-dependence, using a single toy dataset and fluctuating the asymmetry maps for the (a) merged and (b) resolved  $\pi^0$  categories.

this study can be found in Appendix E.

## 7.10 Additional cross-checks

This section contains several cross-checks of the analysis procedure which were used to verify the stability of the measured central value, without assigning additional systematic uncertainties. Some further studies can be found in Appendix F.

### 7.10.1 Effect of L0 trigger selections

No explicit requirements at the L0 trigger level are applied for this analysis. Nonetheless, a possible bias due to L0 trigger requirements is evaluated by per-

forming the analysis in two independent samples of the candidates passing the full selection. In the first sample, the  $D^0$  candidate decay products are required to have fired the L0Hadron trigger line. The second sample contains the orthogonal set of candidates for which the  $D^0$  candidate did not fire the L0Hadron line. The L0Hadron line selects high  $E_T$  deposits in the calorimeter system that are consistent with originating from a hadron. The results are presented in Figures 7.31. The averaged results across all sub-samples are in good agreement for both decay modes.

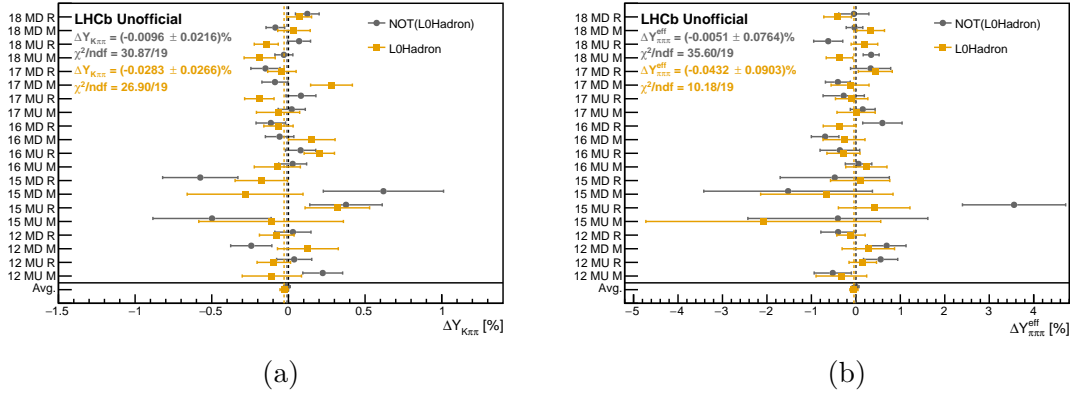


Figure 7.31: Results of L0 trigger selection cross-check in both the (a) control channel and (b) signal channel.

### 7.10.2 Comparison of 2D and 3D kinematic weighting

The kinematic weighting procedure described in Section 6.1.2 differs from the procedure employed in other similar analyses [59], in that weights are computed here from a series of 2D distributions, instead of 3D distributions. The 3D approach is well justified, since it allows the kinematics of, for example, the tagging pion to be fully equalised in a single step, accounting for all correlations. The 2D approach is equivalent only if the weights computed in each stage are factorisable. To test this assumption, the measurement is repeated in the control channel using such a 3D weighting procedure. The weights are computed using 42 bins for  $\theta_x$  in the range  $(-0.3, 0.3)$ , 28 bins for  $\theta_y$  in the range  $(-0.3, 0.3)$  and 12 bins for  $k$  in the range  $(0.0, 0.55)$  c/GeV. Then, a second set of weights are computed using 25 bins for  $\eta(D^0)$  in the range  $(1.7, 4.5)$ , 25 bins for  $p_T(D^0)$  in the range  $(0, 35)$  GeV/c and 15 bins for  $\eta(\pi_{\text{tag}}^\pm)$  in the range  $(1.7, 4.5)$ . All variables have the same meanings as in Section 6.1.2. Figure 7.32 shows a comparison of the results using this approach and

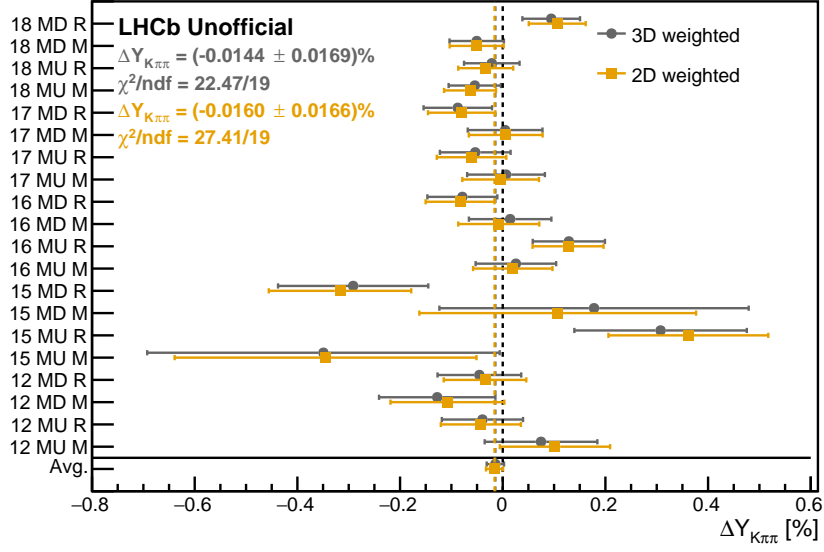


Figure 7.32: Results of 3D kinematic weighting cross-check in the control channel.

the nominal weighting approach. Across all sub-samples, the two approaches are in excellent agreement. The 3D approach is not repeated on the signal channel due to a lack of statistics.

### 7.10.3 Counting method

As an additional test of the stability of the fits to the  $\Delta m$  distributions, the measurement is also performed using an alternative approach that does not rely upon these fits. The regions  $\Delta m \in [143.4, 147.4]$  MeV/ $c^2$  and  $\Delta m \in [143.0, 147.8]$  MeV/ $c^2$ , which correspond to approximately a  $\pm 2\sigma$  window around the signal peak, are defined as the signal regions for resolved and merged candidates, respectively. Then, the asymmetry within each decay time bin is computed by simply counting events in the signal region, neglecting any residual background. The error on the asymmetry is calculated by simply assuming an error of  $\sqrt{N}$  ( $\sqrt{\bar{N}}$ ) on the  $D^0$  ( $\bar{D}^0$ ) yield,  $N$  ( $\bar{N}$ ), and propagating these uncertainties through to the asymmetry. This is only performed in the control channel due to the higher purity of the sample. The results of this cross-check are presented in Figure 7.33. The alternative counting method is in excellent agreement with the nominal method across all sub-samples.

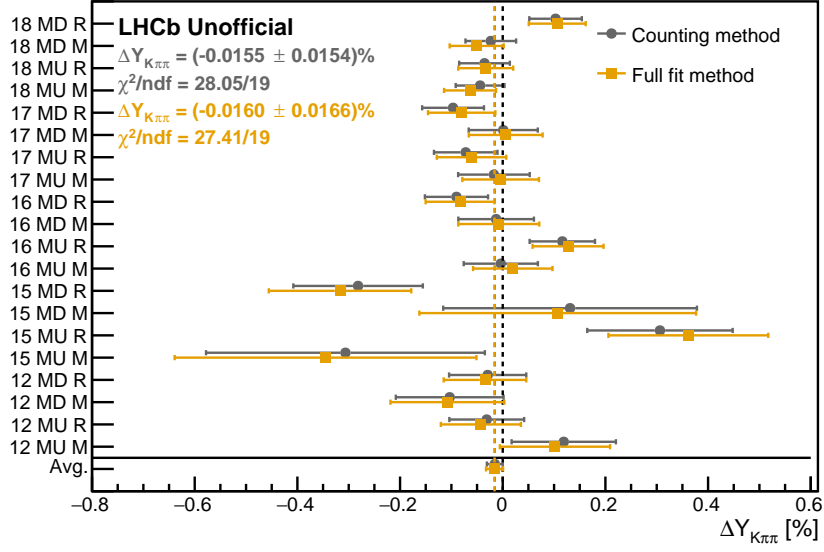
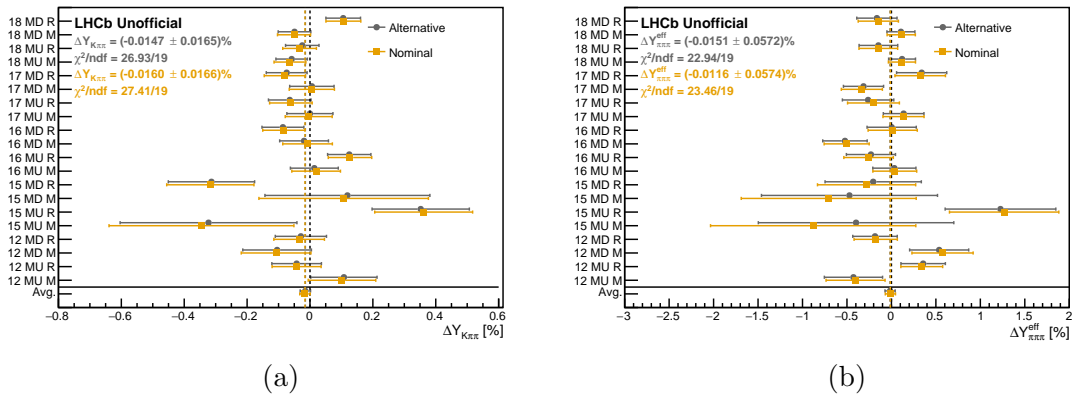


Figure 7.33: Results of counting method cross-check in the control channel.

#### 7.10.4 Alternative $\Delta m$ fit model

As an additional test for a possible bias arising from the choice of  $\Delta m$  fit models, the analysis is performed using an alternative  $\Delta m$  fit model. The alternative model is described in Section 7.1. The results of using this model are shown in Figure 7.34. Excellent agreement is observed between the results using the nominal and alternative models.


 Figure 7.34: Comparison of measured time-dependent  $CP$  asymmetries using the alternative  $\Delta m$  model for both the (a) control channel and (b) signal channel.

Source	Signal channel ( $\times 10^{-4}$ )	Control channel ( $\times 10^{-4}$ )
$\pi\pi/K\pi$ detection asymmetry	1.6	3.4
$t/\tau$ binning	1.0	0.14
Secondary contamination	0.84	0.84
$\Delta m$ fit model (nominal toy study)	0.64	-
$\Delta m$ fit model (alternative toy study)	0.40	0.08
Kinematic weighting binning	0.22	0.22
$t/\tau$ resolution	$3.6 \times 10^{-3}$	$4.8 \times 10^{-3}$
$\tau(D^0)$ uncertainty	$2.9 \times 10^{-3}$	$3.8 \times 10^{-3}$
Total	2.3	3.5

Table 7.4: Absolute value of systematic uncertainties affecting  $\Delta Y_{\pi\pi\pi}^{\text{eff}}$  ( $\Delta Y_{K\pi\pi}$ ) in the signal (control) channel.

## 7.11 Summary

Table 7.4 summarises the systematic uncertainties on  $\Delta Y_{\pi\pi\pi}^{\text{eff}}$  that have been described in the previous sections, for both the signal channel and the control channel. The dominant systematic uncertainties arise from the  $\pi\pi$  and  $K\pi$  detection asymmetry studies detailed in Section 7.9. Additional systematic errors to account for the uncertainty on the external  $F_+$  measurement and possible biases on  $F_+$  due to the phase space acceptance, with values of  $0.036$   $|\Delta Y| = 0.04 \times 10^{-4}$  and  $0.021$   $|\Delta Y| = 0.03 \times 10^{-4}$  respectively, are applied only to the final value of  $\Delta Y$ , and not  $\Delta Y_{\pi\pi\pi}^{\text{eff}}$ .

In addition, a number of cross-checks of the analysis method were performed. The effect of applying explicit hardware trigger requirements was tested, and the measured  $\Delta Y$  in the resulting sub-samples were in good agreement. An alternative kinematic weighting procedure utilising two three-dimensional stages — allowing the tag pion kinematics to be fully constrained in the first stage — was applied to the control channel, and the measured asymmetry gradient was in excellent agreement with the nominal result. Finally, the fits used to determine the asymmetries were studied using an alternative fit model and a simple counting approach; no disagreements with the nominal results were observed.

## Conclusions and outlook

---

THIS thesis has presented the results of a search for time-dependent  $CP$  violation in multi-body  $D^0$  decays, and an absolute luminosity calibration measurement at LHCb with beam-gas imaging. The former represents the first measurement of time-dependent  $CP$  violation in a  $D^0$  decay with a neutral pion in the final state at a hadron collider. Chapter 1 provided a discussion of the relevant background theory, with particular focus on weak interactions and mixing and  $CP$  violation in heavy neutral meson decays. Chapter 2 described the LHCb detector which was used to collect the data analysed for this thesis, and its recent upgrades.

Chapters 3 presented an overview of methods to determine the absolute luminosity at the LHC. The results of the beam-gas imaging analysis applied to luminosity calibration fills for  $pp$  collisions at  $\sqrt{s} = 13$  TeV during Run 2 of the LHC were presented in Chapter 4. A final cross section of

$$\sigma_{\text{Vertex}} = 58.00 \pm 0.02 (\text{stat}) \pm 0.48 (\text{syst}) \text{ mb}$$

was obtained. The dominant systematic uncertainties are uncorrelated between the BGI and vdM analyses, and this therefore has the potential to become the most precise determination of the absolute luminosity at a hadron collider after combining the results of the two analyses [153]. The precision of this measurement is currently limited by knowledge of the beam-gas vertex resolution. The upgraded LHCb detector provides the opportunity to improve the precision of this measurement. The recently installed SMOG2 cell will provide an unprecedented beam-gas interaction luminosity at the LHC. Thus, more stringent selection criteria may be applied while still retaining a reasonable number of events. In particular, imposing tighter selection requirements on the number of tracks in each beam-gas vertex will

allow the effective vertex resolution in the sample to be improved, and therefore reduce the value of the associated systematic uncertainties. The SMOG2 cell will only increase the number of beam-gas vertices produced for one of the LHC beams. However, the overlap integral could, in principle, be determined from only the beam-gas interactions of one beam and beam-beam interactions in the luminous region.

A phase-space integrated, time-dependent measurement of  $CP$  violation in the Cabibbo-suppressed  $D^0 \rightarrow \pi^+\pi^-\pi^0$  decay was presented in Chapters 5, 6, and 7, using data collected during 2012 and 2015–18. Chapter 5 described the selection requirements applied to the 2012 and Run 2 datasets to select candidates from the  $D^0$  decays of interest. Physical backgrounds from mis-identified and mis-reconstructed decays were removed with a sequence of cut-based requirements. A set of multivariate-classifiers were trained to further suppress combinatorial backgrounds. Chapter 6 described the analysis procedure used to determine  $\Delta Y$  by simultaneously fitting the yields of  $D^0$  and  $\bar{D}^0$  in bins of decay time, after applying a weighting procedure to correct for detection asymmetries. Chapter 7 described the studies performed to determine the systematic uncertainties associated with the measurement of  $\Delta Y$ , and a series of cross-checks performed to validate the analysis procedure. The parameter  $\Delta Y_{\pi\pi\pi}^{\text{eff}}$  was measured to be [146]

$$\Delta Y_{\pi\pi\pi}^{\text{eff}} = (-1.2 \pm 6.0 \text{ (stat)} \pm 2.3 \text{ (syst)}) \times 10^{-4},$$

where the statistical error is dominant. The largest systematic uncertainties arise from the choice of  $\Delta m$  fit model, contamination from secondary decays, and the choice of decay-time binning. This corresponds to a measured  $\Delta Y$  of [146]

$$\begin{aligned} \Delta Y &= (-1.3 \pm 6.3 \text{ (stat)} \pm 2.4 \text{ (syst)}) \times 10^{-4} \\ &= (-1.3 \pm 6.8) \times 10^{-4}. \end{aligned}$$

While the uncertainty of this measurement is around 6 times larger than the current world average [43], it nonetheless serves as a test of the universality of the parameter  $\Delta Y$  across different final states, and will add a small contribution to the world average. The Cabibbo-favoured  $D^0 \rightarrow K^-\pi^+\pi^0$  decay, where  $CP$  violating effects are expected to be well below the current precision, is utilised as a control mode. In this channel, the gradient of the time-dependent asymmetry is measured to be [146]

$$\Delta Y_{K\pi\pi} = (-1.7 \pm 1.8 \text{ (stat)} \pm 3.5 \text{ (syst)}) \times 10^{-4},$$

in good agreement with no asymmetry at a level of around  $0.4\sigma$ . The uncertainty on the result in the signal channel is statistically dominated, and so the precision will improve with the increased statistics collected by the upgraded LHCb detector in Runs 3 and 4. The dominant systematic is believed to contain a statistical component, and will likely be reduced with a larger sample of calibration decays. The second largest systematic — arising from the decay-time binning — is potentially a statistical effect only, and should be reduced with a larger data sample; in the control channel, the corresponding decay-time binning systematic uncertainty is around an order of magnitude smaller. Finally, the third largest systematic — arising from contamination of secondary decays — could in principle be reduced by subtracting the secondary asymmetry from the nominally measured asymmetries as in Ref. [59]. There is thus a clear path to improving the precision of this measurement even beyond the current systematic uncertainties with the larger samples of  $D^0$  decays to be collected at LHCb in the near future.

---

# Appendices

---

## A Additional selection MVA plots

This appendix contains additional plots demonstrating the performance of the multivariate classifiers used to suppress combinatorial background at the offline selection stage.

### A.1 Run 1, merged

Figure A.1 shows the distribution of each of the input variables in both the signal and background categories of the data. The background data is taken from the  $\Delta m$  sideband, while the signal data is obtained from the  $\Delta m$  signal region with the background contribution subtracted based on the sideband distributions. Figure A.2 shows the correlations between the input variables in the signal and background samples. Figure A.3 shows the background rejection against signal efficiency of the BDT after training. All of the figures in this section refer to the Run 1 merged classifier.

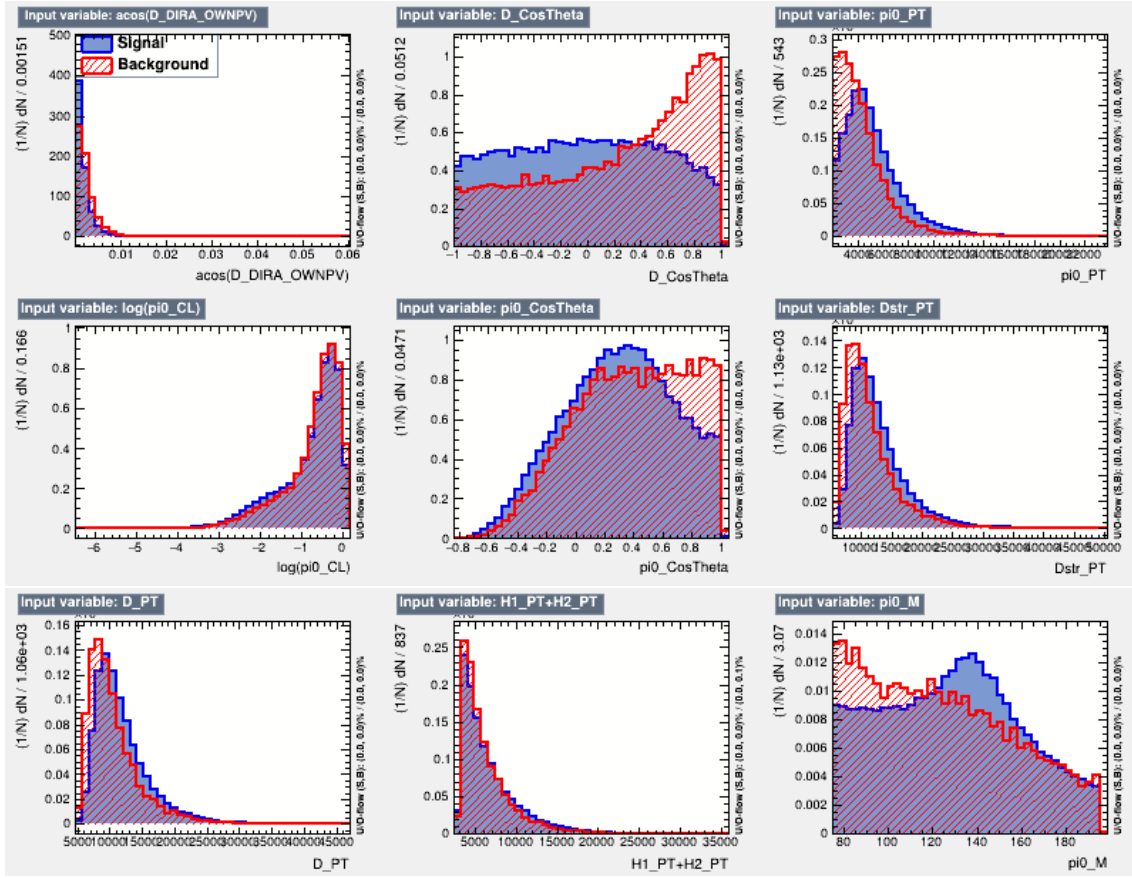


Figure A.1: Input variable distributions for the Run 1 merged BDT.

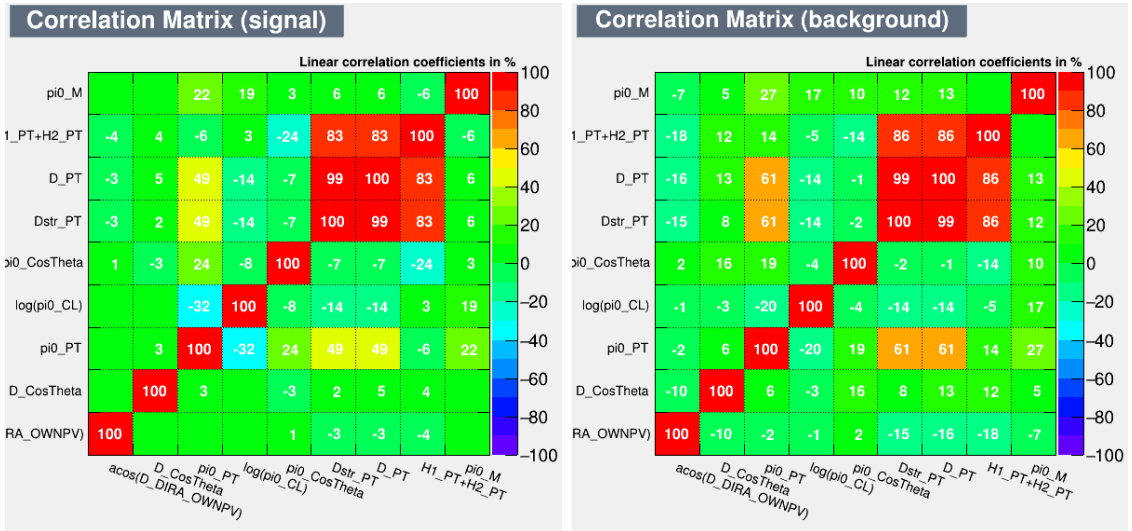


Figure A.2: Input variable correlation matrices for signal (left) and background (right) for the Run 1 merged BDT.

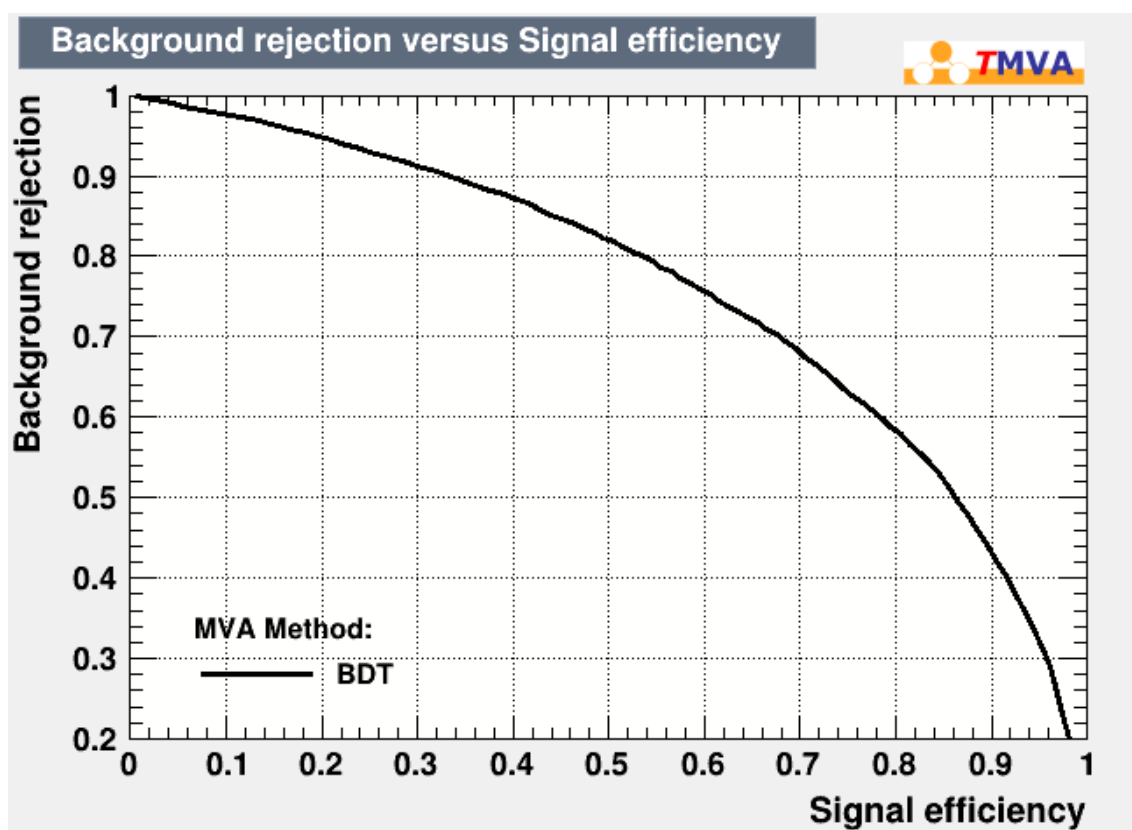


Figure A.3: Background rejection against signal efficiency for the Run 1 merged BDT.

## A.2 Run 1, resolved

Figure A.4 shows the distribution of each of the input variables in both the signal and background categories of the data. The background data is taken from the  $\Delta m$  sideband, while the signal data is obtained from the  $\Delta m$  signal region with the background contribution subtracted based on the sideband distributions. Figure A.5 shows the correlations between the input variables in the signal and background samples. Figure A.6 shows the background rejection against signal efficiency of the BDT after training. All of the figures in this section refer to the Run 1 resolved classifier.

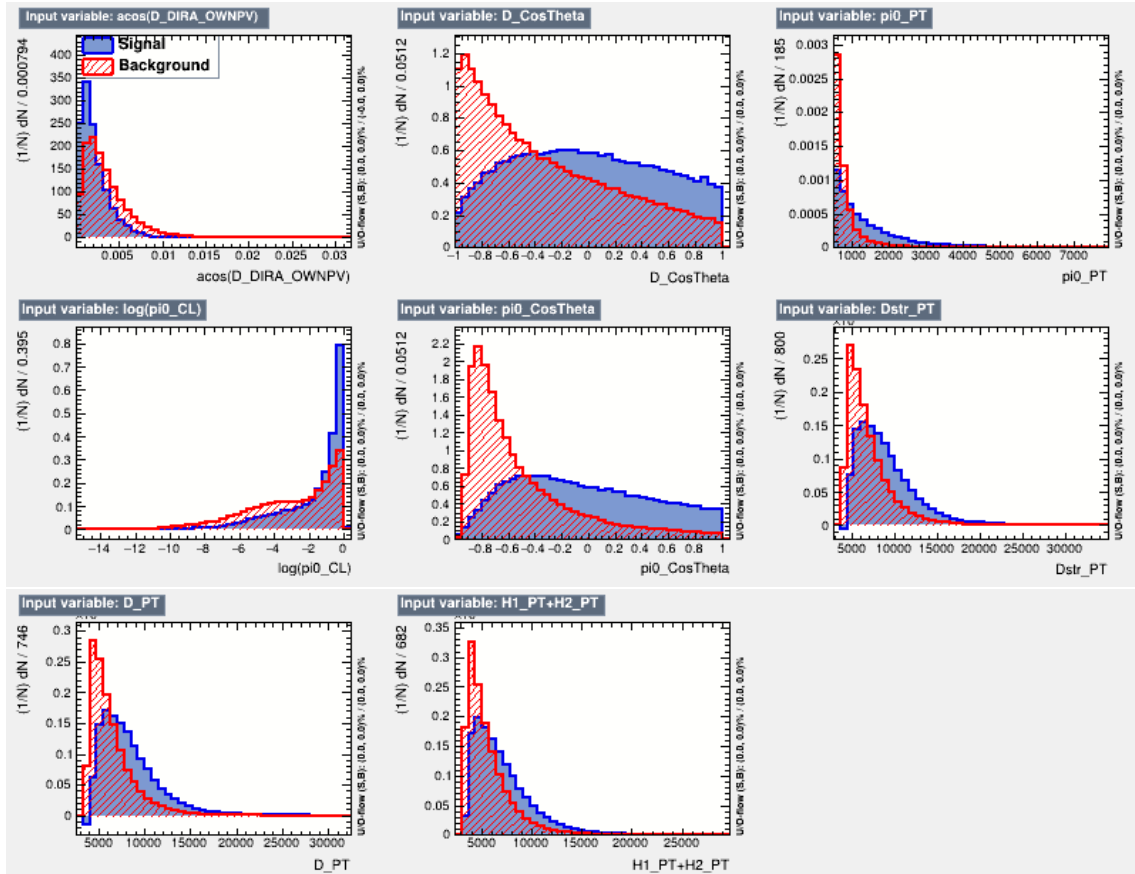


Figure A.4: Input variable distributions for the Run 1 resolved BDT.

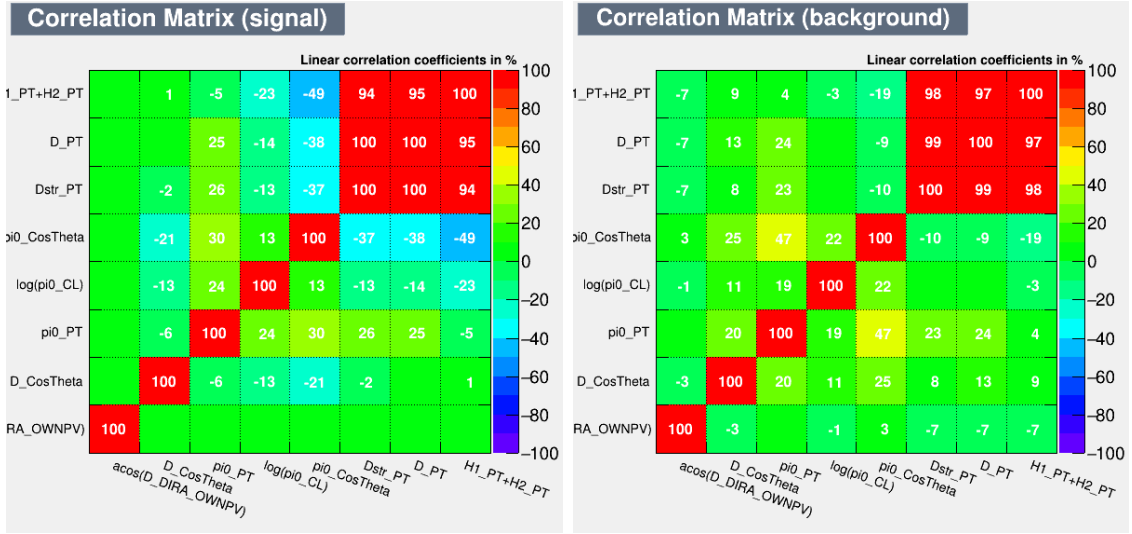


Figure A.5: Input variable correlation matrices for signal (left) and background (right) for the Run 1 resolved BDT.

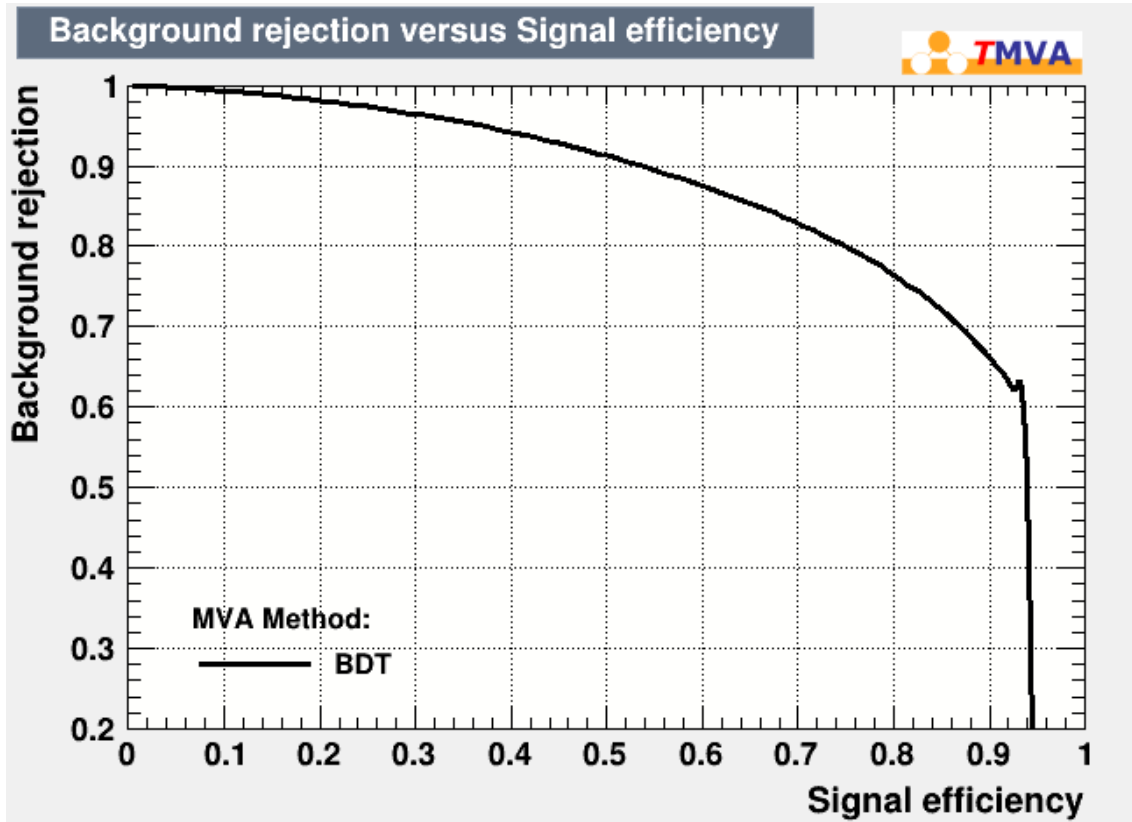


Figure A.6: Background rejection against signal efficiency for the Run 1 resolved BDT.

### A.3 Run 2, merged

Figure A.7 shows the distribution of each of the input variables in both the signal and background categories of the data. The background data is taken from the  $\Delta m$  sideband, while the signal data is obtained from the  $\Delta m$  signal region with the background contribution subtracted based on the sideband distributions. Figure A.8 shows the correlations between the input variables in the signal and background samples. Figure A.9 shows the background rejection against signal efficiency of the BDT after training. All of the figures in this section refer to the Run 2 merged classifier.

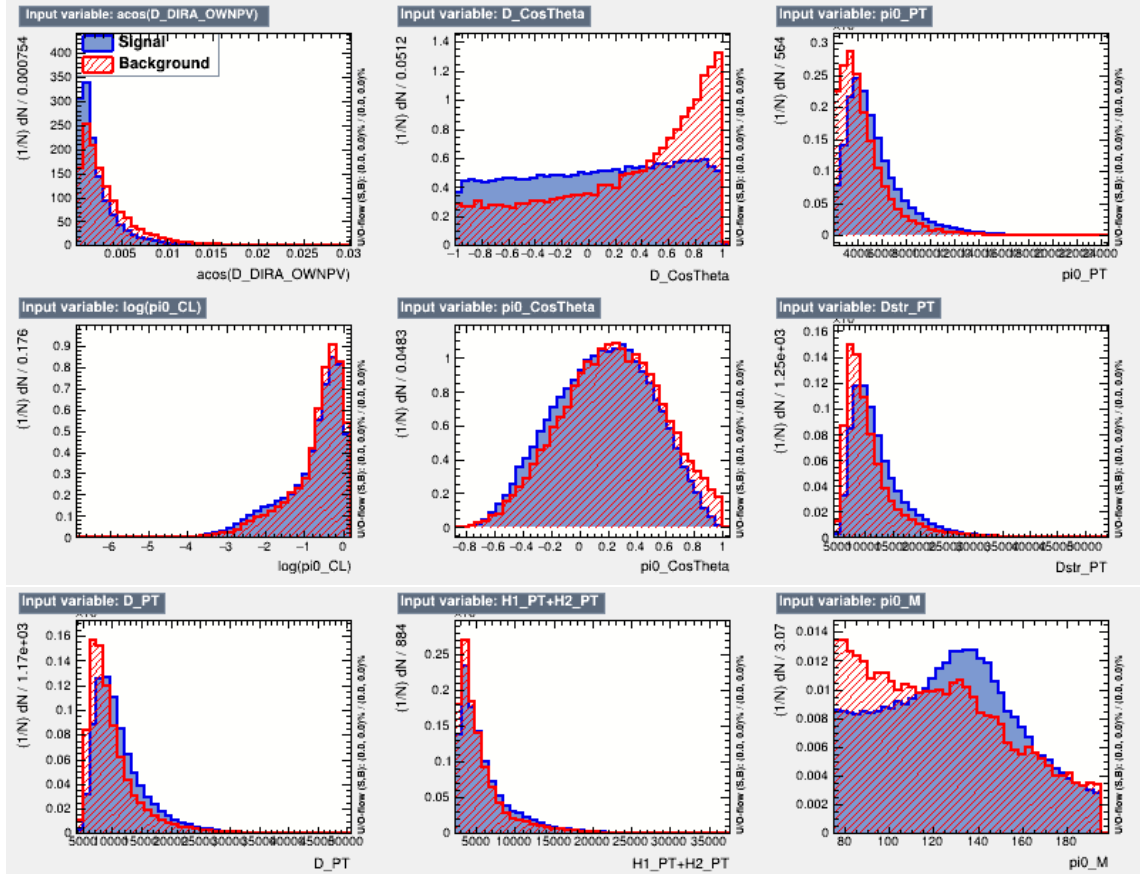


Figure A.7: Input variable distributions for the Run 2 merged BDT.

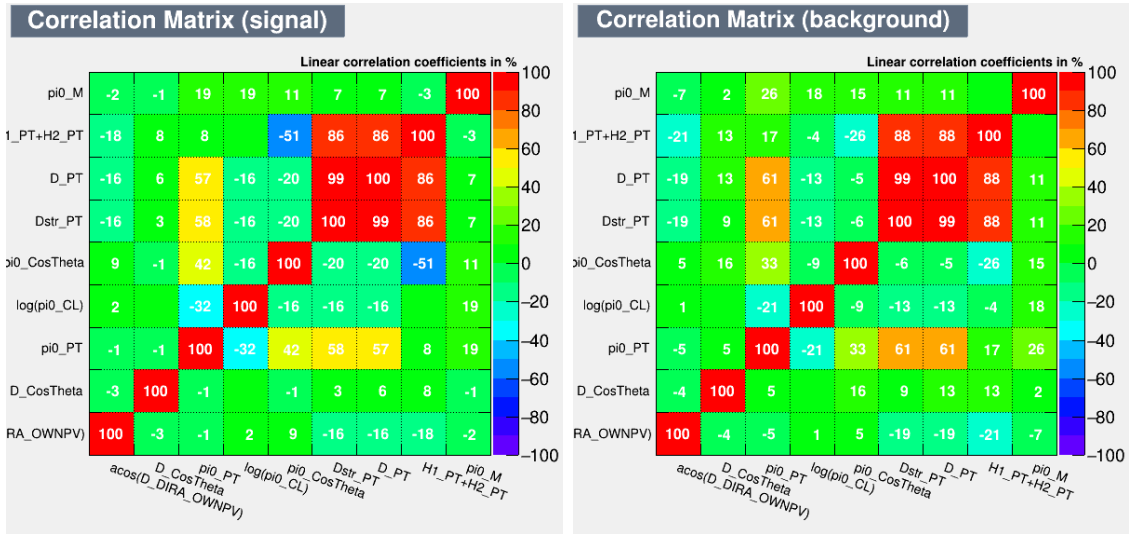


Figure A.8: Input variable correlation matrices for signal (left) and background (right) for the Run 2 merged BDT.

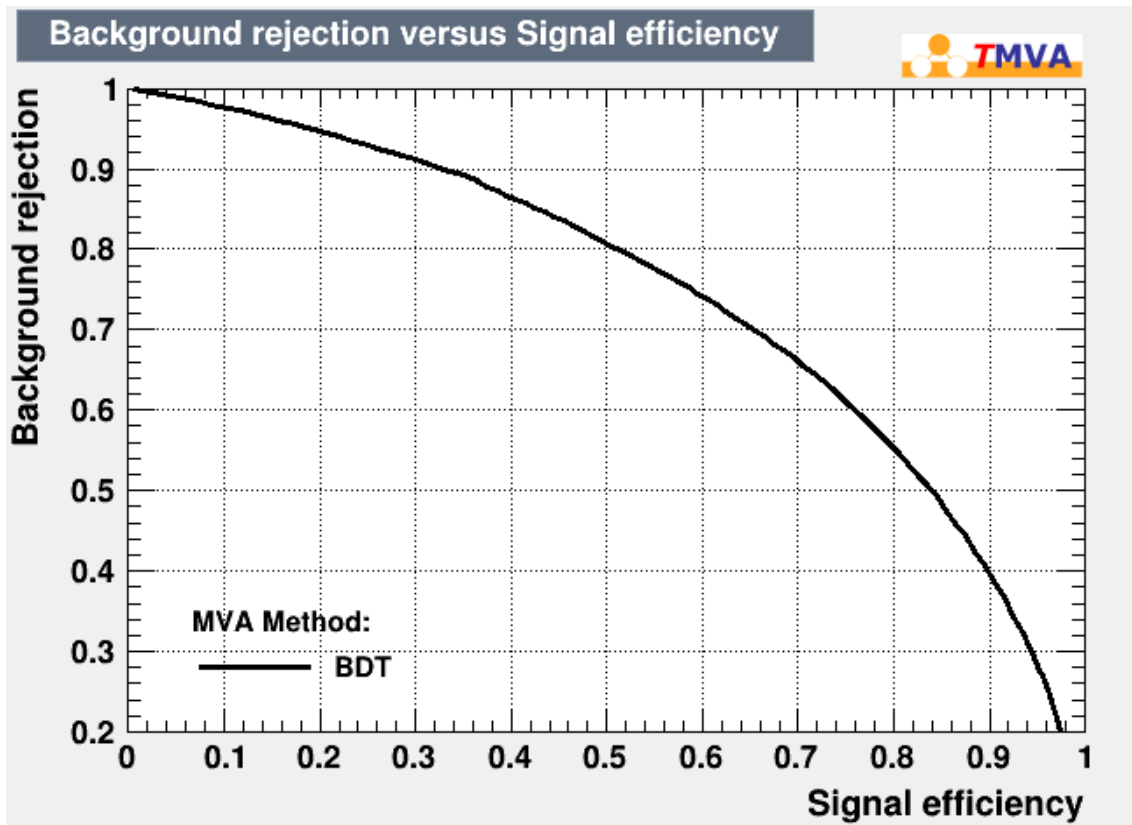


Figure A.9: Background rejection against signal efficiency for the Run 2 merged BDT.

## A.4 Run 2, resolved

Figure A.10 shows the distribution of each of the input variables in both the signal and background categories of the data. The background data is taken from the  $\Delta m$  sideband, while the signal data is obtained from the  $\Delta m$  signal region with the background contribution subtracted based on the sideband distributions. Figure A.11 shows the correlations between the input variables in the signal and background samples. Figure A.12 shows the background rejection against signal efficiency of the BDT after training. All of the figures in this section refer to the Run 2 resolved classifier.

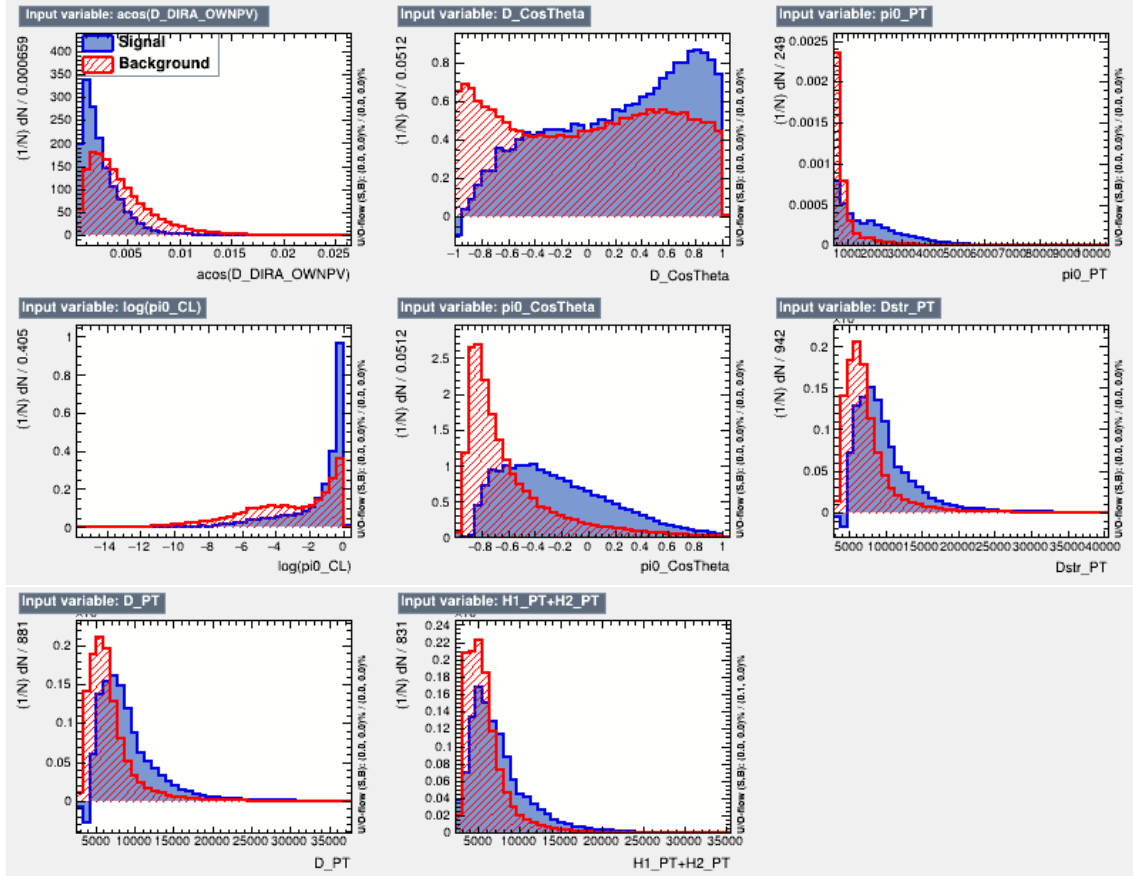


Figure A.10: Input variable distributions for the Run 2 resolved BDT.

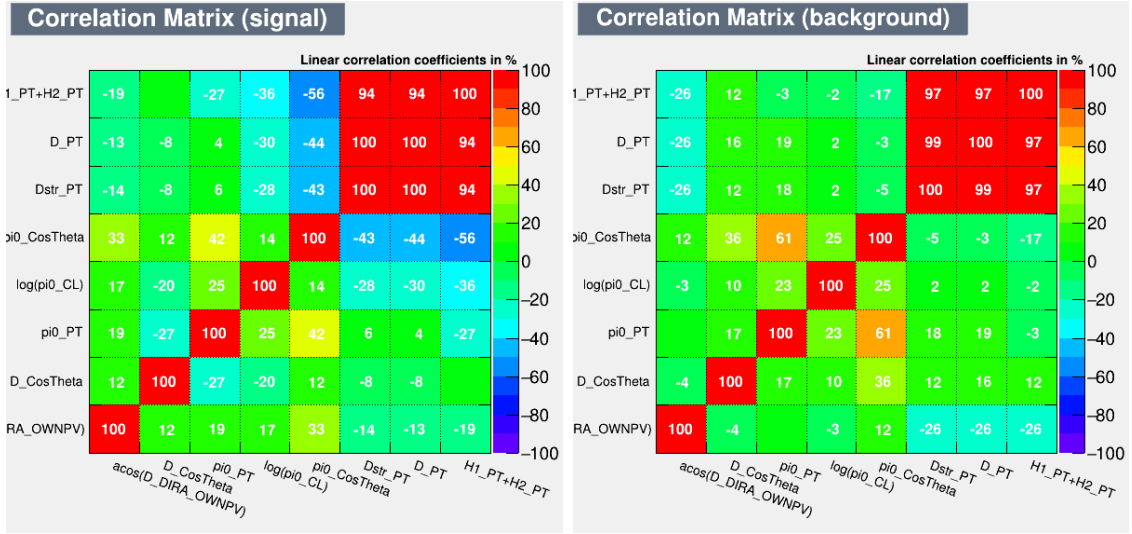


Figure A.11: Input variable correlation matrices for signal (left) and background (right) for the Run 2 resolved BDT.

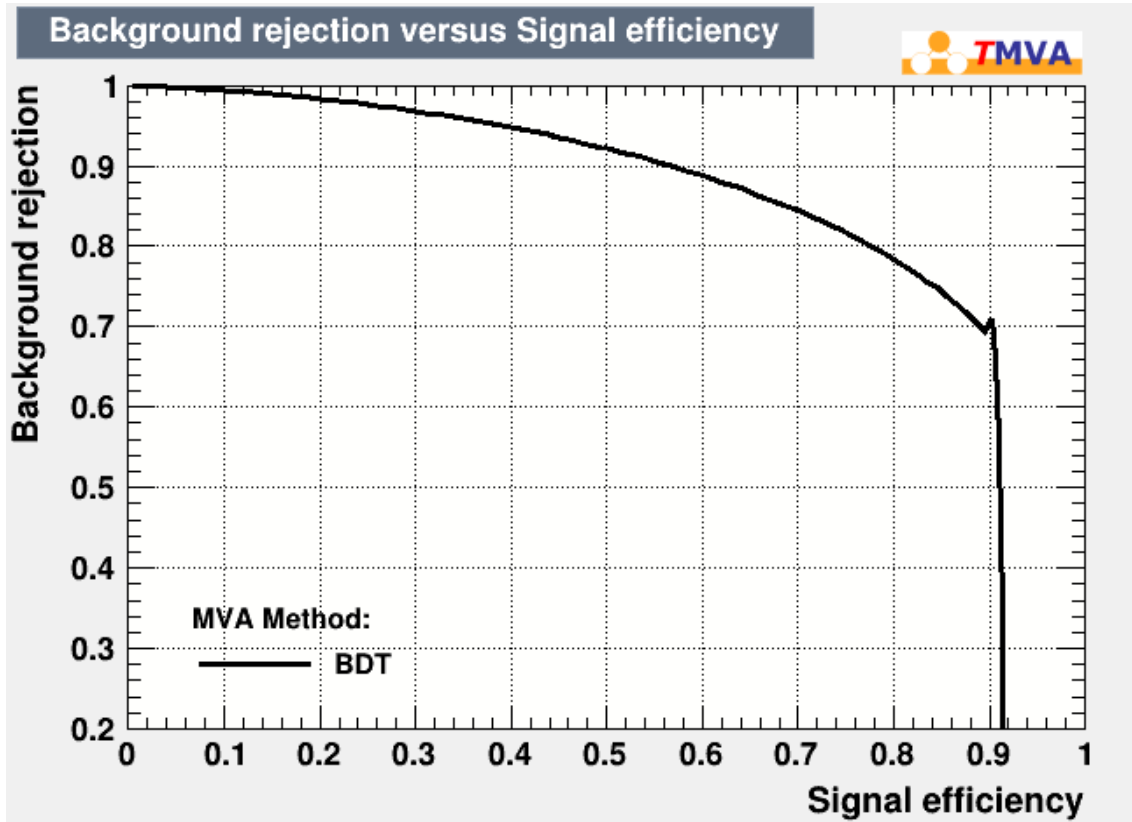


Figure A.12: Background rejection against signal efficiency for the Run 2 resolved BDT.

## A.5 BDT cut optimisation plots

Figure A.13 shows the optimisation metric ( $S/\sigma_S$ ) as a function of the minimum BDT output requirement for the datasets that were not shown in the main body of this thesis. The selection requirements applied to each sample can be found in Table 5.11.

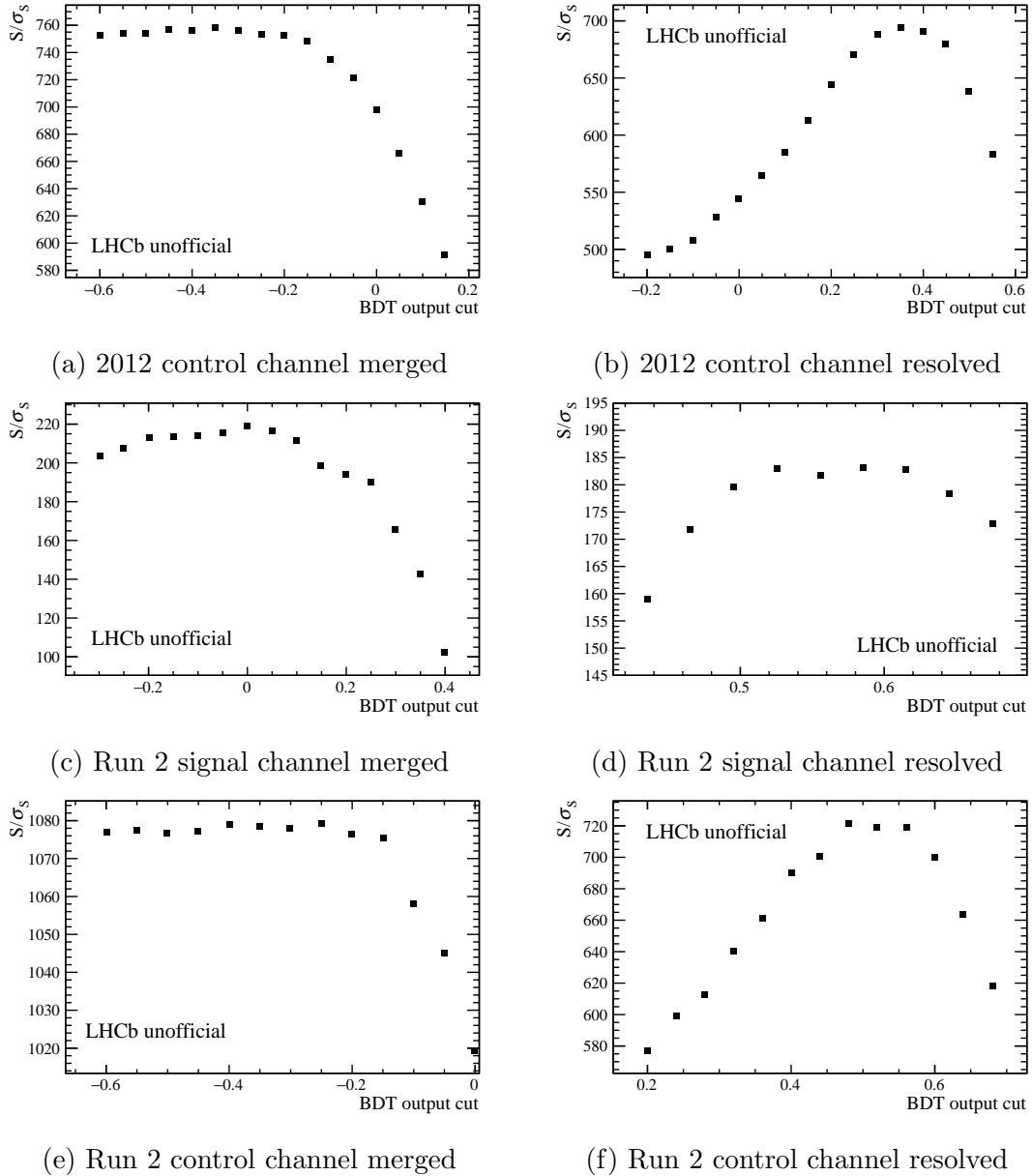


Figure A.13: Optimisation metric as a function of BDT cut for the (top) 2012 control channel data, (middle) Run 2 signal channel data and (bottom) Run 2 control channel data.

## B Potential bias on the measured time-dependent asymmetry from $D^0 \rightarrow K^- \pi^+ \pi^0$ contamination

The residual contamination from  $D^0 \rightarrow K^- \pi^+ \pi^0$  decays was estimated in Section 5.2.4 to be 0.7% (0.8%) for the merged (resolved)  $\pi^0$  category. We estimate here the potential bias on the time-dependent asymmetry gradient based on such contamination. Denote the fraction of  $D^0 \rightarrow K^- \pi^+ \pi^0$  decays in the sample as  $f \neq f(t)$ , assuming the same contamination for  $D^0$  and  $\bar{D}^0$  (a time-independent asymmetry does not change the time-dependent behaviour, and we will consider a possible time-dependent asymmetry later). Define  $n_{\text{true}}(t)$  as the measured true number of  $D^0 \rightarrow \pi^+ \pi^- \pi^0$  candidates (similarly for  $\bar{D}^0$ ). Assume that  $n_{\text{true}}(0) = \bar{n}_{\text{true}}(0) \equiv n$ , i.e. that there is no asymmetry at  $t = 0$  (again, a constant shift in the asymmetry does not change the time-dependent behaviour). We then have

$$n(t) = (1 - f)n_{\text{true}}(t) + fn_{\text{true}}(0) = (1 - f)n_{\text{true}}(t) + fn; \quad (8.1)$$

$$\bar{n}(t) = (1 - f)\bar{n}_{\text{true}}(t) + f\bar{n}_{\text{true}}(0) = (1 - f)\bar{n}_{\text{true}}(t) + fn, \quad (8.2)$$

which, expanding for a small time-dependent asymmetry, gives

$$n_{\text{true}}(t) = n(1 + \Delta Y t); \quad (8.3)$$

$$\bar{n}_{\text{true}}(t) = n(1 - \Delta Y t). \quad (8.4)$$

The time-dependent yields can be expressed as

$$n(t) = n(1 - f)(1 + \Delta Y t) + fn; \quad (8.5)$$

$$\bar{n}(t) = n(1 - f)(1 - \Delta Y t) + fn, \quad (8.6)$$

which gives a time-dependent asymmetry of

$$A_{CP}(t) = \frac{n(t) - \bar{n}(t)}{n(t) + \bar{n}(t)} = \frac{[(1 - f)(1 + \Delta Y t) + f] - [(1 - f)(1 - \Delta Y t) + f]}{[(1 - f)(1 + \Delta Y t) + f] + [(1 - f)(1 - \Delta Y t) + f]} \quad (8.7)$$

$$= \frac{2(1 - f)\Delta Y t}{2} = (1 - f)\Delta Y t. \quad (8.8)$$

Thus, the potential dilution is of the order of the contamination fraction,  $f$ , resulting in a bias of  $\sim 1\%|\Delta Y|$ . Assuming a conservative estimate of  $\Delta Y \sim 10^{-3}$  gives a

bias of  $\sim 10^{-5}$ , c.f.  $\sigma_{\text{stat.}} \sim 6 \times 10^{-4}$ .

Now, we consider the same assumptions as above but allow for a (small) time-dependent asymmetry in the  $D^0 \rightarrow K^- \pi^+ \pi^0$  sample,  $\Delta Y_{K\pi\pi}$ . The time-dependent yields become

$$n(t)/n = (1 - f)(1 + \Delta Y t) + f(1 + \Delta Y_{K\pi\pi} t); \quad (8.9)$$

$$\bar{n}(t)/n = (1 - f)(1 - \Delta Y t) + f(1 - \Delta Y_{K\pi\pi} t), \quad (8.10)$$

which gives a time-dependent asymmetry of

$$A_{CP}(t) = [(1 - f)\Delta Y + f\Delta Y_{K\pi\pi}] t. \quad (8.11)$$

The residual bias remains  $\mathcal{O}(10^{-5})$  if we assume the conservative case of  $\Delta Y = -\Delta Y_{K\pi\pi} = 10^{-3}$  and  $f = 1\%$ . Without any kinematic weighting to remove detection asymmetries, we measure a value of  $\Delta Y_{K\pi\pi} \sim (4.1 \pm 1.7) \times 10^{-4}$  in Section 6.3, albeit with selection requirements optimised for  $D^0 \rightarrow K^- \pi^+ \pi^0$  candidates.

## C Additional kinematic weighting plots

### C.1 Kinematic distributions at intermediate weighting steps

The figures in this section show example kinematic distributions before any kinematic weighting, at an intermediate stage after the weighting of the  $\pi_{\text{tag}}^{\pm}$  kinematics only, and after the full kinematic weighting. Figures C.1 and C.2 show the distributions of the variables used in the kinematic weighting in the 2018 *MagUp* resolved sub-sample of the control channel data before the weighting, after weighting only the  $\pi_{\text{tag}}^{\pm}$  kinematics, and after the full weighting procedure. Figures C.3 and C.4 show the same distributions for the 2018 *MagUp* merged sub-sample of the control channel data.

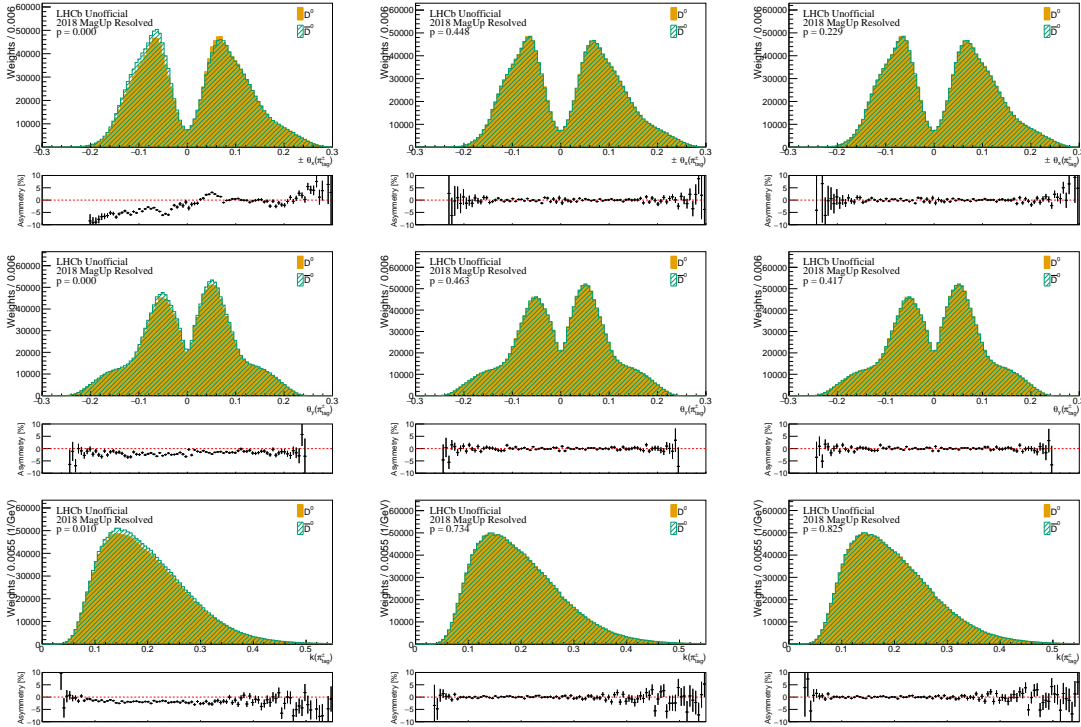


Figure C.1: 2018 *MagUp* resolved control channel tagging pion kinematic distributions (left) before any kinematic weighting, (center) after the  $\pi_{\text{tag}}^{\pm}$  kinematics' weighting and after the full kinematic weighting (right).

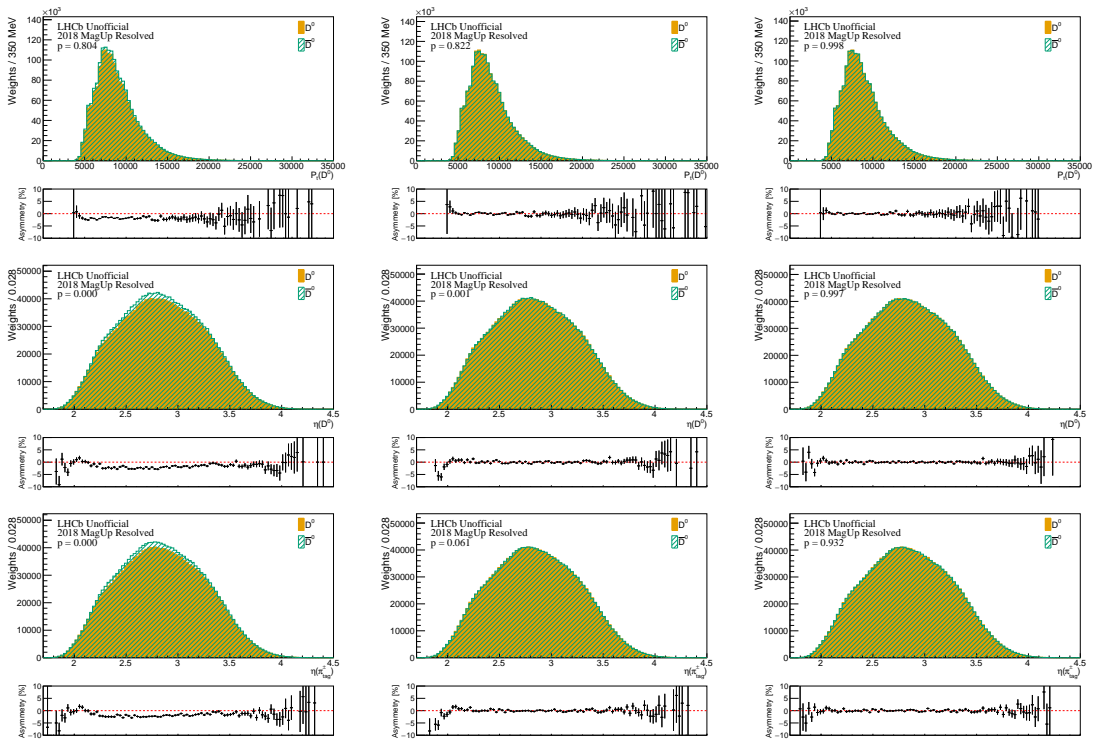


Figure C.2: 2018 *MagUp* resolved control channel  $D^0$  and tagging pion kinematic distributions (left) before any kinematic weighting, (center) after the  $\pi_{\text{tag}}^{\pm}$  kinematics' weighting and (right) after the full kinematic weighting.

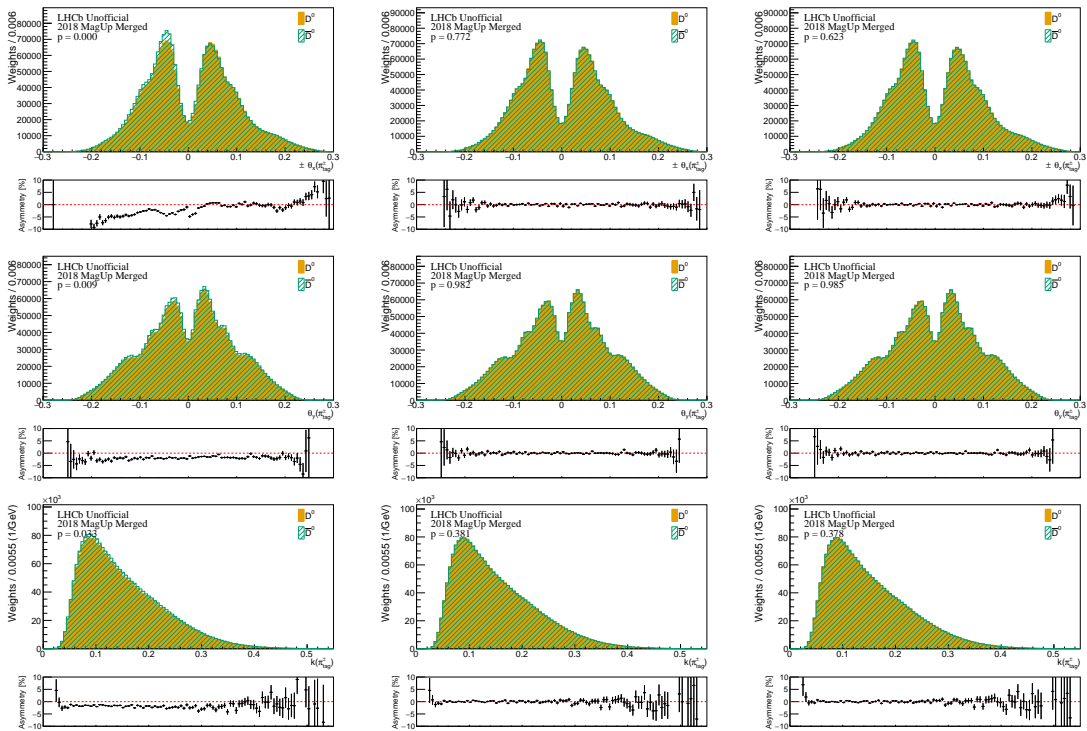


Figure C.3: 2018 *MagUp* merged control channel tagging pion kinematic distributions (left) before any kinematic weighting, (center) after the  $\pi_{\text{tag}}^{\pm}$  kinematics' weighting and (right) after the full kinematic weighting.

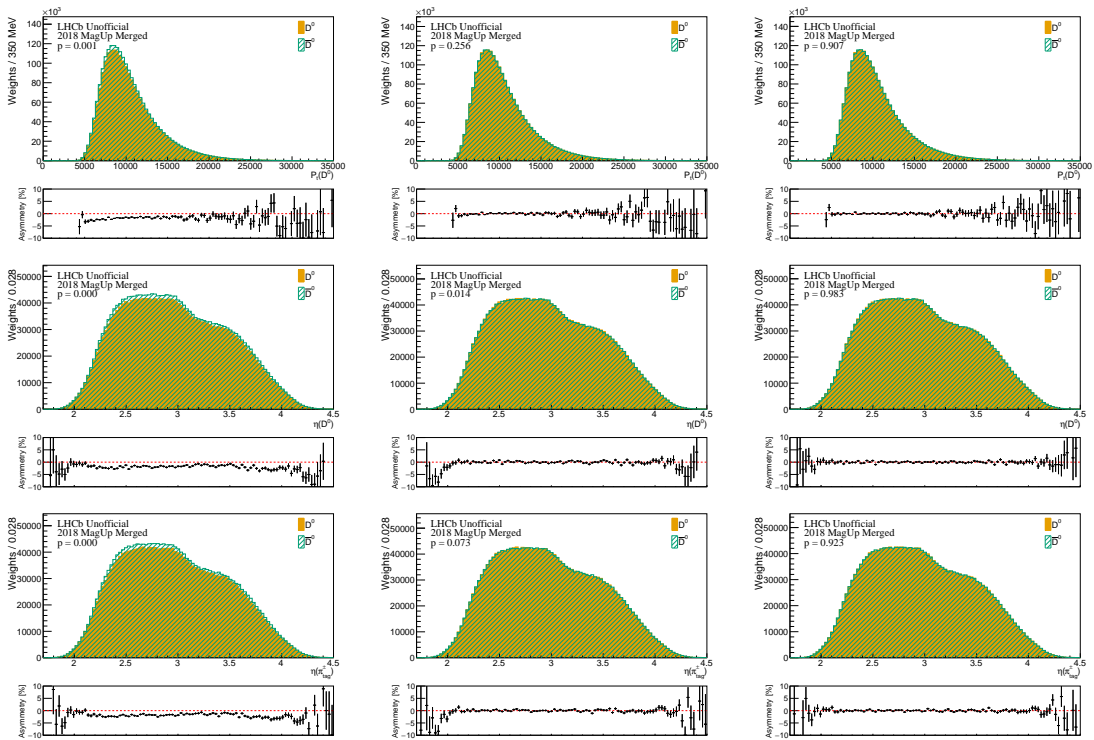


Figure C.4: 2018 *MagUp* merged control channel  $D^0$  and tagging pion kinematic distributions (left) before any kinematic weighting, (center) after the  $\pi_{\text{tag}}^{\pm}$  kinematics' weighting and (right) after the full kinematic weighting.

## C.2 Kinematic distributions in the signal channel

The figures here show some example kinematic distributions from the 2016 *MagUp* merged and resolved signal channel samples before and after the kinematic weighting.

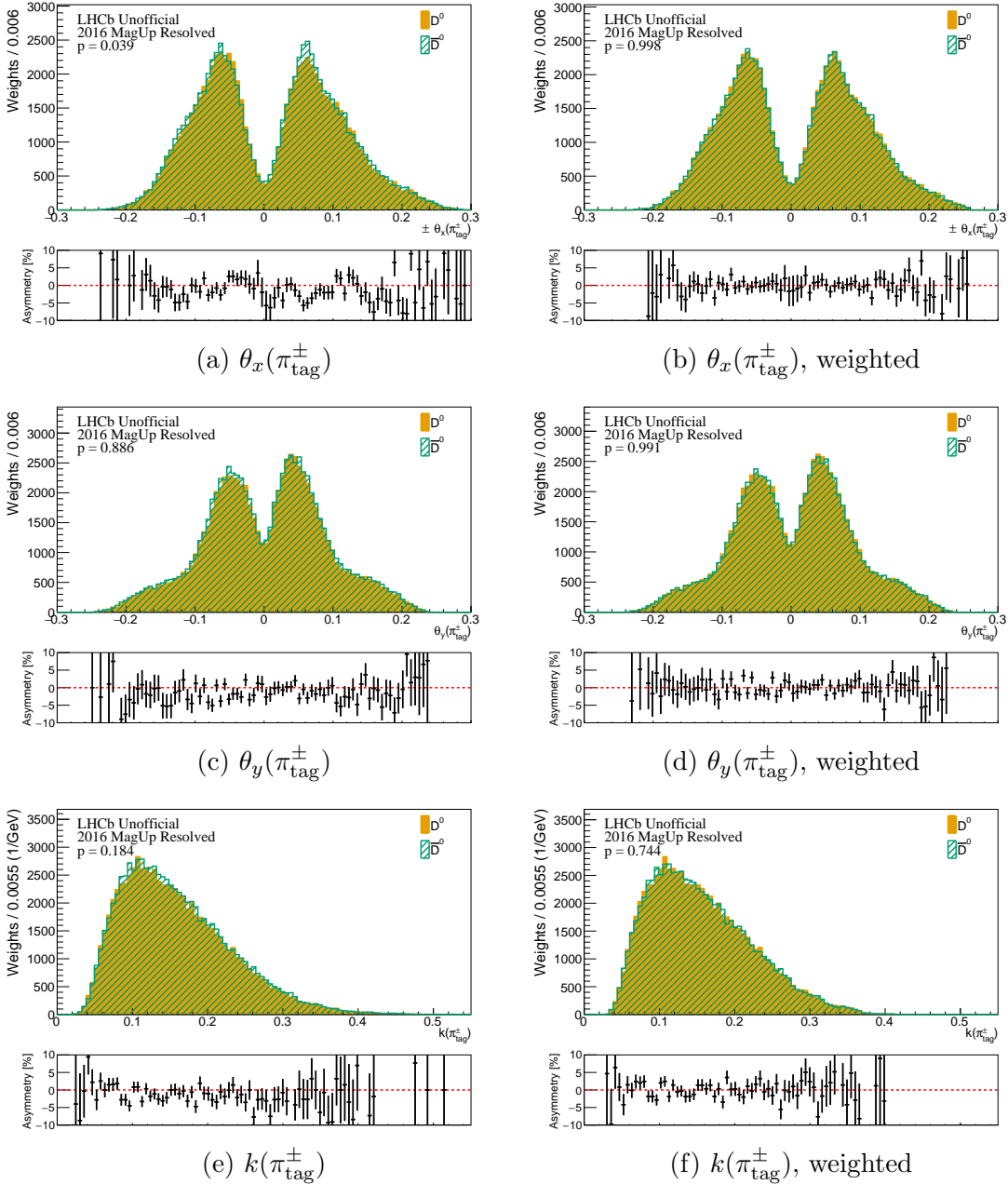


Figure C.5: 2016 *MagUp* resolved signal channel tagging pion kinematic distributions before (left) and after (right) kinematic weighting.

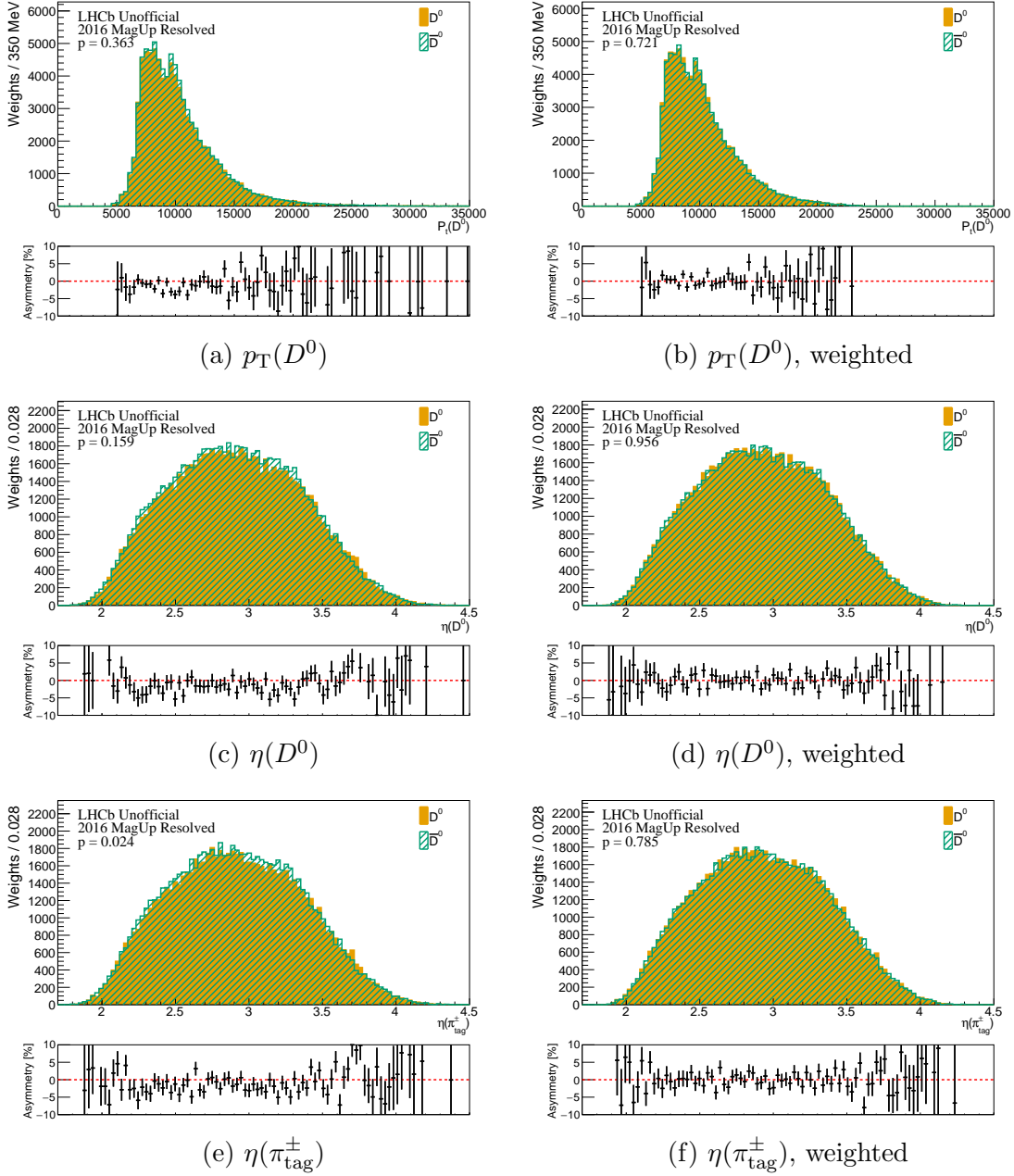


Figure C.6: 2016 *MagUp* resolved signal channel  $D^0$  and tagging pion kinematic distributions before (left) and after (right) kinematic weighting.

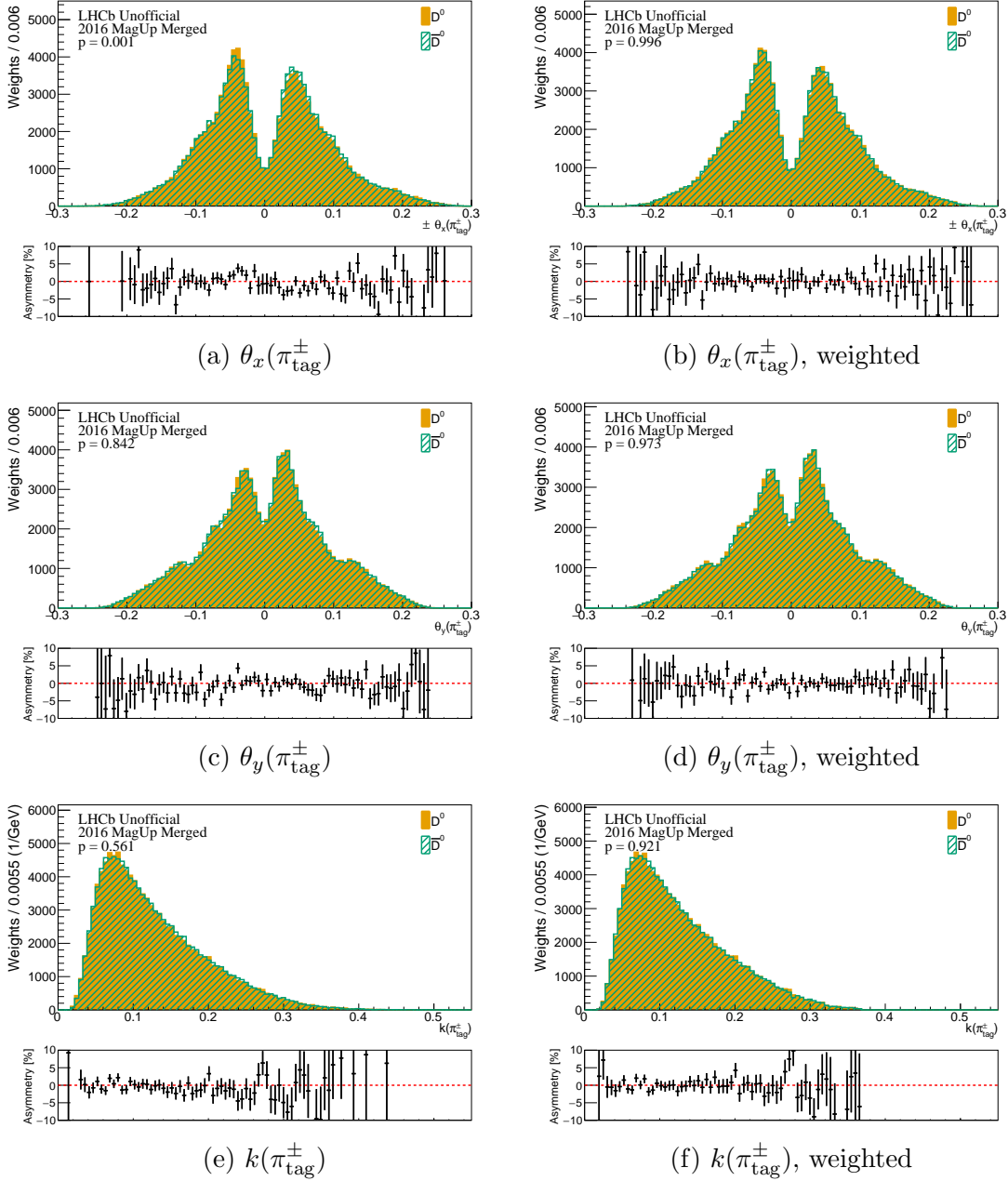


Figure C.7: 2016 *MagUp* merged signal channel tagging pion kinematic distributions before (left) and after (right) kinematic weighting.

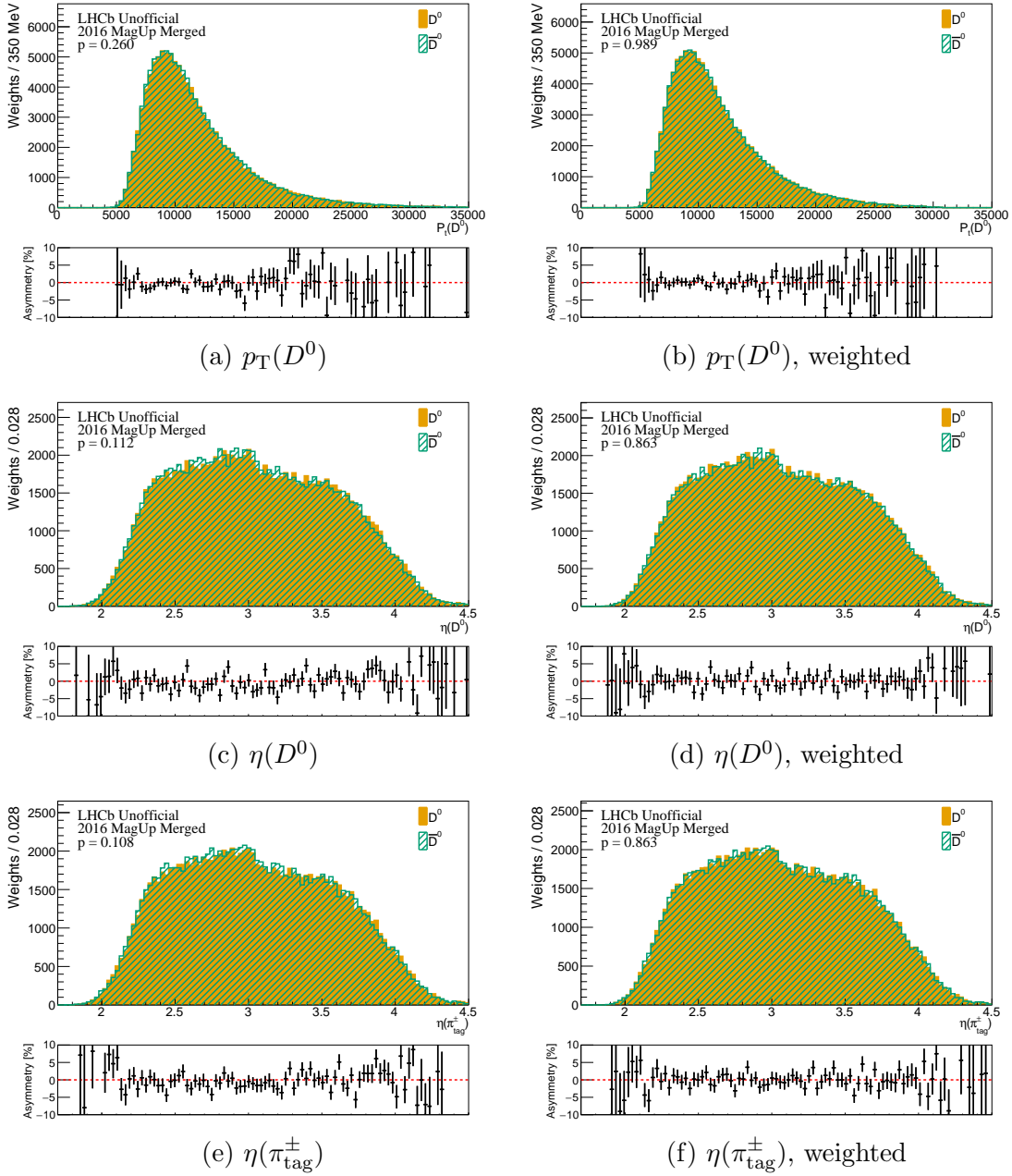


Figure C.8: 2016 *MagUp* merged signal channel  $D^0$  and tagging pion kinematic distributions before (left) and after (right) kinematic weighting.

## D Systematic errors from fit model toy studies

The systematic uncertainties affecting the measured  $\Delta Y$  based on the choice of  $\Delta m$  fit model were described Section 7.1. In particular, a systematic uncertainty given by  $\sqrt{\sigma_{\text{pull}}^2 - 1} \times \sigma_{\text{stat}}$  was assigned based on toys using the nominal fit model, to correct any possible underestimation of the statistical uncertainty. Given some set of measurements of  $\Delta Y$  from toy datasets, the variance is given by

$$\text{Var}(\Delta Y) = \sigma^2, \quad (8.12)$$

where  $\sigma$  is the true statistical uncertainty. If the statistical error is slightly underestimated, it can be expressed as

$$\sigma_{\text{stat}} = (1 - \varepsilon)\sigma, \quad (8.13)$$

where  $\varepsilon > 0$  is some small number. The variance of the pull distribution (for toy datasets generated with  $\Delta Y = 0$ ) is then given by

$$\sigma_{\text{pull}}^2 \equiv \text{Var}\left(\frac{\Delta Y - 0}{\sigma_{\text{stat}}}\right) = \text{Var}\left(\frac{\Delta Y}{(1 - \varepsilon)\sigma}\right) = \frac{1}{(1 - \varepsilon)^2}, \quad (8.14)$$

using the standard properties of the variance in the last equality. The correct statistical uncertainty can be recovered by assigning an additional systematic uncertainty given by

$$\sigma_{\text{syst}} = \sqrt{\sigma_{\text{pull}}^2 - 1} \times \sigma_{\text{stat}}. \quad (8.15)$$

The total uncertainty becomes

$$\begin{aligned} \sigma_{\text{tot}}^2 &= \sigma_{\text{stat}}^2 + \sigma_{\text{syst}}^2 \\ &= (1 - \varepsilon)^2 \sigma^2 + \left[ \frac{1}{(1 - \varepsilon)^2} - 1 \right] (1 - \varepsilon)^2 \sigma^2 \\ &= \sigma^2. \end{aligned} \quad (8.16)$$

## E Additional $h^+h'^-$ asymmetry study plots

This section contains additional plots related to the detection asymmetry studies detailed in Section 7.9.

### E.1 Phase-space distributions of $D_{(s)}^+ \rightarrow 3h$ decays

Figure E.1 shows the phase-space distribution of reconstructed and selected candidates in the control channel, split by  $\pi^0$  reconstruction category. Figure E.2 shows the corresponding distribution of candidates for the  $D^+ \rightarrow K^-\pi^+\pi^+$  decay used in the  $K\pi$  detection asymmetry studies. Figure E.3 shows the phase-space distribution of reconstructed and selected candidates in the signal channel, split by  $\pi^0$  reconstruction category. Figure E.4 shows the corresponding distribution of candidates for the  $D^+ \rightarrow \pi^+\pi^+\pi^-$  and  $D_s^+ \rightarrow \pi^+\pi^+\pi^-$  decays used in the  $K\pi$  detection asymmetry studies.

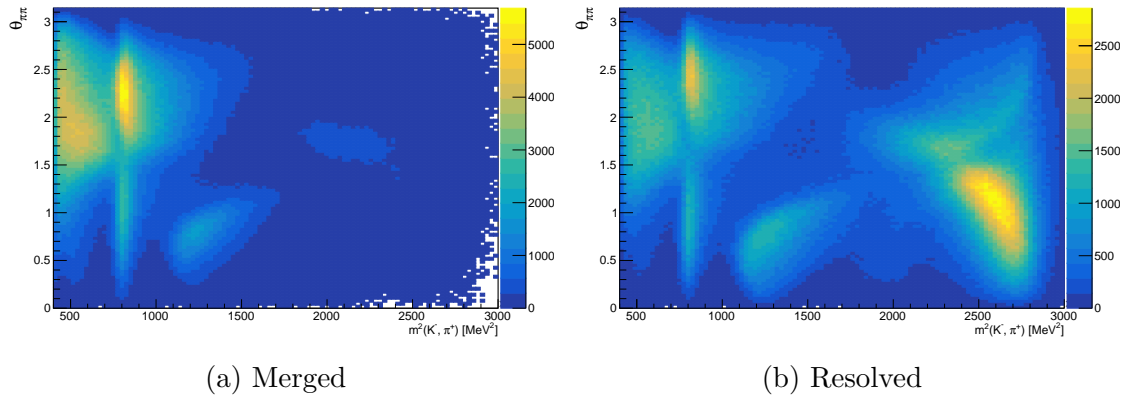


Figure E.1: Phase-space distribution of reconstructed and selected  $D^0 \rightarrow K^-\pi^+\pi^0$  candidates, split by  $\pi^0$  reconstruction category.

### E.2 Alternative description of time-dependent $K\pi$ asymmetry maps

Figures E.5, E.6, E.7 and E.8 show a complementary set of  $K^-\pi^+$  detection asymmetry studies to those documented in Section 7.9.3, with the time dependence of the asymmetry maps is expressed in terms of  $m^2(K^-, \pi^+)$  instead of  $\theta_{K\pi}$ . A systematic uncertainty of  $3.33 \times 10^{-4}$  is obtained, which is extremely compatible with the result from the nominal approach of  $3.37 \times 10^{-4}$ .

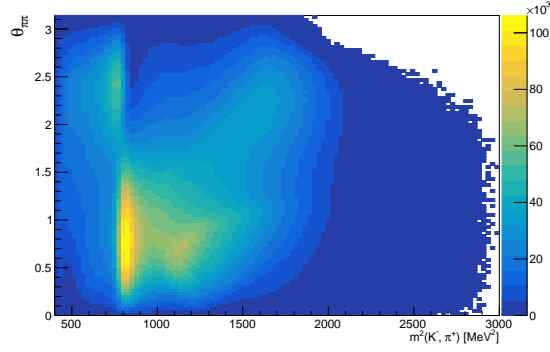


Figure E.2: Phase-space distribution of reconstructed and selected  $D^+ \rightarrow K^- \pi^+ \pi^+$  candidates.

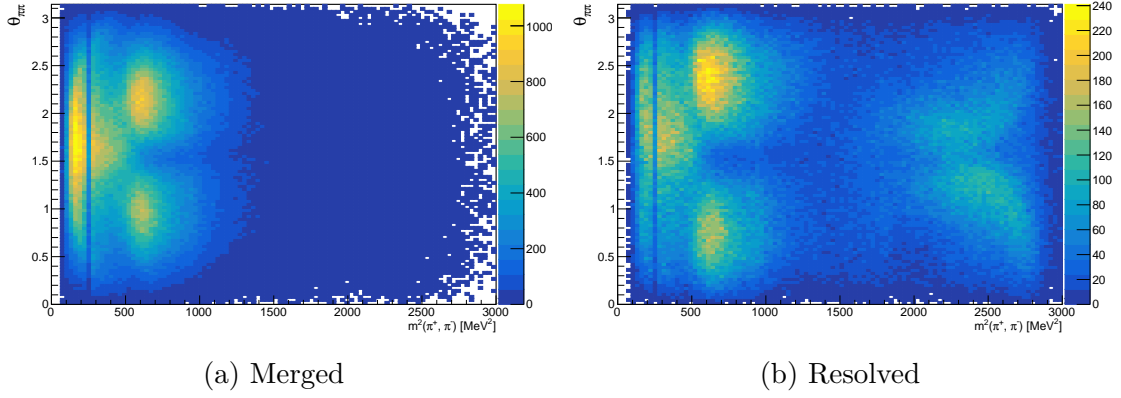


Figure E.3: Phase-space distribution of reconstructed and selected  $D^0 \rightarrow \pi^+ \pi^- \pi^0$  candidates, split by  $\pi^0$  reconstruction category.

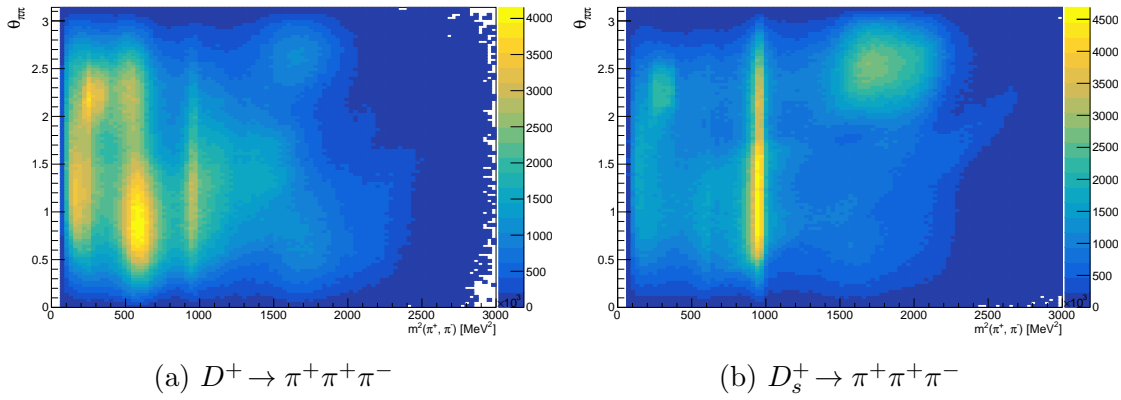
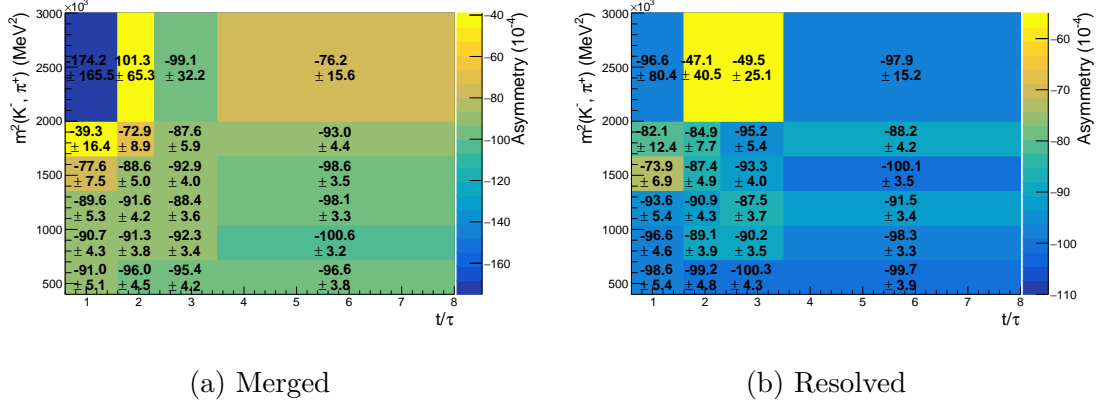
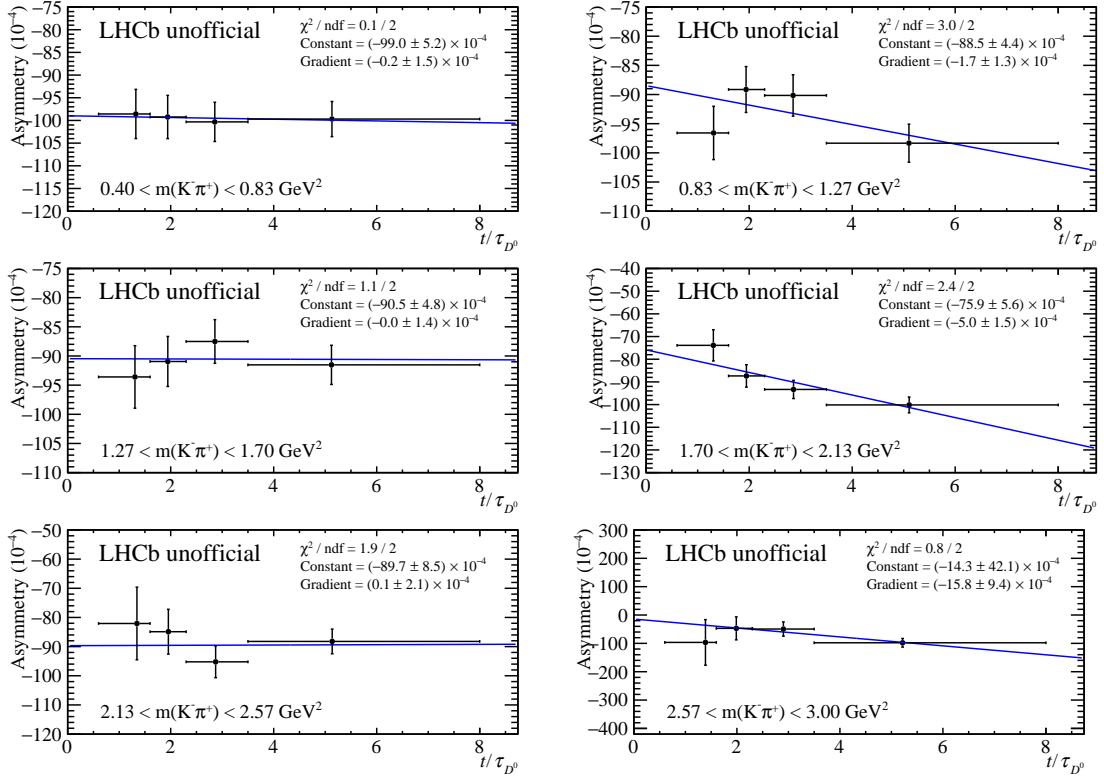


Figure E.4: Phase-space distribution of reconstructed and selected  $D^+ \rightarrow \pi^+ \pi^+ \pi^-$  (left) and  $D_s^+ \rightarrow \pi^+ \pi^+ \pi^-$  (right) candidates.

Figure E.5:  $K\pi$  detection asymmetry maps split by  $\pi^0$  reconstruction category.Figure E.6: Linear fit to the time-dependent asymmetry in each  $m^2(K^-, \pi^+)$  bin for the resolved category.

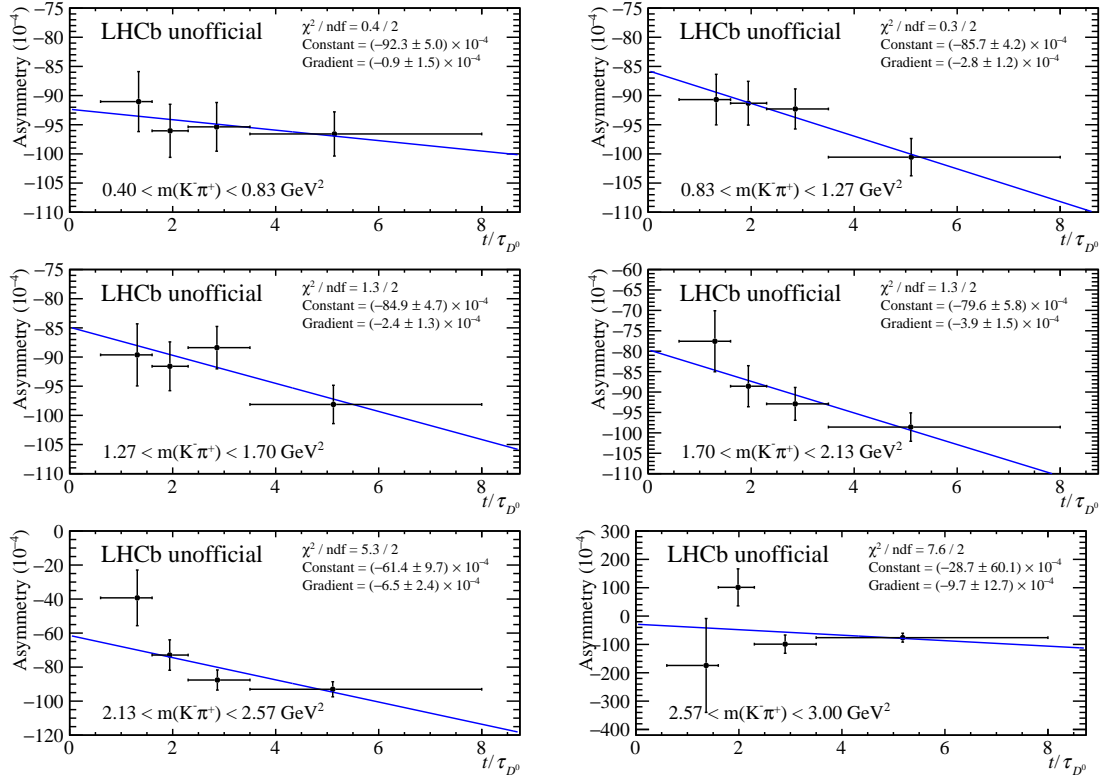


Figure E.7: Linear fit to the time-dependent asymmetry in each  $m^2(K^-, \pi^+)$  bin for the merged category.

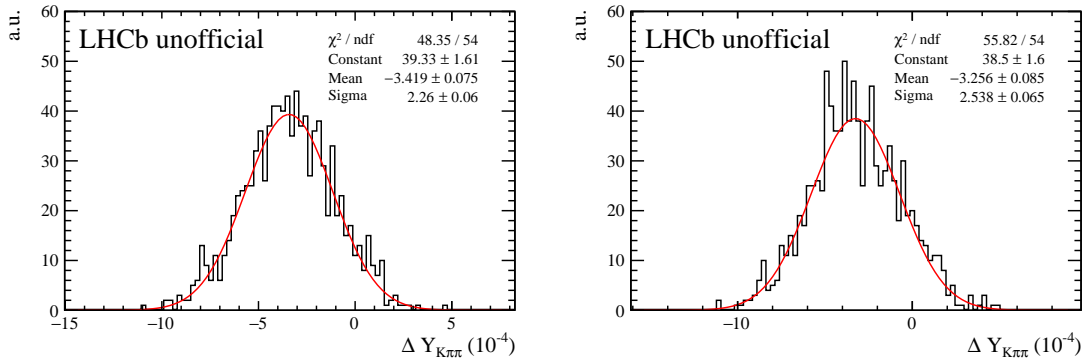


Figure E.8:  $A_{\text{det}}^{K\pi}$  toy study results with time-dependence parameterised in terms of  $m^2(K^-, \pi^+)$  in the asymmetry maps for merged (left) and resolved (right).

## F Stability checks

To test the stability of the measured asymmetries, and for the presence of ‘hidden’ variables, the final measurement has been re-performed in bins of different variables. Firstly, the measurement is performed in two bins of  $\log(\chi_{\text{IP}}^2(D^0))$  to ensure that the systematic uncertainty associated with contamination from secondary decays is not underestimated. The resulting measurements are presented in Figure F.1. Similar studies where the data is divided by  $p_T$  of the  $D^0$  meson and the tagging pion are presented in Figures F.2 and F.3, respectively. Finally Figure F.4 shows a similar measurement where the data is divided by HLT1 trigger line. ‘TwoTrack’ refers to the requirement that the  $D^0$  candidate fires TOS on the Hlt1TwoTrackMVA line. ‘Track’ refers to the requirement that the  $D^0$  meson fires TOS on the Hlt1TrackMVA line, and does not fire TOS on the Hlt1TwoTrackMVA line, to ensure the two samples are independent. The 2012 dataset is excluded from this study since it originates from only a single trigger line at HLT1 level. Table 8.1 lists the measured values and p-values when each of the two independent sub-samples for each study are combined. The p-value is drawn from a  $\chi^2$  fit with a single degree of freedom to determine the combined measurement of the two sub-samples. In all cases, the sub-samples are found to be consistent up to statistical fluctuations.

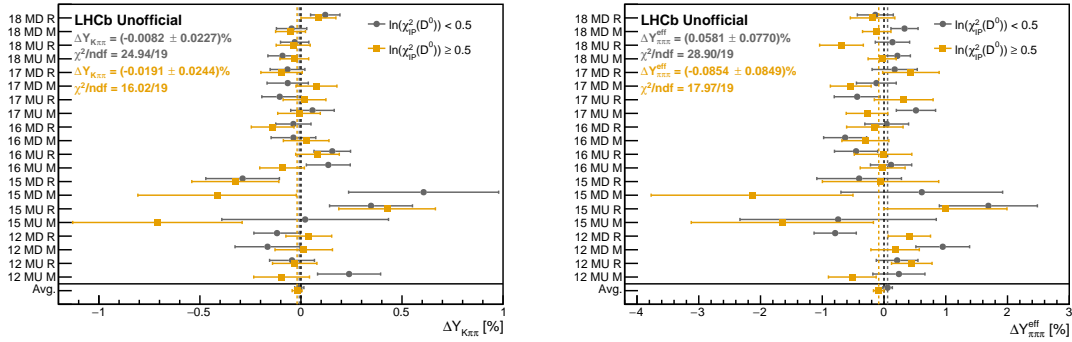


Figure F.1: Measured asymmetries in the control (left) and signal (right) channels when the data is divided by  $\log(\chi_{\text{IP}}^2(D^0))$ .

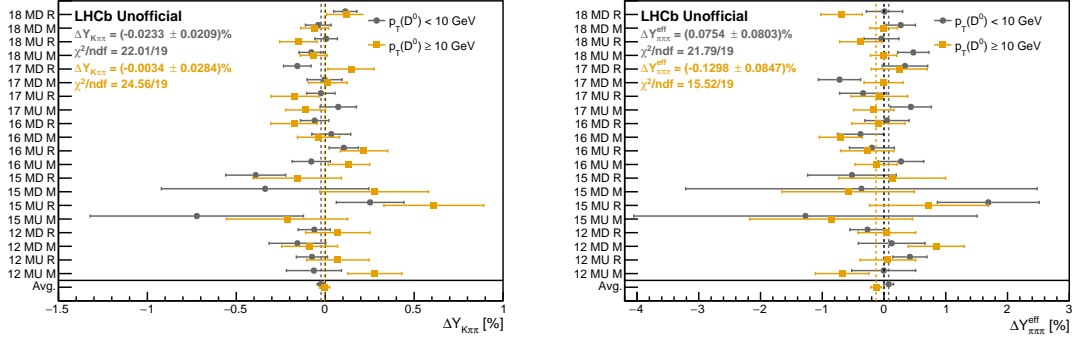


Figure F.2: Measured asymmetries in the control (left) and signal (right) channels when the data is divided by  $D^0$  meson  $p_T$ .

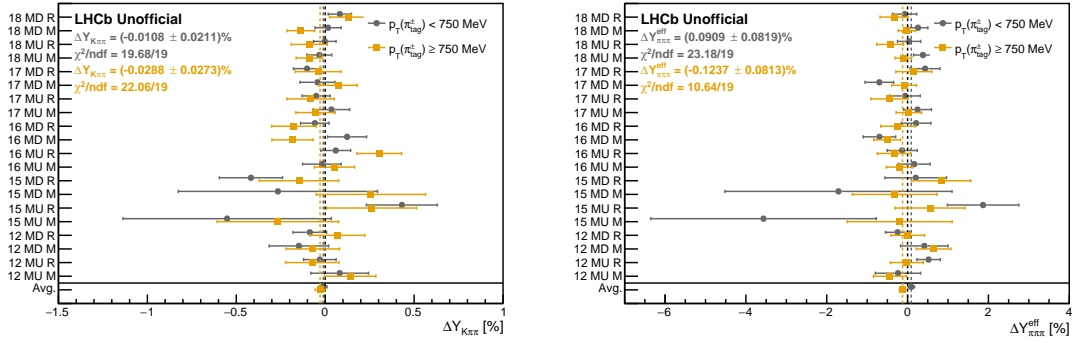


Figure F.3: Measured asymmetries in the control (left) and signal (right) channels when the data is divided by tagging pion  $p_T$ .

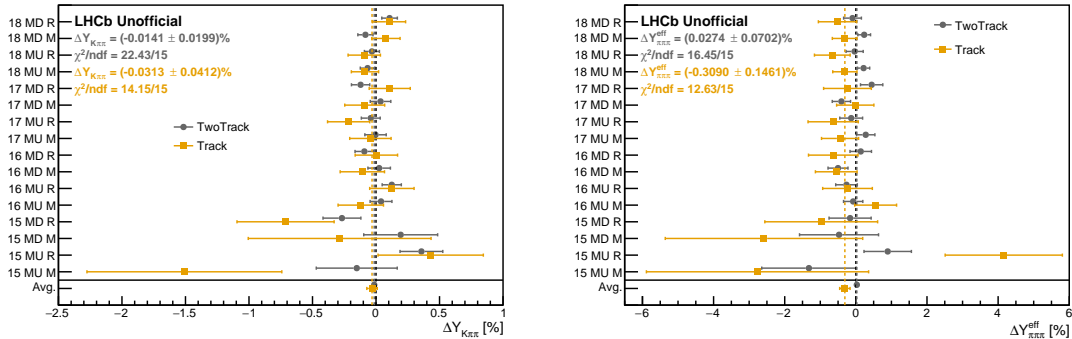


Figure F.4: Measured asymmetries in the control (left) and signal (right) channels when the data is divided by HLT1 trigger line.

Stability check	Control channel		Signal channel	
	$\Delta Y_{K\pi\pi} (\times 10^{-4})$	p-value (%)	$\Delta Y_{\pi\pi\pi}^{\text{eff}} (\times 10^{-4})$	p-value (%)
$\log(\chi_{\text{IP}}^2(D^0))$	$-1.33 \pm 1.66$	74	$-0.67 \pm 5.70$	21
$p_{\text{T}}(D^0)$	$-1.63 \pm 1.68$	57	$-2.17 \pm 5.83$	7.9
$p_{\text{T}}(\pi_{\text{tag}}^{\pm})$	$-1.75 \pm 1.67$	60	$-1.72 \pm 5.77$	6.3
HLT1 line	$-1.74 \pm 1.79$	71	$-3.57 \pm 6.33$	3.8

Table 8.1: Results of combining the independent sub-samples from each stability test in both the signal and control channels.

---

# Bibliography

---

- [1] T. D. Lee and C. N. Yang, *Question of parity conservation in weak interactions*, Phys. Rev. **104** (1956) 254. (Pages 1 and 5)
- [2] S. L. Glashow, J. Iliopoulos, and L. Maiani, *Weak interactions with lepton-hadron symmetry*, Phys. Rev. D **2** (1970) 1285. (Page 1)
- [3] M. Kobayashi and T. Maskawa, *CP Violation in the Renormalizable Theory of Weak Interaction*, Prog. Theor. Phys. **49** (1973) 652. (Pages 1 and 12)
- [4] P. W. Higgs, *Spontaneous symmetry breakdown without massless bosons*, Phys. Rev. **145** (1966) 1156. (Pages 1 and 9)
- [5] F. Englert and R. Brout, *Broken symmetry and the mass of gauge vector mesons*, Phys. Rev. Lett. **13** (1964) 321. (Pages 1 and 9)
- [6] V. Trimble, *Existence and Nature of Dark Matter in the Universe*, Ann. Rev. Astron. Astrophys. **25** (1987) 425. (Page 1)
- [7] L. Canetti, M. Drewes, and M. Shaposhnikov, *Matter and Antimatter in the Universe*, New J. Phys. **14** (2012) 095012, [arXiv:1204.4186](https://arxiv.org/abs/1204.4186). (Page 1)
- [8] Particle Data Group, R. L. Workman *et al.*, *Review of particle physics*, Prog. Theor. Exp. Phys. **2022** (2022) 083C01. (Pages 2, 3, 19, 23, 29, 169, and 172)
- [9] *Mug with the Lagrangian equation and the CERN logo*, <https://visit.cern/content/standard-model-mug>. Accessed 1/2/24. (Page 3)
- [10] A. Einstein, *On the electrodynamics of moving bodies*, Annalen Phys. **17** (1905) 891. (Page 4)

- [11] E. Noether, *Invariante variationsprobleme*, Nachrichten von der Gesellschaft der Wissenschaften zu Göttingen, Mathematisch-Physikalische Klasse **1918** (1918) 235. (Page 4)
- [12] S. Weinberg, *The Making of the standard model*, Eur. Phys. J. C **34** (2004) 5, [arXiv:hep-ph/0401010](#). (Page 4)
- [13] G. Luders, *Proof of the TCP theorem*, Annals Phys. **2** (1957) 1. (Page 5)
- [14] C. S. Wu *et al.*, *Experimental test of parity conservation in beta decay*, Phys. Rev. **105** (1957) 1413. (Pages 5 and 6)
- [15] J. H. Christenson, J. W. Cronin, V. L. Fitch, and R. Turlay, *Evidence for the  $2\pi$  Decay of the  $K_2^0$  Meson*, Phys. Rev. Lett. **13** (1964) 138. (Page 6)
- [16] A. D. Sakharov, *Violation of CP Invariance, C asymmetry, and baryon asymmetry of the universe*, Pisma Zh. Eksp. Teor. Fiz. **5** (1967) 32. (Page 6)
- [17] KTeV collaboration, A. Alavi-Harati *et al.*, *Observation of direct CP violation in  $K_{S,L} \rightarrow \pi\pi$  decays*, Phys. Rev. Lett. **83** (1999) 22, [arXiv:hep-ex/9905060](#). (Page 6)
- [18] BaBar collaboration, B. Aubert *et al.*, *Observation of CP violation in the  $B^0$  meson system*, Phys. Rev. Lett. **87** (2001) 091801, [arXiv:hep-ex/0107013](#). (Page 6)
- [19] Belle collaboration, K. Abe *et al.*, *Observation of large CP violation in the neutral B meson system*, Phys. Rev. Lett. **87** (2001) 091802, [arXiv:hep-ex/0107061](#). (Page 6)
- [20] LHCb collaboration, R. Aaij *et al.*, *First observation of CP violation in the decays of  $B_s^0$  mesons*, Phys. Rev. Lett. **110** (2013) 221601, [arXiv:1304.6173](#). (Page 6)
- [21] LHCb collaboration, R. Aaij *et al.*, *Observation of CP violation in two-body  $B_{(s)}^0$  decays to charged pions and kaons*, JHEP **03** (2021) 075, [arXiv:2012.5319](#). (Page 6)
- [22] M. Dine and A. Kusenko, *The Origin of the matter - antimatter asymmetry*, Rev. Mod. Phys. **76** (2003) 1, [arXiv:hep-ph/0303065](#). (Page 6)

- [23] T2K collaboration, K. Abe *et al.*, *Constraint on the matter–antimatter symmetry-violating phase in neutrino oscillations*, Nature **580** (2020) 339, [arXiv:1910.03887](#), [Erratum: Nature 583, E16 (2020)]. (Page 6)
- [24] M. Fukugita and T. Yanagida, *Baryogenesis Without Grand Unification*, Phys. Lett. B **174** (1986) 45. (Page 6)
- [25] S. L. Glashow, *Partial Symmetries of Weak Interactions*, Nucl. Phys. **22** (1961) 579. (Page 6)
- [26] A. Salam and J. C. Ward, *Electromagnetic and weak interactions*, Phys. Lett. **13** (1964) 168. (Page 6)
- [27] S. Weinberg, *A Model of Leptons*, Phys. Rev. Lett. **19** (1967) 1264. (Page 6)
- [28] J. Goldstone, *Field Theories with Superconductor Solutions*, Nuovo Cim. **19** (1961) 154. (Page 9)
- [29] N. Cabibbo, *Unitary symmetry and leptonic decays*, Phys. Rev. Lett. **10** (1963) 531. (Page 12)
- [30] B. Pontecorvo, *Inverse beta processes and nonconservation of lepton charge*, Zh. Eksp. Teor. Fiz. **34** (1957) 247. (Page 12)
- [31] Z. Maki, M. Nakagawa, and S. Sakata, *Remarks on the unified model of elementary particles*, Prog. Theor. Phys. **28** (1962) 870. (Page 12)
- [32] CKMfitter group, J. Charles *et al.*, *Current status of the standard model CKM fit and constraints on  $\Delta F = 2$  new physics*, Phys. Rev. **D91** (2015) 073007, [arXiv:1501.05013](#), updated results and plots available at <http://ckmfitter.in2p3.fr/>. (Page 13)
- [33] L. V. Silva, *CKM matrix status in 2023*, 12th International Workshop on the CKM Unitarity Triangle (CKM 2023), 2023. (Page 13)
- [34] K. Lande, L. M. Lederman, and W. Chinowsky, *Report on long-lived  $K^0$  mesons*, Phys. Rev. **105** (1957) 1925. (Page 14)
- [35] UA1 collaboration, C. Albajar *et al.*, *Search for  $B^0$ - $\bar{B}^0$  oscillations at the CERN proton-antiproton collider*, Phys. Lett. B **186** (1987) 247, [Erratum: Phys.Lett.B 197, 565 (1987)]. (Page 14)

- [36] ARGUS collaboration, H. Albrecht *et al.*, *Observation of  $B^0$  - anti- $B^0$  Mixing*, Phys. Lett. B **192** (1987) 245. (Page 14)
- [37] CDF Collaboration, A. Abulencia *et al.*, *Observation of  $B_s^0$ - $\bar{B}_s^0$  oscillations*, Phys. Rev. Lett. **97** (2006) 242003. (Page 14)
- [38] LHCb collaboration, R. Aaij *et al.*, *Precision measurement of the  $B_s^0$ - $\bar{B}_s^0$  oscillation frequency in the decay  $B_s^0 \rightarrow D_s^- \pi^+$* , New J. Phys. **15** (2013) 053021, [arXiv:1304.4741](#). (Page 14)
- [39] LHCb collaboration, R. Aaij *et al.*, *Precise determination of the  $B_s^0$ - $\bar{B}_s^0$  oscillation frequency*, Nature Physics **18** (2022) 1, [arXiv:2104.04421](#). (Page 14)
- [40] SNO Collaboration, *Measurement of the Rate of  $\nu_e + d \rightarrow p + p + e^-$  Interactions Produced by  $^8B$  Solar Neutrinos at the Sudbury Neutrino Observatory*, Phys. Rev. Lett. **87** (2001) 071301. (Page 14)
- [41] V. Weisskopf and E. P. Wigner, *Calculation of the natural brightness of spectral lines on the basis of Dirac's theory*, Z. Phys. **63** (1930) 54. (Page 15)
- [42] V. Weisskopf and E. Wigner, *Over the natural line width in the radiation of the harmonius oscillator*, Z. Phys. **65** (1930) 18. (Page 15)
- [43] Y. Amhis *et al.*, *Averages of  $b$ -hadron,  $c$ -hadron, and  $\tau$ -lepton properties as of 2021*, Phys. Rev. **D107** (2023) 052008, [arXiv:2206.07501](#), updated results and plots available at <https://hflav.web.cern.ch>. (Pages 16, 19, 21, 23, 24, 29, and 186)
- [44] M. Gersabeck *et al.*, *On the interplay of direct and indirect CP violation in the charm sector*, J. Phys. G **39** (2012) 045005, [arXiv:1111.6515](#). (Page 18)
- [45] LHCb collaboration, Aaij, R. and others, *Observation of the mass difference between neutral charm-meson eigenstates*, Phys. Rev. Lett. **127** (2021) 111801, [arXiv:2106.03744](#). (Pages 19, 24, 34, and 172)
- [46] LHCb collaboration, R. Aaij *et al.*, *Model-independent measurement of charm mixing parameters in  $\bar{B} \rightarrow D^0(\rightarrow K^{*0} \pi^+ \pi^-) \mu^- \bar{\nu}_\mu X$  decays*, Phys. Rev. **D108** (2023) 052005, [arXiv:2208.06512](#). (Pages 19 and 172)

- [47] I. I. Y. Bigi and N. G. Uraltsev,  *$D^0$  - anti- $D^0$  oscillations as a probe of quark hadron duality*, Nucl. Phys. B **592** (2001) 92, [arXiv:hep-ph/0005089](#). (Page 21)
- [48] A. Lenz and G. Wilkinson, *Mixing and CP Violation in the Charm System*, Ann. Rev. Nucl. Part. Sci. **71** (2021) 59, [arXiv:2011.04443](#). (Pages 22 and 23)
- [49] BaBar collaboration, B. Aubert *et al.*, *Search for CP Violation in Neutral D Meson Cabibbo-suppressed Three-body Decays*, Phys. Rev. D **78** (2008) 051102, [arXiv:0802.4035](#). (Page 22)
- [50] LHCb collaboration, R. Aaij *et al.*, *Measurement of the time-integrated CP asymmetry in  $D^0 \rightarrow K^- K^+$  decays*, Phys. Rev. Lett. **131** (2023) 091802, [arXiv:2209.03179](#). (Pages 22, 23, and 34)
- [51] A. L. Kagan and L. Silvestrini, *Dispersive and absorptive CP violation in  $D^0 - \bar{D}^0$  mixing*, Phys. Rev. D **103** (2021) 053008, [arXiv:2001.07207](#). (Page 23)
- [52] LHCb collaboration, R. Aaij *et al.*, *Observation of CP violation in charm decays*, Phys. Rev. Lett. **122** (2019) 211803, [arXiv:1903.08726](#). (Pages 23 and 34)
- [53] BaBar collaboration, J. P. Lees *et al.*, *Measurement of the neutral D meson mixing parameters in a time-dependent amplitude analysis of the  $D^0 \rightarrow \pi^+ \pi^- \pi^0$  decay*, Phys. Rev. D **93** (2016) 112014, [arXiv:1604.00857](#). (Pages 23, 166, and 169)
- [54] H.-Y. Cheng and C.-W. Chiang, *Revisiting CP violation in  $D \rightarrow PP$  and  $VP$  decays*, Phys. Rev. D **100** (2019) 093002, [arXiv:1909.03063](#). (Page 23)
- [55] BaBar collaboration, J. P. Lees *et al.*, *Measurement of  $D^0 - \bar{D}^0$  Mixing and CP Violation in Two-Body  $D^0$  Decays*, Phys. Rev. D **87** (2013) 012004, [arXiv:1209.3896](#). (Page 23)
- [56] Belle collaboration, M. Starič *et al.*, *Measurement of  $D^0 - \bar{D}^0$  mixing and search for CP violation in  $D^0 \rightarrow K^+ K^-, \pi^+ \pi^-$  decays with the full Belle data set*, Phys. Lett. B **753** (2016) 412, [arXiv:1509.08266](#). (Page 23)

- [57] CDF collaboration, T. A. Aaltonen *et al.*, *Measurement of indirect CP-violating asymmetries in  $D^0 \rightarrow K^+K^-$  and  $D^0 \rightarrow \pi^+\pi^-$  decays at CDF*, Phys. Rev. D **90** (2014) 111103, [arXiv:1410.5435](#). (Page 23)
- [58] LHCb collaboration, R. Aaij *et al.*, *Updated measurement of decay-time-dependent CP asymmetries in  $D^0 \rightarrow K^+K^-$  and  $D^0 \rightarrow \pi^+\pi^-$  decays*, Phys. Rev. D **101** (2020) 012005, [arXiv:1911.01114](#). (Page 23)
- [59] LHCb collaboration, R. Aaij *et al.*, *Search for time-dependent CP violation in  $D^0 \rightarrow K^+K^-$  and  $D^0 \rightarrow \pi^+\pi^-$  decays*, Phys. Rev. D **104** (2021) 072010, [arXiv:2105.09889](#). (Pages 23, 34, 181, and 187)
- [60] LHCb collaboration, R. Aaij *et al.*, *Measurement of the charm mixing parameter  $y_{CP} - y_{CP}^{K\pi}$  using two-body  $D^0$  meson decays*, Phys. Rev. D **105** (2022) 092013, [arXiv:2202.09106](#). (Pages 24 and 34)
- [61] S. Malde, C. Thomas, and G. Wilkinson, *Measuring CP violation and mixing in charm with inclusive self-conjugate multibody decay modes*, Phys. Rev. D **91** (2015) 094032, [arXiv:1502.04560](#). (Page 25)
- [62] S. Malde *et al.*, *First determination of the CP content of  $D \rightarrow \pi^+\pi^-\pi^+\pi^-$  and updated determination of the CP contents of  $D \rightarrow \pi^+\pi^-\pi^0$  and  $D \rightarrow K^+K^-\pi^0$* , Phys. Lett. B **747** (2015) 9, [arXiv:1504.05878](#). (Pages 27 and 167)
- [63] O. S. Brüning *et al.*, *LHC Design Report*, CERN Yellow Reports: Monographs, CERN, Geneva, 2004. (Page 31)
- [64] M. Schaumann *et al.*, *First Xenon-Xenon Collisions in the LHC*, in *9th International Particle Accelerator Conference*, 2018. (Page 31)
- [65] R. Bruce *et al.*, *Studies for an LHC Pilot Run with Oxygen Beams*, in *12th International Particle Accelerator Conference*, 2021. (Page 31)
- [66] G. Aad *et al.*, *Observation of a new particle in the search for the Standard Model Higgs boson with the ATLAS detector at the LHC*, Physics Letters B **716** (2012) 1. (Page 31)
- [67] S. Chatrchyan *et al.*, *Observation of a new boson at a mass of 125 GeV with the CMS experiment at the LHC*, Physics Letters B **716** (2012) 30. (Page 31)

- [68] J. Wenninger, *The LHC collider*, Comptes Rendus Physique **16** (2015) 347. (Pages 32 and 33)
- [69] M. Vretenar *et al.*, *Linac4 design report*, vol. 6 of *CERN Yellow Reports: Monographs*, CERN, Geneva, 2020. (Page 32)
- [70] LHCb collaboration, R. Aaij *et al.*, *LHCb detector performance*, Int. J. Mod. Phys. **A30** (2015) 1530022, [arXiv:1412.6352](#). (Pages 33, 38, 39, 44, 46, 50, 51, 52, 58, 59, 60, and 62)
- [71] F. Follin and D. Jacquet, *Implementation and experience with luminosity levelling with offset beam*, in *ICFA Mini-Workshop on Beam-Beam Effects in Hadron Colliders*, 183–187, 2014, [arXiv:1410.3667](#). (Page 34)
- [72] R. Lindner, *LHCb layout*, LHCb Collection, URL: <https://cds.cern.ch/record/1087860>, 2008. (Page 35)
- [73] LHCb collaboration, C. Elsasser,  *$\bar{b}b$  production angle plots*, URL: [https://lhcb.web.cern.ch/lhcb/speakersbureau/html/bb\\_ProductionAngles.html](https://lhcb.web.cern.ch/lhcb/speakersbureau/html/bb_ProductionAngles.html), Accessed 05/02/24. (Page 36)
- [74] R. Aaij *et al.*, *Performance of the LHCb Vertex Locator*, JINST **9** (2014) P09007, [arXiv:1405.7808](#). (Pages 36, 39, 52, 53, and 70)
- [75] LHCb collaboration, *LHCb reoptimized detector design and performance: Technical Design Report*, CERN-LHCC-2003-030, 2003. (Page 37)
- [76] T. J. V. Bowcock *et al.*, *VELO geometry optimisation*, LHCb-2000-090, 2000. (Page 37)
- [77] LHCb collaboration, *LHCb VELO (VERTex LOcator): Technical Design Report*, CERN-LHCC-2001-011, 2001. (Pages 37 and 70)
- [78] LHCb collaboration, A. A. Alves Jr. *et al.*, *The LHCb detector at the LHC*, JINST **3** (2008) S08005. (Pages 37, 38, 39, 40, 41, 42, 43, 44, 46, 50, 53, 54, 55, 57, 58, and 59)
- [79] M. Agari *et al.*, *Beetle: A radiation hard readout chip for the LHCb experiment*, Nucl. Instrum. Meth. A **518** (2004) 468. (Page 39)

- [80] G. Haefeli, A. Bay, F. Legger, and L. Locatelli, *TELL 1: A common data acquisition board for LHCb*, in *9th Workshop on Electronics for LHC Experiments*, pp.129-133, 2003. (Page 39)
- [81] LHCb VELO collaboration, E. Jans, *Operational aspects of the VELO cooling system of LHCb*, PoS **Vertex2013** (2013) 038. (Page 40)
- [82] S. Bachmann and A. Pellegrino, *Geometry of the LHCb Outer Tracker (Part I)*, LHCb-2003-035, 2003. (Page 45)
- [83] R. Arink *et al.*, *Performance of the LHCb Outer Tracker*, JINST **9** (2014) P01002, [arXiv:1311.3893](#). (Page 46)
- [84] R. Fruhwirth, *Application of Kalman filtering to track and vertex fitting*, Nucl. Instrum. Meth. A **262** (1987) 444. (Page 46)
- [85] O. Callot and S. Hansmann-Menzemer, *The Forward Tracking: Algorithm and Performance Studies*, LHCb-2007-015, CERN-LHCb-2007-015, 2007. (Page 49)
- [86] M. Needham, *Performance of the Track Matching*, LHCb-2007-129, CERN-LHCb-2007-129, 2007. (Page 49)
- [87] M. Needham and J. Van Tilburg, *Performance of the track matching*, LHCb-2007-020, CERN-LHCb-2007-020, 2007. (Page 49)
- [88] LHCb collaboration, R. Aaij *et al.*, *Measurement of the track reconstruction efficiency at LHCb*, JINST **10** (2015) P02007, [arXiv:1408.1251](#). (Page 51)
- [89] LHCb collaboration, R. Aaij *et al.*, *Measurement of the CP-violating phase  $\phi_s$  in the decay  $B_s^0 \rightarrow J/\psi\phi$* , Phys. Rev. Lett. **108** (2012) 101803, [arXiv:1112.3183](#). (Page 53)
- [90] S. Ogilvy, *Branching ratios of charmed baryons in the LHCb experiment*, Available at: <https://theses.gla.ac.uk/6463/> (Accessed 21/05/2024), 2015. PhD thesis. (Page 54)
- [91] C. Abellan Beteta *et al.*, *Calibration and performance of the LHCb calorimeters in Run 1 and 2 at the LHC*, [arXiv:2008.11556](#), submitted to JINST. (Pages 57 and 58)

- [92] C. Coca *et al.*, *The hadron calorimeter prototype beam-test results*, LHCb-2000-036, 2000. (Page 57)
- [93] LHCb collaboration, D. Derkach, M. Hushchyn, and N. Kazeev, *Machine Learning based Global Particle Identification Algorithms at the LHCb Experiment*, EPJ Web Conf. **214** (2019) 06011. (Page 60)
- [94] LHCb collaboration, Derkach, Denis and Hushchyn, Mikhail and Likhomanenko, Tatiana and Rogozhnikov, Alex and Kazeev, Nikita and Chekalina, Victoria and Neychev, Radoslav and Kirillov, Stanislav and Ratnikov, Fedor, *Machine-Learning-based global particle-identification algorithms at the LHCb experiment*, J. Phys. Conf. Ser. **1085** (2018) 042038. (Page 60)
- [95] R. Calabrese *et al.*, *Performance of the LHCb RICH detectors during LHC Run 2*, JINST **17** (2022) P07013, [arXiv:2205.13400](#). (Page 60)
- [96] LHCb collaboration, *Trigger Schemes*, URL: <http://lhcb.web.cern.ch/lhcb/speakersbureau/html/TriggerScheme.html>, Accessed 15/02/24. (Page 61)
- [97] C. Barschel, *Precision luminosity measurement at LHCb with beam-gas imaging*, CERN-THESIS-2013-301, 2014. PhD thesis. (Pages 63, 70, 77, 87, 100, 108, and 109)
- [98] LHCb collaboration, R. Aaij *et al.*, *Measurement of antiproton production in  $pHe$  collisions at  $\sqrt{s_{NN}} = 110$  GeV*, Phys. Rev. Lett. **121** (2018) 222001, [arXiv:1808.06127](#). (Pages 63 and 72)
- [99] LHCb collaboration, R. Aaij *et al.*, *First measurement of charm production in fixed-target configuration at the LHC*, Phys. Rev. Lett. **122** (2019) 132002, [arXiv:1810.07907](#). (Page 63)
- [100] LHCb collaboration, R. Aaij *et al.*, *Charmonium production in  $pNe$  collisions at  $\sqrt{s_{NN}} = 68.5$  GeV*, Eur. Phys. J. **C83** (2023) 625, [arXiv:2211.11645](#). (Page 63)
- [101] LHCb collaboration, R. Aaij *et al.*, *Measurement of antiproton production from antihyperon decays in  $pHe$  collisions at  $\sqrt{s_{NN}} = 110$  GeV*, Eur. Phys. J. **C83** (2023) 543, [arXiv:2205.09009](#). (Page 63)

- [102] LHCb collaboration, R. Aaij *et al.*, *The LHCb Upgrade I*, [arXiv:2305.10515](#), to appear in JINST. (Page 64)
- [103] LHCb collaboration, *LHCb VELO Upgrade Technical Design Report*, CERN-LHCC-2013-021, 2013. (Page 64)
- [104] LHCb collaboration, *LHCb Tracker Upgrade Technical Design Report*, CERN-LHCC-2014-001, 2014. (Page 64)
- [105] LHCb collaboration, *LHCb PID Upgrade Technical Design Report*, CERN-LHCC-2013-022, 2013. (Page 64)
- [106] LHCb collaboration, *LHCb Upgrade GPU High Level Trigger Technical Design Report*, CERN-LHCC-2020-006, 2020. (Page 65)
- [107] LHCb collaboration, *LHCb SMOG Upgrade*, CERN-LHCC-2019-005, 2019. (Page 65)
- [108] LHCb collaboration, E. Franzoso, *Fixed-target program upgrade and prospects at LHCb*, EPJ Web Conf. **259** (2022) 13010. (Page 65)
- [109] LHCb collaboration, *LHCb PLUME: Probe for Luminosity Measurement*, CERN-LHCC-2021-002, 2021. (Page 66)
- [110] ALEPH Collaboration, *Measurement of the absolute luminosity with the ALEPH detector*, Z. Phys. C **53** (1991) 375. (Page 68)
- [111] DELPHI collaboration, P. Abreu *et al.*, *Performance of the DELPHI detector*, Nucl. Instrum. Meth. A **378** (1996) 57. (Page 68)
- [112] BaBar collaboration, J. P. Lees *et al.*, *Time-Integrated Luminosity Recorded by the BABAR Detector at the PEP-II  $e^+e^-$  Collider*, Nucl. Instrum. Meth. A **726** (2013) 203, [arXiv:1301.2703](#). (Page 68)
- [113] D. Acosta *et al.*, *The performance of the CDF luminosity monitor*, Nucl. Instrum. Meth. A **494** (2002) 57. (Page 69)
- [114] B. C. K. Casey *et al.*, *The D0 Run IIb Luminosity Measurement*, Nucl. Instrum. Meth. A **698** (2013) 208, [arXiv:1204.0461](#). (Page 69)

- [115] S. van der Meer, *Calibration of the effective beam height in the ISR*, CERN-ISR-PO-68-31, ISR-PO-68-31, 1968. (Page 69)
- [116] C. Rubbia, *Measurement of the luminosity of  $p\bar{p}$  collider with a (generalized) Van der Meer Method*, CERN-p $\bar{p}$ -Note-38, 1977. (Page 69)
- [117] V. Balagura, *Non factorization at LHCb: Two-dimensional vdM scans*, LHC Lumi Days, 2019. (Page 69)
- [118] Møller, C. , *General Properties of the Characteristic Matrix in the Theory of Elementary Particles I*, K. Danske Vidensk. Selsk. Mat. -Fys. Medd. **23** (1945) 1, Available at: <http://publ.royalacademy.dk/books/79/497?lang=en> (Accessed 17/05/2024). (Page 69)
- [119] V. Balagura, *Notes on van der Meer Scan for Absolute Luminosity Measurement*, Nucl. Instrum. Meth. A **654** (2011) 634, [arXiv:1103.1129](https://arxiv.org/abs/1103.1129). (Page 70)
- [120] M. Ferro-Luzzi, *Proposal for an absolute luminosity determination in colliding beam experiments using vertex detection of beam-gas interactions*, Nucl. Instrum. Meth. **A553** (2005) 388. (Page 70)
- [121] LHCb collaboration, R. Aaij *et al.*, *Precision luminosity measurements at LHCb*, JINST **9** (2014) P12005, [arXiv:1410.0149](https://arxiv.org/abs/1410.0149). (Pages 70, 71, 77, 101, 109, 112, and 116)
- [122] G. R. Coombs, *Beam-Gas Imaging at the LHCb experiment*, CERN-THESIS-2021-058, 2021. PhD thesis. (Pages 70, 73, 78, and 83)
- [123] B. J. Holzer, *Introduction to Transverse Beam Dynamics*, in *CERN Accelerator School: Course on Superconductivity for Accelerators*, 27–45, 2013, [arXiv:1404.0923](https://arxiv.org/abs/1404.0923). (Page 71)
- [124] P. Odier, M. Ludwig, and S. Thoulet, *The DCCT for the LHC Beam Intensity Measurement*, CERN-BE-2009-019, 2009. (Page 73)
- [125] D. Belohrad *et al.*, *The LHC Fast BCT system: A comparison of Design Parameters with Initial Performance*, CERN-BE-2010-010, 2010. (Page 73)
- [126] C. Barschel *et al.*, *Results of the LHC DCCT Calibration Studies*, CERN-ATS-Note-2012-026, 2012. (Pages 73 and 81)

- [127] C. Ohm and T. Pauly, *The ATLAS beam pick-up based timing system*, Nucl. Instrum. Methods Phys. Res. , A **623** (2010) 558, [arXiv:0905.3648](#), Comments: Submitted to NIM A for the proceedings of TIPP09 (Tsukuba, Japan). (Page 74)
- [128] A. Alici *et al.*, *Study of the LHC ghost charge and satellite bunches for luminosity calibration*, CERN-ATS-Note-2012-029, 2012. (Pages 77 and 83)
- [129] A. Jeff *et al.*, *Longitudinal density monitor for the LHC*, Phys. Rev. ST Accel. Beams **15** (2012) 032803. (Page 78)
- [130] A. Jeff *et al.*, *First results of the LHC longitudinal density monitor*, Nucl. Instrum. Methods Phys. Res. , A **659** (2011) 549. (Page 78)
- [131] G. Anders *et al.*, *Study of the relative LHC bunch populations for luminosity calibration*, CERN-ATS-Note-2012-028, 2012. (Page 79)
- [132] LHCb collaboration, M. Gonzalez-Berges *et al.*, *Ghost charge measurements with beam-gas imaging in November 2022*, LHCb-FIGURE-2023-003, 2023. (Page 82)
- [133] McHugh, Niall, *Luminosity at LHCb in Run 3*, in *31st International Symposium on Lepton Photon Interactions at High Energies (Lepton Photon 2023)*, Melbourne, Australia., 2023. (Page 82)
- [134] M. Ferro-Luzzi, *Luminosity and luminous region shape for pure Gaussian bunches*, LHCb-PUB-2012-016, 2012. (Pages 94, 95, and 107)
- [135] W. Verkerke and D. P. Kirkby, *The RooFit toolkit for data modeling*, eConf **C0303241** (2003) MOLT007, [arXiv:physics/0306116](#). (Pages 104 and 146)
- [136] M. De Cian, S. Farry, P. Seyfert, and S. Stahl, *Fast neural-net based fake track rejection in the LHCb reconstruction*, LHCb-PUB-2017-011, CERN-LHCb-PUB-2017-011, 2017. (Page 122)
- [137] LHCb collaboration, R. Aaij *et al.*, *Search for CP violation in  $D^0 \rightarrow \pi^- \pi^+ \pi^0$  decays with the energy test*, Phys. Lett. **B740** (2015) 158, [arXiv:1410.4170](#). (Page 123)

- [138] R. Aaij *et al.*, *Performance of the LHCb trigger and full real-time reconstruction in Run 2 of the LHC*, JINST **14** (2019) P04013, [arXiv:1812.10790](#). (Page 124)
- [139] V. V. Gligorov and M. Williams, *Efficient, reliable and fast high-level triggering using a bonsai boosted decision tree*, JINST **8** (2013) P02013, [arXiv:1210.6861](#). (Page 125)
- [140] W. D. Hulsbergen, *Decay chain fitting with a Kalman filter*, Nucl. Instrum. Meth. **A552** (2005) 566, [arXiv:physics/0503191](#). (Page 126)
- [141] L. Breiman, J. H. Friedman, R. A. Olshen, and C. J. Stone, *Classification and Regression Trees (1st ed.)*, Chapman and Hall/CRC, 1984. (Page 127)
- [142] H. Voss, A. Hoecker, J. Stelzer, and F. Tegenfeldt, *TMVA - Toolkit for Multivariate Data Analysis with ROOT*, PoS **ACAT** (2007) 040. (Page 129)
- [143] Particle Data Group, P. A. Zyla *et al.*, *Review of particle physics*, Prog. Theor. Exp. Phys. **2020** (2020) 083C01. (Pages 132, 156, and 170)
- [144] L. Anderlini *et al.*, *The PIDCalib package*, LHCb-PUB-2016-021, CERN-LHCb-PUB-2016-021, 2016. (Page 132)
- [145] G. A. Cowan, D. C. Craik, and M. D. Needham, *RapidSim: an application for the fast simulation of heavy-quark hadron decays*, Comput. Phys. Commun. **214** (2017) 239, [arXiv:1612.07489](#). (Page 132)
- [146] LHCb collaboration, R. Aaij *et al.*, *Search for time-dependent CP violation in  $D^0 \rightarrow \pi^+\pi^-\pi^0$  decays*, [arXiv:2405.06556](#), LHCb-PAPER-2024-003, CERN-EP-2024-111. (Pages 135, 136, 148, 149, 175, 179, and 186)
- [147] P. Marino, *Measurement of the CP violation parameter  $A_\Gamma$  in  $D^0 \rightarrow K^+K^-$  and  $D^0 \rightarrow \pi^+\pi^-$  decays*, CERN-THESIS-2017-007, 2017. PhD thesis. (Page 141)
- [148] R. Brun and F. Rademakers, *ROOT: An object oriented data analysis framework*, Nucl. Instrum. Meth. A **389** (1997) 81. (Page 146)
- [149] N. L. Johnson, *Systems of frequency curves generated by methods of translation*, Biometrika **36** (1949) 149. (Page 155)

- [150] A. Rogozhnikov, *Reweighting with boosted decision trees*, J. Phys. Conf. Ser. **762** (2016) 012036, [arXiv:1608.05806](https://arxiv.org/abs/1608.05806), [https://github.com/aarogozhnikov/hep\\_ml](https://github.com/aarogozhnikov/hep_ml). (Page 173)
- [151] A. Davis *et al.*, *Measurement of the instrumental asymmetry for  $K^-\pi^+$ -pairs at LHCb in Run 2*, LHCb-PUB-2018-004, 2018. (Page 178)
- [152] L. Dufour, *High-precision measurements of charge asymmetries at LHCb*, CERN-THESIS-2019-281, 2019. PhD thesis. (Page 178)
- [153] ATLAS collaboration, G. Aad *et al.*, *Luminosity determination in pp collisions at  $\sqrt{s} = 13$  TeV using the ATLAS detector at the LHC*, Eur. Phys. J. C **83** (2023) 982, [arXiv:2212.09379](https://arxiv.org/abs/2212.09379). (Page 185)